Università degli studi di Catania

Dipartimento di Fisica e Astronomia
Dottorato di Ricerca in Fisica - XXXI CICLO

DOCTORAL THESIS

High resolution linear spectropolarimetry: a study of the potentiality in probing stellar atmospheres and circumstellar environments

Manuele Ettore Michel Gangi

Supervisor Chiar.mo Prof. Francesco Leone

Manuele Ettore Michel Gangi
High resolution linear spectropolarimetry: a study of the potentiality in probing stellar atmospheres and circumstellar environments
Supervisors: Chiar.mo Prof. Francesco Leone

Università degli studi di Catania
Dottorato di Ricerca in Fisica - XXXI CICLO

Dipartimento di Fisica e Astronomia
Via S. Sofia, 64
95123 and Catania

Abstract

Polarimetry is considered as an important searching tool in Astronomy and it deserves to be a standard observational technique for a variety of astrophysical environments. Many phenomena, in fact, can contribute to the polarisation of radiation and so, its observation can potentially provide information about their basic causes. In particular, in a stellar context high resolution spectropolarimetry can potentially: (i) investigate the physics of the shaping mechanisms of the protoplanetary nebulae (PNe) and the possible interaction between the central star and the very close surrounding, (ii) investigate stellar photospheric inhomogeneities (e.g. pulsations, granulations, hot spots and magnetic activity), (iii) play a key role in the exoplanet research. Despite this, however, the difficulties involved in the measurements and in the theoretical interpretation made this technique not as widespread as it deserves.

The main goal of this work is to demonstrate the diagnostic potential of high resolution linear spectropolarimetry. At this purpose, we studied the polarised spectrum of the post-AGB binary system 89 Herculis on the basis of data collected with the high resolution *Catania Astrophysical Observatory Spectropolarimeter* (CAOS) and *HArps-North POlarimeter* (HANPO), in addition to archive data taken with the *Echelle SpectroPolarimtric Device for the Observation of Stars* (ESPaDOnS). We found the existence of linear polarisation in the metal lines in absorption and in some of the metal lines in emission: this is the first *Second Solar Spectrum* ever observed in a star different than the Sun. We have then analyzed the observed polarisation properties. Firstly, regarding the polarisation measured across the absorption lines, we found that the complex Stokes Q and U morphologies vary with the orbital period of the system. We then rule out magnetic field, continuum depolarisation due to pulsations and hot spots as a possible origin. We found that in the framework of optical pumping due to the secondary star, the observed periodic properties of the spectral line polarisation can be justified by two jets, with a flow velocity of a few tens of $km\ s^{-1}$, at the basis of that hourglass structure characterizing 89 Herculis. Regarding the emission lines, numerical simulations show that these polarised profiles could be formed in an undistrupted circumbinary disk rotating at $\leq 10\ km\ s^{-1}$ and with an orientation in the sky in agreement with optical and radio interferometric results. We have concluded that the study of aspherical envelopes, the origin of which is not yet completely understood, of PNe and already present in post-AGBs can benefit

from high resolution spectropolarimetry and that this technique can shape envelopes still too far away for interferometry.

In addition, we have conducted a large spectropolarimetric survey on a sample of F-G-K bright stars to understand if the presence of intrinsic linear polarisation is a rare case or it is widespread in these type of stars. Surprisingly, we have found linear polarisation across metal lines in absorption for about $71\ \%$ of stars of our sample. Some of them clearly show temporal variability, to be characterized with further data. Despite this study is neither exhaustive nor conclusive we speculated that the presence of linear polarisation in the stars is not rare: a broad and in-depth spectropolarimetric study is then necessary.

Contents

1 Introduction

> *My goal is simple. It is a complete understanding of the universe, why it is as it is and why it exists at all.*
>
> **— Stephen Hawking**

The knowledge of the Universe has been based for a long time exclusively on the study of its light. Over the time the advancement of the knowledge of light physics on the one hand and technological improvement on the other, has allowed us to *open new windows* for astrophysical investigation. So it happened passing from the study of the *quantity* of light emitted from the stars (*photometry*) to the *composition* of the light itself (*spectroscopy*). This work is devoted to another aspect of light that, although discovered more than a century ago, has only recently become widespread among a very small group of astrophysicists. This aspect is related to the *orientation* of the electric field vector in time and space and it seems to be an important and promising diagnostic tool for a variety of astrophysical environments: we are talking about *polarisation*. Many phenomena, in fact, can contribute to the polarisation of radiation and so, its observation can potentially provide information about their basic causes.

In this introductory chapter we will present the most important astrophysical contexts where *linear polarisation* could play a key role (Sec. 1.1); consequently, we give the motivations that have fueled the work carried out through these phD years (Sec. 1.2). Finally, the structure of this Thesis is presented in Sec. 1.3.

1.1 Astrophysical contexts of interest

1.1.1 AGB, post-AGB stars and circumstellar environments

In this section we describe the main characteristics of the final stage of low and intermediate mass stars and the related circumstellar envelopes. We then show the role played by polarimetry in this context.

References of this Section are Herwing (2005), Hilditch (2001), Klochkova (2014), Van Winckel (2003) and Martínez González et al. (2015).

AGB evolution

The Asymptotic Giant Branch (AGB) is a region ot the Hertzsrpung-Russel diagram where evolved cool luminous stars are placed. They are low and intermediate mass stars ($0.6 - 10 M_{\odot}$) in an evolved phase of their life.

During the early AGB (E-AGB) phase, the star has an inert and degenerate carbon-oxygen core, surrounded by a helium burning shell and by a more external hydrogen shell. The latter is surrounded, in turn, by a very extended stellar envelope. In this situation, nuclear production is dominated by helium shell burning via 3-alpha process, that is very temperature sensitive.

When the helium shell runs out of fuel, the star begins the late stage of AGB phase, called *thermally pulsing* AGB (TP-AGB). Now, nuclear production is dominated by hydrogen shell burning. Helium shell, in fact, is restricted in a very thin layer and its fusion becomes inefficient. The layers above it contract, thus heating the hydrogen shell until it is re-ignited. As the hydrogen burning occurs, helium is again rebuilt and there is an increase of helium shell until it ignites explosively in a process called *helium shell flash*. Depending of the core mass, the helium shell flash luminosity can reach values of the order of $L_{He} = 10^8 L_{\odot}$, but it decreases exponentially over just a few years. The excess of energy released during the first helium shell flash pushes outwards the layers above helium shell. Due to this expansion, the temperature decrease shuts off the hydrogen shell burning and causes a strong convection zone between the two shells. When, due to the convection and helium burning, there is an increase of temperature near the base of hydrogen shell, it is reignited and the cycle begins again with a second helium flash and so on: in this phase hydrogen and helium shell burning alternate. Figure 1.1 shows a schematic structure of an AGB star during its thermally pulsing phase.

An important characteristic of this phase is the strong mass loss ($10^{-8} - 10^{-4} M_{\odot}$ yr^{-1}). Actually there are two different evolutionary phases where this occurs. The first is in red giants before large amplitude pulsation starts. These mass loss rates are slow ($< 10^{-8} M_{\odot}\ yr^{-1}$) and occurs mostly on the RGB and on E-AGB. The other one is in AGB stars with large amplitude pulsations (e.g. *Mira variable stars*). In this case rates can be as high as $10^{-4} M_{\odot}\ yr^{-1}$ and these are know as *superwinds*.

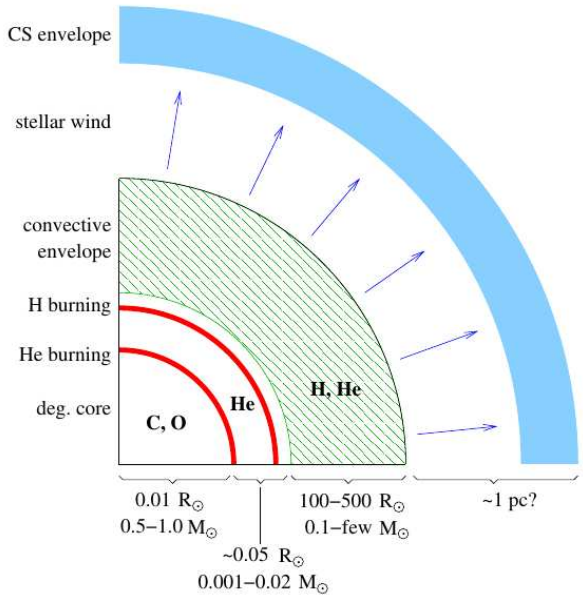

Fig. 1.1.: Schematic structure of an ABG star. Figure adapted from https://astro.uni-bonn.de/ nlanger/siu_web/ssescript/new /chapter10.pdf.

Mass loss is a very important feature not only for stellar evolution but also for the galactic chemical evolution. In fact, AGB phase is terminated when mass loss has removed the envelope of the star and a post-AGB object is formed. The time scale of the AGB phase for a particular source depends on its mass loss rate. Thanks to the mass loss mechanism, the synthesized products of AGB evolution are spread into the interstellar medium and leads to the chemical enrichment. However the causes of mass loss phenomenons are still not clear. Probably a combination of dynamical pulsations and radiation pressure on dust particles formed in the stellar atmosphere plays a crucial role in this context.

post-AGB evolution

Post-AGB evolution begins when mass loss has removed the envelope of AGB star and it evolves on a fast track in the H-R diagram towards higher effective temperatures at roughly constant luminosity. The typical time scale of this phase is of the order of $10^4\ yr$.

In this stage the hydrogen burning shell is still fully active and the star moves towards higher effective temperatures due to the decreasing mass of the envelope, which is eroded at the bottom by hydrogen shell burning and at the top by continuing mass loss. At the end of post-AGB phase, when $T_{eff} > 1.5 \cdot 10^4 K$, a strong UV flux is formed and it destroys the dust grains in the inner shells of circumstellar envelope,

dissociates molecules and ionizes the gas. This leads to the formation of outstanding sources with a variety of striking morphologies known as *Planetary Nebulae* (PNe) (Fig. 1.2).

Finally, when the envelope mass is such that the hydrogen burning shell is extinguished, the luminosity starts decreasing and the star moved into the final stage of *white dwarf*.

The circumstellar environments

It is believed that the mass loss process along the evolution in the AGB phase is spherically symmetric. However, as we can see in figure 1.2, many circumstellar environments are characterized by aspherical geometries that include elliptical, bipolar or multipolar shapes, involving axisymmetric outflows or equatorial density enhancements (Bujarrabal, 2001). Consequently, during the mass loss process and subsequently stages, star and circumstellar envelope must undergo fundamental and rapid changes in structure, mass loss mode and geometry. Unfortunately it is not yet clear what are the main processes that occurs at this stage and this is still a matter of discussion. For example, despite many theories invoke magnetic fields to explain the rich variety of aspherical components observed in PNe, no direct observational evidence of such fields has yet been established (Leone et al. 2011; Jordan et al. 2012; Leone et al. 2014; Asensio Ramos et al. 2014; Sabin et al. 2015). A further particular case regards the *binary* post-AGB with a common circumbinary envelope: it seems that the shape and the shaping of PNe are here strictly connected with the binary dynamics.

The work of Balick & Franck (2002) reviewed in great detail the shape and shaping of PNe; here we summarize the main characteristics of the geometric structures. The most common description of global morphology is given by Balick (1987) who performed a classification scheme based on the outline of the spatially resolved nebulae. He distinguished four main morphological types of PNe: **Round** (R), **Elliptical** (E), **Bipolar** (Bp) and **Irregular**. Bipolar class is subdivided into **Butterfly** and **Bilobed**. The first is characterized by the fact that the waist is pinched into the center while the second has a pair of larger outer lobes connected to a central R or E nebula. In general butterfly PNe shows a more complex structure and kinematic patterns than bilobed PNe. Observational studies revealed that butterfly PNe are often characterized by a luminous and cool central star with spectral features of symbiotic or Miras. Another description of global morphology is based on the highest degree of overall symmetry of the nebular interior (Manchado, 2000). There are four basic morphological types: **Axisymmetric**, **Reflection Symmetric**, **Point-**

symmetric and **Asymmetric**. The first is a symmetry around the major and minor axes, the second is a reflection symmetry about the minor axis only, the third is a reflection symmetry about the nebular center and the last has no symmetry about on axis or point. In general, point-symmetric nebulae tend to be S-shaped, corkscrew-like or multipolar, while reflection-symmetric nebulae are very rare.

Observational evidences

There are many observational evidences that give us different constraints about nature and physical conditions of PNe. Most of them reveal the presence of a stable disk that is probably in a Keplerian motion. In particular:

- the *spectral energy distribution* (SED) shows that both hot and cold dust must be present in the circumstellar environment. One of the most remarkable features is that the dust excess starts at dust sublimation temperature ($T_{dust} \sim 1200K$), irrespective of the effective temperature of the central star. This means that, using the equation of thermal equilibrium of blackbody dust grains, a limit on the distance d of these dust grains from the central star can be found by:

$$1200K = T_{dust} = \left(\frac{R_*}{2d}\right)^{1/2} T_*, \tag{1.1}$$

  with R_* and T_* the radius and the effective temperature of the star (Deroo Pieter, 2007);

- the strong infrared excess is not accompanied by a strong circumstellar reddening. This means that there is no line-of-sight extinction and this support the idea of an aspherical dust distribution;

- some objects, in the case of post-AGB binary, show variable extinction in phase with the orbital motion. This phenomenon is most plausible if the dust is not distributed in a spherical shell but in a disk surrounding the system. In fact, in this way, if the disk is observed under high inclinations the amount of the dust in the line-of-sight is largest at inferior conjunction and this explain the extinction variations;

- for many objects there is observational evidence that the circumstellar environment must be very stable. In fact, much higher degrees of crystalline dust grains are found and there is also a significant fraction of large grains and macro-structures that can be formed only in a stable environment.

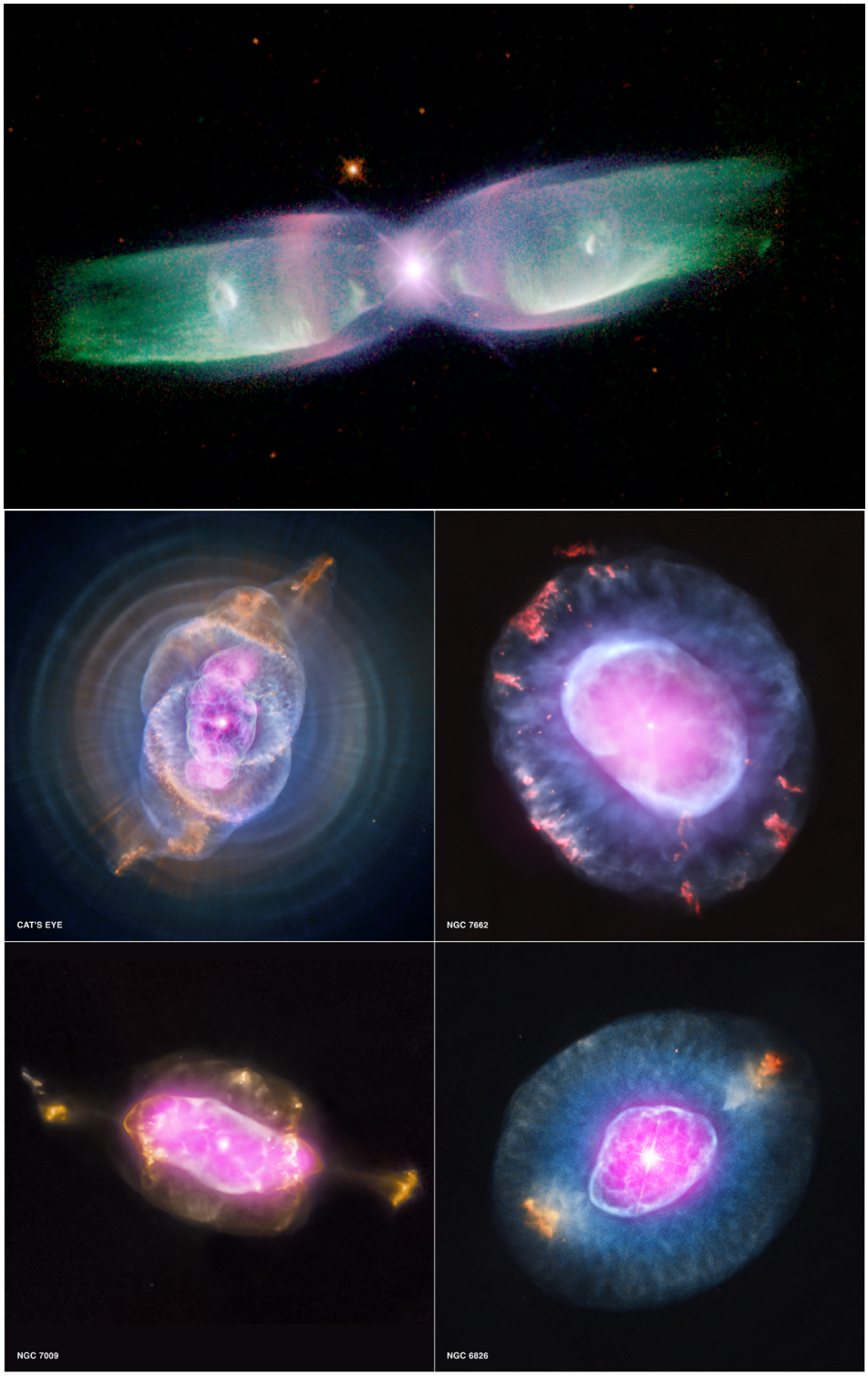

Fig. 1.2.: A sample of the wide variety of morphologies observed at the planetary nebula phase. From top to bottom and from left to right: M2-9 (also know as "Butterfly Nebula", credit B. Balick), NGC 6543 (also know as Cat's Eye), NGC 7662, NGC 7009, NGC 6826 (Credit NASA's Chandra X-ray Observatory).

In addition, many peculiarities in the optical spectra of these systems are present (Klochkova 2009, 2014). In particular, the most important spectral features are:

- low and moderate intensity metal absorptions, whose symmetric profiles show no apparent distortions;

- complex profiles of neutral hydrogen lines, which vary with time and include absorption and emission components;

- strong metal lines in absorption with low excitation potentials of the lower level; their variable profiles are often distorted by envelope features that make the profile asymmetric or split into several components. It could be associated with the kinematic of the circumstellar environment;

- absorption or emission bands of molecules mostly containing carbon;

- envelope components of the Na I and K I resonance lines;

- narrow permitted or forbidden emission metal lines that form in envelopes.

The role of linear polarisation

From what has been said, it is of fundamental importance to understand the structure of the PNe and then investigate the possible shaping mechanisms. The most widespread technique used for this purpose is certainly *interferometry*; optical, infrared and radio interferometry could provide the highest resolution images ever achieved in astronomy (see e.g. Monnier, 2003; Thompson et al. 2017). However:

- data interpretation is strongly model dependent: in absence of complementary information, the identification of the source of emission/scattering and, consequently, the structure of PNe remain often inconclusive;

- the inner regions of PNe (where the shaping mechanisms most likely originate) are too far even for the highest resolution interferometry today available.

In this context high resolution spectropolarimetry:

- can investigate the physics of the shaping mechanisms (e.g. scattering on dust particle and/or electrons, magnetic fields, anisotropy of the radiation field);

- can provide geometrical constraints to be compared with the results coming from other techniques (e.g. interferometry);

- can investigate the inner regions of PNe giving information on the possible interaction between the central star and the very close surrounding.

An interesting example is provided by the PNe Red Rectangle (HD44179). Martínez González et al. (2015) carried out high-sensitivity spectropolarimetric observations of the central star to constrain the shaping mechanisms of the PNe biconical structure. They found a $\sim 1.4\%$ continuum linearly polarisation, constant in time, with an angle of $\sim 45°$, that is surprisingly coincident with the position of one of the spikes of the biconical structure (Fig. 1.3). They found also linear polarisation accross the Balmer lines as well as the Ca II K lines with angles that are rotated from $10°$ to $85°$ with respect to the continuum agle ($\sim 45°$). This latter evidence rules out the possibility of *continuum depolarisation*[1] and allow for *resonant scattering*, i.e., polarisation in spectral lines. Resonant scattering is in turn indicative of the presence of an *anisotropic radiation field*.

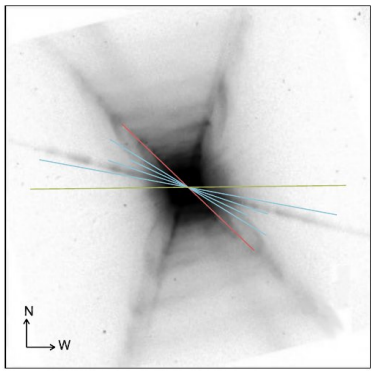

Fig. 1.3.: The Red Rectagle PNe seen in the red (Koning et al. 2011). The red line represent the direction of the polarisation of the continuum that is coincident with one of the two spikes of the biconical shape. The blue lines represent the direction of the polarisation of the Balmer lines, while the green one represent the direction of Ca II K line. Image adapted from Martínez González et al. (2015).

In the light of these evidences, the authors conclude that the continuum polarisation is due to scattering in a not uniform bipolar outflow or in a dense collimated jet. Moreover, local density accumulations that produce modification in the anisotropy of the radiation field must be present to explain the polarisation features observed in the Balmer and Ca II K lines.

Here we want to stress that the not well conclusive result of this study is only because of the few observational data available; spectropolarimetry at high resolution in these kind of environments could be a very powerful instrument of investigation

[1] When the continuum flux is polarised, the presence of lines (i.e. *local* decreases of the continuum flux) led to *local* depolarisation. In high resolution spectropolarimetry the continuum polarisation is usually set to zero and what was a depolarisation signal becomes a net signal over zero.

to probe the physics and the geometry of large and small structures. We have the theoretical models and we only need data.

1.1.2 Stellar photospheric inhomogeneities

Photometric and spectroscopic variabilities are often due to many phenomena that occur at photosperic level, such as pulsations, granulations or, more in general, short and long term evolution of active regions and magnetic cycles. The *General Catalogue of Variable Stars* lists more than 100 types and subtypes of variable stars, depending on the variability properties of their light curves and on the physical causes of their variability (Fig. 1.4, Samus et al. 2009). A deep study of these causes is required not only for understanding the atmospheric phenomena themselves, but also because they may limit our capabilities to interpret the observational data of the most presently interesting case of planet searches (see e.g. Moulds et al. 2013).

In this Section we give some basic concepts on stellar pulsations, granulations and activity, to show the role that linear spectropolarimetry can play in these contexts. References of this Section are Aerts (2010) and Gray (2005).

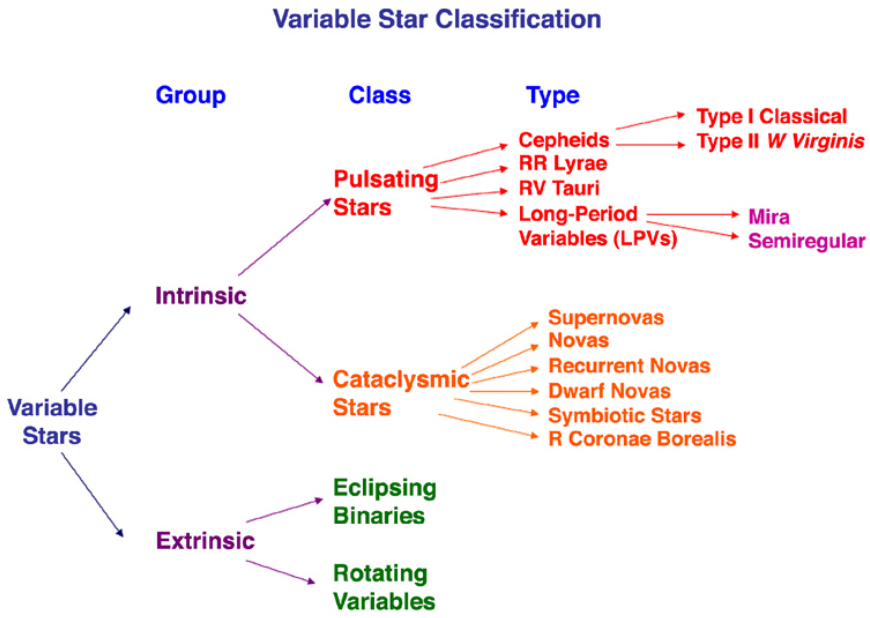

Fig. 1.4.: Variable star classification. Image adapted from http:// chandra.harvard.edu.

Pulsations

Variable pulsating stars are found in specific regions of the HR diagram, as illustrated in Fig. 1.5. Many types of pulsating variables are, in fact, confined to a narrow, rather vertical, strip in the HR diagram called the *instability strip*. This suggests that there are one or more mechanisms operating in a variety of stars in different luminosity classes, but over a relatively narrow range of surface temperatures, that leads to pulsational instability. In particular there are three *driving mechanisms* responsible of generating oscillations in all the main class of pulsators:

- *k-mechanism*: this mechanism is connected with the opacity. In particular, if a layer contains partially ionized gas, the opacity blocks radiation. This leads an increase of temperature and pressure with a consequent expansion. But at the same time, a portion of energy flowing into the layer can go into more ionization. The ionization of the gas reduces the opacity, radiation flows through, the gas cools and the star contracts. During the compression there is a recombination of ions with electrons, the opacity increase and the cycle begins again. For most stars there are two significant zones of partial ionization, corresponding to the possible stages of ionization for hydrogen and helium;

- *stochastic mechanism*: this is the major driving mechanism that operates in the Sun and solar-like oscillators. In these stars the acoustic energy of the convective motion, which is comparable to the sound speed, is sufficient to cause resonance at a star's natural frequencies where a part of the energy is transferred into global oscillation modes;

- ϵ*-mechanism*: this mechanism is, in principle, important for the stability of very massive stars (of order $100M_{\odot}$). In this case variations in the energy generation rate in the core of the star could drive global pulsations. However until today there is no evidence on the existence of class of pulsating stars that are driven by this mechanism alone.

Granulations

Granulation is the surface-visible signature of convection. The latter, in turn, is a central parameter in the construction of stellar models. In fact, it influence the energy transport through the atmosphere and the replenishment of nuclear fuels in the core. It probably supplies the energy for generating magnetic fields, heating stellar chromospheres and coronae and driving stellar winds.

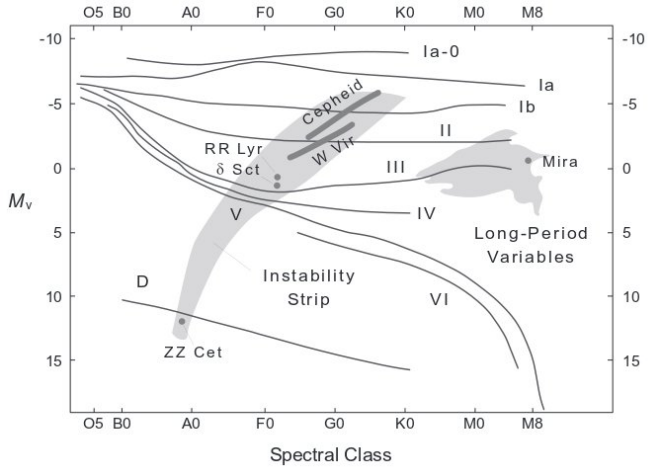

Fig. 1.5.: The instability strip and the region of long-period variables in the HR diagram. Image taken from http://eagle.phys.utk.edu/guidry.

Granulation structures were first discovered on the solar surface (Herschel, 1801) and nowadays their properties are well explained. In the stellar case, all stars with a convective envelope show granulation, evolving in time and producing quasi-periodic brightness fluctuations on a wide range of timescales and amplitudes (see e.g. Mathur et al. 2011).

In addition to photometric variations, granulation can be studied through subtle spectral line asymmetries. These asymmetries are extremely powerful in giving us information on photospheric velocity fields. Fig. 1.6 shows an asymmetric line profile and its bisector[2]. The asimmetry arises due to the different numbers of photons contribution of rising and falling material to the flux spectrum.

Short and long term evolution of stellar activity and magnetic fields

With stellar activity it is intended the whole of the phenomena related to the presence of magnetic fields. In the presence of convection, magnetic fields are responsible of phenomena similar to the solar case, such as sunspots, prominences, highly structured coronal regions and dynamo cycle, involving all of the stellar atmospheric layers. On the contrary, stars without convective envelope possess stable magnetic fields. The study of stellar magnetism is then important for the understanding of the structure and evolution of stars, their atmospheres and the related energy release mechanism in hot plasma. It is also important in order to investigate possible false detections of exoplanets and to characterize star-planet interactions. Furthermore,

[2]The bisector is a locus connecting the midpoints of line segments running horizontally between the sides of the profile.

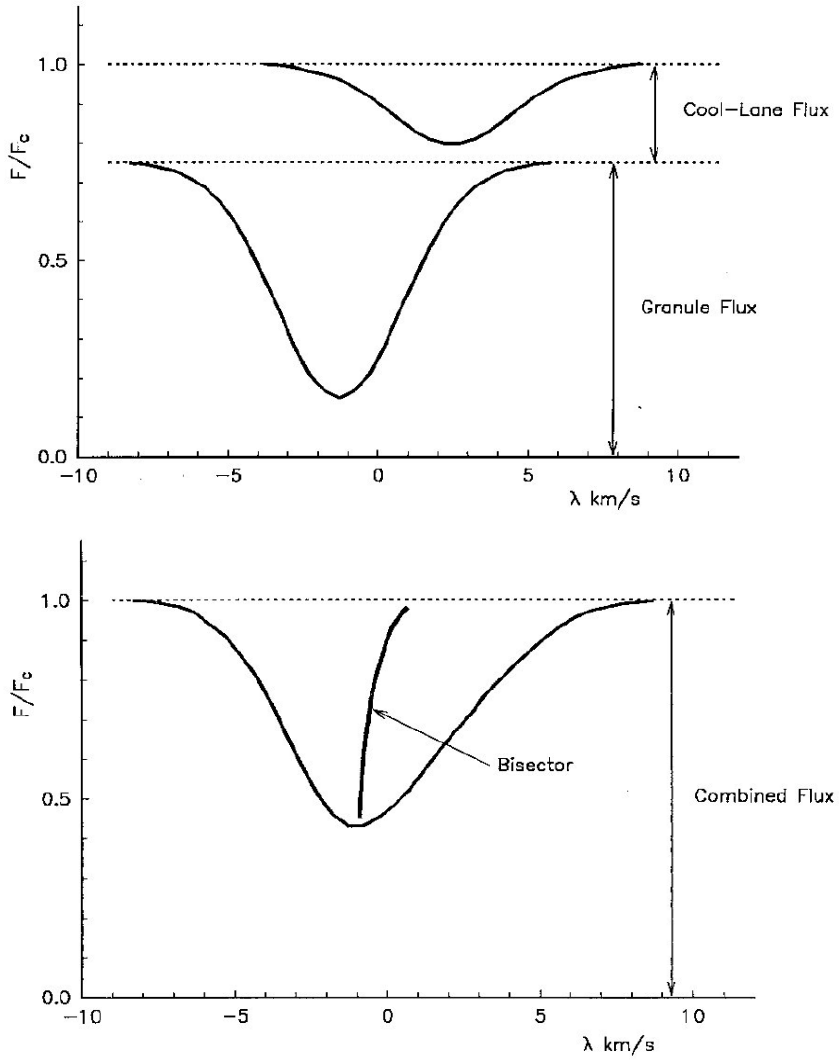

Fig. 1.6.: Top: spectrally blue-shiftde profiles from hot, briht and rising elements contribute more photons than the darker, cool and sinking ones. Bottom: the resuling line profile, after averaging on stellar surface, becomes asymmetric and its "C" shaped bisector demonstrates the asymmetry of the line. Figure adapted from Gray (2005).

the analysis of the temporal variability is used not only to characterize the activity, but also to estimate important stellar parameters.

Magnetic fields were detected in almost all the stages of stellar evolution; from pre main sequence stars (e.g. Johns-Krull, 2007; Hussain & Alecian, 2014) to solar like stars (e.g. Valenti et al., 1995; Reiners, 2012), upper main sequence stars (e.g. Babcock, 1947; Mathys, 2017), giant stars (e.g. Konstantinova-Antova et al., 2008; Aurière et al., 2015) and dwarfs (e.g. Kemp et al., 1970; Ferrario et al., 2015). Despite this, it is not yet clear how magnetic field evolves during stellar evolution.

The role of linear polarisation

In the presence of surface magnetic fields of Gauss level, the Zeeman effect is the major contributor to the linear polarisation. In this case the intensity of circular polarisation is about one order greater than the linear polarisation (Wade et al., 2000). In addition, instrumental smearing is more destructive for Stokes Q and U profiles, because their variations are more complex and occur on shorter wavelength scales (Leone et al. 2003). In this context, therefore, different techniques have been developed to measure the magnetic field only from Stokes V. In particular, a method suggested by Bagnulo et al. (2002) allow to determine the effective longitudinal field $B_{||}$ through a linear fitting of Stokes V against the gradient of Stokes I, according to the equation (Mathys, 1989):

$$\frac{V_\lambda}{I_\lambda} = -4.67 \cdot 10^{-13} \bar{g} \lambda^2 B_{||} \frac{1}{I_\lambda} \frac{\partial I_\lambda}{\partial \lambda} \tag{1.2}$$

where $\bar{g}$ is the so called *effective Landé factor* and it is related to the Landé factors g_1 and g_2 of the involved energy levels:

$$\bar{g} = 0.5(g_1 + g_2) + 0.25(g_1 - g_2)d \tag{1.3}$$

with

$$d = [J_1(J_1 + 1) - J_2(J_2 + 1)], \tag{1.4}$$

and J_1 and J_2 the angular momenta of the levels. But, in order to obtain a complete magnetic topology, it is also necessary a measure of the transverse magnetic component $B_\perp$. Leone et al. (2017) extended the method of Bagnulo et al. (2015) to obtain a direct measurement of the transverse component of stellar magnetic fields by the regression of Stokes Q and U as a function of the second derivative of Stokes I, according to the equations (Degl'Innocenti & Landolfi, 2006):

$$\frac{Q_\lambda}{I_\lambda} = -5.45 \cdot 10^{-26} \bar{G} \lambda^4 B_\perp^2 \cos 2\chi \frac{1}{I_\lambda} \frac{\partial^2 I}{\partial \lambda^2} \tag{1.5}$$

$$\frac{U_\lambda}{I_\lambda} = -5.45 \cdot 10^{-26} \bar{G} \lambda^4 B_\perp^2 \sin 2\chi \frac{1}{I_\lambda} \frac{\partial^2 I}{\partial \lambda^2} \tag{1.6}$$

where

$$\bar{G} = \bar{g}^2 - \delta \tag{1.7}$$

is the second order effectibe Landé factor, with

$$\delta = (g_1 - g_2)^2(16s - 7d^2 - 4)/80 \tag{1.8}$$

$$s = [J_1(J_1 + 1) + J_2(J_2 + 1)]. \tag{1.9}$$

On the contrary, if there is a strong linear polarisation, larger than Stokes V, we are not in the Zeeman regime (i.e. we have to rule out the presence of Gauss or sub-Gauss photosperic magnetic fields). In this case linear polarisation signatures occur because of the breaking of certain symmetries. These may be due, for example, to rotational deformities, aspherical winds, tidal distortions in binary systems, the Chandrasekhar effect during eclipse of binary systems (Chandrasekhar, 1946) or, more in general, radiation anisotropies induced by photospheric inhomogeneities with the possible influence of very weak magnetic fields (i.e. μG or nG). We will discuss these physical mechanisms in great detail in Chapter 4.

Historically, the discovery of the linearly polarised spectrum of the Sun (the so called *Second Solar Spectrum*) opened up a "new window for diagnostics of the Sun" (Stenflo & Keller, 1997). In that case the observed linear polarisation has two contributions: (i) depolarisation of the continuum by absorption and scattering lines and (ii) intrinsic polarisation of lines due to anisotropy releated to center-to-limb variation.

In stellar case, if the same mechanism is taken into account, the disk-integrated linear polarisation would be zero. However, McLean & Cogne (1978) and Fabas et al. (2011) discovered a high polarisation degree, up to 7%, across Balmer lines of variable Mira stars. The same occur also for the resonance line of Ca I at 422.6 nm (Boyle et al. 1986). Harrington & Kuhn (2009b,a) and Lèbre et al. (2011) have shown that linear polarisation is often present in the Balmer lines of evolved stars. In addition Lèbre et al. (2014) and Aurière et al. (2016) discovered linear polarisation across individual metal lines in absorption for the Mira star χCygni and for the red supergiant Betelgeuse respectively. In particular Aurière et al. (2016) interpreted the observed linear polarisation as due to scattering off two bright spots located near the eastern and southern limbs of the Betelgeuse stellar disk. Using the Least Squares Deconvolution (LSD, Donati et al. 1997), Tessore et al. (2015) found evidence of linear polarisation in the spectral lines of the RV Tau variable R Scuti and Sabin et al. (2015) in the lines of the RV Tau variable U Monoceroti as well in the post-AGB star 89 Herculis.

It appears, therefore, that in the case of cool and evolved low- and intermediate-mass stars it is possible to detect intrinsic linear polarisation. Such *Second Stellar Spectrum* could traces the presence of surface inhomogeneities and it can be useful to better characterize stellar photospheres.

1.1.3 Earth and Exoplanets Atmospheres

The presence of a layer of gases surrounding our planet is of fundamental importance for life. The atmosphere of Earth, in fact, protects life by creating pressure allowing for liquid water, warming the surface through the greenhouse effect, absorbing ultraviolet solar radiation and reducing the diurnal temperature variation. A deeper knowledge of the chemistry, physics and dynamics in the different layers within Earth's atmosphere (Fig. 1.7) is required from meteorology to fly engineering, from volcanology to astrophysics. For astrophysicists, in fact, the Earth's atmosphere is considered a starting point for the diagnostics of planet and exoplanets atmospheres.

For these reasons, during the years different instruments and techniques have been developed; also in this case, low and high resolution polarimetry stands as a powerful diagnostic tool.

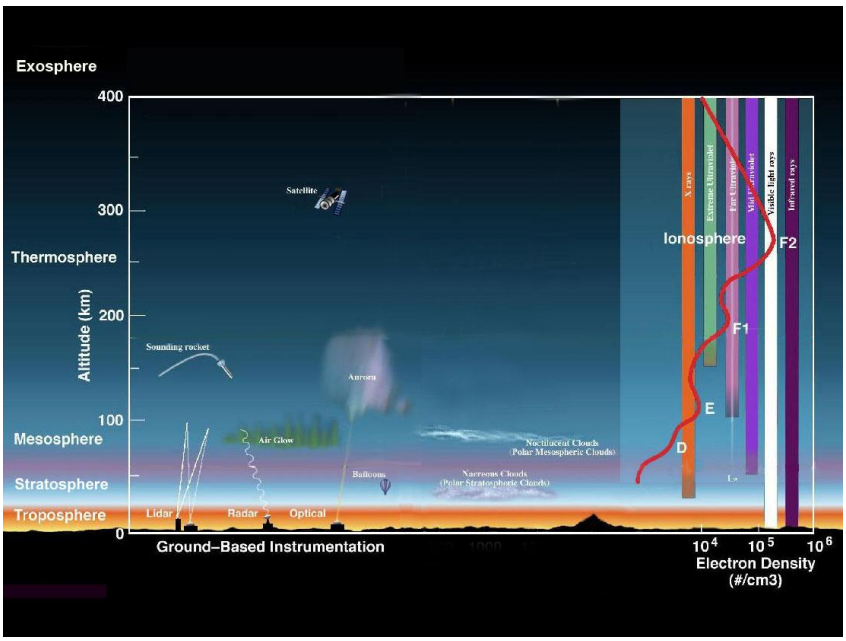

Fig. 1.7.: Diagram of the layers within Earth's atmosphere and instruments used for probing it. Image adapted from www.nasa.gov.

The role of linear polarisation

In the Earth's atmosphere light is strongly linearly polarised by reflection from oceans and land, and by scattering by air molecules, aerosols and cloud particles (Stam 2008). In particular, polarisation measurements are highly sensitive to particle

microphysics and that could be used, for example, to easily monitoring the effect of aerosols on the Earth's climate (Emde et al. 2010).

Sterzik et al. (2012), using the Focal Reducer/Low-dispersion Spectrograph (FORS, Appenzeller et al. 1998) attached at the Very Large Telescope in Chile, measured the disk-integrated linear polarisation of *Earthshine*[3] (Fig. 1.8): they were able to determine the fractional contribution of clouds, ocean surface and the visible areas of vegetation. This work represent an important support for observational study of the atmospheric composition, mean cloud height and surfaces of exoplanets. In principle, in fact, polarimetry enhances the contrast between a star and an exoplanet and hence it could allow for a direct detection of exoplanets and a characterization of their atmospheres.

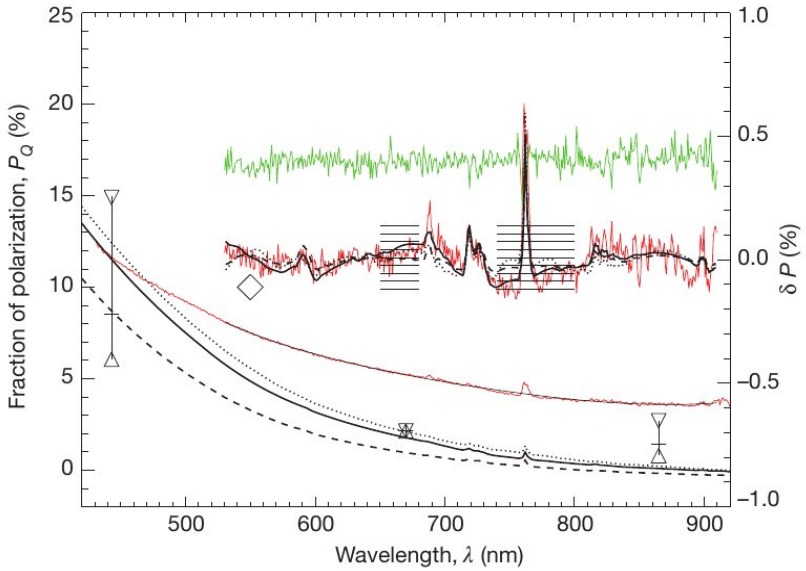

Fig. 1.8.: Earthshine polarisation spectra: fractional polarisation P_Q (red lines) and P_U (green lines) plotted with the model spectra for comparison (black line). Image adapted from Sterzik et al. (2012).

From the theoretical point of view, many efforts have been made in the last years. For example, Seager et al. (2000), Saar & Seager (2003) and Hough & Lucas (2003) performed numerical calculation of flux and degree of polarisation of gaseous exoplanets that are spatially unresolvable from their stars; in this case a large background of stellar flux, that is *assumed* to be *totally unpolarised*, it is taking into account. Stam (2003) and Stam et al. (2003, 2004, 2005) considered, on the contrary, the case of spatially resolvable planets with only a small unpolarised stellar background signal. Berdyugina et al. (2016), by building a bio-polarimetric laboratory experiment (BioPol), modelled intensity and polarised spectra of a representative sample of Earth

[3] With Earthshine it is intended the sunlight that has been first reflected by Earth and then reflected back to Earth by the Moon

plants. They showed that linear polarisation provide very sensitive and unambigous detection of photosynthetic pigments that, if detected in exoplanet atmospheres, could be an indicator for extraterrestial life.

From the observational point of view, many ground-based telescope instruments that use polarimetry for exoplanet research were built. For example:

- **PlanetPol** (Hough et al. 2003), an optical polarimeter attached at the William Herschel Telescope. Now de-comissioned;

- **SPHERE** (Spectro-Polarimetric High-contrast Exoplanet REsearch, Beuzit et al. 2008), operating at ESO's Very Large Telescope, is an extreme adaptive optics system and coronagraphic facility feeding three science instruments: IRDIS, IFS, and ZIMPOL. The latter (Zurich IMaging POLarimeter, Schmid et al. 2005, Gisler et al. 2004) allow for differential polarimetric imaging;

- **DIPol** (Piirola et al. 2005), a double image CCD polarimeter attached of the remotely controlled 60 cm KVA telescope on La Palma, Spain;

- **POLISH** (POLarimeter for Inclination Studied of HIgh mass x-ray binaries/Hot jupiter, Wiktorowicz & Matthews, 2008), a visible light polarimeter attached at the Hale 5m telescope at Palomar Observatory, California;

- **TurPol** (Piirola, 1973, 1988), a U B V R I polarimeter attached at the 2.5 m Nordic Optica Telescope (NOT).

Despite the great effort made both from the theoretical and instrumental point of view, there was only one successful detection of extrasolar planet using polarimetry. It was the case of HD189733 b, a planet discovered in 2005 using transits technique, whose polarised scattered light was detected by Berdyugina et al. (2008). This result was however denied by Wiktorowicz (2009) and later recorfirmed by Berdyugina et al. (2011); this represents well the difficulties involved in these types of measures.

In the light of what has been said in Sec. 1.1.2, we believe that in this context the basic assumption of totally unpolarised stellar radiation should not be underestimated: an in-depth study of the possible presence of intrinsic stellar linear polarisation is necessary.

1.2 Motivation and Problem Statement

From what has been said in the previous Section, high resolution linear spectropolarimetry could be an important diagnostic tool for a variety of astrophysical sources. However, the difficulties involved in the measurements and in the theoretical interpretation made this technique not as widespread as it deserves.

The main goal of the work carried out during my PhD was to demonstrate the diagnostic potential of high resolution linear spectropolarimetry. A great effort was made from an observational point of view, by using the *Catania Astrophysical Observatory Spectropolarimeter* (CAOS) on a large sample of stars and improving the data acquisition and analysis. An equally great effort was made from a theoretical point of view, with the use of numerical codes to interpret the acquired data and cooperating with a group of theoretical researchers from the University of Potsdam.

In particular, most of the time was devoted to a spectropolarimetric monitoring of the post-AGB binary system 89 Herculis. The interpretation of the data has then allowed us to provide new constraints on the complex circumbinary environment characterizing this system. In addition, a large spectropolarimetric survey was made on F-G-K bright stars to understand if the presence of intrinsic linear polarisation is a rare case or it is widespread in these type of stars.

1.3 Thesis Structure

Chapter 2

In this Chapter we deal with the description of polarised radiation presenting, in particular, its mathematical definition (Sec. 2.1). We introduce then the *Stokes parameters* to describe polarisation in practical terms (Sec. 2.2).

Chapter 3

In this Chapter we deal with the *problem of measuring polarisation* across spectral lines at high resolution. We introduce the optical components (Sec. 3.1) and a kind of prototype polarimeter with the main elements that are commonly used in these types of measures (Sec. 3.2, 3.3). In Sec. 3.4 we focus on the description of CAOS spectropolarimeter, whose measures constitute the basis of this work, and the data reduction procedure. Finally, in Sec. 3.5, we present the *Least Square Deconvolution Method* (LSD) that was applied to obtain very high signal to noise polarised spectral line profiles.

Chapter 4

In this Chapter we deal with the theory of linear polarisation. In particular we will focus on the possible mechanisms that lead to continuum polarisation (Sec. 4.1) and to atomic polarisation (4.2), which will be taken into account in the interpretation of our data.

Chapter 5

In this Chapter we deal with the major results achieved during my PhD. A large fraction of time has been devoted to a spectropolarimetric monitoring of 89 Herculis (Sec. 5.1). This allowed us to point out the presence of linear polarisation across absorption (Sec. 5.2) and emission lines (Sec. 5.4) and, for the first time, to use analitical ad numerical model to interpret the observational data in a general scenario (Sec. 5.3, 5.5). Finally, in Sec. 5.6 we focus on the spectroscopic manifestations of 89 Herculis circumstellar envelope: we discuss the long-term episodic mass-loss enhancements (Sec. 5.6.1) and the variability of 6141.713 Å BaII and 5087.418 Å YII lines (Sec. 5.6.2).

Chapter 6

In this Chapter we present the spectropolarimetric survey on F-G-K bright stars that we have conducted in these years. In Sec. 6.1 we present the observed sample of stars while the spectropolarimetric measurements are present in Sec. 6.2. We then investigate the properties of the observational data (Sec. 6.3) and give some comments on single stars (Sec. 6.4).

2 Description of polarised radiation

> *The nature of light is defined by two things, its period of vibration, and its state of polarization.*
>
> **— George Gabriel Stokes**

The history of polarisation and its description is relatively ancient and complex, given that polarisation has a lot of aspects that were discovered many times in different contexts. A first report on a physical effect related to what we call today *polarisation* was given by *Erasums Bartholinus* in 1669, who described the strange effects of the interaction of light with a piece of calcite crystal. After many years, it was *Etienne Louis Malus* who first introduced in the scientific literature the term *polarisation* in his article *Sur une proprieté de la lumière réfléchie* (1809), even if he gave a wrong interpretation of the effect. The important contributions of *Francois Arago*, *Jean-Baptiste Biot*, *David Brewster*, *William Nicol* and *Michael Faraday* later led to a better understanding of the phenomenon. Only in 1852 *George Gabriel Stokes*, in his work entitle *On the composition and resolution of streams of polarized light from different sources*, gave a fully consistent description in mathematical terms of polarised radiation through what are today called *Stokes parameters*.

Despite the long history of polarisation, the *astronomical polarisation* is relatively recent. It begins with *George Ellery Hale* who succeeds in 1908 in observing the spectrum of a sunspot in two opposite direction of circular polarisation and, for the first time, he deduced the existence of a magnetic field on the sun. From then on innumerable steps forward have been made in the use of polarisation in astrophysics.

This chapter is devoted to the description of polarised light. In Sec. 2.1 we give some theoretical outline about polarisation, while in Sec. 2.2 we introduce the Stokes parameters, with their most important characteristics.

The mathematical description and nomenclature in this Chapter follows Degl'Innocenti & Landolfi (2006).

2.1 Polarisation of radiation

An electromagnetic radiation is polarised when there is a non-random distribution of the electric vectors of the wave. Typically two types are distinguished: *linear* and *circular* polarisation, which belong to the general case of *elliptical* polarisation. In the first case the electric vectors are parallel each other and have constant direction, while in the latter the electric vector rotates with the radiation frequency. In general, an electromagnetic radiation is *partially* polarised and any polarisation state can be considered as a composition of different polarisation states.

If the radiation is considered to be propagating along the z axis of a three-dimensional rectangular coordinate system, the components of the electric vectors along the axes are:

$$E_x = a_1 cos(\phi + \theta) \tag{2.1}$$

$$E_y = b_1 cos(\phi + \psi) \tag{2.2}$$

$$E_z = 0 \tag{2.3}$$

with $\phi = wt - \beta z$ and θ, ψ the phases.

Suppose now that the phase difference $\delta = \psi - \theta$ is a time constant, we can rewrite 2.1 and 2.2 as:

$$\frac{E_x}{a_1} = cos(\phi + \theta) \tag{2.4}$$

$$\frac{E_y}{b_1} - cos(\phi + \theta)cos\delta = -sin(\phi + \theta)sin\delta. \tag{2.5}$$

By squaring both members of 2.5 and substituting the 2.4 into the 2.5, we obtain:

$$\left(\frac{E_y}{b_1}\right)^2 + cos^2(\phi + \theta)cos^2\delta - 2\frac{E_y}{b1}cos(\phi + \theta)cos\delta = sin^2(\phi + \theta)sin^2\delta$$

$$\left(\frac{E_y}{b_1}\right)^2 + \left(\frac{E_x}{a_1}\right)^2 cos^2\delta - 2\frac{E_y}{b_1}\frac{E_x}{a_1}cos\delta = sin^2\delta - \left(\frac{E_x}{a_1}\right)^2 sin^2\delta$$

that we can write as:

$$\left(\frac{E_x}{a_1}\right)^2 + \left(\frac{E_y}{b_1}\right)^2 - 2\frac{E_x}{a_1}\frac{E_y}{b_1}cos\delta = sin^2\delta. \tag{2.6}$$

Eq. 2.6 represents a conical; the specific kind of this conical depends on the sign of the quadratic invariant. The quadratic invariant of 2.6 is:

$$\frac{1}{a_1^2 b_1^2} - \frac{cos^2\delta}{a_1^2 b_1^2} \geq 0 \qquad (because\ 0 \leq cos^2\delta \leq 1). \tag{2.7}$$

From the sign of Eq. 2.7 we can deduce that Eq. 2.6 represents an *ellipse*. Therefore the geometric locus of the vector of components E_x, E_y is an ellipse on the plane xy: the radiation is *elliptically polarised*. Note that we had assumed that the phases θ and ϕ are time constants. On the contrary, if θ and ϕ are random variables of time, there is no polarisation.

If $\delta = m\pi$ (with $m \in \mathbb{k}^0$), Eq. 2.6 becomes:

$$\frac{E_y}{E_x} = (-1)^m \frac{b_1}{a_1}. \tag{2.8}$$

This is the equation of a line and in this case we have *linear polarisation*. If $\delta = m\pi/2$ (with $m \in \mathbb{k}$) and $a_1 = b_1 = a$, Eq. 2.6 becomes:

$$E_x^2 + E_y^2 = a^2. \tag{2.9}$$

This is the equation of a circle and in this case we have *circular polarisation* (Figure 3.7). We can also distinguish between *right-hand* polarisation and *left-hand* polarisation. It is shown that if $sin\delta > 0$ there is right-hand polarisation while if $sin\delta < 0$ there is left-right polarisation.

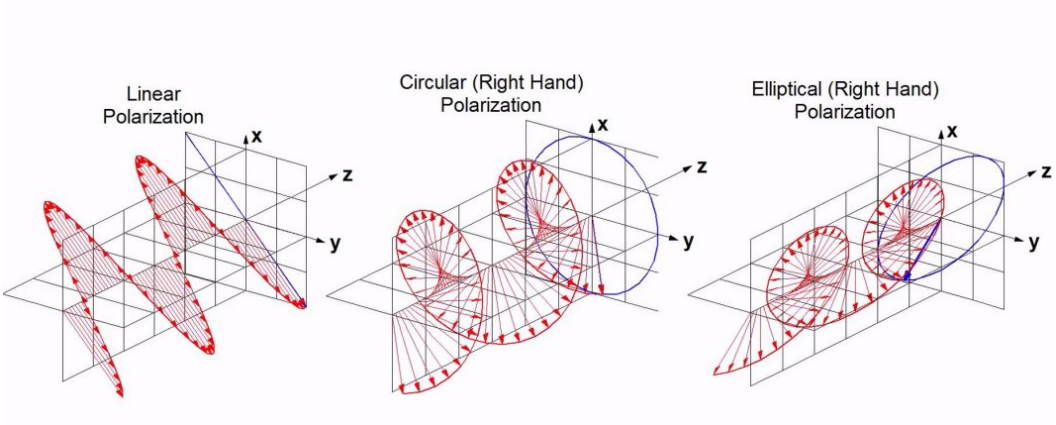

Fig. 2.1.: Pictoric representation of the three types of polarisation.

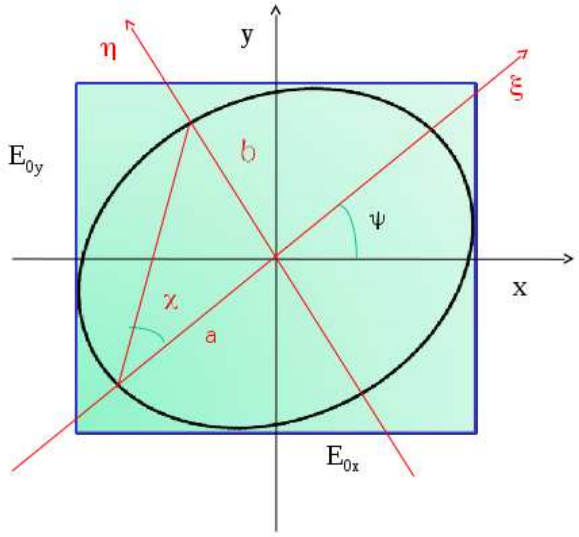

Fig. 2.2.: Polarisation ellipse in the Cartesian system Oξ̂ŷ.

2.2 The Stokes Parameters

In 1852 G.G. Stokes introduced four parameters, nowadays called *Stokes' parameters*, that are used to describe the polarisation state of a radiation. If a and b are, respectively, the semi-major axis and the semi-minor axis of the polarisation ellipse and Ψ is the angle between the x axis and the semi-major axis of the ellipse (Figure 2.2), referring to Eq. 2.6, the Stokes' parameters are defined by:

$$Q = a_1^2 - a_2^2 = \frac{a^2 - b^2}{a^2 + b^2} cos(2\psi) I_p \tag{2.10}$$

$$U = 2a_1 a_2 cos\delta = \frac{a^2 - b^2}{a^2 + b^2} sin(2\psi) I_p \tag{2.11}$$

$$V = 2a_1 a_2 sin\delta = \frac{2ab}{a^2 + b^2} I_p \tag{2.12}$$

$$I = I_u + I_p \tag{2.13}$$

where I_p represents the intensity of the polarised component of the radiation while I_u is the intensity of the unpolarised component of the radiation. Therefore, the fourth Stokes' parameter is simply the total intensity of the polarised radiation.

The four Stokes parameters are not independent; combining Eq. 2.10 with 2.11 and 2.12 we obtain:

$$I_p = \sqrt{Q^2 + U^2 + V^2}. \tag{2.14}$$

Linear polarisation is often expressed also in term of the *polarisation position angle* Θ, that is the angle that the major axis of the polarisation ellipse forms with the

x-axis of the reference system, reckoned counterclockwise for an observer looking at the radiation source. The correct expression, for $Q \neq 0$, is:

$$\Theta = \frac{1}{2} \arctan\left(\frac{U}{Q}\right) + \Theta_0 \tag{2.15}$$

with:

$$\Theta_0 = \begin{cases} 0 & if \quad Q > 0 \quad and \quad U \geq 0 \\ \pi & if \quad Q > 0 \quad and \quad U < 0 \\ \frac{\pi}{2} & if \quad Q < 0 \end{cases} \tag{2.16}$$

while, for $Q = 0$, is:

$$\Theta = \begin{cases} \frac{\pi}{4} & if \quad U > 0 \\ \frac{3}{4}\pi & if \quad U < 0 \end{cases} \tag{2.17}$$

If Q and U are both null, the polarisation position angle is obviously not defined.

2.2.1 Properties of the Stokes Parameters

Stokes parameters have important characteristics, which must be taken into account when working with spectropolarimetry. From Eq. 2.10 ÷ 2.15 it is possible to note that:

- The Stokes Q, U and V parameters depend on the chosen reference system and on the intensity of the polarised component;
- The intensity of the polarised component does not depend on the reference system;
- Any radiation beam can be considered as the incoherent superposition of an unpolarised beam and a totally polarised beam (addition theorem);

- The polarisation position angle does depend on the reference system and does not depend on the intensity of the polarised component.

Furthemore, under rotation of the reference system by an angle χ around the z axis, the new Stokes parameters I', Q', U', V' can be obtained from the older I, Q, U, V through:

$$\begin{bmatrix} I' \\ Q' \\ U' \\ V' \end{bmatrix} = \begin{bmatrix} 1 & 0 & 0 & 0 \\ 0 & \cos(2\chi) & -\sin(2\chi) & 0 \\ 0 & \sin(2\chi) & \cos(2\chi) & 0 \\ 0 & 0 & 0 & 1 \end{bmatrix} \begin{bmatrix} I \\ Q \\ U \\ V \end{bmatrix} \tag{2.18}$$

where we adopted the matrix notation, defining the *Stokes vector* $[I, Q, U, V]$.

From Eq. 2.18 it is possible to note that I and V Stokes parameters are invariant under rotation, while the linear polarisation rotates by an angle 2χ in the $Q - U$ plane.

3

Measurement of polarised radiation

> *The theory without experimental facts would be little better than a study of harmony without practical music: it will be best to begin with experiments.*
>
> — **William Spottiswoode**

The polarisation degree and the Stokes parameters of a source can be measured through different techniques and instruments, called *polarimeters*. The technological difficulties involved in this type of measurements have made the spectropolarimetry a rather recent technique. Moreover typical spectropolarimetric signals are very small and so, conversely, very high signal to noise observations are required. For this reason, at high resolution, the facilities available to perform spectropolarimetry are very limited in number. Nowadays full Stokes polarimeter is possible with **ESPaDonS** (R=68000) at the 3.6 m Canadian-France-Hawaii-Telescope, **NARVAL** (R=65000) at the 2 m Bernard Lyot Telescope and **HARPS** (R=115000) at the ESO 3.6 m telescope. It is also just available **PEPSI** (R=120000) at Large Binocular Telescope and **HANPO** (R=115000) at the Telescopio Nazionale Galileo. Since 2015 **CAOS** (R=55000) is also available at the 0.91 m telescope of the *Catania Astrophysical Observatory*, which was calibrated and used during my Ph.D.

In this Chapter we deal with the *art of measuring polarisation* across spectral lines at high resolution. We introduce the optical components (Sec. 3.1) and a kind of prototype polarimeter with the main elements that are commonly used in these types of measures (Sec. 3.2, 3.3). In Sec. 3.4 we focus on the description of CAOS spectropolarimeter, whose measures constitute the basis of this work, and the data reduction procedure. Finally, in Sec. 3.5, we present the *Least Square Deconvolution Method* (LSD) that was applied to the reduced data to obtain very high signal to noise polarised spectral line profiles.

The mathematical description and nomenclature in this Chapter, where it is not otherwise specified, follows Degl'Innocenti & Landolfi (2006).

3.1 Optical components for polarimetry

Polarimeters usually contain a number of components that are optically active in the sense that they alter the state of polarisation of the radiation. In general they cannot be easily classified into an unique scheme. In any case we can distinguish between *polarisers* and *retarders*. In the following subsections we introduce their basic concepts.

3.1.1 Polarisers

An ideal polariser is an optical device that is totally transparent to a radiation whose electric field vector vibrates along a particular axis and totally opaque to electric fields vibrating along an axis perpendicular to the former. In this way a polariser returns a lineraly polarised beam, independently of the polarisation state of the incident radiation.

There are two main categories of polarisers. The first one consists of the so-called *absorptive polarisers* while the second one consists of the so-called *beam-splitting polarisers*. In the absorptive polarisers the unwanted polarisation states are absorbed while in the beam-splitting polarisers the unpolarised beam is splitted into two beams (called *ordinary* and *extraordinary* rays) characterized by orthogonal polarisation states. For astronomical measures it is hence preferred the last category of polarisers, because the waste of light that occurs with the absorptive polarisers gets worse the measurement accuracy.

The most widely used and simple polarising beam-splitters are based on *birefringent crystals* (Fig. 3.1). These materials have different refractive index for radiation propagating in the direction of refraction:

$$n_x \neq n_y \neq n_z. \tag{3.1}$$

In particular, in the so-called *uniaxial crystals* there is only one axis with different index of refraction and it is called *optic axis* or *principal axis*. An important properties is the *birefringence*. If we denote with μ_o and μ_e respectively the index of refraction relating to the ordinary ray and the index of refraction relating to the extraordinary one, the birefringence of a polariser is defined as:

$$J = \mu_E - \mu_O. \tag{3.2}$$

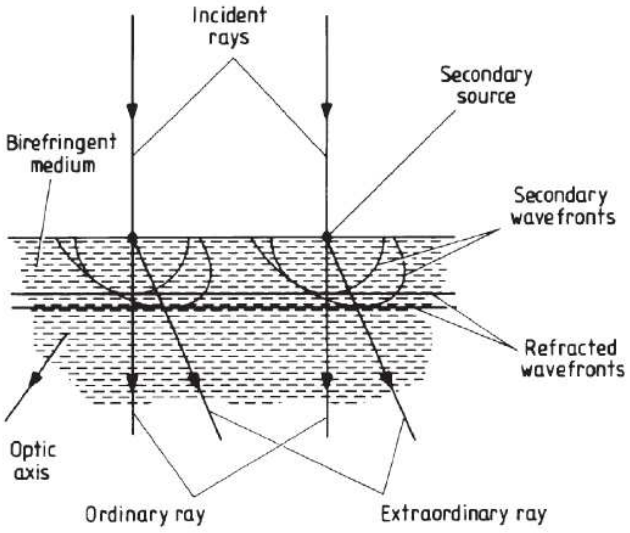

Fig. 3.1.: Formation of ordinary and extraordinary rays in a birefringent medium. Ordinary ray follows the *Snell's law* and its trajectory can be built from the incident point, considering the spherical envelopes of the *Huygens wave front*. These latter spread with uniform velocity. Extraordinary ray, on the contrary, does not follow the *Snell's law* and the *Huygens* envelopes are elliptical. Figure adapted from Kitchin (2003).

Between materials used, it is used calcite ($CaCO_3$) with $J = -0.172$ and quartz (SiO_2) with $J = 0.009$. Calcite, in particular, is transparent from about 0.24 to 1.8 μm and it can be employed from the UV to the IR.

There are many types of beam-splitter commonly used for astronomical purpose. Here we describe only the kinds implemented in the instruments used in this work. They are:

- The ***Wollaston prism*** (Fig. 3.2). The Wollaston prism is made of two crystals cemented together with optic axis perpendicular to each other and to the direction of the incident beam. In this way the two emerging beam are physically split with an high angular separation. This configuration is adopted in the *Echelle SpectroPolarimetric Device for the Observation of Stars* (ESPaDOnS, Donati et al. 2006) at the Canadian-france-Hawaii Telescope;

- The ***Foster prism*** (Fig. 3.3). The Foster prism (Foster, 1938) is made of glass with a sliver of calcite separating the two pieces. The beam hits the surface of calcite so that the optical axis of the two pieces are parallel but the extraordinary ray is totally reflected at the surface of calcite and it is brought through the side of the prism. On the contrary, the ordinary ray pass

straight through the prism. This configuration is adopted in the *HArps-North POlarimeter* (HANPO, Leone et al. 2016b) at the Telescopio Nazionale Galileo (Roque de Los Muchachos Astronomical Observatory, La Palma, Spain);

- The ***Savart plate configuration*** (Fig. 3.4). Savart plate is manufactured from two equal thickness plates of birefringent material cemented together, each with their optic axes at $45°$ to the surface normal and perpendicular to each other. When the beam arrives to the first plate, it is resolved into ordinary and extraordinary ray. The ordinary ray propagates undisturbed, but the extraordinary ray is displaced parallel to one edge. On entering the second crystal, the ordinary ray in the first crystal becomes the extraordinary ray in the second crystal and it is displaced in a direction perpendicular to the first beam displacement. In this way the two emerging beam are physically split without angular separation and it can be used on the same focal plane. This configuration is adopted in the *Catania Astrophysical Observatory Spectropolarimeter* (CAOS, Leone et al. 2016a) at the 0.91 m telescope of the stellar station of the Catania Astrophysical Observatory (*G. M. Fracastoro* Stellar Station, Serra La Nave, Mt. Etna, Italy).

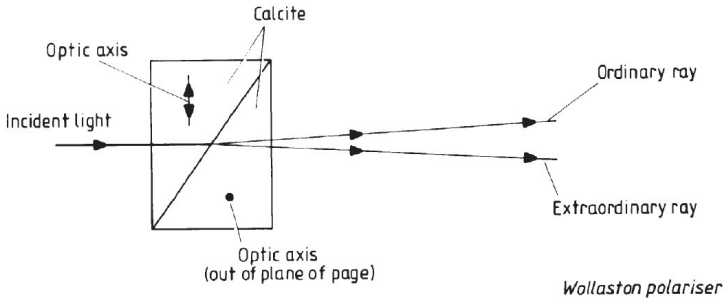

Fig. 3.2.: Wollaston prism operating sketch. The optic axis of the two crystals are perpendicular to each other and to the direction of the incident beam. Figure adapted from Kitchin (2003).

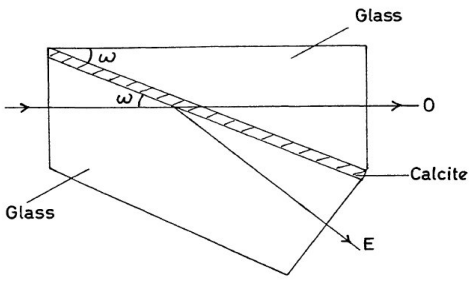

Fig. 3.3.: Foster prism operating sketch. The extraordinary ray is totally reflected at the surface of calcite, while the ordinary ray pass straight through the prism. Figure adapted from Clarke (1965).

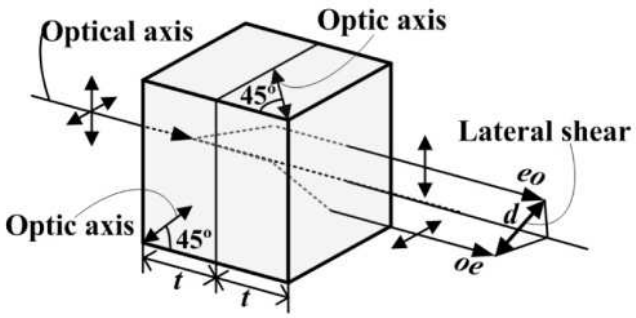

Fig. 3.4.: Savart plate operating sketch. The two emerging beam are physically separated without angular separation. Figure adapted from Mu et al. (2014).

3.1.2 Retarders

An ideal retarder is an optical device that alters the phase relation between orthogonally resolved components of a light beam. They are composed by a birefringent material characterized by two axis, *fast* and *slow*, which have two different indexes of refraction (n_f and n_s). Here we give a detailed description in the case of *plate retarder*, which is implemented in CAOS.

When a linearly polarised monochromatic wave hits the plate perpendicularly, a phase difference between the component of the wave with electric vectors parallel to the optical axis and with electric vectors in the perpendicular direction, is created, due to the different propagation velocities. The two beams will come out overlapping with a phase displacement, and then they will combine in a still polarised wave, but with a different polarisation status. The phase displacement will depend on the thickness of the plate. Considering a retarder extending between $z = 0$ and $z = l$, the electric vector propagating inside the plate can be written as:

$$E_f(z,t) = \epsilon_f e^{i(k_f z - \omega t)} \tag{3.3}$$

$$E_s(z,t) = \epsilon_s e^{i(k_s z - \omega t)} \tag{3.4}$$

where ϵ_f and ϵ_s are, respectively, the complex amplitudes of the electric vector along the fast and slow axes. The wavenumbers k_f and k_s are given by:

$$k_f = n_f \frac{2\pi}{\lambda} \tag{3.5}$$

$$k_s = n_s \frac{2\pi}{\lambda}. \tag{3.6}$$

The amplitudes of the electric vector outgoing from the retarder becomes:

$$\epsilon'_f = e^{i\psi}\epsilon_f \tag{3.7}$$

$$\epsilon'_s = e^{i\psi}\epsilon_s e^{i\delta} \tag{3.8}$$

where the phase ψ does not change the polarisation status of the wave and the so called *retardance* δ is given by:

$$\delta = 2\pi(n_s - n_f)\frac{l}{\lambda}. \tag{3.9}$$

The retardance corresponds to the phase difference introduced by the retarder. When the thickness of the retarder is such that $\delta = \pi/2$, the retarder is called *quarter-wave plate* ($\lambda/4$), while when $\delta = \pi$ the retarder is called *half-wave plate* ($\lambda/2$). They are used for measure circular and linear polarisation respectively.

One of the biggest problems in the use of retarders concerns the strong dependence with the wavelength (Fig. 3.5). For this reason the instrumental implementation require the use of particular kinds of retarders:

- CAOS and HANPO polarimeters are equipped with *achromatic retarders*. They are made of quartz and MgF_2 and allow independence from the wavelength in the spectral range of interest (380-850 nm);

- ESPaDonS polarimeter are equipped with *Fresnel Rhombs*. They are used as $\lambda/4$ or as $\lambda/2$ by combining two rhombs of very low birefringence $BK7$ glass and a $MgF2$ coating. The phase retarder here is induced using the total reflections effect (Fig. 3.6).

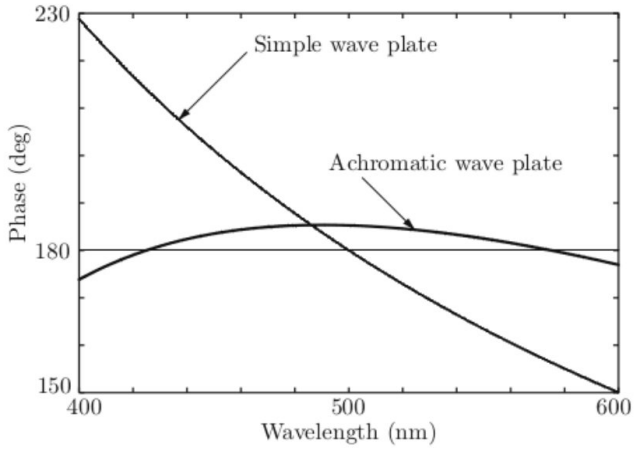

Fig. 3.5.: Comparison between the phase delay of a simple wave plate with that of an achromatic wave plate versus wavelength. Figure adapted from Clarke (2009).

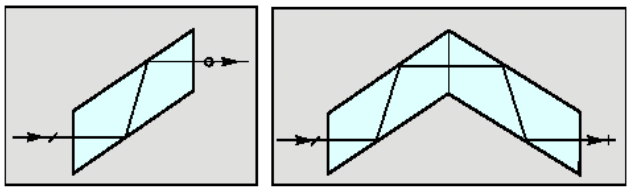

Fig. 3.6.: Fresnel rhombs operating sketch: quarter-wave (left) and half-wave (right). Figure adapted from http://www.ofr.com/oc-27_bb_retarders.htm

3.2 A prototype polarimeter

After describing the optical components for polarimetry, here we introduce a prototype of polarimeter as the one sketched in figure 3.7. It is composed by a retarder and a polariser. The wave plate introduced a phase delay δ. In the picture, β is the angle between the transmission direction of the polariser and the reference axis while α is the angle between the reference direction and the fast axis of the retarder.

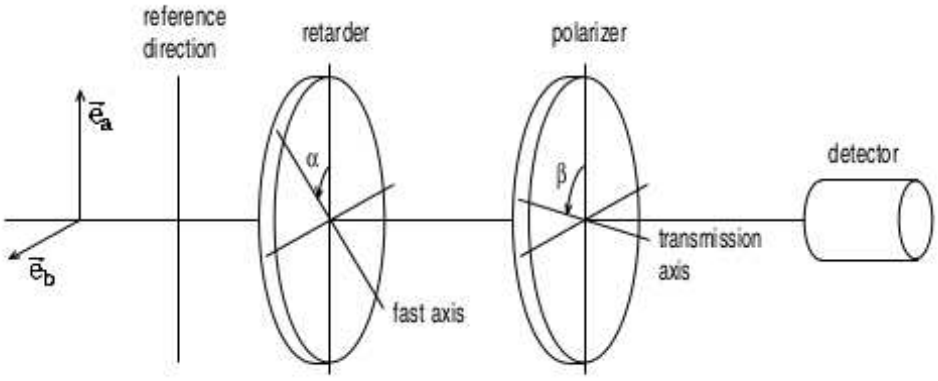

Fig. 3.7.: Schematic representation of a prototype polarimeter. Figure adapted from Degl'Innocenti & Landolfi (2006).

Let's consider, at the entrance of the retarder, the components of the electric field along the unit vectors $\overrightarrow{e_1}$ and $\overrightarrow{e_2}$ expressed as:

$$E_1 = \epsilon_1 e^{-iwt} \tag{3.10}$$

$$E_2 = \epsilon_2 e^{-iwt}. \tag{3.11}$$

The components along the fast and slow axes are:

$$E_f = (\epsilon_1 cos\alpha + \epsilon_2 sin\alpha) e^{-iwt} \tag{3.12}$$

$$E_s = (-\epsilon_1 sin\alpha + \epsilon_2 cos\alpha) e^{-iwt}. \tag{3.13}$$

Apart from the inessential phase factor, at the exit of the retarder the component along the slow axis is retarded:

$$E_s = (-\epsilon_1 sin\alpha + \epsilon_2 cos\alpha)e^{i\delta}e^{-iwt}. \tag{3.14}$$

At this point the ray crosses the polariser. The only component transmitted is the one along the acceptance axis E_a, that is given by:

$$\begin{aligned} E_a(t) &= (cos(\beta-\alpha)E_f + sin(\beta-\alpha)E_s) \\ &= \{cos(\beta-\alpha)(\epsilon_1 cos\alpha + \epsilon_2 sin\alpha) + \\ &+ sin(\beta-\alpha)[-\epsilon_1 sin\alpha + \epsilon_2 cos\alpha]e^{i\delta}\}e^{-iwt}. \end{aligned} \tag{3.15}$$

The detector will then respond with a signal proportional to $\langle E_a^*(t)E_a(t)\rangle$; indicating such a signal with the symbol $S(\alpha,\beta,\delta)$, we obtain through the definition of the Stokes parameters:

$$\begin{aligned} S(\alpha,\beta,\delta) &= \frac{1}{2}\{I + (Qcos2\alpha + Usin2\alpha)cos[2(\beta-\alpha)] + \\ &-(Qsin2\alpha - Ucos2\alpha)sin[2(\beta-\alpha)]cos\delta + Vsin[2(\beta-\alpha)]sin\delta\}. \end{aligned} \tag{3.16}$$

The method for measuring the Stokes parameters is hence to set the various devices at particular angles.

3.3 Measuring Stokes Parameters: instrumental implementation

Let's consider again the prototype of polarimeter that we have just shown. For the measurement of linear polarisation, the wave-plate can either be removed ($\delta = 0°$), or aligned with its fast axis along the acceptance axis of the polariser ($\alpha = \beta$). In both of cases Eq. 3.16 becomes:

$$S'(\beta) = \frac{1}{2}\{I + Qcos2\beta + Usin2\beta\}, \tag{3.17}$$

and the Stokes parameters can be measured by:

$$I = S'(0°) + S'(90°) \tag{3.18}$$

$$Q = S'(0°) - S'(90°) \tag{3.19}$$

$$U = S'(45°) - S'(135°), \tag{3.20}$$

with β arbitrary. These measurements, however, have the problem of implying a rotation of the exit polariser, that is impossible for large instrument. To avoid these

problems we can employ a half-wave plate ($\delta = 180°$) and keep the polariser fixed at $\beta = 0°$.

In this way Eq. 3.16 becomes:

$$S''(\alpha) = \frac{1}{2}\{I + Qcos4\alpha + Usin4\alpha\}, \tag{3.21}$$

and the Stokes parameters can be measured through the following settings of the half-wave plate:

$$I = S''(0°) + S''(45°) \tag{3.22}$$
$$Q = S''(0°) - S''(45°) \tag{3.23}$$
$$U = S''(22.5°) - S''(67.5°). \tag{3.24}$$

For the measurement of circular polarisation a quarter-wave plate ($\delta = 90°$) is needed. Keeping the polariser fixed ($\beta = 0°$), Eq. 3.16 becomes:

$$S'''(\alpha) = \frac{1}{2}\{I + Qcos^2 2\alpha + Usin^2 2\alpha cos2\alpha - Vsin2\alpha\}, \tag{3.25}$$

and the Stokes parameters can be measured through:

$$I = S'''(-45°) + S'''(45°) \tag{3.26}$$
$$V = S'''(-45°) - S'''(45°). \tag{3.27}$$

3.3.1 The two beam technique

Measurement of Stokes parameters requires a careful instrumental setup. The extra noise of the system, that is an important disadvantage since polarisation signals are very small, can be eliminated if both beams are recorded by a two beam analyser. In particular, the so called *two beam technique* (Tinbergen & Rutten, 1992) allows to obtain the polarisation information through the ratio of the intesities of two exposures with opposite sign of polarisation. The inversion in the sign can be performed through a certain rotation of the wave-plate.

For linear polarisation, the inversion can be done by rotating the half-wave plate by $45°$ to measure the Stokes parameter Q and with two exposure with the half-wave plate at $22.5°$ and $67.5°$ to measure Stokes U. For circular polarisation the inversion can be done by rotating the quarter-wave plate by an angle of $90°$.

Let's consider now two consecutive exposures (1 and 2), both of them performed in the same instrumental conditions with a two beam analyzer, that records both

beams for each exposure. We indicate with the function G the component of the signal that is polarisation-dependent and time-independent, while with the function F the component of the signal that is time-dependent and polarisation-independent. F contains all of the effects that we wish to eliminate from our measure, such as atmospheric transmission, seeing and variations in shutter timing. We use the symbol $||$ in order to indicate the o-spectra, while with the symbol $\perp$ we indicate the e-spectra. The four frames are then:

$$i_{1,||} = \frac{1}{2}(I+S)G_{||}F_1 \tag{3.28}$$

$$i_{1,\perp} = \frac{1}{2}(I-S)G_{\perp}F_1 \tag{3.29}$$

$$i_{2,||} = \frac{1}{2}(I-S)G_{||}F_2 \tag{3.30}$$

$$i_{2,\perp} = \frac{1}{2}(I+S)G_{\perp}F_2. \tag{3.31}$$

We can combine them obtaining:

$$R = \sqrt{\frac{i_{1,||}/i_{1,\perp}}{i_{2,||}/i_{2,\perp}}}. \tag{3.32}$$

In this way the contamination introduced from the function F is eliminated. R is closely related to the S component of the degree of polarisation P_S:

$$P_S = \frac{S}{I} = \frac{R-1}{R+1}. \tag{3.33}$$

In addition we can define the *Null spectrum* (Donati et al., 1997):

$$\frac{N}{I} = \frac{R_N - 1}{R_N + 1}, \tag{3.34}$$

with:

$$R_N = \sqrt{\frac{i_{1,||}/i_{2,\perp}}{i_{2,||}/i_{1,\perp}}}. \tag{3.35}$$

This quantity is important because it indicates the noise of Stokes profile. In an ideal case the null spectrum is flat. Any deviation is indicative of the presence of spurious polarisation contribution introduced by errors during the observation or data reduction phases. For example, we found out that if during an exposure CAOS is not thermally stabilized in temperature within a 0.01 K rms an important deviation from the flat condition is obtained. The same occurs if a precise wavelenght calibration is not performed. In general, we consider as *true* polarised signal a signal which is more than 3σ.

In our measurements we take usually two more exposures, with a total of four images per Stokes parameter. In this way we improve the accuracy of the measurement. The extra frames are expressed by:

$$i_{3,||} = \frac{1}{2}(I - S)G_{||}F_3 \tag{3.36}$$

$$i_{3,\perp} = \frac{1}{2}(I + S)G_{\perp}F_3 \tag{3.37}$$

$$i_{4,||} = \frac{1}{2}(I + S)G_{||}F_4 \tag{3.38}$$

$$i_{4,\perp} = \frac{1}{2}(I - S)G_{\perp}F_4. \tag{3.39}$$

The R parameter is:

$$R = \sqrt[4]{\frac{\frac{i_{2,\perp}}{i_{2,||}} \cdot \frac{i_{3,\perp}}{i_{3,||}}}{\frac{i_{1,\perp}}{i_{1,||}} \cdot \frac{i_{4,\perp}}{i_{4,||}}}} \tag{3.40}$$

and the R_N parameter:

$$R_N = \sqrt[4]{\frac{\frac{i_{1,\perp}}{i_{1,||}} \cdot \frac{i_{3,\perp}}{i_{3,||}}}{\frac{i_{2,\perp}}{i_{2,||}} \cdot \frac{i_{4,\perp}}{i_{4,||}}}}. \tag{3.41}$$

Finally, using Eq. 3.33 and 3.34 we obtain the Stokes parameters and the Null spectrum (Donati et al., 1997).

3.4 The CAOS spectropolarimeter

The *Catania Astrophysics Observatory Spectropolarimeter* (CAOS, Leone et al. 2016a) is a high resolution (R = 55000) echelle spectrograph, characterized by high efficiency ($> 20\%$), high stability, low scattered light and feeded by two optical fibers placed at the telescope focus. It covers a wide spectral range ($370 \div 1121\ nm$) and has a full spectral coverage in one exposure. It is able to analyze both the direct light (integral light mode) and the light coming from the two output beams of the polariser (polarimetric mode). The latter can be easily put above the optical fibers that send the light to CAOS.

CAOS is attached at the 0.91 m telescope of the stellar station of the Catania Astrophysical Observatory (*G. M. Fracastoro* Stellar Station, Serra La Nave, Mt. Etna, Italy). The telescope is a classical Cassegrain and its mount is German. The main mirror has a diameter of 0.91 m, a focal length of 4.143 m and a focal ration of $f/4.6$. The secondary mirror has a diameter of 0.24 m and a focal length of -1.427

m. The equivalent focal length of the Cassegrain focus is then 14.275 m with an equivalent focal ratio of $f/16$.

In the following subsections we give some description on the spectrograph and polarimeter. Further details can be found in Leone et al. (2016a).

3.4.1 The spectrograph

The CAOS spectrograph optical layout is realized in a *white-pupil configuration* (Figure 3.8, Dekker et al. 2000). In a white-pupil design, an intermediate spectral image is formed, which is subsequently relayed by auxiliary optics to a final detected image. In this way the highest possible resolution is achieved. At the entrance slit CAOS has a *preslit collimator* consisting of an achromatic doublet and a singles lens (Figure 3.9). In this way the two 100μ optical fibers appears in the focal plane with 280μ diameter. With the same system, fibers are then rotated to have a projected distance as equal as to 560μ to avoid overlappping of spectral orders.

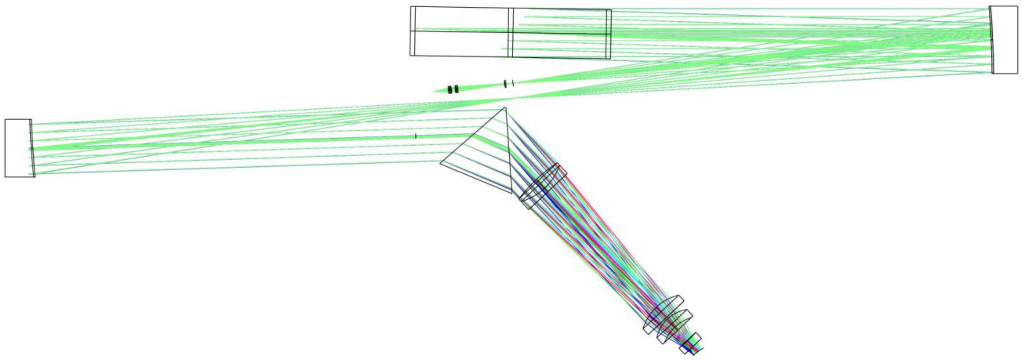

Fig. 3.8.: CAOS optical layout.

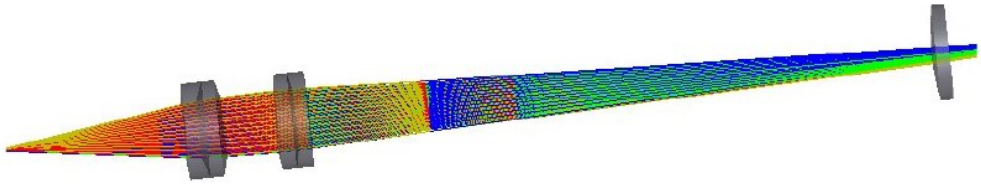

Fig. 3.9.: Pre-slit collimator.

The collimator mirrors consists of a $F/2.4$ paraboloidal mirror in Astrosital, with $400\ mm$ clear area and a focal length of $1000\ mm$. The mirror is cutted in two off-axis portions (Figure 3.10). The larger one is used off-axis as a $F/10$ collimator.

The mirror is used a second time to create an intermediate focal plane with light dispersed by the echelle grating. The other portion of the mirror is used to collimate the light towards the cross disperser. Both collimators are coated with enhanced silver for high reflectivity ($> 97\%$).

The dispersive element is a grating made of a *Zerodur* substrate with a blazed angle of $76°$ and $41.59\ gr/mm$ over a $102 \times 408\ mm$ ruled area. The latter has an aluminium reflection coating. It works in *Littrow* configuration, i.e. the incident and the reflected angles on the grating are almost coincident.

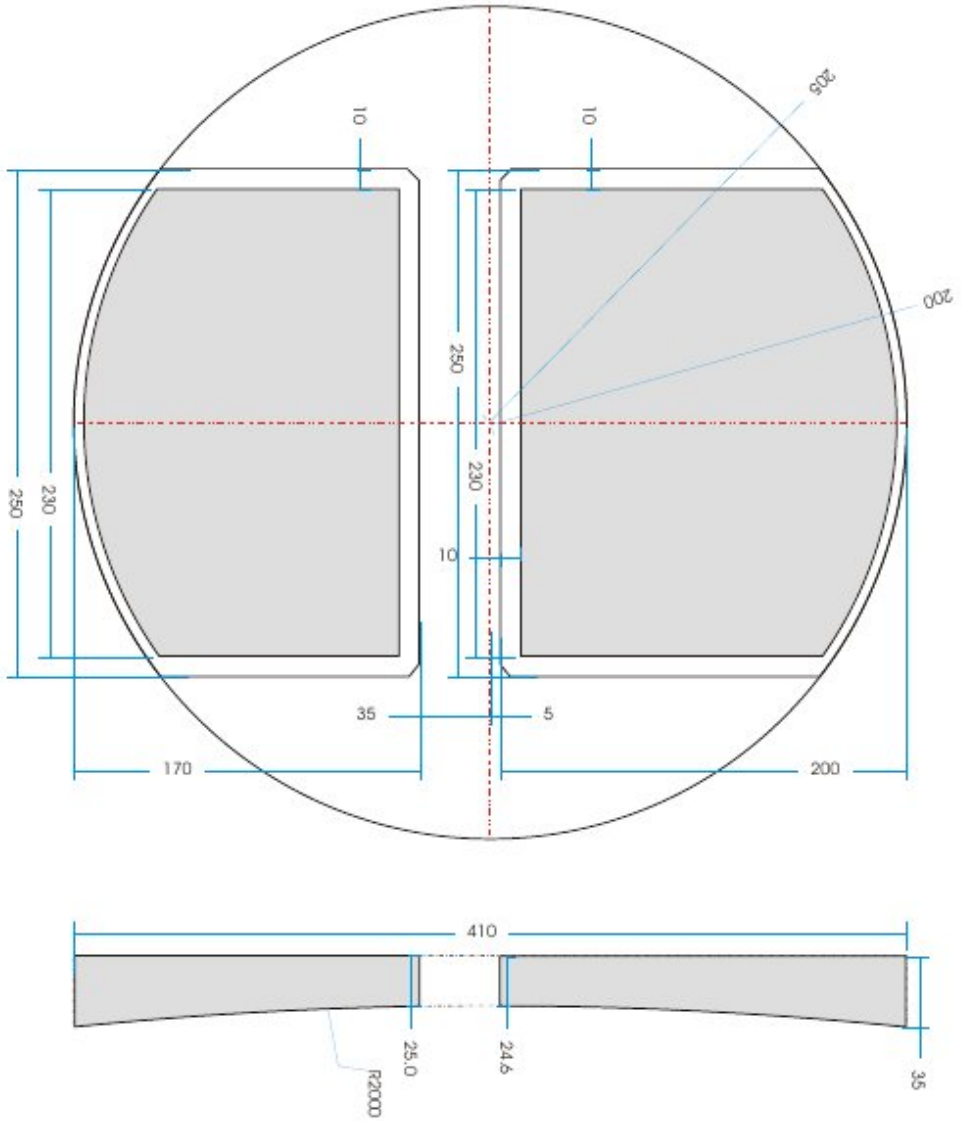

Fig. 3.10.: Collimators have been extruded from a $F/2.4$, 400 mm parabolic mirror. Measures are given in millimeter. The largest mirror works as first collimator.

The cross disperser is a $140 \times 160 \times 160\ mm$ prism with an apex angle of $53.1°$ (Figure 3.11). An *anti-reflective* coating gives an average efficiency better than 90%.

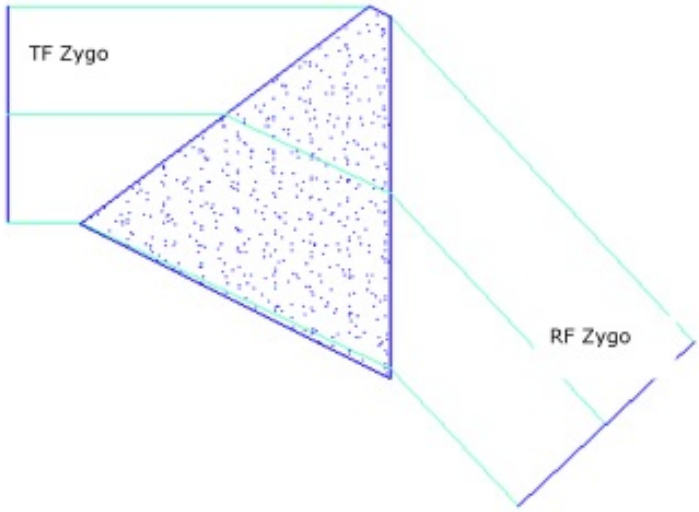

Fig. 3.11.: Optical sketch of cross-disperser prism.

Fig. 3.12.: Optical design of CAOS $F/2.1$ camera. Note the tilted focal plane to correct for axial chromatism.

The $F/2.1$ camera consists of five lenses mounted in three groups: a double, two separate lenses, a field flattener acting also as dewar window (Figure 3.12). All surfaces are spherical or plane. Due to the fixed spectral format, axial chromatism has been corrected tilting the focal plane.

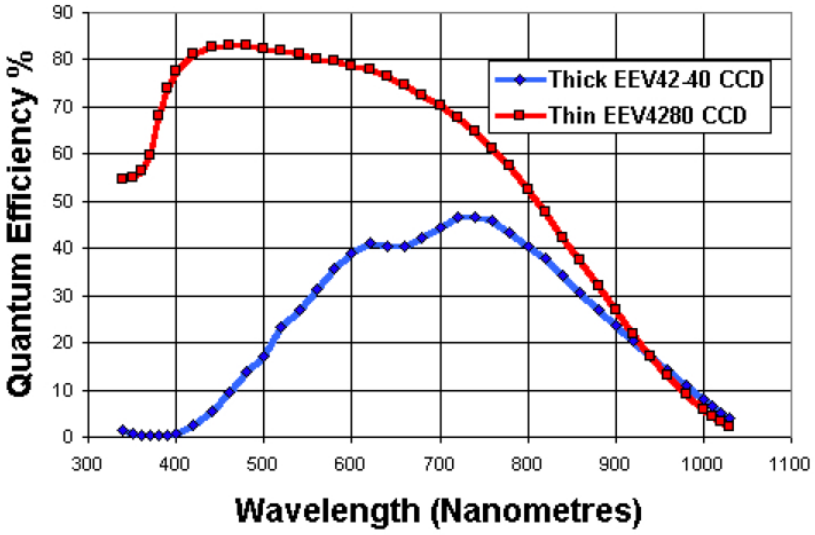

Fig. 3.13.: CAOS works with a thinned back-illuminated E2V-4240 CCD whose quantum efficiency is reported in re as a function of the wavelength. For comparison the quantum efficiency of a Thick CCD is also reported.

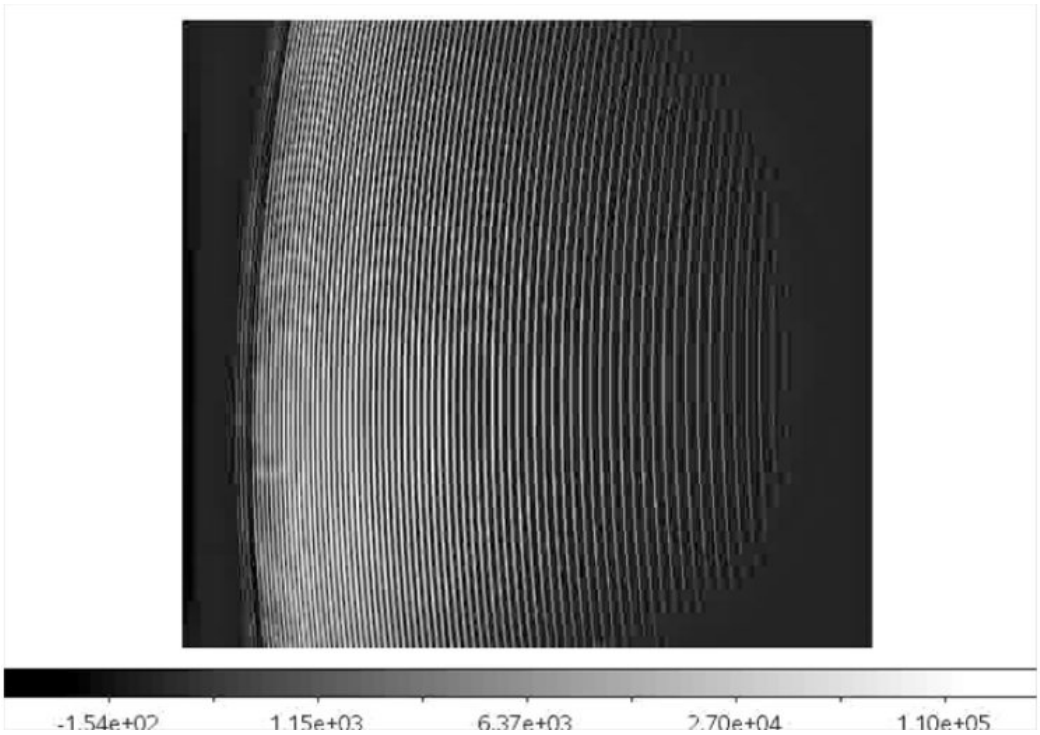

Fig. 3.14.: CAOS echellogram.

The CCD used is an E2V42-40 Thin and Back Illuminated High Performance Charge Coupled Device. It is a 2048×2048 matrix with pixel of $13.5\ \mu$ and an overall area of $27.6 \times 27.6\ mm$ that covers a wide field on the telescope focal plane. It has a very large *quantum efficiency* that peaks even at 89% at $450\ nm$ (Figure 3.13). In

order to minimize the thermal noise, the CCD works at cryogenic temperature in a vacuum environment. In particular, the CAOS CCD, is placed into a dewar where the combined action of two pumps maintains a ultra high vacuum ($P \approx 10^{-7}\ mbar$) while a N_2 system of nitrogen maintains a constant temperature of $-135\ C°$.

The obtained CAOS echellogram is made of 82 orders that covers wavelengths from 370 and $1121\ nm$; orders between 44 and 125 are recorded (Figure 3.14).

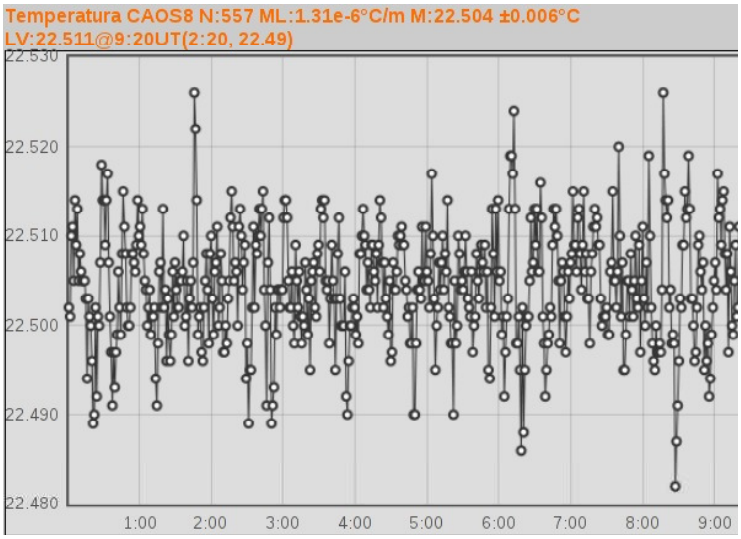

Fig. 3.15.: CAOS temperature stability.

Finally, the spectrograph is installed onto an optical bench ($2.4 \times 1.2\ m$) in a thermally and mechanically isolated environment inside a room below the telescope level, allowing a stable echellogram position. Figure 3.15 shows that the temperature is stabilized with a 0.006 K rms, along a full night.

3.4.2 The polarimeter

The CAOS polarimeter follows the same design adopted for the SARG spectrograph of the Telescopio Nazionale Galileo (Leone et al. 2003). It is based on the double beam technique and it consists of a $\lambda/2$ and a $\lambda/4$ retarder with a Savart plate working as a beam splitter.

The polariser is made of two blocks of calcite cemented togeter with a total length of 32 mm. The resulting beam separation is of 2.5 mm in the visible range and the calcite is oriented so that the ordinary and extraordinary images lies along the direction of the two fibers. The block of calcite can be put before the Cassegrain focus; a threaded ring fix its position so that it is not altered by the movement of the telescope during the measurements.

The retarders plates are placed before the block of calcite; position and handling are controlled via software. They are achromatic optical devices that induce a retardance of $\pm 3\%$ in a range of 450-700 nm.

In the previous Sections we have discussed the general theory of polarimeters and the measurement techniques of Stokes parameters. The different exposures of the star are performed by rotating the wave plate between each exposure. In particular, for linear spectropolarimetry the $\lambda/2$ plate is rotated of $22.5°$ while for circular polarisation the $\lambda/4$ plate is rotated of $90°$. These two sequences are illustrated in Tab. 3.1.

The exposure time was established on the basis of the star's magnitude and of the desired signal to noise level. In general, for each position of the retarder it was $T_{exp} \sim 120\ sec$ for the brightest stars ($V_{mag} \sim 2.0$) and $T_{exp} \sim 600\ sec$ for the weaker stars ($V_{mag} \sim 5.5$). After a new aluminizing of the telescope principal mirror occured in July 2017 we could reduce the exposure times by about 15%, obtaining the same signal to noise levels.

LINEAR POLARIZATION

$\lambda/2$	$\lambda/2$+22.5°	$\lambda/2$+45°	$\lambda/2$+67.5°	$\lambda/2$+67.5°	$\lambda/2$+45°	$\lambda/2$+22.5°	$\lambda/2$
1.1	2.1	3.1	4.1	4.2	3.2	2.2	1.2

CIRCULAR POLARIZATION

$\lambda/4$	$\lambda/4$+45°	$\lambda/4$+45°	$\lambda/4$
5.1	6.1	6.2	5.2

Tab. 3.1.: Sequences of spectropolarimetric measurements.

3.4.3 Data reduction process

CAOS data were reduced according to the standard procedures for spectroscopic observations by using the IRAF (*Image Reduction and Analysis Facility*) packages. The process develops in different steps:

- The first step concerns the *bias correction* (Fig. 3.17, left). The output signal from CCD after an exposure with closed shutter is not null, due to the thermal noise. For this reason, in each night, 5 exposures with closed shutter were performed (time of exposure $0.002s$). From these bias images, with the IRAF

task *zerocombine* a *master Bias* was calculated. It is simply the average of the 5 bias frames. As it is shown in Fig. 3.16, for CAOS's CCD the zero level is about 9700 ADU. The latter was then subtracted to the images of the star and to the flat field images with the IRAF task *imarith*;

- The second step is the *light scattered correction*. Despite the bias correction, the level between the orders is not exactly zero, due to the photons that are scattered and reflected during the acquisition. In order to make this correction, we have first selected the orders relating the ordinary image and those relating the extraordinary one, using interactively the IRAF task *apsum*. Then, with the IRAF task *apscatter* a bi-dimensional fit of the intra-order space was created, excluding the orders selected before (Figure 3.18). For each image was, therefore, extracted the ordinary image (*image A*) and the extraordinary one (*image B*);

- The third step is the *flat fielding correction* (Figure 3.17, right). Each pixel of the CCD could have different *quantum efficiency*. The latter can be evaluated by illuminating homogeneously the CCD with an halogen lamp. For this reason, in each night, were performed 5 exposures of a 100W halogen lamp (time of exposure $0.5s$). From these flat field images, with the IRAF task *flatcombine* a mean flat was calculated. Similarly to what was done previously, the scattered light was subtracted to the mean flat. Finally, with the IRAF task *imarith*, the mean flat was scaled around the unit by dividing it with an opportune value;

- The fourth step is the *wavelength calibration*. The CCD associates to each pixel a signal and we don't know the corresponding wavelength. For this reason the CCD was illuminated by radiation whose spectrum is known. In particular, in each night, were performed 5 exposures of a *ThAr* lamp (Fig. 3.19), whose lines can be easily identified by the *National Optical Astronomy Observatory* (NOAO) ThAr catalogue were here used. This operation was performed with the IRAF task *ecidentify* that creates a polynomial representation of the CCD (Figure 3.19). We have computed the polynomial function with a *root mean square* (rms) of about 10^{-4}. This representation is, then, used as *reference* by the IRAF task *refspectra* that assigns the calibration to the spectrum. Finally, the IRAF task *dispcor* assigns to each pixel the corresponding wavelength;

- The fifth step is the *heliocentric correction*. In this operation the effect due to the terrestrial motions is corrected. This is very important when we want to compare measurements obtained in different times and/or places. The IRAF task used in this regard is *rvcorrect* that calculate the heliocentric velocity knowing the geographical coordinates of the observatory (for Serra La Nave: longitude +14 58' 4", latitude +37° 41' 5", altitude 1725 m a.s.l.). The IRAF

task *dopcor* applies, then, the correction to the input images using the equation of Doppler effect:

$$\lambda_{new} = \lambda_{old}\sqrt{\frac{1+\frac{v}{c}}{1-\frac{v}{c}}} \tag{3.42}$$

with v the heliocentric velocity and c the speed of light. Finally, the spectra were divided by the flat, using the IRAF task *imarith*.

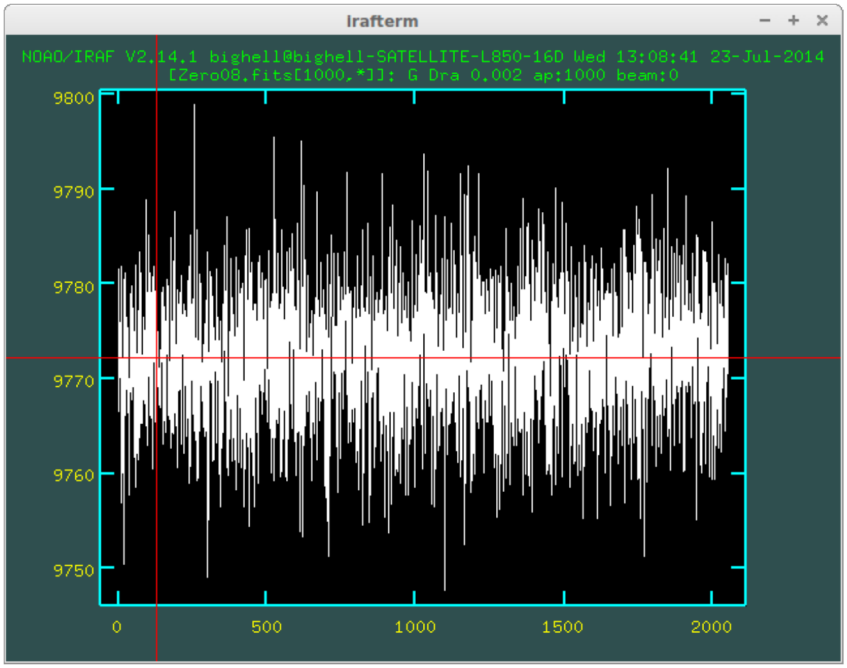

Fig. 3.16.: Master bias.

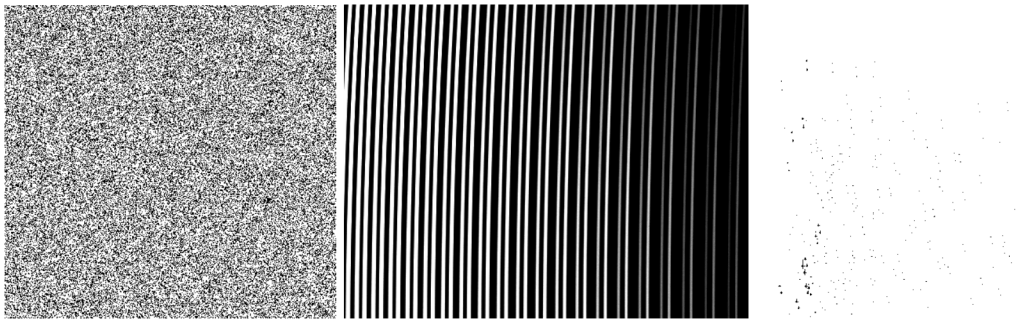

Fig. 3.17.: Left: Bias image. Center: Flat image. Right: ThAr image (inverted colours).

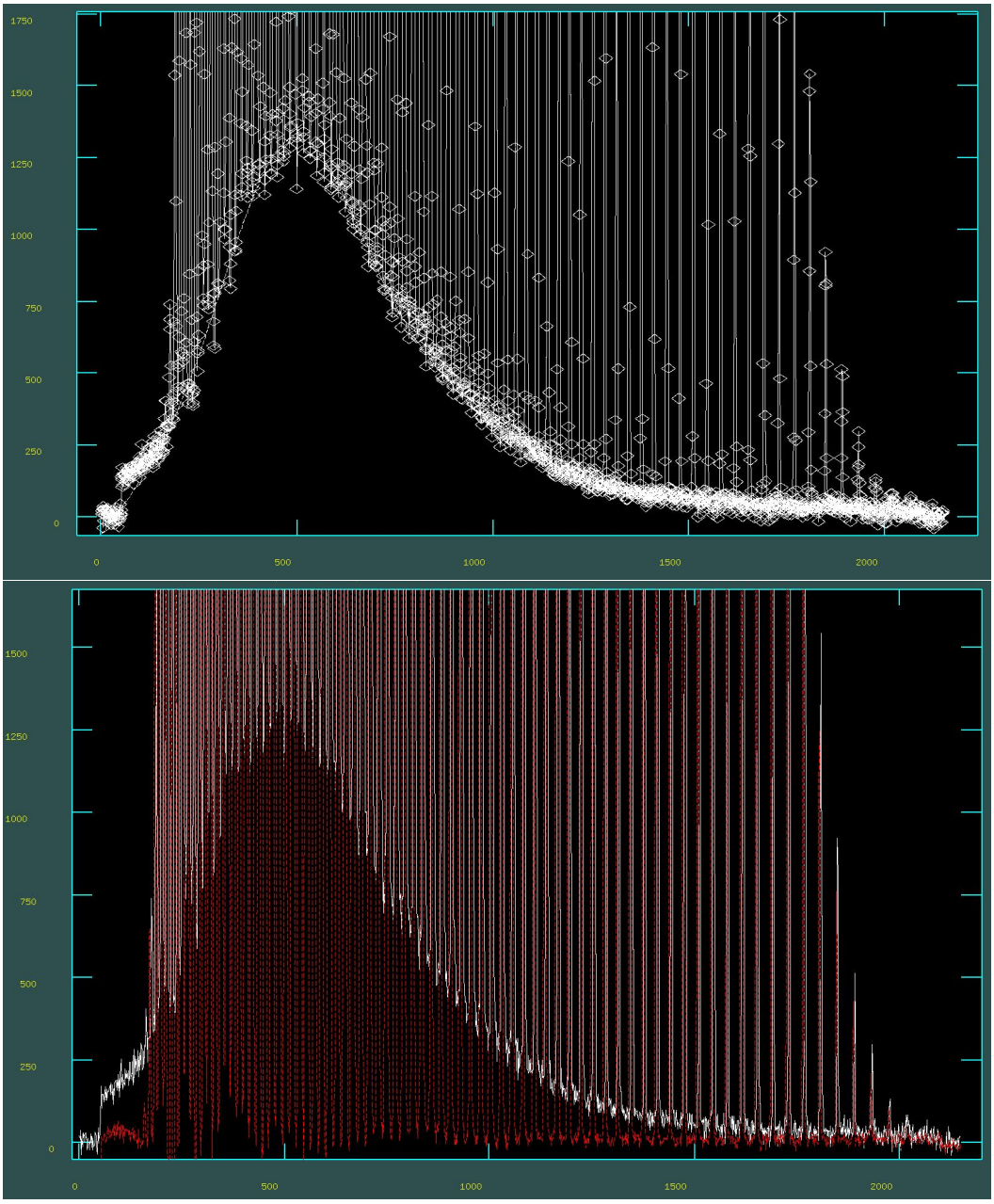

Fig. 3.18.: Top: section of CCD frame showing the 1% scattered light level and its fitting with a polynomial function. Bottom: comparison after scattered light subtraction.

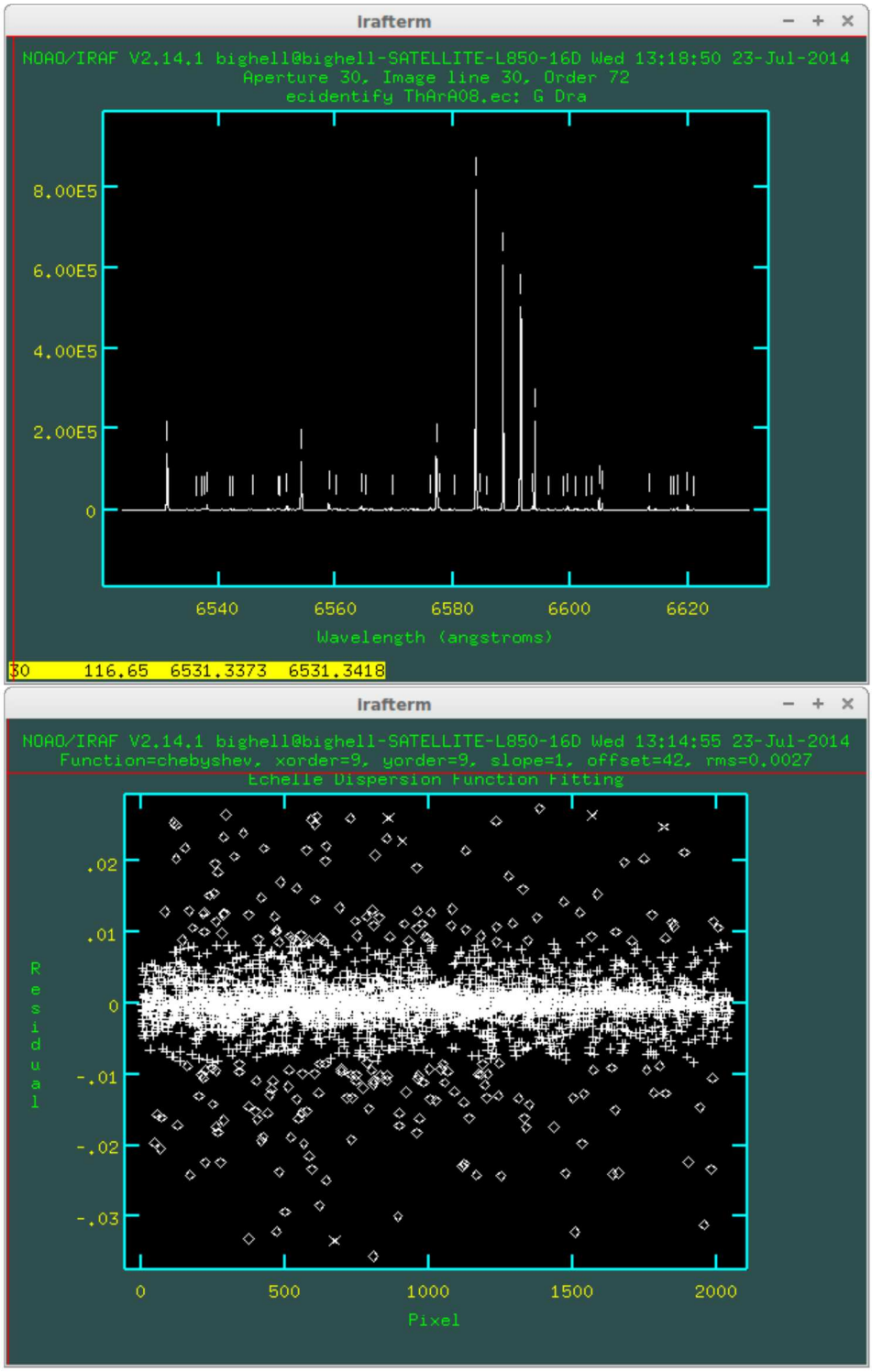

Fig. 3.19.: Top: calibration of the ThAr lamp with the IRAF task *ecidentify*. Bottom: fit of the dispersion function.

With these procedures we have extracted the spectra of the star. The Stokes' profile were calculated according to what we have described in section 3.3. In particular, making reference to the notation shown in table 3.1, if we call with $im_{x.x}A$ the x.x ordinary image and with $im_{x.x}B$ the x.x extraordinary image, the Stokes Q profile is extracted by the following operations:

$$\sqrt[4]{\frac{\frac{im_{1.1}A}{im_{1.1}B}\cdot\frac{im_{1.2}A}{im_{1.2}B}}{\frac{im_{3.1}A}{im_{3.1}B}\cdot\frac{im_{3.2}A}{im_{3.2}B}}} = R \tag{3.43}$$

$$\frac{R-1}{R+1} = im\_Q. \tag{3.44}$$

Similarly for the Stokes U profile:

$$\sqrt[4]{\frac{\frac{im_{2.1}A}{im_{2.1}B}\cdot\frac{im_{2.2}A}{im_{2.2}B}}{\frac{im_{4.1}A}{im_{4.1}B}\cdot\frac{im_{4.2}A}{im_{4.2}B}}} = R \tag{3.45}$$

$$\frac{R-1}{R+1} = im\_U. \tag{3.46}$$

The images obtained in 3.44 and in 3.46 were, then, normalized to the continuum with the IRAF task *continuum*. All of the operations just illustrated were performed with the IRAF task *sarith*, which works by interpolation in wavelength (unlike *imarith* that works pixel by pixel). Finally, the Stokes I profile was obtained by adding all the images.

3.5 Multiline techniques

As we have already mentioned, one of the biggest problems of high resolution stellar spectropolarimetry is the presence of very weak polarisation signatures which are generally below the photon noise level of the pixels. Usually, a direct detection in individual spectral lines requires a signal to noise $S/N \sim 1000$ (Donati et al. 1992) which is not easy to be reached even with the biggest telescopes, especially for the faintest objects. The initial interest of the scientific community was addressed almost exclusively to the circular component with the aim of detect weak magnetic fields in stars across the entire Hertzsprung-Russel diagram. For this reason, during the years, many indirect measurement techniques for circular polarisation have been developed.

Semel (1989) and Semel & Li (1996) suggested to average polarisation measurements of many spectral lines to obtain medium Stokes V and I profiles with higher S/N. Donati et al. (1997) refined this simple *line addition* procedure into the *Least square deconvolution* (LSD) method. Despite the fact that other techniques such as the *Principal Components Analysis* (Semel et al. 2009), the *Zeeman Components De-*

composition (Sennhauser & Berdyugina 2010) or the *Multi-line slope method* (Scalia et al. 2017) have been later proposed, the most widely accepted and used method remains the LSD technique. Nowadays there is a rich available literature for the LSD analysis of circular polarisation (e.g., Alecian et al. 2008, Donati et al. 2008, Morin et al. 2008, Petit et al. 2008, Lignieres et al. 2009, Auriere et al. 2009).

The LSD was also extended to the Stokes Q and U spectra by Wade et al. (2000) and very interesting results are recently emerging (Lebre et al. 2014, Tessore et al. 2015, Sabin et al. 2015, Auriere et al. 2016, Mathias et al. 2018).

During my Ph.D. the IDL routine based on the LSD method and numerically implemented for the circular component by Scalia et al. (2017) has been extended to the Stokes Q and U. In the following subsection we give the theoretical outline of the implemented method, following Kochukhov et al. (2010).

3.5.1 The Least Square Deconvolution method

In order to apply the LSD method, some basic assumptions are needed. In particular it is supposed that each line, for each Stokes spectrum, can be approximately described by the same line shape, simply scaled by a certain factor and that overlapping line profiles add up linearly. These assumptions are valid under the general physical hypothesis of *weak-field magnetic approximation* (i.e. for $B << kG$). In fact, if the magnetic field strength is so large that individual Zeeman splitting patterns of spectral lines are resolved, the similarity of the spectral lines shape is loss.

Under these assumptions, a Stokes spectrum can be simply represented as a sum of scaled and shifted identical profiles $Z(v)$:

$$Y(v) = \sum_i \omega_i \delta(v - v_i) Z(v_i), \tag{3.47}$$

where $Y(v)$ is the residual intensity $(1 - 1/I_c)$ or the normalized polarisation spectrum (Q/I_c, U/I_c and V/I_c), $v_i = c\Delta\lambda_i/\lambda_i$ is the position in velocity of the i^{th} line and w_i is the weight with which the line is scaled. Calling $M(v) = \sum_i \omega_i \delta(v - v_i)$ the *line pattern function*, we can rewrite Eq. 3.47 as a convolution between M and Z:

$$Y = M * Z, \tag{3.48}$$

which is equivalent to the matrix multiplication

$$\mathbf{Y} = \mathbf{M} \cdot \mathbf{Z}, \tag{3.49}$$

where **Y** is a *n*-element matrix representing a Stokes spectrum, **Z** is a *m*-element matrix representing the common profiles whose size is given by the velocity sampling and the *line mask matrix* **M** (Donati et al. 1997) is a $n \times m$ matrix containing information on the line positions and relative strengths.

The goal of the LSD approach is therefore to solve the inverse problem of Eq. 3.49 giving the mean line profile **Z** for an input observed Stokes spectrum $\mathbf{Y}^0$ (with associated errors σ) and line mask matrix **M**. It is performed numerically by the least-square minimization of the χ^2 function:

$$\chi^2 = (\mathbf{Y}^0 - \mathbf{M} \cdot \mathbf{Z})^T \cdot \mathbf{S}^2 \cdot (\mathbf{Y}^0 - \mathbf{M} \cdot \mathbf{Z}), \tag{3.50}$$

with **S** the square diagonal matrix containing the inverse errors $1/\sigma_i$ calculated for each pixels in the input spectrum. The solution of Eq. 3.50 is then given by:

$$\mathbf{Z} = (\mathbf{M}^T \cdot \mathbf{S}^2 \cdot \mathbf{M})^{-1} \cdot \mathbf{M}^T \cdot \mathbf{S}^2 \cdot \mathbf{Y}^0, \tag{3.51}$$

which represent the common LSD profile.

From the numerical point of view, the difficulty of implementation consists in the construction of the line mask matrix **M**, that could be reach a dimension of $10^6 \times 10^3$ (Kochukhov et al. 2010). It is built starting from each spectral line with central wavelength λ_l and weigth ω_l. The $M_{i,j}$ and $M_{i,j+1}$ components are given by:

$$M_{i,j} = \frac{\omega_l (v_{j+1} - v_i)}{(v_{j+1} - v_j)} \tag{3.52}$$

$$M_{i,j+1} = \frac{\omega_l (v_i - v_j)}{(v_{j+1} - v_j)}, \tag{3.53}$$

with

$$v_i = \frac{c(\lambda_i - \lambda_l)}{\lambda_l} \tag{3.54}$$

and

$$v_j \leq v_i \leq v_{j+1}. \tag{3.55}$$

Here index i represent the i^{th} selected line while index j corresponds to the velocity points of the LSD profile.

At this point it is important to set the weight values, the velocity sampling and a normalization criteria. In particular:

- The choice of weights to be adopted in Eq. 3.52, 3.53 depends on the particular Stokes parameter to be calculated; for I, Q and U parameters we have adopted:

$$\omega_l = d, \tag{3.56}$$

while for V parameter:

$$\omega_l = d\lambda_l g_{eff,l} \tag{3.57}$$

with d the depth of the line and g_{eff} the effective Landé factor of the specific transition. Eq. 3.56 and 3.57 are supported by the works of Semel et al. (2009) and Paletou (2012);

- The choice of the velocity sampling depends on the spectral resolution of the instrument and on the characteristics of the detector. For the instruments used in this work we have adopted:

$$incr_{vel} = 2.38\ kms^{-1}\ for\ CAOS \tag{3.58}$$
$$incr_{vel} = 1.84\ kms^{-1}\ for\ ESPaDOnS \tag{3.59}$$
$$incr_{vel} = 1.00\ kms^{-1}\ for\ HANPO; \tag{3.60}$$

- We decided to normalize the LSD profiles to the mean value of Stokes I depth for Stokes I, Q and U and to the mean value of the product between Stokes I depth, Landé factor and central wavelength for Stokes V:

$$Z_{I,Q,U} = \overline{d} Z_{I,Q,U} \tag{3.61}$$
$$Z_V = \overline{d\lambda g_{eff}} Z_V. \tag{3.62}$$

Finally, another important issue is related to the line selection procedure. In this work lines are selected from a synthetic spectrum computed for each observed star with SYNTHE (Kurucz 1993), using appropriate stellar parameters provided by the literature. To avoid saturated lines we have excluded profiles whose Stokes I residual is larger then 0.2. Furthermore, specific elements like H_α, H_β, CaI, NaI which are expected to trace shocked regions, chromosphere or circumstellar medium were also excluded.

4 Linear polarisation theory

> *Without doubt, the experimental fact is the omnipotent guide; but its verdict is applied only based on a powerful and delicate work. And the theorist must perform this gigantic work with the clear conscience of perhaps being called to justify the death sentence of his theory.*
>
> **— Albert Einstein**

In this Chapter we deal with the theory of linear polarisation. In particular we will focus on the possible mechanisms that lead to continuum polarisation (Sec. 4.1) and to line polarisation (4.2), which will be taken into account in the interpretation of our data. References of this Chapter are Degl'Innocenti & Landolfi (2006) and Yan & Lazarian (2006, 2007, 2012).

4.1 Continuum polarisation

4.1.1 Thomson scattering

Thomson scattering is the elastic scattering of electromagnetic radiation by a free charged particle. The particle kinetic energy and photon frequency are the same before and after the scattering. The electric field of the incident radiation accelerates the charged particle. The latter, in turn, emits radiation at the same frequency as the incident wave, and thus the wave is scattered. The moving particle radiates most strongly in a direction perpendicular to its acceleration and that radiation will be polarised along the direction of its motion. The light scattered from a small volume element may appear, therefore, to be more or less linearly polarised.

Considering the scattering plane (i.e. the plane containing the incident and scattered radiation), the outgoing electromagnetic wave associated with the photon can be resolved into two components: $E_{\parallel}$ and $E_{\perp}$ (figure 4.1). They refer, respectively, to the directions of the electric field vector parallel and perpendicular to the scattering plane. Upon scattering, the amplitude of the electric vector $E_{\parallel}$ is reduced by $cos^2\theta$

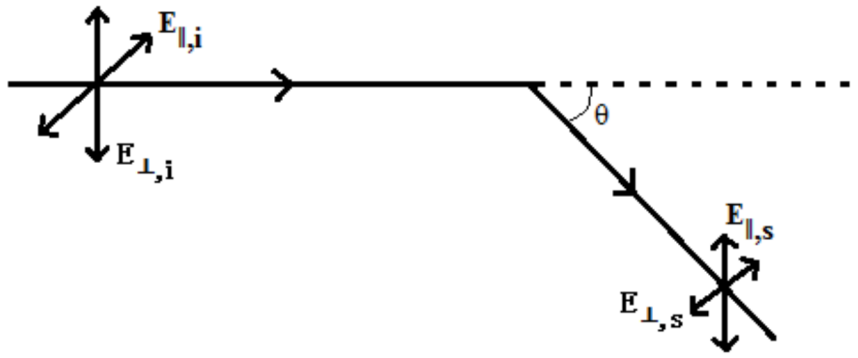

Fig. 4.1.: Schematic view of Thomson scattering.

(where θ is the scattering angle), while the component $E_\perp$ is unaltered. In the case of scattering off spherical particle, the relation between the incoming and scattered electric fields is:

$$\begin{bmatrix} E_{\parallel,s} \\ E_{\perp,s} \end{bmatrix} = \begin{bmatrix} S_2(\theta) & 0 \\ 0 & S_1(\theta) \end{bmatrix} \begin{bmatrix} E_{\parallel,i} \\ E_{\perp,i} \end{bmatrix}, \tag{4.1}$$

where the so-called scattering matrix elements $S_1(\theta)$ and $S_2(\theta)$ describes the angular redistribution of light upon scattering. In the case of Thomson scattering, they are given by:

$$S_1(\theta) = cos^2\theta \tag{4.2}$$

$$S_2(\theta) = 1. \tag{4.3}$$

The degree of polarisation of the scattered radiation is the ratio of the difference between the parallel and perpendicular intensities to the total intensity of the radiation field. Since intensity is proportional to the square of the amplitude of the electric vector, the degree of linear polarization is given by:

$$P = \frac{I_\perp - I_\parallel}{I_\perp + I_\parallel} = \frac{1 - cos^2\theta}{1 + cos^2\theta}. \tag{4.4}$$

When unpolarised stellar radiation is scattered off electrons within a circumstellar environment, the net polarisation is determined by summing the Stokes parameters of the individual polarisation vectors throughout the entire volume. Stokes parameters are, in fact, subjected to the usual rules of vector addition. Consequently, any intrinsic polarisation from Thomson scattering must arise from asymmetric environ-

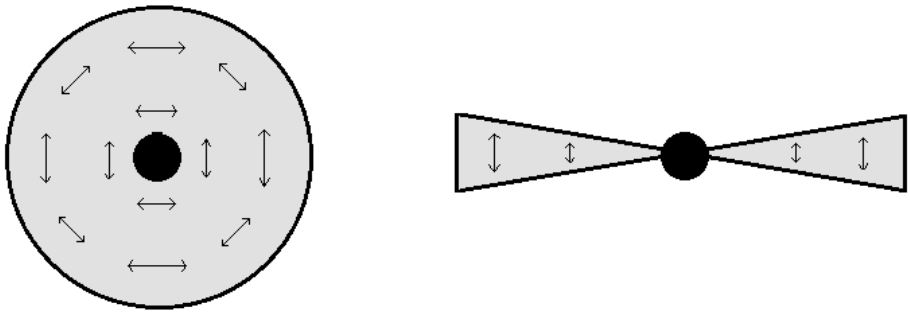

Fig. 4.2.: Polarisation vectors arising from scattering radiation from a point source in a spherically symmetric circumstellar envelope and in an equatorial circumstellar disk. In the first case each vector will cancel with a vector that is exactly one quadrant away, so the net polarisation from the unresolved spherical scattering region is zero. In the second case the scattered polarisation vectors are perpendicular to the disk and the net polarisation from the unresolved disk is parallel to the rotational symmetry axis of the disk; there is no cancellation from the polar region.

ment. In fact, considering a point source at the center of a spherical envelope, at any position within this region the local polarisation vector is perpendicular to the scattering plane and hence it is perpendicular to the radial line from the central point source. Due to the symmetry, for any sight line, the local polarisation vector cancel the other one that is exactly one quadrant away. There is, therefore, zero polarisation from the entire scattering volume. On the contrary, considering an non-spherical structure, such as a disk, if it is not viewed pole-on, and hence there is no rotational symmetry about the line of sight to the observer, a net total polarisation is obtained (figure 4.2).

4.1.2 Molecules and dust scattering

When the electromagnetic radiation is scattered off molecules or dust particles, the mathematical description of the emergent polarisation became more complex. This because, if on the one hand the emerging polarisation still follows Eq. 4.4, the calculation of the scattering matrix elements must take into account the geometrical and physical properties of the scattering particles.

At this purpose, let's consider a cylindrical column region with length L and unit cross-sectional area, filled by spherical particles (i.e. dust grains or molecules) of radius a distributed uniformly with number density n_d per unit volume. The total number of particles within this region is then $N_d = n_d L$. Considering an element of

column with length dL, if the starlight radiation with intensity I passes through this region its fractional reduction is given by:

$$\frac{dI}{I} = -n_d \sigma_{ext} dL \tag{4.5}$$

with σ_{ext} the extinction cross-section. Integrating this equation over the entire path-length we obtain:

$$I = I_0 e^{-\tau} \tag{4.6}$$

with I_0 the initial value of I and $\tau = n_d \sigma_{ext} L$. Equation 4.6 represents, therefore, the reduction of the intensity of the radiation that pass through a region of space filled by particles. This will depend on the physical and geometrical properties of these particles that can be expressed by the *extinction efficiency factor*:

$$Q_{ext} = \frac{\sigma_{ext}}{\pi a^2}, \tag{4.7}$$

with a the radius of the particle. The extinction efficiency factor can be expressed as the sum of corresponding factors for absorption and scattering:

$$Q_{ext} = Q_{abs} + Q_{sca}. \tag{4.8}$$

These efficiencies are, in turn, functions of two quantities, a dimensionless size parameter,

$$x = \frac{2\pi a}{\lambda} \tag{4.9}$$

and a composition parameter, the *complex refractive index* of the grain material,

$$m = n - ik. \tag{4.10}$$

From the value of x we can distinguish three different regimes:

- $x \ll 1$ (the *Rayleigh regime*): the particle is much smaller than the wavelength. In this case we have the simple theory of *Rayleigh scattering*;

- $x \simeq 1$: the particle size is comparable with the wavelength. This is the most complex regime because it requires the full solution of the Maxwell equations;

- $x \gg 1$ (*geometric optics regime*): the particle size is much larger than the wavelength. In this case reflection on the surface and refraction in the interior can still be quite complex and today it can be calculated using *ray-tracing* technique (Spencer et al., 1962).

The problem is then to calculate Q_{abs} and Q_{sca} for any assumed particle model. A solution was formulated in 1908 by Mie who solved the Maxwell equations for electromagnetic scattering off spheres having a homogeneous refractive index and dimensions in the range of the incoming wavelength ($x \backsimeq 1$). In the Rayleigh regime, Mie theory produces the same scattering cross sections as Rayleigh theory, while in the geometric optics regime Mie theory becomes more and more difficult to apply; in this case, the best way to perform the calculation is the ray-tracing method. From Mie theory further quantities of interest, describing the scattering properties of the grains, may be deduced. The *albedo* is defined by:

$$\gamma = \frac{Q_{sca}}{Q_{ext}} = \frac{\sigma_{sca}}{\sigma_{ext}} \tag{4.11}$$

and is hence specified as a function of wavelength for a given grain model. This quantity is important in order to place constraints on the imaginary component of the refractive index and hence it is important in order to determine the amount of radiation that is is scattered or absorbed. In fact, as $\sigma_{ext} \geq \sigma_{sca} \geq 0$, we have $0 \leq \gamma \leq 1$. For pure dielectrics ($k = 0$), $\sigma_{ext} = \sigma_{sca}$ and hence $\gamma = 1$. On the contrary, for strong absorbers ($k \sim n$), $\sigma_{sca} \backsimeq 0$ and thus $\gamma \backsimeq 0$.

In the Rayleigh regime the scattering and absorption efficiency factors are:

$$Q_{sca} = \frac{8}{3}\left(\frac{2\pi a}{\lambda}\right)^4 \left|\frac{m^2-1}{m^2+2}\right|^2 \tag{4.12}$$

$$Q_{abs} = 4\left(\frac{2\pi a}{\lambda}\right) \Im\left\{\frac{m^2-1}{m^2+2}\right\}. \tag{4.13}$$

Considering equation 4.7, the corresponding scattering cross sections on a single particle are:

$$\sigma_{sca} = \frac{2}{3}\pi^5 \frac{(2a)^6}{\lambda^4} \left|\frac{m^2-1}{m^2+2}\right|^2 \tag{4.14}$$

$$\sigma_{abs} = \pi \frac{(2a)^3}{\lambda} \Im\left\{\frac{m^2-1}{m^2+2}\right\}. \tag{4.15}$$

From equations 4.14 and 4.15 we want to stress that in the Rayleigh regime the scattering opacity goes roughly as $1/\lambda^4$ while the absorption opacity goes roughly as $1/\lambda$.

When $x \simeq 1$, Mie theory predicts more complicated solutions. The basic idea is that to expand the outgoing radiation radiated from a spherical particle after the scattering with an ingoing radiation, using *vector spherical harmonics*. The expansion

coefficients, the so-called *scattering coefficients*, are usually written as a_n and b_n, where n is the expansion index going from $n = 1$ to $n \to \infty$. They are given by:

$$a_n = \frac{m\psi_n(mx)\psi_n'(x) - \psi_n(x)\psi_n'(mx)}{m\psi_n(mx)\xi_n'(x) - \xi_n(x)\psi_n'(mx)} \tag{4.16}$$

$$b_n = \frac{\psi_n(mx)\psi_n'(x) - m\psi_n(x)\psi_n'(mx)}{\psi_n(mx)\xi_n'(x) - m\xi_n(x)\psi_n'(mx)}, \tag{4.17}$$

with ψ and ξ the *Riccati-Bessel functions*. From these, the scattering cross section is given by:

$$\sigma_{sca} = \frac{2\pi}{k^2}\sum_{n=1}^{\infty}(2n+1)(|a_n|^2 + |b_n|^2), \tag{4.18}$$

where $k = 2\pi/\lambda$ is the wave number of the incident radiation. The extinction cross section is given by:

$$\sigma_{ext} = \frac{2\pi}{k^2}\sum_{n=1}^{\infty}(2n+1)\Re\{a_n + b_n\}. \tag{4.19}$$

The absorption cross section is then given by:

$$\sigma_{abs} = \sigma_{ext} - \sigma_{sca}. \tag{4.20}$$

The number of terms that have to be included in the sum depends on the value of x; typically, for $x \gtrsim 1$ we need $n \simeq x$ terms. For this reason, when $x \gg 1$, the computing difficulty greatly increases.

Finally the scattering matrix elements, defined in Eq. 4.1, in the case of dust scattering, are:

$$S_1(\theta) = \frac{2\pi}{k^2}\sum_{n=1}^{\infty}\frac{2n+1}{n(n+1)}[a_n\pi_n + b_n\tau_n] \tag{4.21}$$

$$S_2(\theta) = \frac{2\pi}{k^2}\sum_{n=1}^{\infty}\frac{2n+1}{n(n+1)}[a_n\tau_n + b_n\pi_n]. \tag{4.22}$$

4.2 Line polarisation

Polarisation across spectral lines are due to different mechanisms. These latter can be related with the presence of an external magnetic field (Zeeman effect) or with the existence of some kind on anisotropy in the excitation of the atomic system (optical pumping).

4.2.1 Zeeman effect

Here we present a quantum description of the Zeeman effect following Degl'Innocenti & Landolfi (2006).

Considering a system of atoms in an external and uniform magnetic field, we can write the Hamiltonian of the system as the sum of an unperturbed Hamiltonian H_0 and a *magnetic Hamiltonian* H_B. The latter is given by:

$$H_B = \frac{e_0 h}{4\pi mc}(\vec{L} + 2\vec{S}) \cdot \vec{B} + \frac{e_0^2}{8mc^2}(\vec{B} \times \vec{r})^2, \tag{4.23}$$

with $\vec{L}$ and $\vec{S}$ the total orbital angular momentum and total spin, $\vec{B}$ the magnetic field vector and $\vec{r}$ the position operator. The second term of Eq. 4.23 is the so-called *diamagnetic term* and it can be neglected in the most common astrophysical scenario[1]. In this case, Eq. 4.23 can be written as:

$$H_B = \frac{e_0 h}{4\pi mc}(\vec{L} + 2\vec{S}) \cdot \vec{B} = \mu_0(\vec{L} + 2\vec{S}) \cdot \vec{B}, \tag{4.24}$$

where $\mu_0 = 9.17 \times 10^{-21}\ erg\ G^{-1}$ is the so-called *Bohr magneton*.

If the magnetic field is so weak that the magnetic energy is much smaller than the energy intervals relative to the unperturbed Hamiltonian H_0, we are in the *Zeeman regime*; we can describe the effects of the magnetic field by using the perturbation theory. In this case the corrections of the unperturbed energy levels $E_{\alpha J}$ are given by:

$$\langle \alpha JM | H_B | \alpha JM' \rangle = \mu_0 B g M \delta_{MM'} \tag{4.25}$$

with J the total angular momentum, M its projection on the z-axis and g the *Landè factor*:

$$g = 1 + \frac{\langle \alpha J || \vec{S} || \alpha J \rangle}{\sqrt{J(J+1)}}, \tag{4.26}$$

with $J \neq 0$.

The first order eigenvalues of the total Hmiltonian $(H_0 + H_B)$ are then given by:

$$E_{\alpha J} + \mu_0 g B M, \tag{4.27}$$

with $M = -J, -J+1, ..., J$.

[1] In the case of very large magnetic fields that can be found, for example, in magnetic white dwarfs, the diamagnetic term cannot be neglected.

In other words, Eq. 4.27 represents the energy splitting due to the presence of a magnetic field. Here it is possible to note how the splitting is proportional to the Landè factor, as well as to the magnetic field. It is therefore important to have the correct values of the Landé factor. The general and analytical expressions can be obtained in the cases of coupling between angular momentums (the simplest of these is the LS coupling) and a detailed derivation is beyond the scope of this Chapter. Moreover in many cases the Landè factors are know empirically from experimental work carried out in spectroscopic laboratories.

In order to show the polarisation properties of the Zeeman effect, we consider now the simple case of a transition between two atomic levels characterized by angular momentum J and J' and Landé factor g and g'. The spectral line will be splitted in a collection of components whose frequencies are given by:

$$\nu_{MM'}^{JJ'} = \nu_0 + \nu_L(g'M' - gM), \tag{4.28}$$

where $\nu_L = 1.3996 \times 10^6 B$ is the *Larmor frequency*.

Eq. 4.28 can be expressed in terms of wavelength as follow:

$$\lambda_{MM'}^{JJ'} = \lambda_0 - \Delta\lambda_B(g'M' - gM), \tag{4.29}$$

with λ_0 the wavelength of the unperturbed line and

$$\Delta_B = \lambda_0^2 \frac{\nu_L}{c} = \frac{\lambda_0^2 e_0 B}{4\pi m c^2}. \tag{4.30}$$

Among the various Zeeman components described in the above equation, only a limited number is actually observed, due to the selection rules. The latter depend, in turn, on the interaction between atoms and radiation field. In the simplest case of electric-dipole transitions we have:

$$\Delta M = M' - M = 0, \pm 1, \tag{4.31}$$

obtaining three distinct groups of Zeeman components (Fig. 4.3):

- $\Delta M = -1$: these components are called σ_r, they are red-shifted with respect to the unperturbed line and they generally show elliptical polarisation which degenerates into circular polarisation, when observed among the direction of the magnetic field and into linear polarisation, when observed in the plane perpendicular to the magnetic field;

- $\Delta M = +1$: these components are called σ_b, they are blue-shifted with respect to the unperturbed line and they show the same polarimetric behaviour of the above components, except for the handedness of circular polarisation;

- $\Delta M = 0$: these components are called π, fall in between those of the σ_r and σ_b components and they show linear polarisation with direction always parallel to the magnetic field.

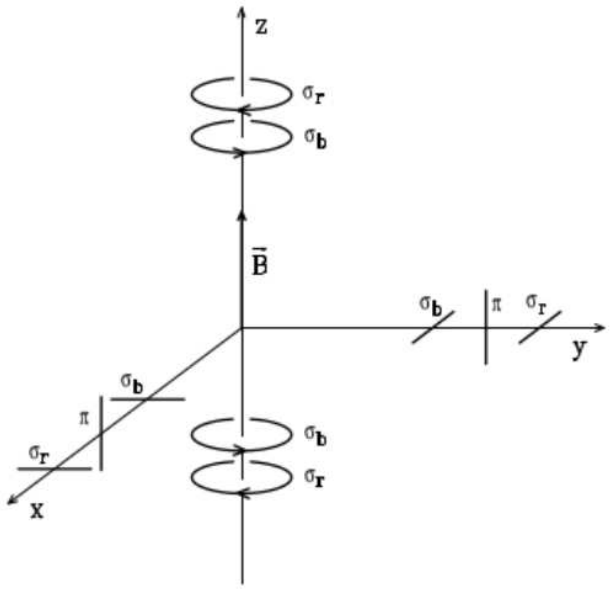

Fig. 4.3.: Polarisation properties of the Zeeman effect. Image adapted from Degl'Innocenti & Landolfi (2006).

4.2.2 Optical pumping

Optical pumping led to *atomic level polarisation*; in this case polarisation results because the lower state magnetic atomic sublevels are unequally populated by the action of an anisotropic incident radiation. As a result, this *optically pumped* gas has an opacity that will depend on the electric field direction of the incident flux. In this way an unpolarised radiation incident on such absorbing gas can emerge polarised without scattering.

Optical pumping was discovered by the Nobel prize Kastler (1950) and has been demonstrated in the laboratory by Happer (1972). There have been a lot of applications based on this process, ranging from atomic cloks, magnetometer, quantum optics and spin-polarised nuclei (see review by Cohen-Tannoudji et al., 1969; Budker & Romalis, 2007). From the astrophysical point of view, optical pumping has been discussed in the context of sensitive solar observations by Trujillo Bueno & Landi Degl'Innocenti (1997), which emphasize that the presence of a magnetic field is

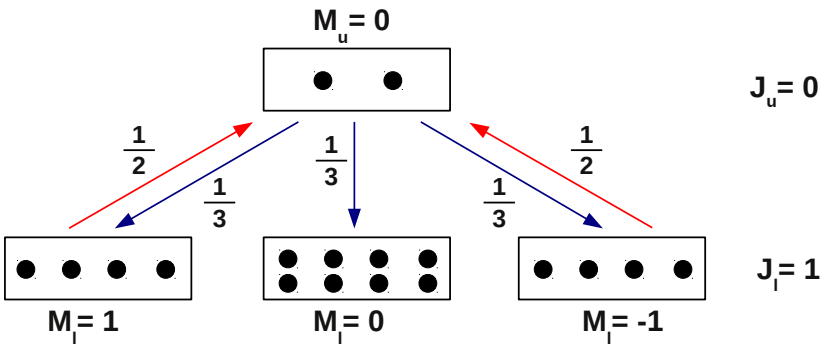

Fig. 4.4.: Toy model to illustrate the optical pumping mechanism. Atoms accumulate in the ground magnetic sublevel $M_l = 0$ as an anisotropic radiation removes atoms from the ground states $M_l = \pm 1$. The numbers at the arrows indicate the probability of populating the corresponding levels.

not necessary for the operation of this processes. However, Yan & Lazarian (2007) considered the effects of the presence of a magnetic field; we will deal with this case in the next Section.

The basic principle of such mechanism can be understood simply from the classical point of view. Consider, for example, a two-level atom with a lower level characterized by a total angular momentum $J_l = 1$ (which is nominally degenerate with magnetic sublevels $M_l = \pm 1, 0$) and with a not degenerate upper levele with $J_u = 0$. In a Cartesian coordinate system, we represent the substates with classical oscillators that are aligned in the x-y plane for $M = \pm 1$ and in the z-direction for $M = 0$. If we impose that the anisotropic radiation is in the z-direction, only the $M = \pm 1$ transitions can be excited because the incident transverse electric field lies in the x-y plane. On the other hand, the spontaneous de-excitation from the upper level populated with equal probability all of the lower magnetic sublevels. As a result, the $M = 0$ substate will be overpopulated (Fig. 4.4).

During the spontaneous de-excitation, however, collisions could redistribute atoms to different sublevels, reducing or even canceling the alignment effect. Nevertheless, several experimental studies (see, for example Kastler, 1957) highlight how in many astrophysical enviroments such as the outer layers of stellar atmospheres, the interplanetary, interstellar and intergalactic medium, the randomization of the ground state is less efficient of the optical pumping.

In conclusion, to make this mechanism possible are necessary: (i) atoms with fine or hyperfine structure (i.e. atoms with quantum angular momentum number ≥ 1); (ii) anisotropic incident flux; (iii) collisional rate lower than radiative pumping rate.

A detailed derivation of the equations that govern the optical pumping theory is rather complex and it is beyond the scope of this work. However, in the next Section we will give the basic results in the case of absorption line and taking into account the presence of a weak magnetic field. The mathematical description that will be presented will follow Landi Degl'Innocenti & Landolfi (2004) and the works of Yan & Lazarian (2006, 2012), were it is possible to find the complete treatment.

4.2.3 Optical pumping and magnetic fields

The presence of a magnetic field induces precession, realigning the atomic species that were optically pumped by an anisotropic radiation field. This realignment is sensitive to extremely weak magnetic fields ($1G \geq B \geq 10^{-15}G$), Yan & Lazarian 2012). Therefore, if this mechanism takes place, it is possible, at least in principle, to probe the 3D orientation and strenght of extremely weak magnetic field through linear polarisation signatures.

In this context, it is important to evaluate the behavior of different atomic (ionic) species because of the different relevant timescales involved in the specific transitions. In particular, taking into account (i) the rate of Larmor precession, ν_L, (ii) the rate of optical pumping, τ_R^{-1}; (iii) the rate of collisional mixing, τ_C^{-1} and (iv) the rate of transition within ground state, τ_T^{-1}, different situations are possible:

- if $\nu_L > \tau_R^{-1} > \tau_C^{-1}, \tau_T^{-1}$ (that is the most frequent case), magnetic precession will realign the atoms in their ground state;

- if $\nu_L < \tau_R^{-1}$ the magnetic field does not affect the atomic occupations and atoms are influenced only by the anisotropy radiation field. We are in the *pure* optical pumping regime;

- if ν_L is comparable to any of the other rates the linear polarisation is sensitive only to the strength of the magnetic field.

Let us now consider an atomic system characterized by multiple upper levels J_u, M_u and lower level J_l, M_l. The interaction with a radiation induces absorption, emission and magnetic precession among the sublevels of the state. The balance of these

three processes will determine the atomic occupation. The statistical equations for the upper and ground state are:

$$\dot{\rho}^k_q(J_u) + 2\pi i \nu_L g_u q \rho^k_q(J_u) = -\sum_{J_l} A(J_u \rightarrow J_l)\rho^k_q(J_u) + \sum_{J_l K Q k' q'} [J_l] B(J_l \rightarrow J_u) \times (-1)^{k'+q'} (3[k,k',K])^{1/2} \begin{Bmatrix} 1 & J_u & J_l \\ 1 & J_u & J_l \\ K & k & k' \end{Bmatrix} \begin{pmatrix} k & k' & K \\ q & q' & Q \end{pmatrix} \bar{J}^K_Q \rho^{k'}_{-q'}(J_l), \tag{4.32}$$

$$\dot{\rho}^k_q(J_l) + 2\pi i \nu_L g_l q \rho^k_q(J_l) = \sum_{J_u} (-1)^{J_l+J_u+k+1} [J_u] \begin{Bmatrix} J_l & J_l & K \\ J_u & J_u & 1 \end{Bmatrix} A(J_u \rightarrow J_l)\rho^k_q(J_u) - [J_l] \sum_{J_u K Q k' q'} B(J_l \rightarrow J_u)(-1)^{J_l-J_u+k+k'+q'+1} (3[k,k',K])^{1/2} \begin{Bmatrix} 1 & 1 & K \\ J_l & J_l & J_u \end{Bmatrix} \times \begin{Bmatrix} k & k' & K \\ J_l & J_l & J_l \end{Bmatrix} \begin{pmatrix} k & k' & K \\ q & q' & Q \end{pmatrix} \bar{J}^K_Q \rho^{k'}_{-q'}(J_l). \tag{4.33}$$

Eq. 4.32 describes the evolution of the upper level $\dot{\rho}^k_q(J_u)$ while the ground state evolution $\dot{\rho}^k_q(J_l)$ is described by Eq. 4.33; ρ^k_q and $\bar{J}^K_Q$ are the irreducible form of the density matrices of atoms and radiation, respectively. The second terms on the left-hand side of Eq. 4.32 and 4.33 represent mixing by a magnetic field, where g_u and g_l are the Landé factors for the upper and ground level. The two terms on the right-hand side of Eq. 4.32 and 4.33 are due to spontaneous emissions and the excitations from ground level with A and B the Einstein spontaneous emission rate and Einstein coefficients for stimulated transitions, respectively.

The radiation tensor of the incident radiation averaged over the whole solid angle Ω and the line profile $\xi(\nu - \nu_0)$ is given by:

$$\bar{J}^K_Q = \int d\nu \frac{\nu_0^2}{\nu^2} \xi(\nu - \nu_0) \oint \frac{d\Omega}{4\pi} \sum_{i=0}^{3} J^K_Q(i,\Omega) S_i(\nu,\Omega), \tag{4.34}$$

with $S_i = [I, Q, U, V]$ the Stokes parameters. The nonzero elements of the radiation tensor in the (θ_r, ϕ_r) direction are:

$$\begin{aligned} \bar{J}^0_0 &= I_*, & \bar{J}^2_0 &= \tfrac{W_a}{2\sqrt{2}W}(2 - 3\sin^2\theta_r) I_*, \\ \bar{J}^2_{\pm 2} &= \tfrac{\sqrt{3}W_a}{4W} \sin^2\theta_r I_* e^{\pm 2i\phi_r}, & \bar{J}^2_{\pm 1} &= \mp \tfrac{\sqrt{3}W_a}{4W} \sin 2\theta_r I_* e^{\pm i\phi_3}, \end{aligned} \tag{4.35}$$

with W the *diluition factor* of the radiation field, which can be divided into an anisotropic part W_a and an isotropic part W_i. It is convenient also to parameterize the radiation field in terms of the so called *anisotropy factor*, defined as:

$$\omega = \sqrt{2}\frac{\bar{J}^2_0}{\bar{J}^0_0}, \tag{4.36}$$

that is zero for an isotropic radiation field and 1 for an unidirectional radiation beam.

By setting the first terms on the left-hand side of Eq. 4.32 and 4.33 to zero, we obtain the following linear equations for the steady state occupations in the ground states of atoms:

$$2\pi i\rho^k_q(J_l)qg_l\nu_L - \sum_{J_u}\frac{A(J_u\rightarrow J_l)}{\sum_{J'_l}A(J_u\rightarrow J'_l)}\sum_{J'_l}[J'_l]B(J'_l\rightarrow J_u)\sum_{k'q'}\rho^{k'}_{-q'}(J'_l)\sum_{KQ}(-1)^{k+k'+q'}$$
$$\times(3[k,k',K]^{1/2})\begin{pmatrix}k & k' & K\\ q & q' & Q\end{pmatrix}\bar{J}^K_Q\left[(-1)^{J_l+J_u}[J_u]\begin{Bmatrix}J_l & J_l & k\\ J_u & J_u & 1\end{Bmatrix}\begin{Bmatrix}1 & J_u & J'_l\\ 1 & J_u & J'_l\\ K & k & k'\end{Bmatrix}+\right.$$
$$\left.-(-1)^{J_l-J_u}\delta_{J_lJ'_l}\begin{Bmatrix}1 & 1 & K\\ J_l & J_l & J_u\end{Bmatrix}\begin{Bmatrix}k & k' & K\\ J_l & J_l & J_l\end{Bmatrix}\right] = 0. \tag{4.37}$$

Finally, the general expression of the Stokes parameters for finite optical depth is:

$$\begin{aligned} I &= (I_0+Q_0)e^{-\tau(1+\eta_1/\eta_0)}+(I_0-Q_0)e^{-\tau(1-\eta_1/\eta_0)},\\ Q &= (I_0+Q_0)e^{-\tau(1+\eta_1/\eta_0)}-(I_0-Q_0)e^{-\tau(1-\eta_1/\eta_0)},\\ U &= U_0e^{-\tau}, V = V_0e^{-\tau}, \end{aligned} \tag{4.38}$$

with I_0, Q_0, U_0 and V_0 the Stokes parameters of the background radiation, d is the thickness of the medium while η_0, η_1 and η_2 are the corresponding absorption coefficients. The degree of polarisation P per unit optical depth τ is then given by:

$$\frac{P}{\tau} = \frac{Q}{I\eta_0 d} \simeq \frac{-\eta_1}{\eta_0} = \frac{1.5\sigma^2_0(J_l,\theta_r)\sin^2\theta\omega^2_{J_lJ_u}}{\sqrt{2}+\sigma^2_0(J_l,\theta_r)(1-1.5\sin^2\theta)\omega^2_{J_lJ_u}}, \tag{4.39}$$

where $\sigma^2_0 = \rho^2_0/\rho^0_0$ quantifies the degree of atomic alignment, while $\omega^2_{J_lJ_u}$ is a parameters determined by the atomic structure:

$$\omega^K_{J_lJ_u} = \frac{\begin{Bmatrix}1 & 1 & K\\ J_l & J_l & J_u\end{Bmatrix}}{\begin{Bmatrix}1 & 1 & 0\\ J_l & J_l & J_u\end{Bmatrix}}. \tag{4.40}$$

To make concrete what has been said, let us consider, as an example, the case of the single ground level specie Cr I; as we will see later this atomic species will be particularly important.

Cr I has a ground state $7S_3$ and excited state $7S_{2,3,4}$. The density matrix for the Cr I state has seven component with $K = 3-3, 3-2, ..., 3+3 = 0, 1, 2, 3, 4, 5, 6, 7$. To calculate the steady state occupation in the ground state we have to taking into account all of the possible transitions. This is because they all affect the ground populations and hence the degree of polarisation. Inserting all of the values of J_u, J_l, k, k', K and, from Eq. 4.35, J_Q^K into Eq. 4.37, we obtain three linear equations of $\rho_0^{0,2,4,6}(J_l)$. By solving them we have:

$$\begin{Bmatrix} \sigma_0^2(J_l) \\ \sigma_0^4(J_l) \\ \sigma_0^6(J_l) \end{Bmatrix} = \frac{\begin{Bmatrix} 35.829\cos 2\theta_r & -12.593\cos 4\theta_r & +0.253\cos 6\theta_r & +1.932 \\ 0.671\cos 2\theta_r & +1.2648\cos 4\theta_r & -0.6092\cos 6\theta_r & +1.7263 \\ -1.0902\cos 2\theta_r & -0.5032\cos 4\theta_r & -0.2516\cos 6\theta_r & -0.5404 \end{Bmatrix}}{(-322\cos 2\theta_r) + 1.24\cos 4\theta_r + 568}. \tag{4.41}$$

Finally, by inserting this result into Eq. 4.39 we can get the polarisation of Cr I absorption lines.

5 The post-AGB binary 89 Herculis

> *The nitrogen in our DNA, the calcium in our teeth, the iron in our blood, the carbon in our apple pies were made in the interiors of collapsing stars. We are made of starstuff.*
>
> **— Carl Sagan**

The post-AGB binary star 89 (V441) Herculis is a bright member of the *UU Herculis stars* (Tab. 5.1). These stars are considered as a prototype of a new class of post-AGB binaries, characterized by the presence of a common circumbinary disk. Different studies of this class of systems have placed important questions about the understanding of binary systems of post-AGB stars and the physics of the circumbinary envelopes, as we have discussed in Sec. 1.1.1.

For these reasons 89 Herculis is a well studied system, observed in photometry, spectroscopy, interferometry and polarimetry; stellar and binary parameters are shown in Tab. 5.2. These parameters suggest that the companion star is still in the main sequence and its distance from the primary is $< 1\ AU$. From this it is evident that the primary star has had a more rapid evolution than its companion and the mass loss, during the different evolutionary phases, has built and shaped a common envelope within the two stars are orbiting.

In this Chapter we deal with the major results achieved during my PhD. A large fraction of time has been devoted to a spectropolarimetric monitoring of 89 Herculis (Sec. 5.1). This allowed us to point out the presence of linear polarisation across absorption (Sec. 5.2) and emission lines (Sec. 5.4) and, for the first time, to use analitical ad numerical model to interpret the observational data in a general scenario (Sec. 5.3, 5.5). Finally, in Sec. 5.6 we focus on the spectroscopic manifestations of 89 Herculis circumstellar envelope: we discuss the long-term episodic mass-loss enhancements (Sec. 5.6.1) and the variability of BaII 6141.713 Å and YII 5087.418 Å lines (Sec. 5.6.2).

The most important characteristics of 89 Herculis obtained through different observational techniques are presented in the next subsections.

Name		89 Her
		HR6685
		HD163506
Coordinates	α	17 55 25.19
(ep=J2000)	δ	+26 02 59.97
Galactic	l	51.43
coordinates	b	+23.19
Mean magnitude	B	5.70
	V	5.36
	J	5.24
	K	3.35
Spectral Type		F2Ibe
Radial velocity		$-28.5\ km\ s^{-1}$

Tab. 5.1.: Basic data for 89 Herculis (SIMBAD database).

Parameter	Value	Error	Reference
Sp. T.	F2Ibe	-	-
Teff(K)	6550	100	**1** - **2**
log g	0.55	0.25	**1** - **2**
Fe/H	-0.5	0.2	**1** - **2**
P_{orb} (d)	288.36	0.71	**3**
e	0.189	0.074	**3**
$a_l\ sini$ (AU)	0.080	0.007	**3**
f(m) ($M_\odot$)	0.00084	0.00022	**3**
i (°)	12	3	**4**
π (mas)	0.76	0.23	**5**
d (kpc)	1.5	$^{+1.0}_{-0.5}$	**5**

Tab. 5.2.: Stellar and binary parameters of 89 Herculis. Reference: **1** Luck (1990), **2** Kipper (2011), **3** Waters (1993), **4** Bujarrabal (2001), **5** Van Leeuwen (2007).

Photometry

89 Herculis is classified as a *semiregular pulsating star* and it is variable in radial velocity (RV) and light. From a photometric point of view the variability was first noted by Worley (1956) and has been studied especially by Fernie (1981, 1983, 1986, 1989, 1990, 1991), Fernie & Seager (1993) and Donahue et al. (1993). They found a short photometric period of about 65 days. This period appears to be due to radial pulsation. Percy et al. (2000) detected, in addition, a long photometric period of about 283 days which was previously observed in radial velocity only and ascribed to binarity.

In Fig. 5.1 we calculate the CLEANED (Roberts et al. 1987) Periodogram (Scargle 1982) of about 28 years of photometric data taken from the *America Association of*

Variable Star Observers (AAVSO, Kafka et al. 2016) database; here the presence of a short (~ 65 day) and long (~ 288 day) photometric period is confirmed.

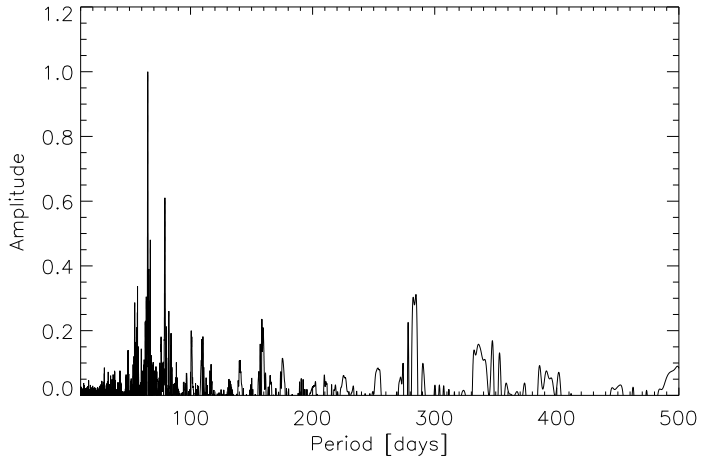

Fig. 5.1.: CLEANED (Roberts et al. 1987) Periodogram (Scargle 1982) of photometric data of 89 Herculis. The highest peak is close to the ~ 65 day pulsational period, while a peak at ~ 288 day orbital period is also present.

Spectroscopy

Kipper (2011) performed a chemical analysis through high resolution spectra of 89 Herculis. He found that the star is slightly metal-poor and this indicates that it has been originated in the Galaxy thick disk. Carbon and Nitrogen are overabundant and this agrees with the post-AGB status. On the contrary, the anhancements of heavy s-process elements were not found.

In addition, spectroscopic observations have shown a typical P Cygni profile for the H_α line, where the simultaneous presence of absorption and emission lobes around the central wavelength of the line, suggest the presence of an expanding gas envelope.

Several studies have been carried out about 89 Herculis spectral variability. Burki et al. (1980) performed an observational study of radial velocity. They observed a regular cycle of variation of period between 50 and 75 days in radial velocity. They note also that quasi-erratic variations are observed in radial velocity when simultaneous light variations are quite smooth (Fig. 5.2). Arellano Ferro (1984) performed an analysis of the variability of radial velocities and interpreted them supposing that 89 Herculis is a pulsating star in a binary system with an orbital period $P_{orb} = 285$ days and a pulsationals period $P_{puls} = 63.5$ days. However, the given orbital solution dos not fully justify the observational data (Fig. 5.3). Waters

(1993) made a study on the variability of radial velocities and found an orbital period $P = 288.36 \pm 0.71$ days, with ephemeris:

$$JD(RV_{max}) = 2446013.73(\pm 16.95) + 288.36(\pm 0.71) \quad days. \tag{5.1}$$

He costructed a qualitative model for the circumstellar envelope and suggested that it is a highly non-spherical environment as a result of binary evolution. As we can see in Fig. 5.4, Waters noted that the variations in radial velocities are also caused by instabilities in the stellar atmosphere.

These instabilities were also pointed out by looking at specific lines. In particular Böhm-Vitense (1956) firstly discovered important variations in the structure of the hydrogen and sodium D lines, which were later ascribed to the presence of an expanding circumnstellar envelope (Sargent & Osmer 1969). Kipper (2011) showed that the H_α blue wing changes fast with a time scale less than a month, as well as the Na ID lines (Fig. 5.5). On the other hand, Khalilov et al. (2010) pointed out a long-period variability in the equivalenth widths (EW) of the P Cygni-like H_α line. In particular they determined a period of 6553.6 day for the absorption component and a period of 10922.7 day for the emission ones. However, none of them investigated the causes of these variations.

Medium and high resolution spectroscopy also allowed the detection of many emission lines: discovered by Osmer (1968), more than 300 weak metal lines in emission have been identified by Kipper (2011) in the spectrum of 89 Herculis. Kipper pointed out that these lines: 1) present the velocity of the binary system, 2) are due to neutral metals with a rather low (<6 eV) excitation levels, and 3) are not due to forbidden and ionic transitions. Kipper concluded that these emission lines are formed in the circumbinary disk. Already Waters et al. (1993) have interpreted these weak, neutral or low-excitation-level emission lines of metals as a proof of the collisionally excited interaction between the stellar wind and the circumbinary disk.

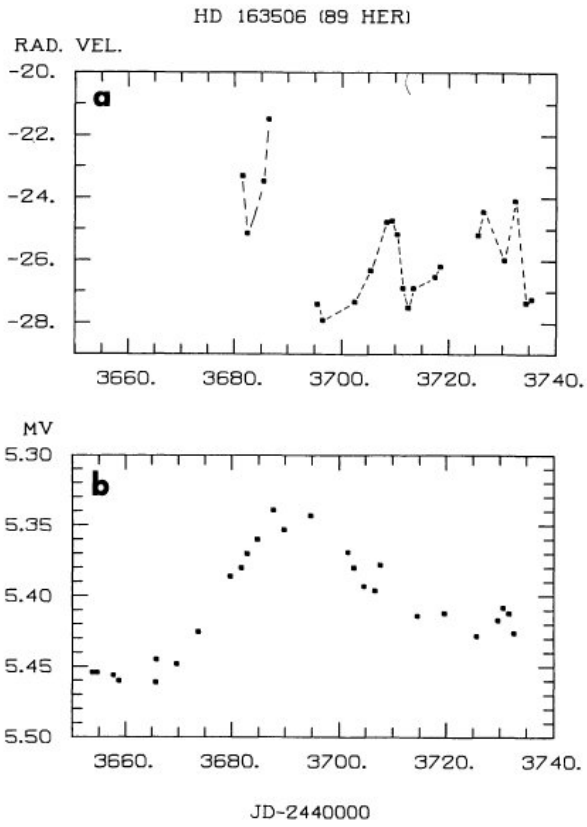

Fig. 5.2.: Simultaneous measurements of 89 Herculis in **(a)** radial velocity and **(b)** photometry (Percy et al. 1979).

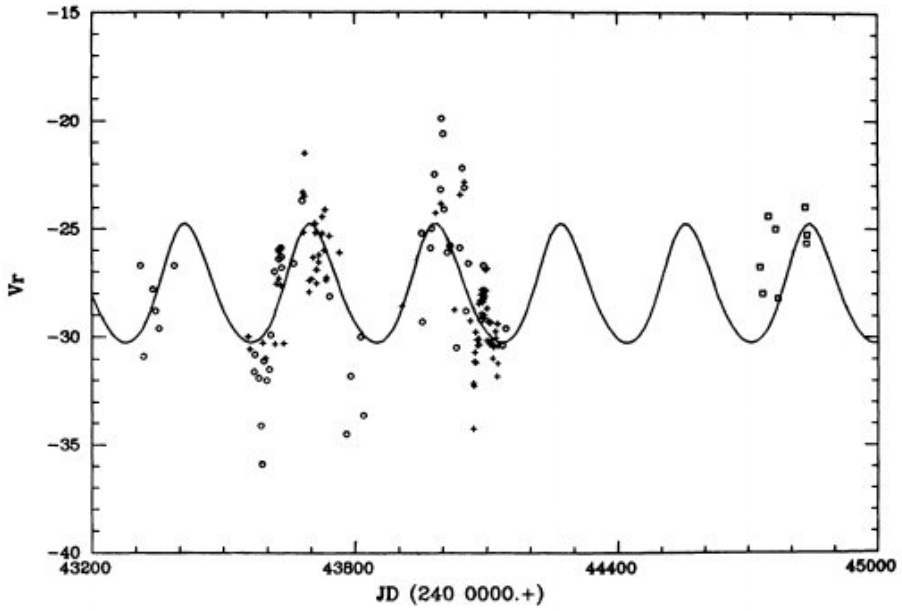

Fig. 5.3.: 89 Herculis radial-velocity variations from 1977 to 1981. The solid curve is the orbital solution found by Ferro (1984).

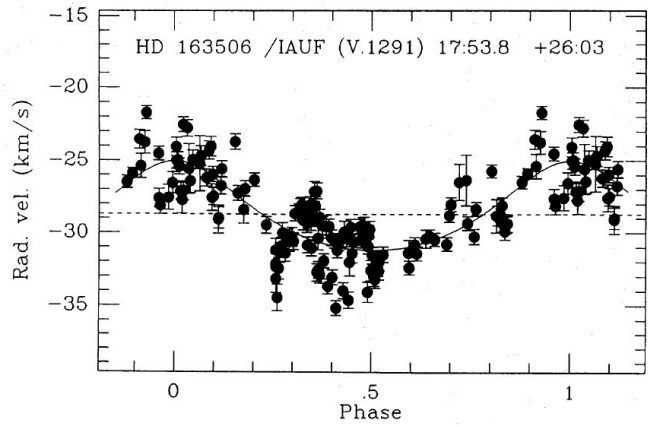

Fig. 5.4.: Radial velocity measurements of 89 Hercuis folded with a period of 288.36 days (Waters 1993).

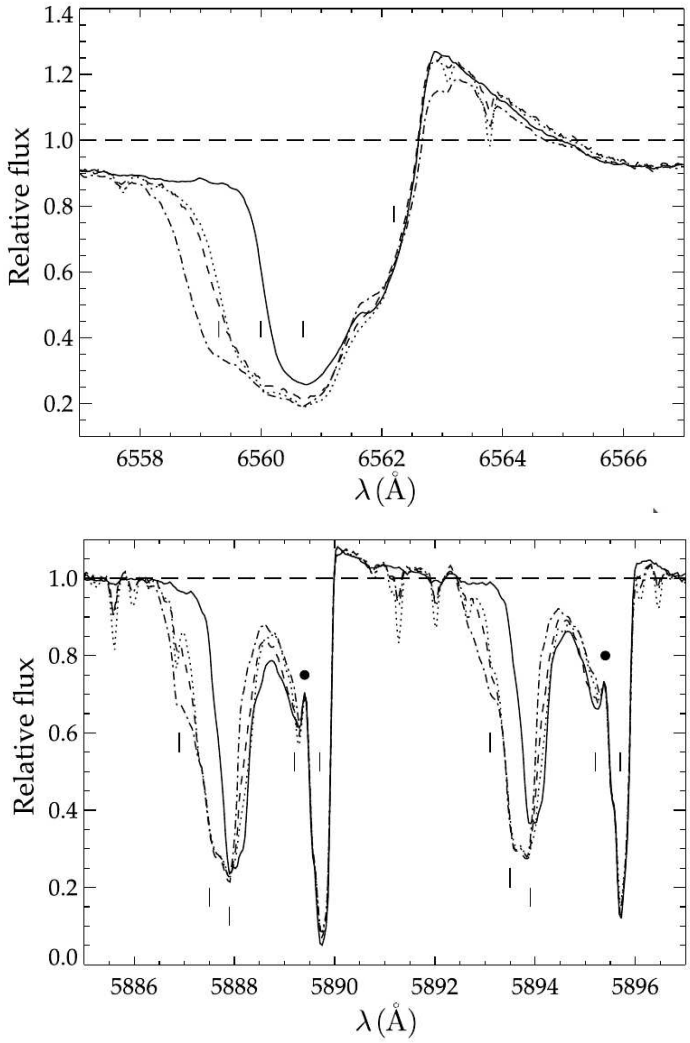

Fig. 5.5.: Changes in the H_α line (top) and in the Na ID doublet (bottom) observed on 2010-02-01 -full line, on 2009-10-05 - dotted line, on 2009-09-28 - dashed line and on 2009-09-07 - dahs dotted line. Image adapted from Kipper (2011).

Bujarrabal et al. (2007) performed a high-resolution interferometric study of 89 Herculis with the IRAM Plateau de Bure Interferometer in the nm range using the $^{12}CO(1-0)$ and $^{12}CO(2-1)$ lines and in the NIR with the VTL/MIDI instrument. Interferometric data have been interpreted with two nebular components: an expanding hour-glass structure and an unresolved circumbinary Keplerian disk. Bujarrabal and coworkers concluded that the hour-glass axis is tilted with respect to the Line-of-Sight (LoS) of $\theta_{LoS} = 15°$ with a Position Angle $\theta_{PA} = 45°$ (Fig. 5.6).

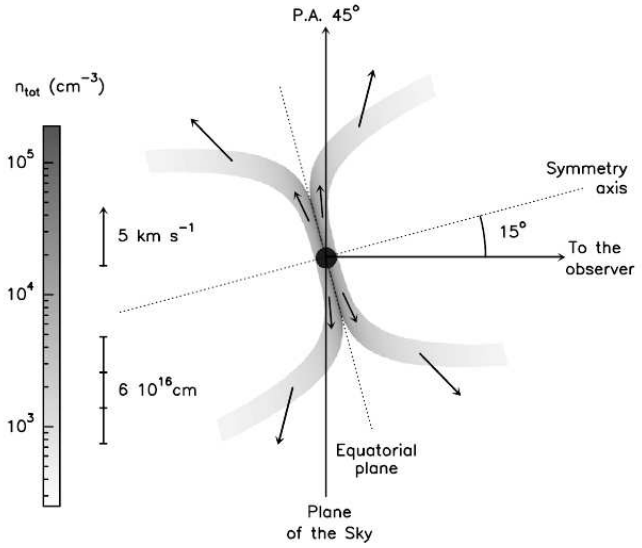

Fig. 5.6.: Geometry of the 89 Herculis circumbinary environment proposed by Bujarrabal et al. (2007).

Hillen et al. (2013, 2014) investigated the continuum circumstellar environment at optical and near-IR wavelengths with the VLTI, NPOI, IOTA, PTI, and the CHARA Array. Using different radiative transfer models, they suggest four cases for the circumbinary environment (Fig. 5.7):

- Case 1: all optical flux is light scattered off the inner rim of a dust disk, with a polar angle α of $67.5°$ and a small viewing angle of $\sim 12°$;
- Case 2: combination between a circumbinary dust disk and an inner gas disk;
- Case 3: circumbinary dust disk with a bipolar outflow seen pole-on. The latter is originated as stellar wind or jet;
- Case 4: circumbinary dust disk with an optically thin halo.

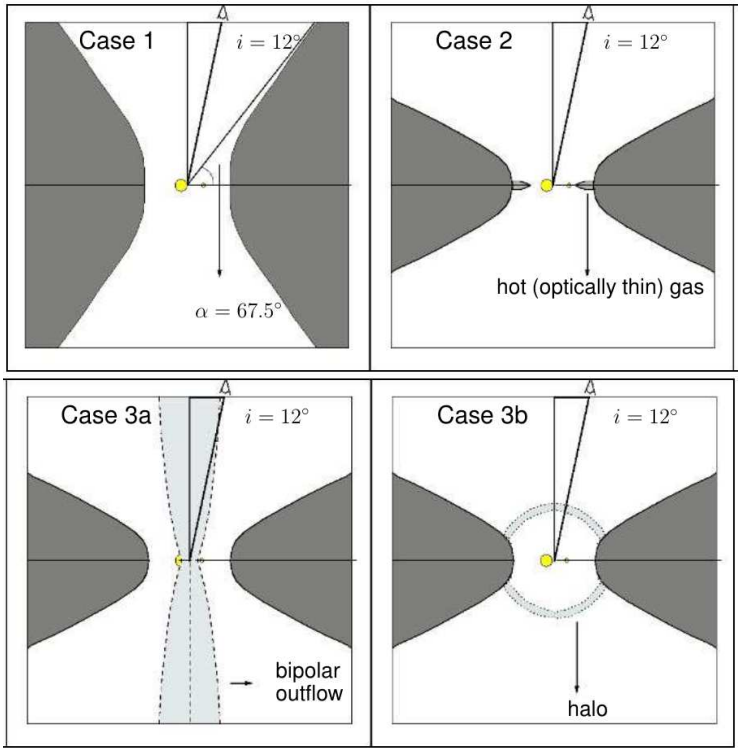

Fig. 5.7.: Geometries of the 89 Herculis circumbinary environment proposed by Hillen et al. (2013).

Polarimetry

Harrington & Kuhn (2009) published an interesting work about the H_α polarised line profiles and its temporal variability in post-AGB and other stellar types. They found that the H_α line profile of 89 Herculis shows linear spectropolarimetry variability on short timescales in the absorption component. The authors propose the optical pumping model (Kuhn et al. 2007) to explain the observed polarimetric signatures, suggesting a near-stellar location of an absorbing gas shell.

Using the LSD technique, Sabin et al. (2015) found evidence of linear polarisation also in the spectral lines in absorption of 89 Herculis. In addition they detected no Stokes V signal across the LSD line profile, establishing an upper limit of 10 G to the effective surface magnetic field.

Finally, from the basis of time resolved broad-band photopolarimetry, Akras et al. (2017) concluded the 89 Herculis is an intrinsic unpolarised source in the visible range.

5.1 Observations

From June 2014 to August 2018, we have performed high resolution spectroscopy and spectropolarimetry of 89 Herculis with the high resolution *Catania Astrophysical Observatory Spectropolarimeter* (CAOS, $R = 55000$, Leone et al. 2016a) at the 0.91 m telescope of the stellar station of the Catania Astrophysical Observatory ($G.M.Fracastoro$ Stellar Station, Serra La Nave, Mt. Etna, Italy). A spectrum in linearly polarised light was acquired on May 27^{th}, 2017 with the HArps-North POlarimeter (HANPO, $R = 115000$, Leone et al. 2016b) of the Telescopio Nazionale Galileo (Roque de Los Muchachos Astronomical Observatory, La Palma, Spain). Data were reduced and Stokes Q/I, U/I and *null* spectra N obtained according to the procedures described in Sec. 3.4.3.

In addition, reduced spectropolarimetric data of 89 Herculis have been retrieved from the Canadian Astronomy Data Centre. Spectra were collected from 2005 to 2009 at the 3.6 m Canadian-France-Hawaii Telescope with the *Echelle SpectroPolarimetric Device for the Observation of Stars* (ESPaDOnS, $R = 68000$, Donati et al. 2006). The logbook of observations is given in Tab. 5.3.

The final observational data consist of time resolved spectra of 89 Herculis with clear evidence of polarisation across the profile of metal lines[1]. We found large differences between absorption and emission lines, as well as important spectroscopic variations on large timescale.

Tab. 5.3.: Logbook of observations. The achieved Signal-to-Noise (S/N) os determined from *null* LSD spectra.

HJD 2400000+	S/N	Instr.	HJD 2400000+	S/N	Instr.
53604.753	11264	ESP	55102.832	5188	ESP
53775.115	10518	ESP	55109.823	12420	ESP
53777.096	19448	ESP	56816.515	2958	CAOS
53961.777	21810	ESP	56862.456	2328	CAOS
54372.821	23880	ESP	56863.347	2388	CAOS
54877.099	4248	ESP	56876.340	3478	CAOS
54878.132	10704	ESP	56894.309	4200	CAOS
54880.076	14710	ESP	56897.301	4126	CAOS
54954.125	12876	ESP	56898.274	4292	CAOS
54955.849	10578	ESP	6904.313	3698	CAOS
54958.121	13982	ESP	57582.248	3712	CAOS
54959.874	8046	ESP	57666.248	2884	CAOS
55081.874	2996	ESP	57900.602	4300	HANPO

[1] In A.1 we report an atlas of what we call *Second Stellar Spectrum* of 89 Herculis with the highest S/N spectra acquired with ESPaDOnS on Aug. 14, 2006.

5.2 Polarisation of metal lines in absorption

As we said in the introduction, Sabin et al. (2015) discovered evidence of linear polarisation in the Stokes Q/I and U/I LSD profiles of 89 Herculis spectra recorded with ESPaDOnS on Feb. 8, 2006. We found that all the archived ESPaDOnS spectra of 89 Herculis, spanning about 1400 days clearly show evidence of linear polarisation across single lines in absorption, despite the photon noise. Stokes Q/I and U/I profiles appear not null and variable in time; Fig. 5.8 provides an example of such variable signals for transitions of Fe II, Cr II and Ti II, while in Tab. 5.4 we report a list of 50 spectral lines with a very high S/N polarisation. From the latter it is evident that Stokes profiles scale with the line depth irrespective of wavelength (Fig. 5.9). We have then selected in the 400-700 nm range a set of about 1000 spectral lines of iron-peak elements whose Stokes I residual is larger then 0.2, excluding blended lines. Lines were selected from a synthetic spectrum computed by SYNTHE (Kurucz 1993) with stellar parameters given in Tab. 5.2. Fig. 5.10 shows the comparison between the ESPaDOnS-LSD and Fe II 4508.288 Å profiles at three different dates.

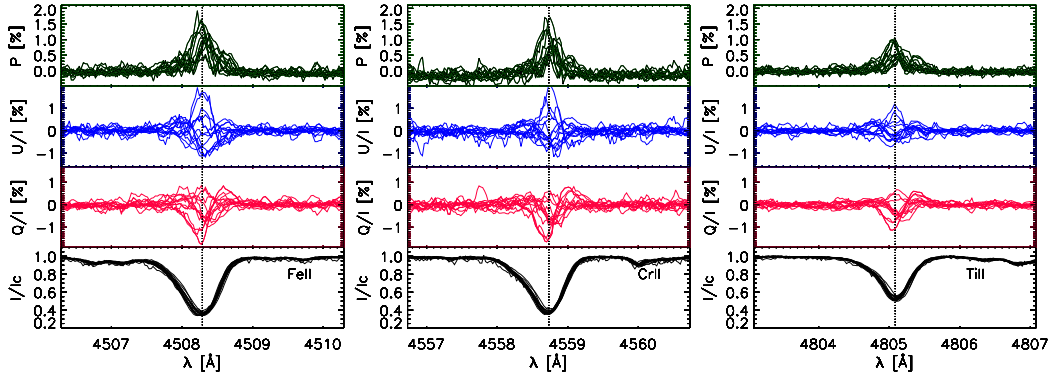

Fig. 5.8.: All 15 ESPaDOnS Stokes I, Q/I, U/I profiles and polarisation $P = \sqrt{(Q/I)^2 + (U/I)^2}$ for the Fe II 4508.288 Å, Cr II 4558.783 Å and Ti II 4805.085 Å lines. Data, collected between 2005 and 2009, present a clearly linear polarisation and a significant morphological variability in time.

In CAOS spectra of 89 Herculis, we don't find any direct evidence of polarisation across single lines. After numerical simulations showing that ESPaDOnS Stokes Q/I and U/I profiles would be hidden in the S/N of CAOS spectra, we have successfully constructed the CAOS-LSD profiles from the spectral line list we selected for the ESPaDOnS-LSD. For consistency, also the HANPO-LSD Stokes profiles were based on the same list of spectral lines. This represent the first scientific result for the HANPO instrument (Fig. 5.11). The complete collection of the variable Stokes Q/I and U/I LSD profiles is shown in Fig. 5.12. S/N achieved in *null* LSD profiles is given in Tab. 5.3.

Tab. 5.4.: A list of 50 single lines which show high S/N polarisation. Atomic data are taken from NIST database; P_{max} indicates the maximum of polarisation measured across the profile, while PN_{max} is the maximum of polarisation calculated from Stokes Q and U that were normalized to an average profile, equal for all transitions. In this way the value of P does not depend on the depth of the specific considered line.

λ [Å]	A_{ki} $[s^{-1}]$	E_i $[eV]$	E_f $[eV]$	J_i	J_f	P_{max} [%]	PN_{max} [%]
C I							
4771.733	8.0e+05	7.48779862	10.08537735	2	2	0.54 ± 0.05	1.12 ± 0.21
4932.025	6.0e+06	7.68476771	10.19792594	1	0	0.57 ± 0.11	1.25 ± 0.10
Ca I							
5688.205	1.21e+07	2.104429184	4.28349644	3/2	5/2	0.34 ± 0.01	0.74 ± 0.19
Mg II							
5528.405	1.39e+07	4.3458028	6.5878559	1	2	0.64 ± 0.05	1.16 ± 0.20
Si II							
5055.984	1.45e+08	10.073880	12.525423	3/2	5/2	0.27 ± 0.07	0.73 ± 0.12
Ca I							
5588.749	4.9e+07	2.5256821	4.7435268	3	3	0.43 ± 0.08	1.05 ± 0.16
6439.075	5.3e+07	2.5256821	4.4506470	3	4	0.58 ± 0.05	1.23 ± 0.08
Sc II							
5031.021	3.5e+07	1.356952	3.820660	2	1	0.55 ± 0.02	1.11 ± 0.22
Ti II							
4518.332		1.07997272	3.82322940	3/2	3/2	0.39 ± 0.21	1.19 ± 0.13
4911.195	1.70e+07	3.12352955	5.64734719	5/2	3/2	0.77 ± 0.04	1.40 ± 0.28
5129.156	1.46e+06	1.89169543	4.30826565	9/2	9/2	0.71 ± 0.08	1.42 ± 0.15
5185.902	1.01e+06	1.89270557	4.28283323	7/2	7/2	0.64 ± 0.64	1.38 ± 0.16
Cr II							
4618.803	6.1e+06	4.07349335	6.75707561	5/2	3/2	1.11 ± 0.09	1.67 ± 0.18
4634.070	8.9e+06	4.07222461	6.74696646	3/2	1/2	1.22 ± 0.09	1.83 ± 0.13
4812.337	4.6e+05	3.86441082	6.44006951	7/2	9/2	0.73 ± 0.02	1.41 ± 0.21
5237.329	1.7e+06	4.07340778	6.44006951	9/2	9/2	0.87 ± 0.15	1.61 ± 0.14
5279.880	2.4e+05	4.07340778	6.42099465	9/2	7/2	0.60 ∓ 0.09	1.33 ± 0.18
5280.054		4.07349335	6.42099465	5/2	7/2	0.62 ± 0.07	1.33 ± 0.18
5305.853		3.82670193	6.16279084	5/2	5/2	0.43 ± 0.03	1.06 ± 0.23
5308.440	6.1e+05	4.07122603	6.40618983	7/2	5/2	0.47 ± 0.05	1.10 ± 0.19
5313.590	8.8e+05	4.07349335	6.40618983	5/2	5/2	0.61 ± 0.18	1.33 ± 0.11
5334.869		4.07222461	6.39561329	3/2	3/2	0.53 ± 0.06	1.26 ± 0.26
Fe I							
5049.820	1.65e+06	2.27860464	4.73314075	2	3	0.48 ± 0.11	1.16 ± 0.07
5074.748	1.4e+07	4.22036207	6.66284109	4	5	0.50 ± 0.08	1.15 ± 0.34
5133.688		4.17769675	6.59213389	5	6	0.60 ± 0.08	1.28 ± 0.13
5364.871	5.59e+07	4.44562722	6.75602278	2	3	0.38 ± 0.10	1.04 ± 0.13
5367.467	7.13e+07	4.41527874	6.7245573	3	4	0.48 ± 0.06	1.11 ± 0.19
5383.369	7.81e+07	4.31247055	6.61492752	5	6	0.68 ± 0.10	1.40 ± 0.07
5403.822	1.92e+06	4.07581088	6.36955300	4	5	0.45 ± 0.08	1.02 ± 0.13
5415.199	7.67e+07	4.38646271	6.67538606	5	6	0.57 ± 0.09	1.23 ± 0.11
5424.068		4.32010004	6.6052808	6	7	0.63 ± 0.09	1.31 ± 0.13
5569.618	2.34e+07	3.41695278	5.64241568	2	1	0.40 ± 0.04	0.90 ± 0.20
5572.842	2.28e+07	3.39650878	5.62068411	3	2	0.55 ± 0.07	1.17 ± 0.12
5586.756	2.19e+07	3.36825637	5.58689271	4	3	0.53 ± 0.09	1.13 ± 0.19
Fe II							
4508.288	7.e+05	2.85551513	5.60488795	3/2	1/2	1.23 ± 0.11	1.41 ± 0.06
4515.339	2.4e+05	2.84411705	5.58919546	5/2	5/2	1.27 ± 0.10	1.50 ± 0.12
4520.224	1.0e+05	2.80665445	5.54876619	9/2	7/2	1.44 ± 0.11	1.73 ± 0.17
4541.524	9.e+04	2.85551513	5.58476794	3/2	3/2	1.37 ± 0.13	1.85 ± 0.11
4576.340	6.4e+04	2.84411705	5.55260574	5/2	5/2	1.20 ± 0.10	1.72 ± 0.18
4620.521	2.5e+04	2.82812243	5.51071386	7/2	7/2	1.11 ± 0.10	1.75 ± 0.17
4666.758	1.3e+04	2.82812243	5.48413595	7/2	9/2	1.10 ± 0.04	1.77 ± 0.34
5197.577	5.5e+05	3.23045934	5.6152225	5/2	3/2	0.91 ± 0.10	1.47 ± 0.11
5254.929	9.0e+06	10.4552113	12.8126136	5/2	7/2	0.73 ± 0.07	1.17 ± 0.09
5256.938	3.45e+07	10.4996321	12.8573817	7/2	9/2	0.46 ± 0.06	1.06 ± 0.13
5325.553	1.6e+04	3.22131341	5.54876619	7/2	7/2	0.80 ± 0.13	1.58 ± 0.13
5362.869	1.50e+07	10.5027942	12.8141044	7/2	9/2	1.02 ± 0.13	1.63 ± 0.05
5425.257	9.e+03	3.19945276	5.48413595	9/2	9/2	0.68 ± 0.12	1.38 ± 0.07
5534.847	3.0e+04	3.24468889	5.48413595	11/2	9/2	0.92 ± 0.01	1.50 ± 0.17
6147.741	1.3e+05	3.88869683	5.9048850	3/2	1/2	0.53 ± 0.04	1.15 ± 0.16
6416.928	4.e+04	3.89161336	5.82322470	5/2	5/2	0.49 ± 0.02	1.07 ± 0.12

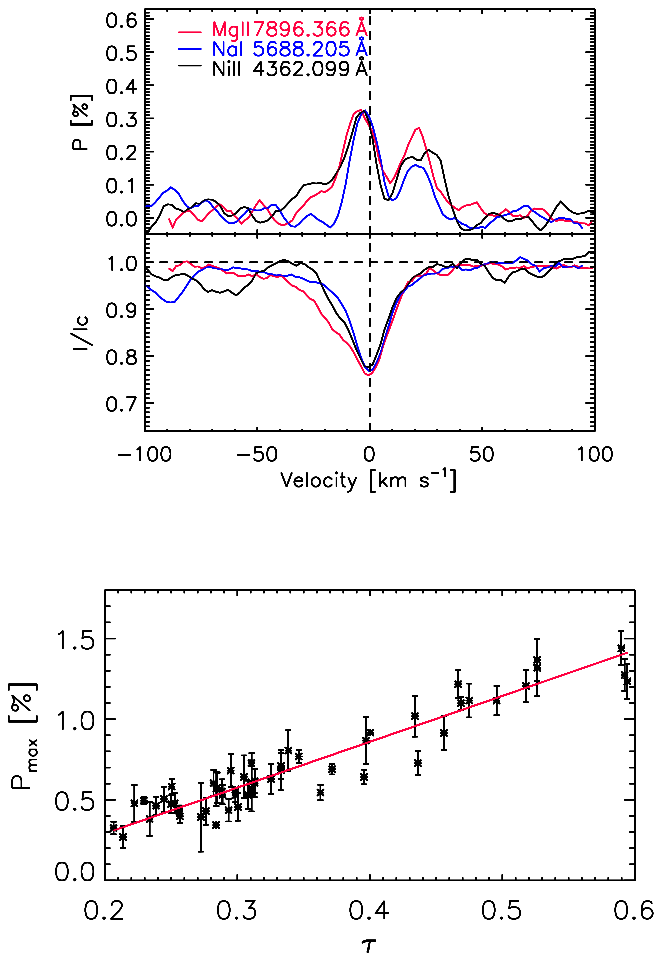

Fig. 5.9.: Top: examples of spectral lines with equal depth showing that, within errors, polarisation does not depend on wavelength. Bottom: maximum of the polarisation across spectral lines versus optical depth.

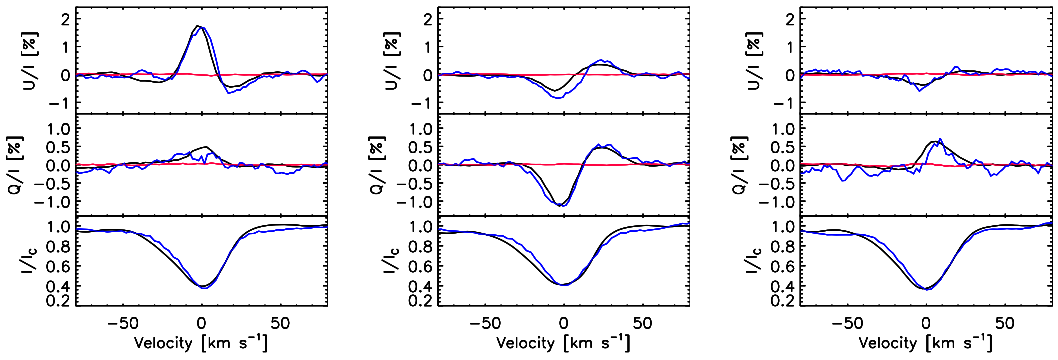

Fig. 5.10.: ESPaDOnS: Comparison between the Stokes parameters of the Fe II 4508.288 Å (black) line and LSD profiles (blue). LSD null polarization in red. From the left, spectra were acquired on HJD53604.753, 53961.777 and 54878.132.

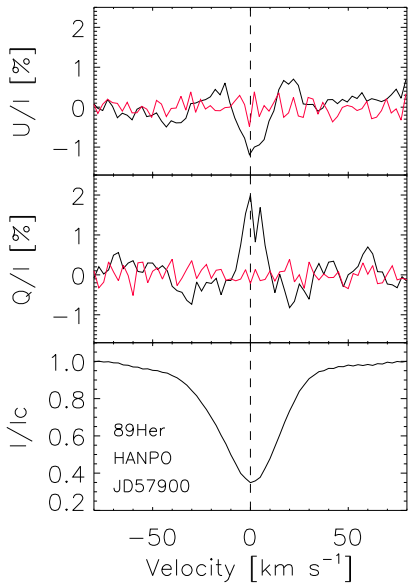

Fig. 5.11.: First scientific result of HANPO; I, Q/I and U/I Stokes LSD profiles of 89 Herculis.

5.3 Origin of linear polarisation of metal lines in absorption

As a first investigation, we have performed a time analysis of the total polarisation measured across the LSD profiles. The Scargle (1982) periodogram, CLEANED following Roberts et al. (1987), presents the highest peak at 294 ± 5 days that is coincident within errors with the orbital period (Fig. 5.13). Fig. 5.13 also shows how the total polarisation changes with the orbital period. A similar variability cannot be statistically confirmed for the Equivalent Widths of Stokes I profiles, whose sinusoidal fit gives an amplitude of 10 ± 9 mÅ.

The consideration that the polarisation of metal lines in absorption is variable with the orbital period implies that the phenomenon responsible for the observed polarisation is on a scale not larger than the circumbinary disk and that it is related to the presence of the secondary. As we have described in Chapter 4, basic mechanisms at the basis of the observed linear polarisation in metal lines are : 1) Large (i.e. Gauss level) magnetic fields due to the Zeeman Effect. 2) The presence of a polarised continuum, e.g. due to scattering by grains, molecules (Rayleigh scattering) or by free electrons (Thomson scattering). In this case, thermal recombination radiation would apppear as spectral lines unpolarising the continuum. An effect that at high

spectral resolution, when the continuum polarisation is settled to zero, results in apparently polarised spectral lines. 3) Anisotropic radiation on emitting atoms, not necessarily in excited Zeeman states (Landi Degl'Innocenti & Landolfi 2004; Trujillo Bueno 2005; Yan & Lazarian 2008). Here we will consider one by one the possible mechanisms:

5.3.1 Large Magnetic Fields

Since Wade et al. (2000) and Bagnulo et al. (2001), linearly polarised metal lines are observed in the spectra of magnetic chemically peculiar stars (Wolff 1983, still offers a complete and gentle introduction to this class of stars) and it is ascribed to the Zeeman effect. The presence of magnetic fields on the surface of 89 Herculis has been ruled out by Sabin et al. (2015) who detected no Stokes V signal across the LSD profile (Fig. 5.14) and established an upper limit of 10G to the effective magnetic field, that is by definition the average over the visible stellar disk of longitudinal components of the fields (Babcock 1947). With CAOS, we have also performed circular spectropolarimetry of 89 Herculis on HJD56853.535 and an upper limit of 50G has been estimated for the effective field from the Stokes V and I LSD profiles (Fig. 5.15), by using the moment technique. Following Leone & Catanzaro (2004), in fact, the effective magnetic field H_{eff} is expressed as:

$$H_{eff} = \frac{R_V^{(1)}}{4.67 \times 10^{-13} g_{eff} \lambda^2}, \tag{5.2}$$

with g_{eff} the effective Landé factor, λ wavelength expressed in Å and H_{eff} in Gauss; $R_V^{(1)}$ is the first moment of the Stokes V line profile (Mathys 1994):

$$R_V^{(1)} = \frac{1}{W} \int \frac{V_c - V_\lambda}{F_{I_c}} (\lambda - \lambda_I) d\lambda \tag{5.3}$$

where W is the equivalent width, V_λ is the flux in Stokes V across the spectral line, V_c the Stokes V flux in the neighbouring continuum, F_{I_c} the unpolarised continuum flux and λ_I is the center of gravity of the Stokes I line profile.

In principle, a linear polarisation in spectral lines associated to a null circular polarisation is possible for a purely transverse field. However, for a large scale organised stellar magnetic field of a rotating star even if the average of the longitudinal components across the visible stellar disk is null, Stokes V profiles are different than zero. We agree with Sabin et al. (2015) conclusion and exclude the possibility we are recording the linear polarisation of Zeeman components.

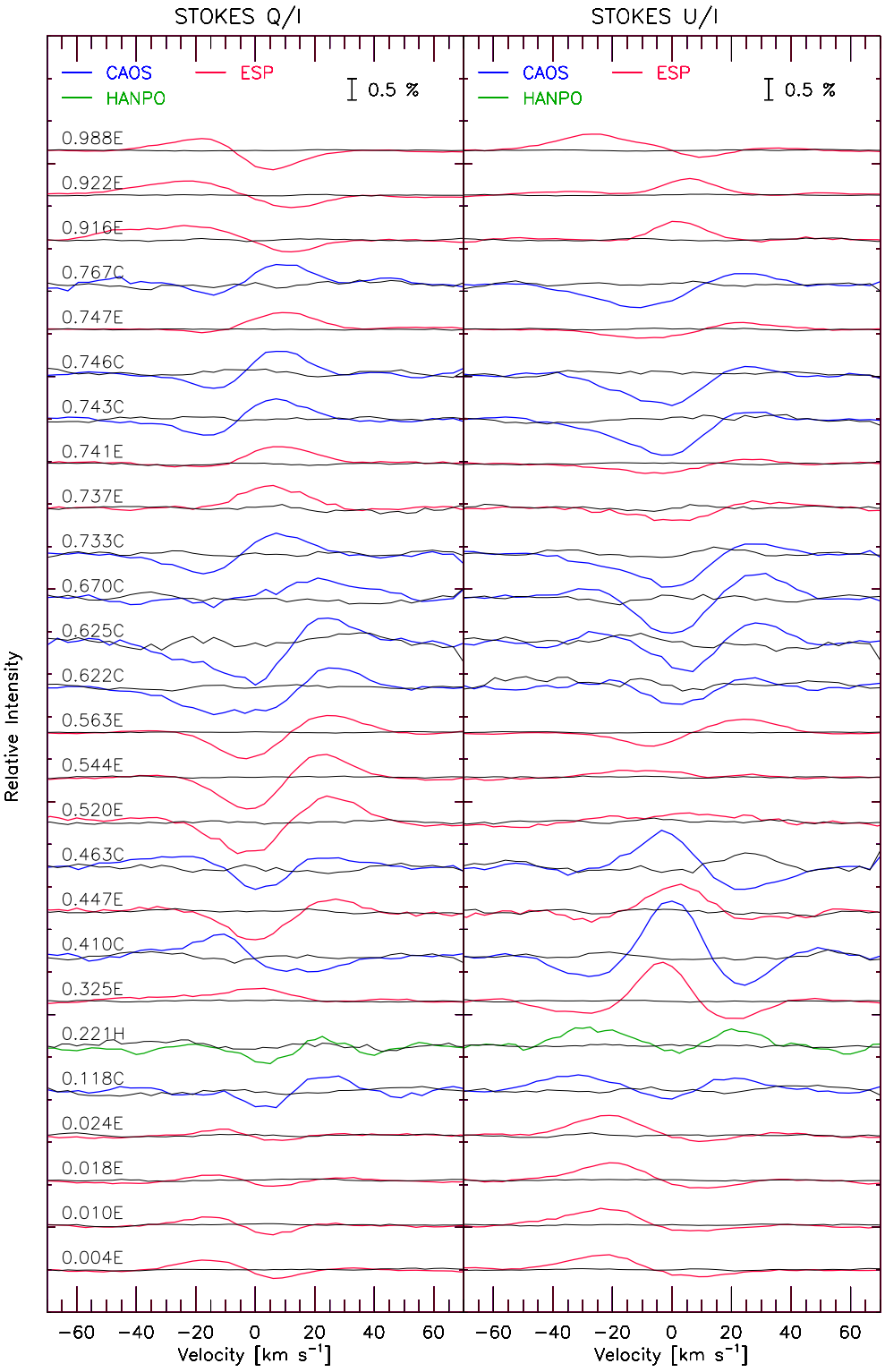

Fig. 5.12.: Observed Stokes Q/I and U/I LSD profiles of 89 Herculis. Null polarisation in black. Profiles are ordered according to the orbital phase computed with Eq. 5.1 and arbitrarily shifted for a better visualisation. After the phase value, E means that the spectra were obtained with ESPaDOnS, C with CAOS and H with HANPO.

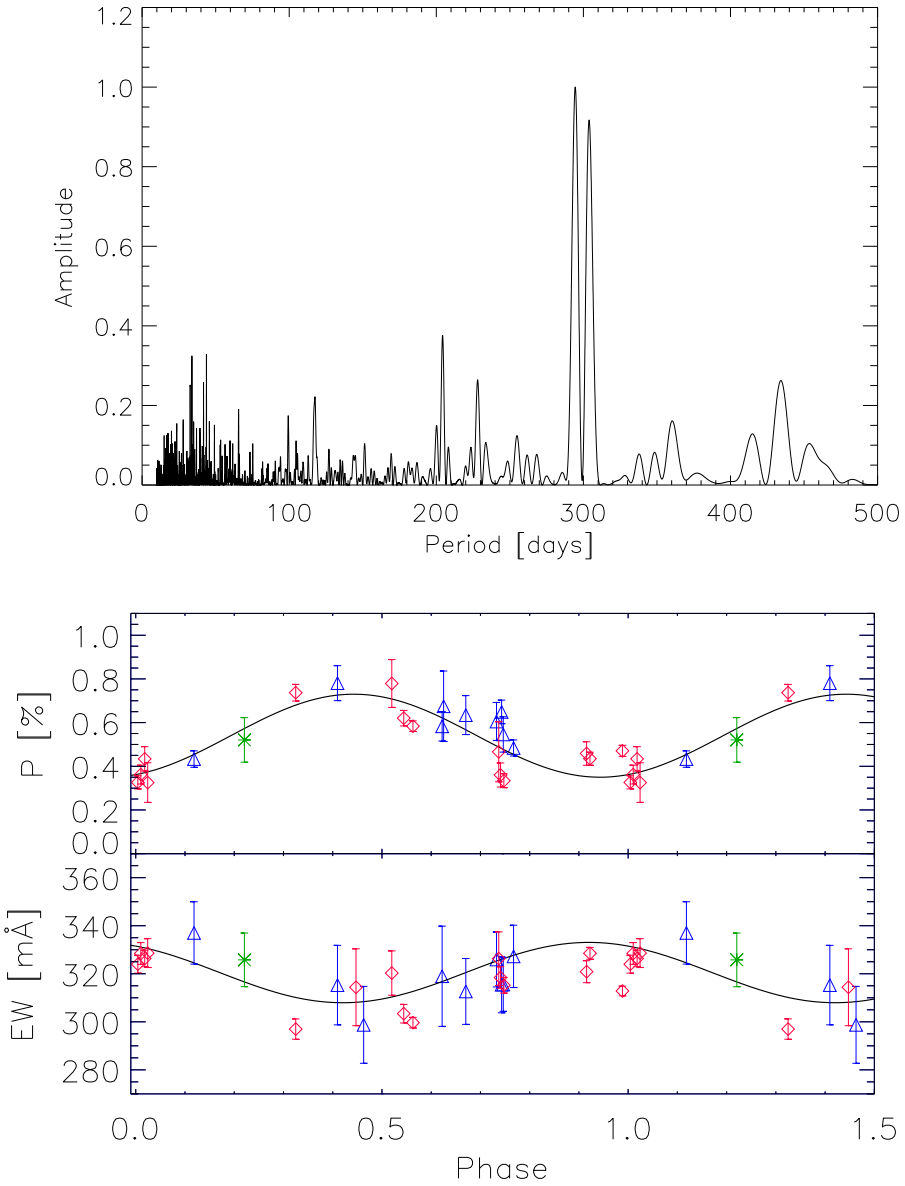

Fig. 5.13.: Top: CLEANED (Roberts et al. 1987) periodogram (Scargle 1982) of LSD polarisation of 89 Herculis. The highest peak is close to the 288.36-day orbital period, while no power is present at the pulsation period of 63.5 days. Bottom: variations of the total polarisation (P) and equivalent width (EW) of LSD profiles, plotted according to the orbital phase; a sine fit of variability is also shown. Symbols are as follow: ⋄ for ESPaDOnS data, △ for CAOS data and ∗ for HANPO data.

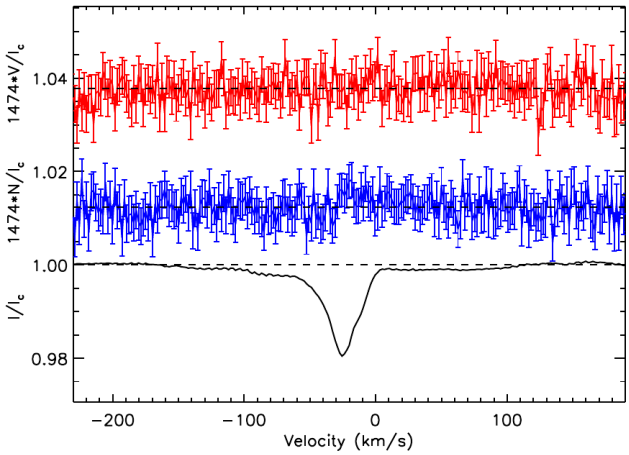

Fig. 5.14.: Stokes V LSD-ESPaDOnS profile, acquired on HJD 56823.535. The upper plot (in red) shows the Stokes V profile, while the middle plot (in blue) shows the null N profile. Image adapted from Sabin et al. (2015).

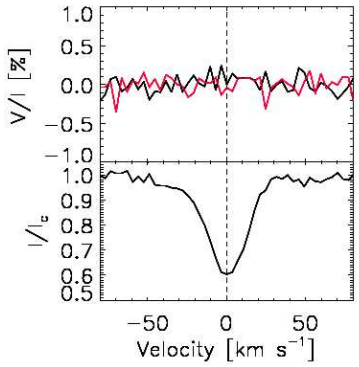

Fig. 5.15.: Stokes V LSD-CAOS profile, acquired on HJD 56853.353; the red line shows the null N profile.

5.3.2 Stellar continuum polarisation

Stellar pulsations

Odell (1979) first introduced the idea that stars with non-radial pulsations show a periodically variable polarisation due to the photospheric electron-scattering opacity; he then observed photopolarimetric variability with an amplitude of 0.045 % in the star BW Vul (Odell 1981). Fabas, Lèbre & Gillet (2011) have associated the variable polarisation presented by the Balmer lines of the pulsating o Ceti with the propagation of shock waves. Later, Lèbre et al. (2014) observed variable polarisation in the metal lines of the Mira star χ Cygni and the RV Tauri star R Sct and they related the polarisation to global asymmetry at the photospheric level induced by pulsations.

We can rule out the possibility that the metal-line polarisation of 89 Herculis is a consequence of pulsations, simply because the observed polarisation is not variable with the 63.5 day pulsation period but rather with the orbital period (Fig. 5.13).

Hot spots

Schwarz & Clarke (1984) and Clarke & Schwarz (1984) have shown that the variable photopolarimetric data of Betelgeuse, with particular reference to the TiO band, can be a consequence of wavelength-independent (e.g. Thomson) scattering and temporal evolution of hot spots. Extending Clarke and Schwarz's interpretation, Aurière et al. (2016) suggested that the linear polarisation observed in the spectral line of Betelgeuse is indeed an effect of the depolarisation of the continuum being set to zero.

Schwarz & Clarke (1984) have computed the expected polarisation of the continuum in the 400-700 nm range due to hot spots. It appears that, whatever the temperature and extension of hot spots, polarisation decreases with wavelength. We can then conclude that, in the case of 89 Her, the observed polarisation across metal lines is not due to hot spots, as was theorised for Betelgeuse. We have found a polarisation degree that is independent of wavelength (Fig. 5.9).

5.3.3 Scattering polarisation from bipolar outflow

Hillen et al. (2013) detected 35-40 % optical circumstellar flux contribution to the luminosity of 89 Herculis; this large fraction of scattered stellar light could be, at least in principle, responsible of the observed linear polarisation across spectral lines in absorption. However, we have always detected linear polarisation across the Ca II 8662-Å line profile (Fig. 5.17), which, as pointed by Kuhn, Geiss & Harrington (2011), cannot be due to scattering (Manso Sainz & Trujillo Bueno 2003). It appears, therefore, that polarisation from free electrons of the circumbinary envelope is not the origin of the polarisation of metal lines in absorption.

Nevertheless, we have carried out numerical tests with the Monte Carlo radiative code STOKES (Marin et al. 2012, Goosman et al. 2014), to understand the role of scattering polarisation from free electrons in the circumstellar environment. Firstly, we have modified the *source-routine* of the program, by introducing an algorithm capable of sampling an observed line in absorption (see A.2 for implementation details). The variability of the polarisation with orbital period rules out a scattering region much larger than the system orbit and we considered only a bipolar outflow. Indeed, as shown in Fig. 5.16 (top panel, left), polarised line profiles at the observed

1 % level are predicted if the Hillen et al. (2013) bipolar outflow with an appropriate ($n_e \sim 10^{11}\ cm^{-3}$) electron density is assumed. However, the ensuing 6 % polarised continuum is not compatible with the finding of Akras et al. (2017) of no polarisation. In addition, we were not able to adapt the outflow properties in order to justify the polarisation variability across spectral lines with the orbital period (Fig. 5.16).

5.3.4 Anisotropic radiation pumping

Kuhn et al. (2007) suggested that the linearly polarised continuum of Herbig Ae(Be stars is due to *anisotropic radiation pumping*. This mechanism has not yet been suggested as an origin of polarisation in the metal spectral lines of stars other than the Sun. As to 89 Herculis, the presence of a very close (0.31 AU, Bujarrabal et al. 2007) companion justifies, at least in principle, the assumption of a non-isotropic radiation field responsible for the observed polarised metal lines, which are seen to vary with the orbital period. A quantitative evaluation based on the anisotropy factor ω (Eq. 4.36), which is zero for an isotropic radiation field and 1 for an unidirectional radiation beam, confirms the presence of a non-isotropic field between the two components of 89 Herculis. We obtain $\omega \sim 0.8$ if (1) we use the stellar parameters given in Tab. 5.2 for the primary component, while for the M0 V main-sequence secondary we use $T_{eff} = 4045K$, $logg = 4.6$, $M = 0.6M_{\odot}$ (Waters et al. 1993) and $R = 0.6R_{\odot}$ (Gray 2005), and (2) the surface fluxes of Kurucz (2005) and limb-darkening of Diaz-Cordoves, Claret & Gimenez (1995) are adopted.

As stated in the previous section, the polarisation observed across the CaII 8662 Å line is evidence of optical pumping (Kuhn et al. 2011). Further direct proof of optical pumping would be the analysis of single line profiles. All 50 line transitions presented in Tab. 5.4 allow for optical pumping (because $J_{low} > 1/2$ and/or $J_{up} > 1/2$) but, more in general, for single lines the achieved S/N (≤ 400) was not enough to clearly highlight the polarisation. For this reason it was necessary to adopt the LSD method to produce a very high S/N ($10^3 - 10^4$, Tab. 5.3) *average line profile*. However, with this method any information on the behaviour of single lines is lost. Despite this, we looked for spectral lines due to transition between levels with $J_{low} = 0$ and $J_{up} = 0$, which are expected to be unpolarised, or only slightly polarised if hyperfine structure is not neglected. Unfortunately, in the visible spectrum of 89 Herculis, the only one (namely Y II 4422.258 Å) of these lines seen is not conclusive, since it is blended with the Fe I 4422.568 Å line of comparable intensity.

To explore numerically the possibility that we are really in the presence of spectral line polarisation induced by a periodically variable anisotropic radiation field due to the orbiting secondary, we compare syntetic FeII 4508.288 Å Stokes profiles computed

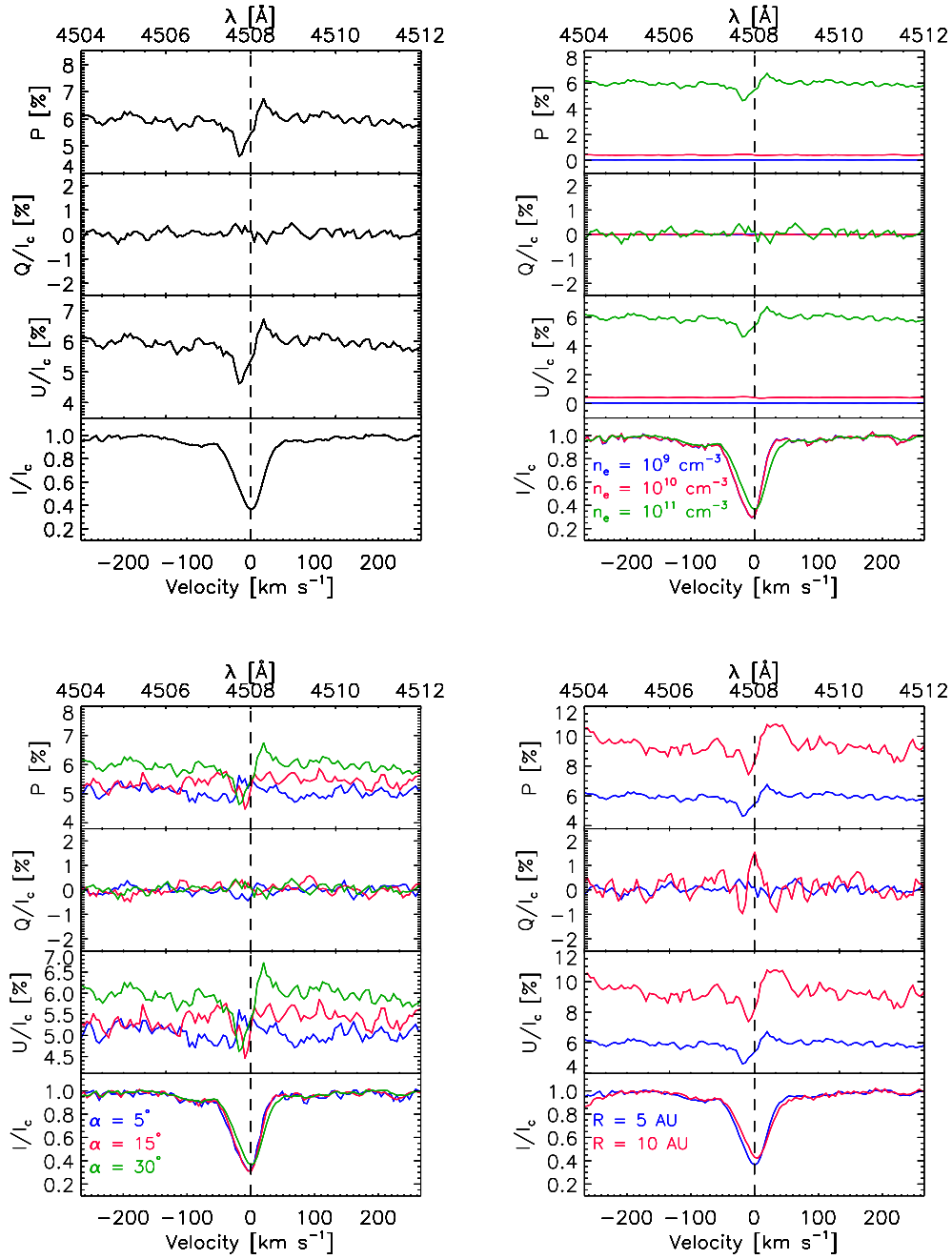

Fig. 5.16.: Linear polarisation computed with the STOKES code for a line in absorption with scattering in a bipolar outflow. Top panel, left: model parameters are: outflow axial extension $R = 5\ AU$, aperture angle $\alpha = 30°$, electron density $n_e = 10^{11}\ cm^{-3}$ and outflow velocity $v_{exp} = 10\ km\ s^{-1}$. Top panel, right: $R = 5\ AU$, $\alpha = 30°$, $v_{exp} = 10\ km\ s^{-1}$ and different electron densities. Bottom panel, left: $R = 5\ AU$, $n_e = 10^{11}\ cm^{-3}$, $v_{exp} = 10\ km\ s^{-1}$ and different aperture angles. Bottom panel right: $\alpha = 30°$, $n_e = 10^{11}\ cm^{-3}$, $v_{exp} = 10\ km\ s^{-1}$ and different outflow axial extensions. Changes in the geometrical and physical properties of the outflow do not justify the observed polarisation variability.

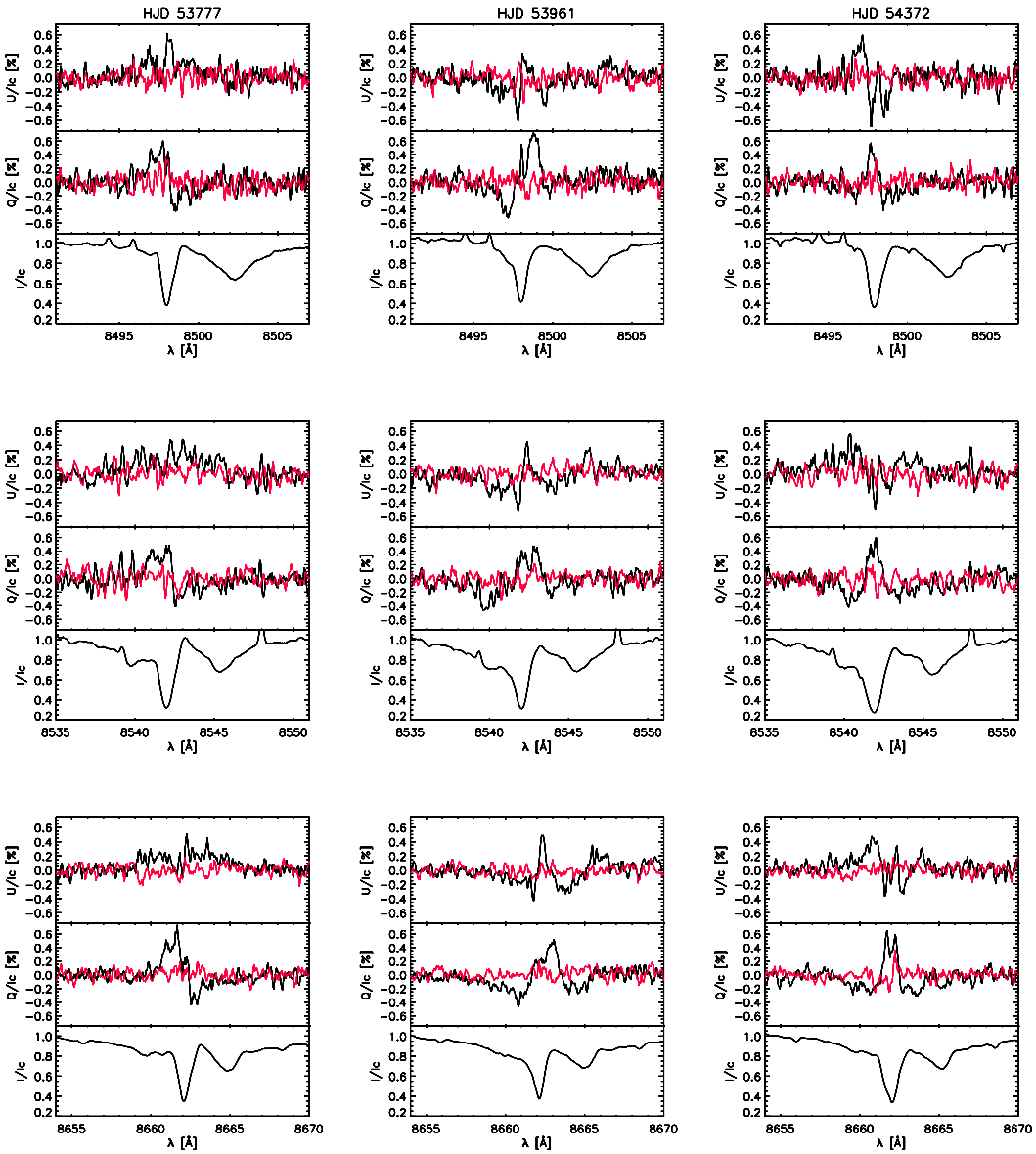

Fig. 5.17.: In black, the Stokes profiles of the IR calcium triplet as observed, from the left, on HJD 53777, 53961 and 54372. According to Kuhn et al. (2011), the very existence of polarisation in the CaII 8662-Åline, appearing equal to the other two lines, rules out scattering polarisation from free electrons. It is compatible with optical pumping instead. In red are null profiles.

with the HAZEL code[2] (Asensio Ramos, Trujillo Bueno & Landi Degl'Innocenti 2008) with the observed LSD profiles. For calculations, observed profiles have been corrected for Doppler shift due to the orbital motion of the primary component. As a first approximation, magnetic fields, which are not necessary to induce a population imbalance (Trujillo Bueno & Landi Degl'Innocenti 1997), have been neglected. In this way we minimize the free parameters to the following: (1) slab velocity v_{sl}, (2) thermal velocity v_{th}, (3) strength of the Stokes I line η_0, (4) angle θ between the LoS

[2]See A.3 for implementation details

and the normal n to the slab and (5) polarisation angle γ, representing the azimuth of the polarisation vector with respect to the north-south direction. Fig. 5.18 shows how the anisotropy factor ω and the angle θ contribute to the polarisation level. Again with the aim of minimizing the number of free parameters, the anisotropy factor has been arbitrarily fixed to the solar value ($\omega'' = 0.37$) at 2 arcsec.

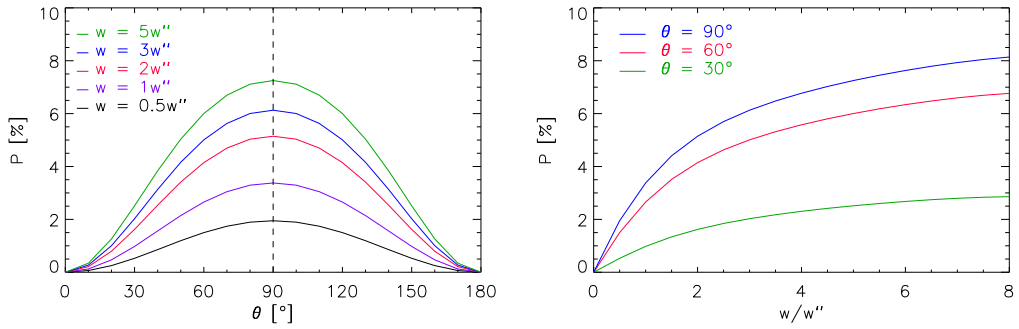

Fig. 5.18.: Spectral line polarisation as a function of angle θ (right) and anisotropy factor ω (Landi Degl'Innocenti & Landolfi 2004), normalized to the Sun's value ($\omega'' = 0.37$) at 2 arcsec (left).

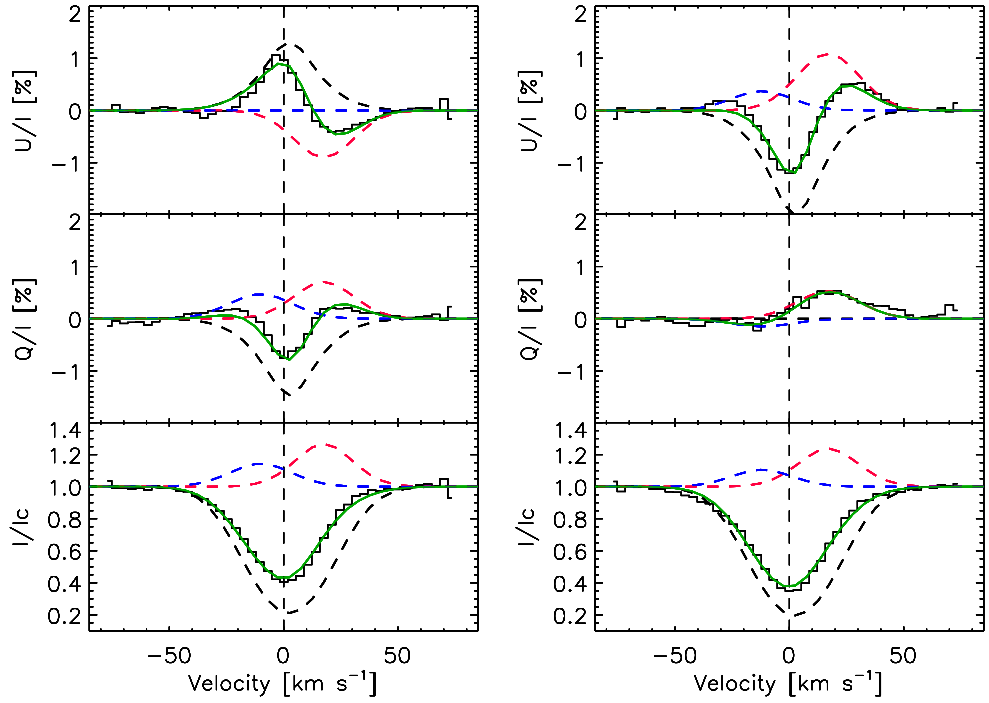

Fig. 5.19.: Example of CAOS-LSD profiles (black) fitted with three components (dashed lines): a stationary feature in absorption (black), a blueshifted (blue) and a redshifted (red) emission lines. The solid (green) continuum is the sum of the three components. From the left, spectra were acquired on HJD56816.515 and 56876.340 respectively.

We found that three slabs are required to fit the variable Stokes Q/I and U/I LSD profiles of 89 Herculis with HAZEL: a stationary feature in absorption (hereafter LINE 2 and due to SLAB 2) and two oppositely Doppler-shifted features, the blueshifted LINE 1 of SLAB 1 and the redshifted LINE 3 of SLAB 3. Fig. 5.19 shows an example of the fit for two CAOS-LSD profiles (the complete collection of figures is presented in A.4). With the exception of the thermal velocity v_{th}, which is constant in time, all fit parameters present a well-defined variability with the orbital period (Fig. 5.20).

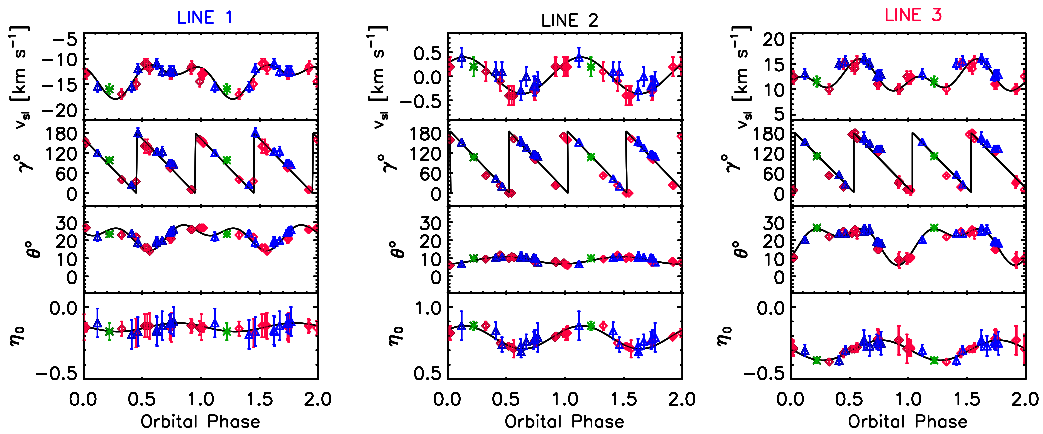

Fig. 5.20.: HAZEL parameters best matching the Stokes LSD profiles are folded with the orbital ephemeris given in Eq. 5.1. Symbols are as in Fig. 5.13. The sawtooth variation of the γ angle, due to its definition in a $0 - 180°$ range, is indicative of a closed loop of the polarisation vector along the orbital motion of the secondary star. The longitude of periastron $\omega = 359.3°$ (Waters et al. 1993) implies that the polarisation vector is north-south oriented ($\gamma = 0°$) in conjunctions and east-west oriented ($\gamma = 90°$) in quadrature. Single and double wave variations have been assumed to match the parameter change, except for the γ one, which has been assumed linear in time.

According to the adopted ephemeris (Eq. 5.1), the radial velocity of the primary component of 89 Herculis binary system presents its maximum at an orbital phase of zero when it moves away from us and the system is in quadrature. Thus the less massive secondary is before the primary (inferior conjunction) at phase 0.25, while the superior conjunction is at phase 0.75. Waters et al. (1993) measured a longitude of periastron $\omega = 359.3°$, orienting the main axis of the elliptical ($e = 0.189$) orbit in the east-west direction. Moreover, 89 Herculis is characterized by an hourglass structure that is orthogonal to the orbital plane, elongated in a direction that forms an angle of $\sim 15°$ with respect to the LoS and with a position angle of $45°$ (Bujarrabal et al. 2007). Fig. 5.21 shows a sketch of 89 Herculis.

We find that the overall behaviour of the fit parameters of the three slabs (Fig. 5.20) can be understood within the preset picture of 89 Herculis: if the stationary SLAB 2 presents the *average* optical and physical properties of the primary component in reflecting and reprocessing radiation from the orbiting secondary, correspondingly the blueshifted SLAB 1 represents the jet pointing towards us and the redshifted

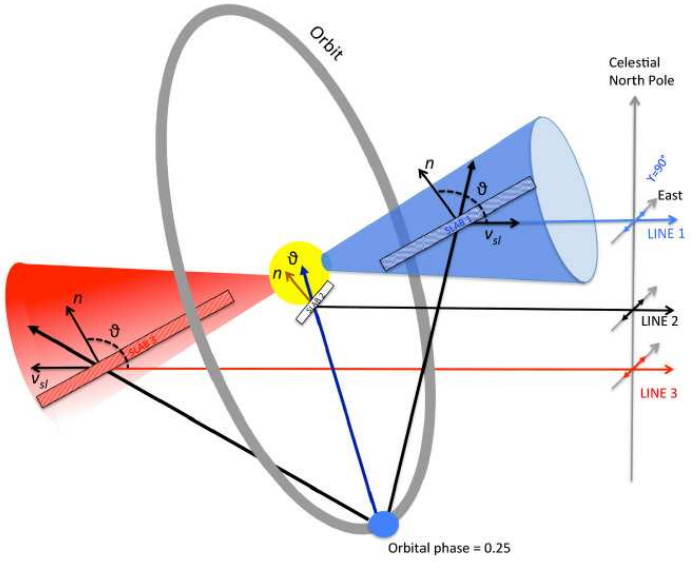

Fig. 5.21.: A (not to scale) sketch of 89 Herculis. The binary presents a major axis aligned with the east-west direction (Waters et al. 1993). An hourglass structure is centred on the primary component and normal to the orbital plane (Bujarrabal et al. 2007). In the framework of anisotropic radiation pumping, the variable Stokes LSD profiles (Fig. 5.12) can be synthesized with the HAZEL (Asensio Ramos et al. 2008) code assuming three slabs: the stationary SLAB 2 presents the *average* optical and physical properties of the primary component in reflecting and reprocessing radiation from the orbiting secondary, correspondingly the blueshifted SLAB 1 represents the jet pointing towards us and the redshifted SLAB 3 represents the receding jet, θ is the angle between the normal n to the slab and the LoS, v_{sl} the velocity of the slab towards the LoS.

SLAB 3 represents the receding jet. In such a hypothesis, it is straightforward to explain the following:

- the always negative SLAB 1 velocity and the always positive SLAB 3 velocity, both of the order of the hourglass expansion velocity, equal to $\sim 6 - 7\ km\ s^{-1}$ (Bujarrabal et al. 2007);

- the constant thermal broadening, as expected for a phenomenon not due to a change of physical properties of the source, for example because of pulsations or spots;

- the synchronous sawtooth variation of γ angles for the three slabs with the orbital period. The continuous variation of γ, defined in the $0 - 180°$ range, shows that the polarisation vector describes a closed loop in the sky, i.e. the scattering plane rotates around the LoS with the secondary star. The orientation of the polarisation vector, aligned with the east-west direction in conjuctions and the north-south direction in quadrature, is due to the east-west orientation of the major axis of the elliptical orbit (Fig. 5.20 and 5.21).

A quantitative evaluation of the fit parameters and a description of their variability would require a 3-D version of HAZEL, which is not yet available, and a detailed knowledge of the 89 Herculis environment. Qualitatively, the variability of fit parameters is due to the imperfect symmetry with respect to the LoS, the non-null eccentricity of the orbit and absorption and occultation phenomena. For example, the weak modulation of SLAB 2 in v_{sl} and θ could be due to orbit eccentricity, or the large modulation of the SLAB 3 θ angle with respect to SLAB 1 could be a consequence of partial occultation of the receding jet by the primary star (Fig. 5.21).

5.4 Polarisation of metal lines in emission

We have analysed the polarisation properties of the emission metal lines crowding the spectrum of 89 Herculis and found, as a general rule, that they present (left panel of Fig. 5.22) about 1 % of polarisation, fully stored in the Stokes U/I profile. However, a few emission lines appear to show the opposite behaviour (right panel of Fig. 5.22), to be confirmed with further observations.

5.5 Origin of linear polarisation of metal lines in emission

As to emission lines, regardless of the proposed (Waters et al. 1993) mechanisms for their origin, polarised profiles are expected from rotating disks (Vink, Harries & Drew 2005) in the presence of free electrons. We have carried out numerical computations with the STOKES code[3] and found that observations are justified by an open undisrupted disk slightly tilted towards the line of sight and rotating at ≤ 10 $km\ s^{-1}$ (Fig. 5.22). This value is in agreement with the conclusion of Bujarrabal et al. (2007) that the characteristic rotation would be $\sim 8\ km\ s^{-1}$. We adopted a density of scattering electrons equal to $10^{10}\ cm^{-3}$, an external radius of 10 AU and a PA of the circumbinary disk equal to $45°$.

In the literature, indirect evidence of free electrons in the circumbinary disk of 89 Herculis is a necessity of the H^- continuum opacity, in order to justify the observed spectral energy distribution (Hillen et al. 2013), a result that rules out the presence of scattering on grains within the circumbinary disk. We also note that mass loss ($\sim 10^{-8} M.yr^{-1}$, Osmer 1968) from the primary star, responsible for the

[3] see A.2 for implementation details

observed H_α P Cygni profile, could be a continuous source of free electrons for the low-temperature circumbinary disk.

The observed Stokes U/I do not rule out a possible variability with orbital period (Fig. 5.22). Further observations are necessary to clarify this possibility and eventually help us to understand better the role of tidal forces induced by orbiting components on the circumbinary disk.

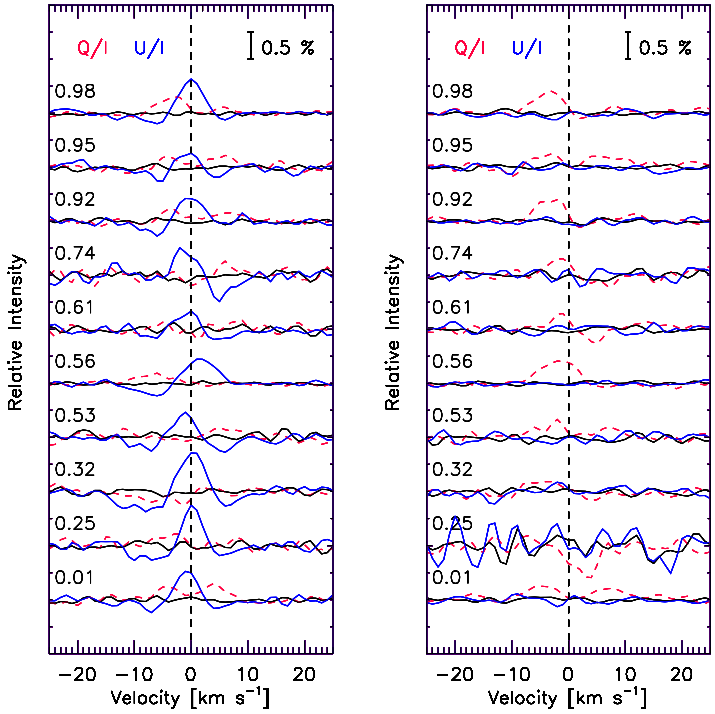

Fig. 5.22.: For any ESPaDOnS spectrum, we plot the average Stokes profiles of metal lines in emission. Phase is computed with the orbital ephemeris given in Eq. 5.1 (Waters et al. 1993). Most cases (left panel) present Stokes U/I (solid blue) profiles clearly different from zero and almost null Stokes Q/I (dashed red) profiles. A few others are characterized by a null Stokes U/I and possibly non-null Stokes Q/I profile (right panel).

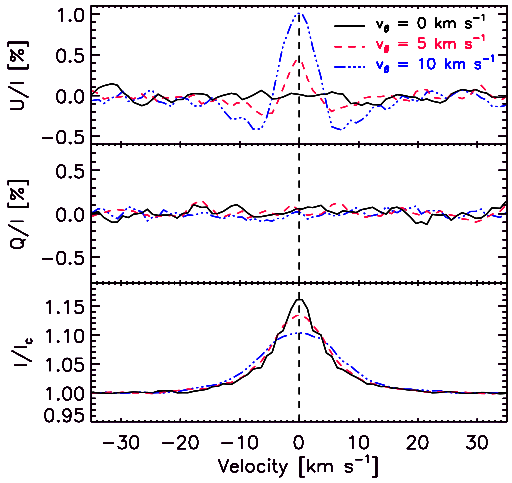

Fig. 5.23.: Polarisation of a spectral line emitted from a $30°$ open undisrupted disk seen at $\cos\theta = 0.85$. The black solid line is for a non-rotating disk, the red dashed line for a disk with rotational velocity $v_\theta = 5\ km\ s^{-1}$ and the blue dashed solid line for a disk with $v_\theta = 10\ km\ s^{-1}$. To justify the null Stokes Q profiles, a $PA = 45°$ has been assumed.

5.6 Circumstellar envelope manifestations

As we said in the introduction, several studies have been carried out about the spectroscopic evidence of 89 Herculis circumstellar envelope (Böhm-Vitense 1956, Sargent & Osmer 1969, Khalilov et al. 2010).

Here we focus on the long term variability of the H_α line profile. To do that, in addition to data taken with CAOS, ESpaDOnS and HANPO, we acquired a spectrum on June, 2^{th}, 2012 with DOLORES (Device Optimized for the LOw RESolution, LRS in short, Molinari et al. 1997) and on June, 25^{th}, 2018 with the HARPS-N spectrograph (R=120000, Cosentino et al. 2012). Moreover, we retrieved spectroscopic data of 89 Herculis from all available archives. In particular from the:

- Ritter Observatory Archive[4]. Spectra were collected from 1993 to 1995 with the echelle spectrograph of the 1m Ritter Observatory Telescope (R=26000);
- BTA[5] (Big Telescope Alt-azimuth) archive. Spectra have been acquired in 1998 and 2010 with the Nasmyth Echelle Spectrograph (NES, $R = 60000$, Panchuk et al. 2007) of the 6m BTA telescope;
- ELODIE[6] archive. A spectrum was acquired on August 18, 2004 with the ELODIE spectrograph at the Observatoire de Haute-Provence 1.93m Telescope (Moultaka et al. 2004);
- ESO[7] archive. A spectrum was acquired on May 9, 2013 at the MPG/ESO 2.2m Telescope with the "Fiber-fed Extended Range Optical Spectrograph" (FEROS, Kaufer et al. 1999).

The complete logbook of the observations is given in Table 5.5.

5.6.1 H_α variability: general appearance

Line variations

The variations across the H_α P Cygni profile, mainly in the absorption component of the line, cover different time scales, reaching from days to years. A quantification is

[4] **http://astro1.panet.utoledo.edu/wwwphys/ritter/archive/main.html**.
[5] https://www.sao.ru/oasis/cgi-bin/fetch?lang=en
[6] http://atlas.obs-hp.fr/elodie/
[7] http://archive.eso.org/eso/eso_archive_main.html

difficult due to the very complex morphologies. In fact there are remarkable changes in intensity and in the structure of the blue-displaced components. As first goal of our analysis we perform a crude estimate by calculating the Equivalent Widths (EW) of the absorption (EW_{abs}) and emission (EW_{em}) components. They were measured in the fixed intervals from -400 to 0 $km\ s^{-1}$ and from 0 to 245 $km\ s^{-1}$, respectively. The emission components has been firstly corrected for the presence of telluric lines through linear interpolation. HJD 57666.248, 58251.592 and 58267.548 data were excluded since the profiles are significantly altered. Measurements are reported in Tab. 5.5.

In order to find out any periodicity, the EW curves were analyzed by application of the Scargle method (Scargle 1982). We find no statistically significative peaks in the CLEANED (Roberts et al. 1987) EW_{ab} periodogram, while a period of ~ 1681 days for the emission component is found (Fig. 5.25).

Fig. 5.24 shows the EW_{ab} measurements against time. Here we can distinguish three regions (labelled in dotted lines) characterized by important EW_{ab} changes. They are separated from each other by about 11 years. In each of them there is a rapid increase in the EW_{ab}, from HJD49433 to HJD49899 in the first event, from HJD53236 to HJD53604 in the second and from HJD57555 to HJD57893 in the third event. Moreover, in the second event we can see a subsequently decrease with a time scale of about 5 years (from HJD53604 to HJD55229).

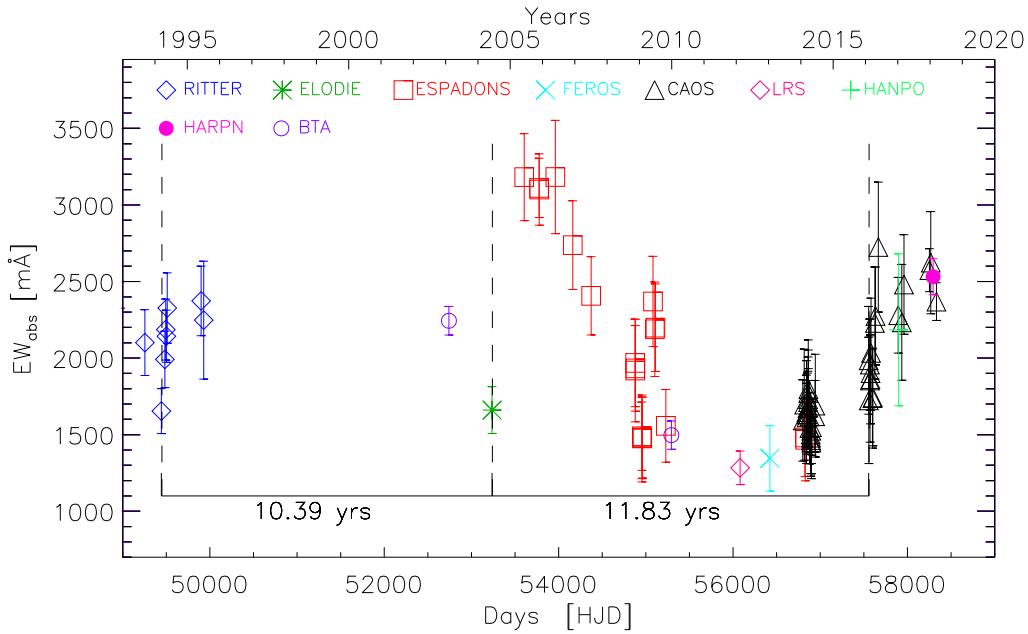

Fig. 5.24.: Equivalent Widths of the H_α absorption component (EW_{ab}) against time.

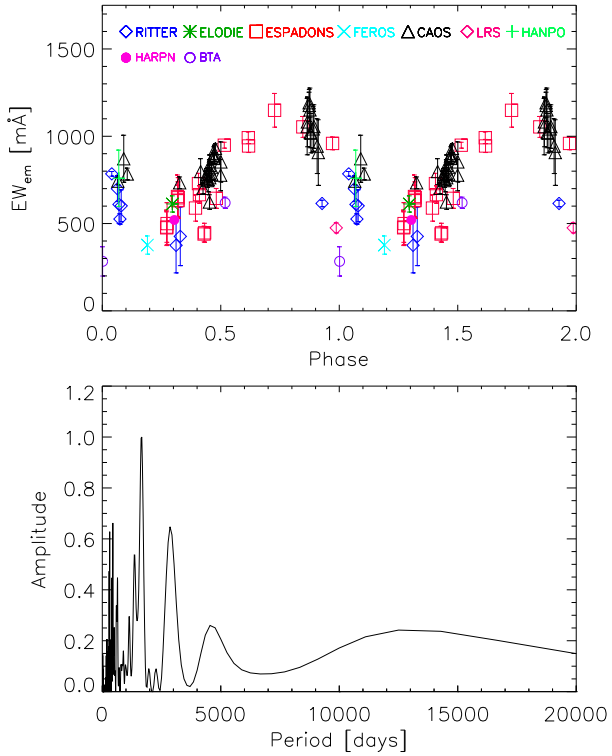

Fig. 5.25.: Bottom panel: CLEANED (Roberts et al. 1987) Periodogram (Scargle 1982) of the Equivalent Widths (EW) measurements of the H_α emission component. The highest peak is at ~ 1681 days while no significant power is present at the period of 10922.7 days found by Khalilov et al. (2010). Variations of EWs are plotted (top panel) folded with the 1681 days period.

The H_α line morphological changes during the three episodes are notable. Qualitatively, we can see that:

- Regarding the absorption blue-displacement component of the profile, the variability observed in the three episodes is different. Fig. 5.26, in fact, shows the $H\alpha$ profiles corresponding to the minimum and maximum of the EW_{ab} measured in each of the three events. In the first event (bottom panel of the figure) there is a moderate increase in the blue-displacement absorption component both in intensity and in velocity. In the second event (middle panel) there is a huge increase in the velocity displacement of the blue component with a moderate increase in its intensity. Finally, in the third event (top panel) there is a moderate increase in velocity displacement and a huge increase in intensity;

- Regarding the emission component of the profile, we point out a short term (on day-to-day timescale) variability. Fig. 5.27 shows a color-scale H_α map in the first and third episodes, which were almost well covered by the observations. In the top panel of the figure it is shown that during the days immediately

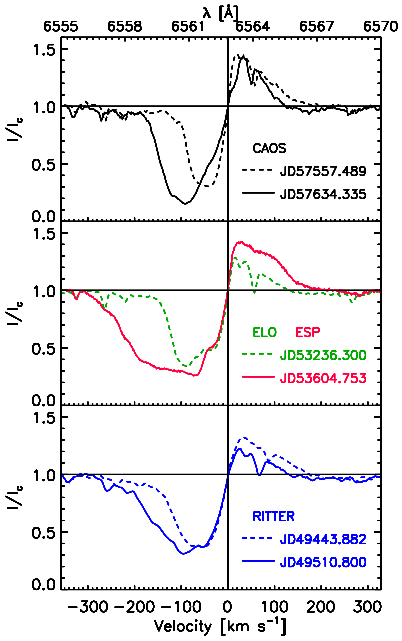

Fig. 5.26.: . H_α profiles corresponding to the minimum and maximum of the EW_{ab} measured in each of the three events.

preceding the third event (HJD 57569 - 57603), the emission component shows an important decreasing of its intensity, while the absorption component is quite stable. The decrease of the emission component intensity continues during the mass loss event (from HJD 57626) and reaches the maximum at the maximum absorption of the blue-displaced component (HJD 57666). Finally, from HJD 57893, when the absorption component begins to return to the initial condition, the emission component begins to increase its intensity. The same behaviour seems to happen in the bottom panel of the figure where it is shown the decrease in intensity of the emission component during the first mass loss event.

From our data we can conclude that the long term recurrent episodes of EW_{ab} changes are not strictly periodic. We do not confirm the period of 6553.6 days found by Khalilov et al. (2010). The mass-loss enhancements take place in less than ~ 450 days and they seems to happen with a time displacement of about 11 years. On the other hand we find out a long term variability of the emission component with a statistically significant period of 1681 days. That means that, as the H_α emission intensity is very sensitive to the mass loss rate (Kunasz & Morrison 1982), the mass loss rate of 89 Herculis is variable on long-term timescale.

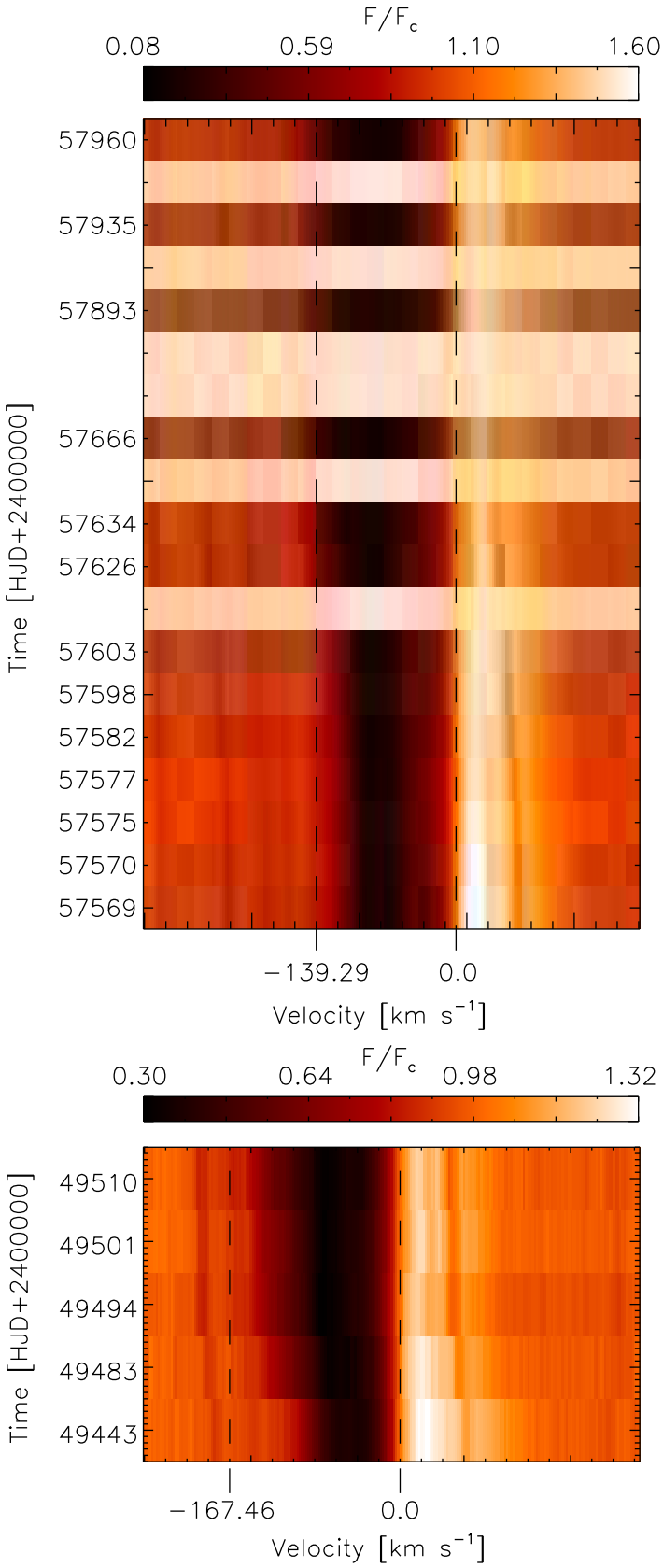

Fig. 5.27.: A color-scale representation of the H_α spectrum variations during the third (top panel) and the first (bottom panel) mass-loss enhancement event.

Polarisation

Discovered by Harrington & Kuhn (2009), the H_α line shows linear spectropolarimetry variability on short timescales in the absorption component. The authors propose the optical pumping model (Kuhn et al. 2007) to explain the observed polarimetric signatures, suggesting a near-stellar location of an absorbing gas shell.

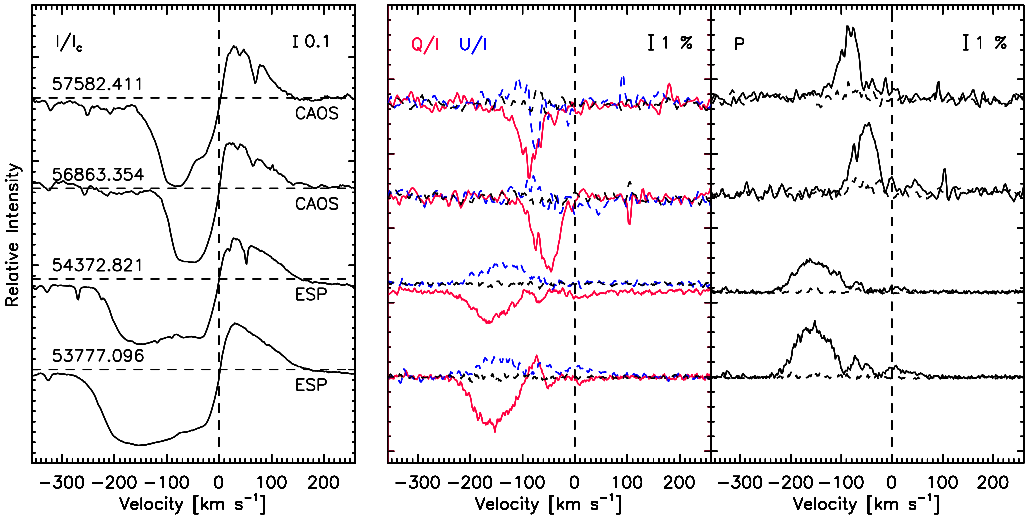

Fig. 5.28.: A representative sub-sample of Stokes Parameters for H_α. Q/I (middle panel, solid red) and U/I (middle panel, dashed blue) shows very complex morphologies. Polarization is present at velocities corresponding to the absorption component of the profile.

Fig. 5.28 shows the the I, Q, U Stokes profiles and the polarisation P for a representative sub-sample of our data. Polarisation is always present at velocities corresponding to the absorption component of the profile. In Tab. 5.6 we report the H_α total polarisation (P_{H_α}) calculated in the fixed interval from -400 to 0 $km\ s^{-1}$. A time analysis of the data reveals no significative peaks in the periodogram. We note however that the polarisation degree scales with the line depth (see Fig. 5.9) and in the case of the H_α profile there are important non-periodic variation in the depth of the line. Thus, for this reason it is not possible to exclude the presence of periodic intrinsic polarisation variability.

A qualitative analysis of the Q and U morphologies reveals that they present multiple components which depend on the I profile:

- When the I absorption blue displacements is maximum (see for example HJD 53777 or HJD54372 in Fig. 5.28) the Stokes Q and U morphologies corresponding at velocity $v \leq -100$ $km\ s^{-1}$ are made up of simple profiles in

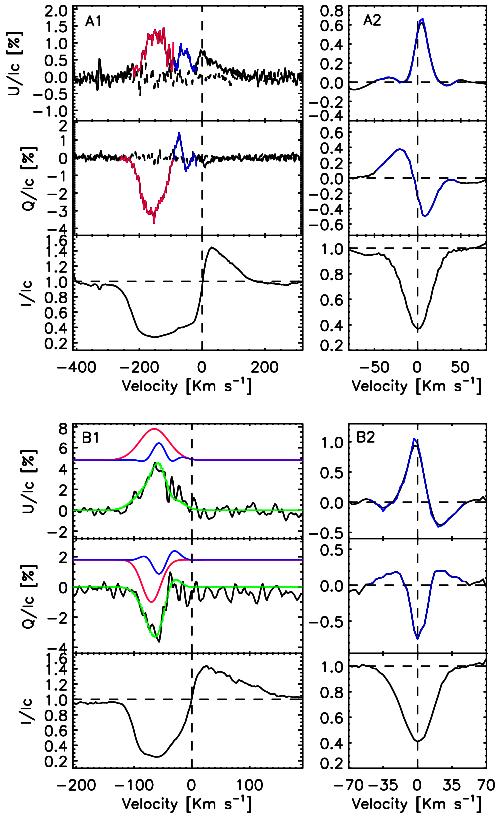

Fig. 5.29.: Comparison between the H_α and the LSD Stokes profiles. At maximum blue displacement (HJD53777.821, top panel) the Stokes morphologies corresponding to the core (blue line) of the H_α absorption line are compatible with the LSD Stokes profiles. When the blue displacement is moderate (HJD56816.519, bottom panel) the H_α Stokes profiles could be result from a combination of simple absorption/emission with the LSD profiles (red and blue lines respectively).

emission or in absorption, while at $-100 \leq v \leq 0\ km\ s^{-1}$ they are complex. We find out that the latter are perfectly compatible with the LSD Stokes morphologies of metal lines in absorption (Fig. 5.29, panel A);

- When the I absorption blue displacements is moderate the Stokes Q and U morphologies could be result from a combination between the simple emission/absorption profiles and the LSD metal lines profiles (Fig. 5.29, panel B).

The Q and U multiple components can be identified looking also at the polarisation position angle. Here we stress that the polarisation angle does not depend on the intensity flux; therefore we can look at its variability without taking into account the depth of the corresponding line. Fig. 5.30 shows the θ angle calculated for the highest signal-to-noise H_α profiles. We point out that at $v \leq -100\ km\ s^{-1}$ the θ angle scales linearly with the velocity, while at $v \geq -100\ km\ s^{-1}$ it shows a very complex behavior. In particular, in the $v \geq -100\ km\ s^{-1}$ range, we note that:

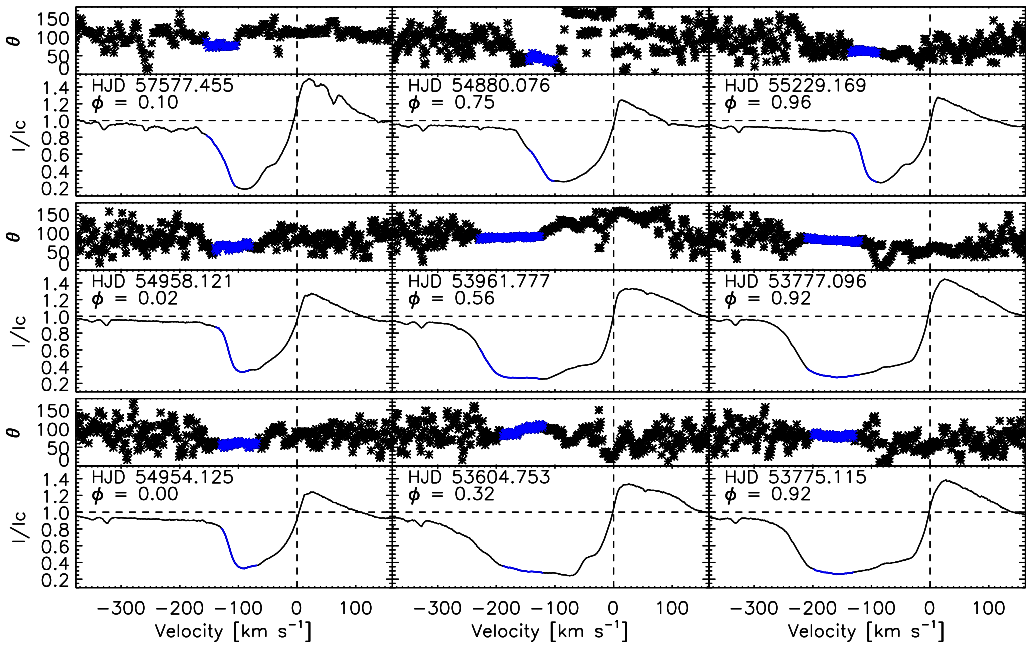

Fig. 5.30.: Polarisation position angle calculated for the highest signal-to-noise H_α lines. Notice that the angle appears randomly scattered outside of the absorption line, which is expected. Position angles at $v \leq -100\ km\ s^{-1}$ scale linearly with the velocity.

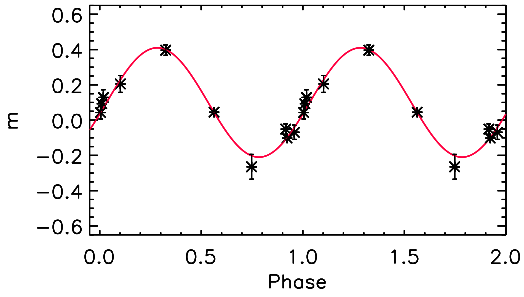

Fig. 5.31.: Variations of the polarisation position angle slope with the orbital phase. The latter was computed adopting the ephemeris determined by Waters et al. (1993).

- When the I absorption blue displacements is moderate (e.g. HDJ 54954.125 and HJD 54880.076 in Fig. 5.30) θ spans on average between $30°$ and $60°$, while at high blue displacements θ spans on average between $70°$ and $100°$;

- The slope of the θ is related to the orbital period. Fig. 5.31 represents the angular coefficient variations of the line crossing θ with the orbital phase. We find a positive maximum slope value at phase $= 0.25$ (inferior conjunction) and a negative minimum slope value at phase $= 0.75$ (superior conjunction). At phase $= 0$ (i.e. when the system is in quadratura) a zero angular coefficient is found.

These evidences all converge toward the idea that the H_α Stokes parameters are made up of at least two components characterized by different geometrical and physical properties. The latter are in turn due to the presence of a structured circumstellar environment.

Tab. 5.5.: Journal of observations and equivalent widths measurements of the $H\alpha$ absorption (EW_{ab}) and emission (EW_{em}) components. OBS: **RIT** Ritter, **ELO** Elodie, **ESP** Espadons, **LRS** DOLORES, **FER** Feros, **CAOS** Caos, **HAN** Hanpo, **HAR** HARPS-N, **BTA** Nasmyth Echelle Spectrograph of the BTA telescope. An asterisk indicates measures in spectropolarimetric mode.

HJD 2400000+	**OBS**	EW_{ab} [mÅ]	EW_{em} [mÅ]
49254.520	RIT	2101 ± 215	615 ± 19
49443.882	RIT	1654 ± 147	785 ± 13
49483.800	RIT	1991 ± 184	699 ± 73
49494.800	RIT	2186 ± 199	609 ± 109
49501.741	RIT	2143 ± 170	526 ± 30
49510.800	RIT	2327 ± 229	601 ± 91
49899.800	RIT	2373 ± 227	375 ± 158
49929.676	RIT	2248 ± 385	426 ± 167
52741.570	BTA	2244 ± 93.	283 ± 84
53236.300	ELO	1660 ± 153	612 ± 46
53604.753	ESP*	3182 ± 284	949 ± 17
53775.115	ESP*	3111 ± 194	991 ± 34
53777.096	ESP*	3100 ± 233	944 ± 37
53961.777	ESP*	3182 ± 370	1148 ± 97
54162.066	ESP*	2737 ± 290	1053 ± 60
54372.821	ESP*	2406 ± 255	959 ± 36
54877.099	ESP*	1968 ± 285	475 ± 101
54878.132	ESP*	1919 ± 335	480 ± 87
54880.076	ESP*	1933 ± 280	500 ± 119
54954.125	ESP*	1489 ± 223	655 ± 123
54955.849	ESP*	1475 ± 284	630 ± 90
54958.121	ESP*	1478 ± 265	634 ± 105
54959.076	ESP*	1482 ± 265	647 ± 116
55081.874	ESP*	2370 ± 295	589 ± 75
55102.832	ESP*	2188 ± 308	729 ± 59
55109.823	ESP*	2198 ± 286	666 ± 50
55229.169	ESP*	1557 ± 237	644 ± 57
55292.470	BTA	1497 ± 92	619 ± 32
56080.575	LRS	1283 ± 109	475 ± 29
56422.404	FER	1345 ± 214	377 ± 52

Continued on next page

Tab. 5.5 – continued from previous page

HJD 2400000+	OBS	EW_{ab} [mÅ]	EW_{em} [mÅ]
56824.035	ESP	1481 ± 254	440 ± 44
56828.007	ESP	1467 ± 268	447 ± 55
56799.619	CAOS*	1592 ± 265	798 ± 74
56816.519	CAOS*	1696 ± 363	701 ± 30
56842.519	CAOS*	1647 ± 336	772 ± 32
56843.397	CAOS*	1631 ± 258	782 ± 34
56844.437	CAOS*	1613 ± 223	755 ± 31
56848.446	CAOS*	1633 ± 220	746 ± 39
56853.442	CAOS*	1673 ± 229	751 ± 69
56860.320	CAOS*	1731 ± 182	787 ± 48
56861.319	CAOS*	1712 ± 295	813 ± 52
56862.463	CAOS*	1772 ± 346	623 ± 42
56863.354	CAOS*	1676 ± 254	833 ± 60
56864.317	CAOS*	1798 ± 255	762 ± 43
56876.348	CAOS*	1543 ± 234	823 ± 24
56877.436	CAOS*	1619 ± 235	783 ± 36
56891.344	CAOS*	1501 ± 271	886 ± 20
56894.317	CAOS*	1480 ± 234	892 ± 48
56895.317	CAOS*	1463 ± 219	876 ± 21
56897.308	CAOS*	1525 ± 214	873 ± 31
56898.283	CAOS*	1449 ± 236	903 ± 46
56904.321	CAOS*	1548 ± 182	931 ± 26
56941.000	CAOS*	1620 ± 234	777 ± 89
56943.000	CAOS	1690 ± 335	853 ± 115
57555.522	CAOS	1985 ± 351	1055 ± 161
57557.489	CAOS	1723 ± 412	1082 ± 142
57569.489	CAOS	1957 ± 296	1192 ± 60
57570.442	CAOS	1853 ± 402	1176 ± 91
57575.513	CAOS*	1862 ± 292	1151 ± 125
57577.455	CAOS*	1902 ± 244	1021 ± 87
57582.411	CAOS*	2034 ± 358	1018 ± 113
57598.420	CAOS	1738 ± 326	1042 ± 128
57603.385	CAOS	1743 ± 316	1055 ± 124
57626.387	CAOS	2229 ± 366	943 ± 157
57634.335	CAOS	2275 ± 319	907 ± 188
57666.248	CAOS	2725 ± 424	
57893.559	CAOS	2280 ± 247	743 ± 20
57900.102	HAN	2185 ± 496	759 ± 161

Continued on next page

Tab. 5.5 – continued from previous page

HJD	OBS	EW_{ab}	EW_{em}
2400000+		[mÅ]	[mÅ]
57935.528	CAOS	2233 ± 378	871 ± 135
57960.374	CAOS*	2480 ± 325	784 ± 34
58251.592	CAOS	2574 ± 140	
58267.548	CAOS	2623 ± 333	
58294.013	HAR	2531 ± 118	520 ± 15
58332.357	CAOS	2369 ± 123	733 ± 33

Tab. 5.6.: Journal of spectropolarimetric observations and total polarisation (P) measured across the H_α absoprtion component. Errors are calculated from *null* spectra.

HJD	OBS	P	HJD	OBS	P
2400000+		[%]	2400000+		[%]
53604.753	ESP	5.74 ± 0.74	56844.437	CAOS	6.00 ± 1.96
53775.115	ESP	6.57 ± 0.96	56848.446	CAOS	5.49 ± 0.82
53777.096	ESP	7.60 ± 0.51	56853.442	CAOS	7.68 ± 1.52
53961.777	ESP	8.49 ± 0.33	56860.320	CAOS	5.76 ± 1.54
54162.066	ESP	3.86 ± 1.92	56861.319	CAOS	5.72 ± 1.42
54372.821	ESP	4.64 ± 0.38	56862.463	CAOS	5.27 ± 1.49
54877.099	ESP	4.05 ± 1.39	56863.354	CAOS	5.90 ± 1.72
54878.132	ESP	3.58 ± 0.61	56864.317	CAOS	5.97 ± 2.21
54880.076	ESP	3.93 ± 0.62	56876.348	CAOS	6.21 ± 1.44
54954.125	ESP	3.50 ± 0.55	56877.436	CAOS	4.16 ± 1.36
54955.849	ESP	3.67 ± 0.68	56891.344	CAOS	3.31 ± 1.58
54958.121	ESP	3.49 ± 0.60	56894.317	CAOS	2.28 ± 0.97
54959.076	ESP	3.35 ± 0.96	56895.317	CAOS	2.00 ± 0.87
55081.874	ESP	5.56 ± 1.74	56897.308	CAOS	2.19 ± 1.16
55102.000	ESP	6.37 ± 0.74	56898.283	CAOS	2.70 ± 0.96
55109.823	ESP	6.37 ± 0.74	56904.321	CAOS	1.66 ± 1.52
55229.169	ESP	4.41 ± 0.41	56941.243	CAOS	4.01 ± 2.29
56799.619	CAOS	6.81 ± 1.95	57575.513	CAOS	5.86 ± 2.90
56816.519	CAOS	4.82 ± 2.03	57577.455	CAOS	4.03 ± 1.33
56842.519	CAOS	5.20 ± 1.26	57582.411	CAOS	6.05 ± 1.52
56843.397	CAOS	7.30 ± 1.57	57960.374	CAOS	4.10 ± 0.87

5.6.2 Ba II and YII lines variability

The hypothesis of a structured circumstellar environment around 89 Herculis can be further investigated looking at specific line transitions of the optical spectrum. Klochkova (2014), in fact, provided the first observational evidences on the presence of circumstellar spectral features of heavy metals in the optical spectra of post-AGB

stars. In particular she found that the splitting or the strong asymmetry of some line profiles (e.g. BaII 4554.033 Å, 5853.675 Å, 6141.712 Å, 6496.898 Å; YI 5087.418 Å; YII 5402.774 Å; LaI 6390.48 Å; LaII 5234.194 Å, 5293.163 Å) can be associated with the kinematic of the circumstellar environment and with the type of its morphology. Furthermore, it is believed that the presence of a companion (and/or a magnetic field) causes the loss of the spherical symmetry of the stellar envelope (Huggins et al. 2009, Leal-Ferreira et al. 2012).

In this context, we decided to analyze the spectra of 89 Herculis in order to find some evidence of dynamics of the structured circumstellar environment. We found that the Ba II 6141.712 Å and YI 5087.418 Å absorption lines are split and variable in time (Fig. 5.32). A comparison with the synthetic spectrum rules out the possibility that the splitting is due to the presence of other close transition lines. To characterize this variability we performed a Gaussian Decomposition of the profiles. The minimum number of Gaussian components able to fit the observed profiles was determined by the χ^2 function minimization. In the case of the BaII 6141.712 Å line, four gaussian components have been necessary, while for the YI 5087.418 Å line three components were enough.

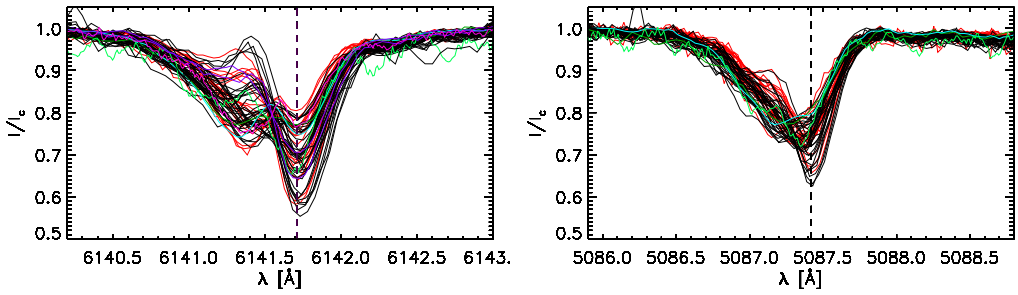

Fig. 5.32.: Spectroscopic variability for the BaII 6141.712 Å line (left) and YI 5087.418 Å line (right).

Fig. 5.33 shows the result of the decomposition for lines whose orbital phase is ~ 0.25 (i.e. system in inferior conjunction), ~ 0.5 (i.e. system in quadrature), ~ 0.75 (i.e. system in superior conjunction) and ~ 1 (i.e. system in quadrature). It seems that there is a correlation between orbital phase and line variability. In particular we note that: (i) when the system is in inferior conjunction there is the maximum splitting; (ii) the splitting decrease while the system is moving towards the superior conjunction where it reach the minimum; (iii) the splitting starts to increase until the system is in quadrature. Regarding the intensity, we note that at $\phi \sim 0.25$ the the central component is deeper than the blueshifted one while in the other phases the components are of comparable intensity.

In Fig. 5.34 we report the CLEANED Periodograms for the relative velocities calculated between the centroid of the two fitted components clearly showing a peak

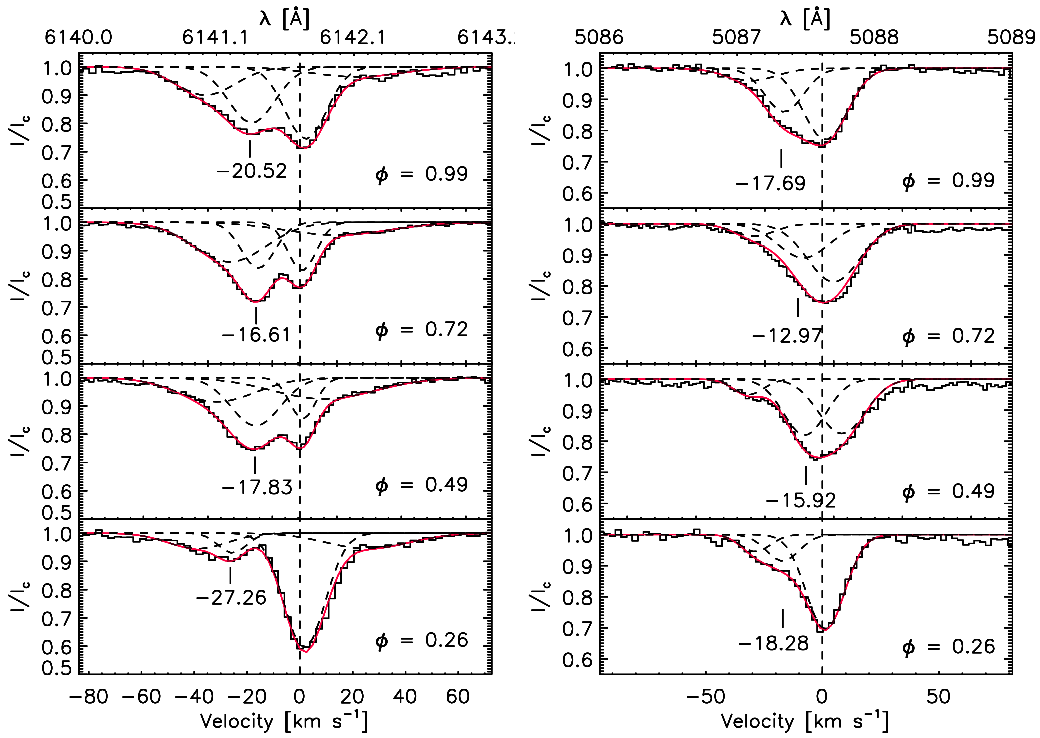

Fig. 5.33.: Example of Gaussian Decomposition for the BaII 6141.712 Å line (left) and YI 5087.418 Å line (right), plotted according to the orbital phase (labelled for each panel). The Gaussian components are plotted in dashed lines, while their sum is in red

close to the orbital period of the system. We report also the equivalent widths of the components. In the case of BaII 6141.712 Å line we find that the EW are variable with the orbital period and they are in anti-phase to each other. On the contrary, the measured EW for the YI 5087.418 Å line does not show any significant variability with the orbital period.

A possible interpretation of what has been obtained is that the blueshifted components of the profiles belongs to a multi-shell structure of the circumstellar environment. This latter, in turn, suffers the tidal interactions of the secondary component. This would explain the variability with the observed orbital period and it would be a further proof of the fact that the presence of a companion is one of the shaping mechanisms in the circumstellar environments of post-AGB stars. Further studies will be needed to confirm this scenario.

1

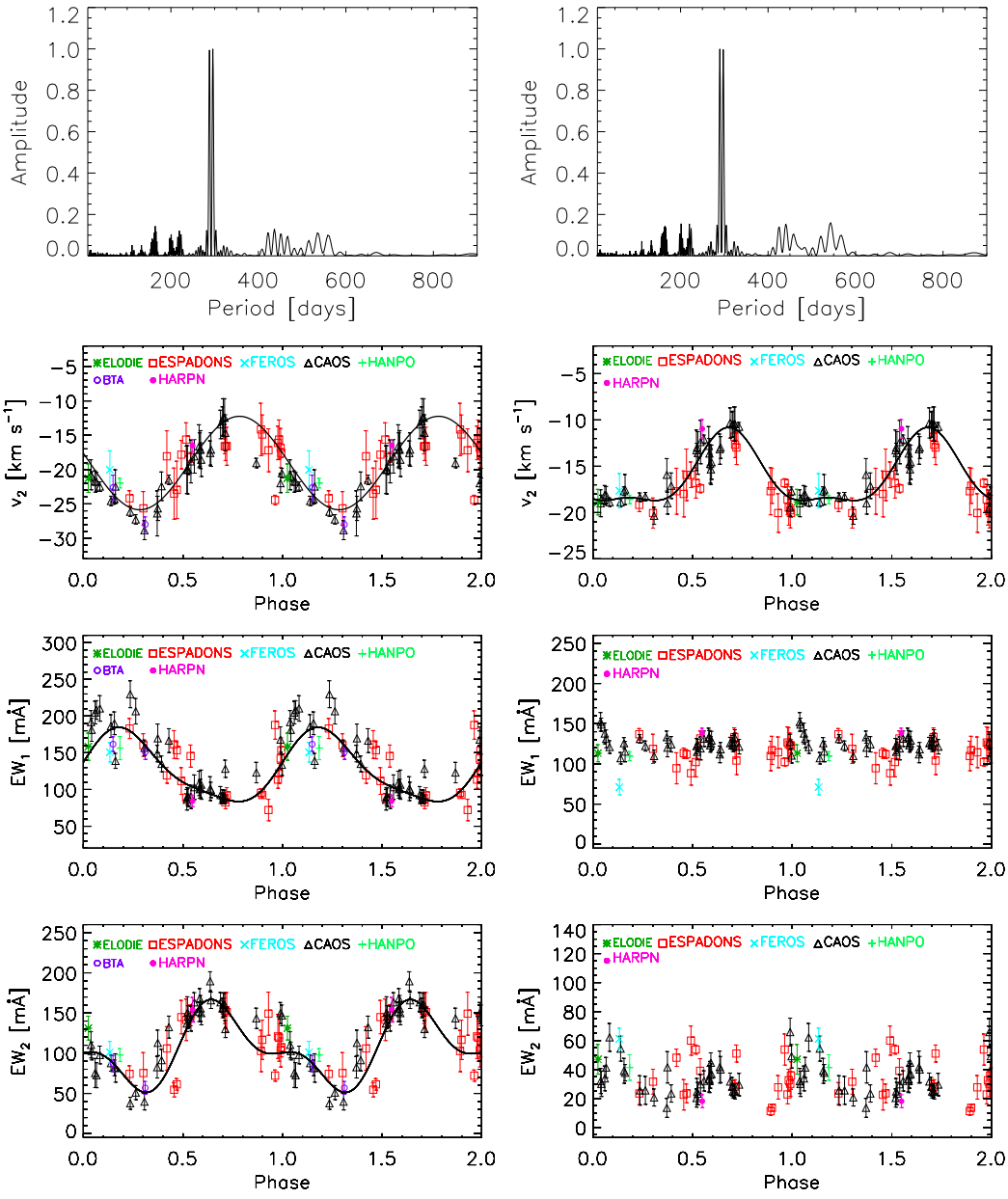

Fig. 5.34.: Gaussian Decomposition results for the BaII 6141.712 Å line (left) and YI 5087.418 Å line (right). From top to bottom: CLEANED Periodogramm of the relative velocity between the centroid of the two components of the profile, clearly showing a peak close to the orbital period; relative velocity in phase with the orbital period; equivalent widths of the central component (EW_1) and of the blue-shifted component (EW_2) again in phase with the orbital period.

6 Linear spectropolarimetry of F-G-K stars

In recent years it has emerged how linear spectropolarimetry can be a powerful diagnostic tool for exoplanets research. In this context it is generally assumed that the background of stellar flux is totally unpolarised. We believe that this latter assumption should not be underestimated and that a study of the possible presence of intrinsic stellar linear polarisation is necessary. For this reason we have decided to undertake a spectropolarimetric observation campaign on a sample of F-G-K stars.

In this Chapter we present the spectropolarimetric survey on F-G-K bright stars that we have conducted in these years. We will see that this work is neither exhaustive nor conclusive: we need much more data to be able to provide greater constraints on the causes of what we have observed.

In Sec. 6.1 we present the observed sample of stars while the spectropolarimetric measurements are present in Sec. 6.2. We then investigate the properties of the observational data (Sec. 6.3) and give some comments on single stars (Sec. 6.4).

6.1 The observed sample

We utilized the Bright Star Catalogue, 5th Revised Ed. (Hoffleit & Warren 1995) to select our sample of stars with spectral classes between F and K. An exception is for HD31964 whose spectral class is A9IaC. We have chosen it as a *spectropolarimetric standard*, since the presence of linear polarisation was previously detected (Geise et al. 2012). Moreover, for all the stars selected, no exoplanets have yet been discovered; the possible presence of linear polarization will therefore be independent of the presence of exoplanets.

The stellar parameters of the sample are shown in Table 6.1. For each star we have tried to use the most homogeneous data set possible. Values of radius R, luminosity

L and rotational period P not present in the literature have been estimated from the following expressions:

$$\frac{L}{L_\odot} = \left(\frac{R}{R_\odot}\right)^2 \cdot \left(\frac{T}{T_\odot}\right)^4 \tag{6.1}$$

$$P = \frac{2\pi R}{v \sin i}. \tag{6.2}$$

Fig. 6.1 shows the distribution in $Log(L/L_\odot)$ versus T_{eff} for the selected stars.

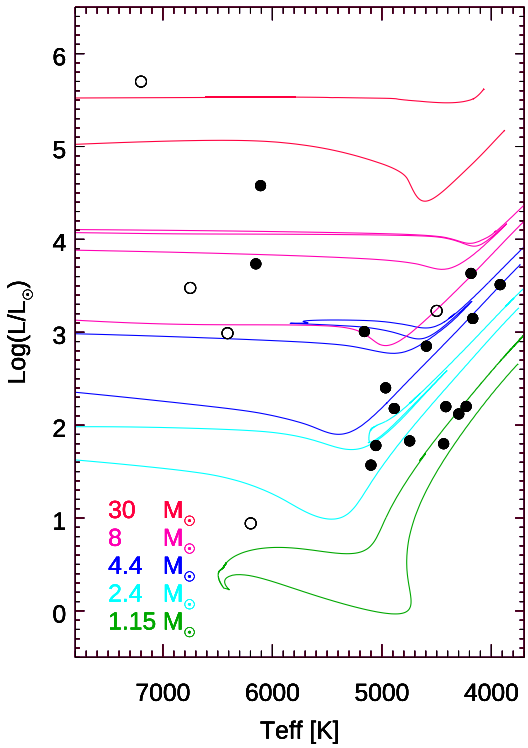

Fig. 6.1.: Distribution in $Log(L/L_\odot)$ versus T_{eff} for the selected stars. The continuum lines represent the PARSEC V1.2s evolutionary tracks (Bressan et al. 2012), for masses $M = 1.15, 2.4, 4.4, 8, 30\ M_\odot$ and metallicity $[Fe/H] = 0.01$. Filled circles represent stars where we detected linear polarisation, while open circles represent stars with zero polarisation.

6.2 Spectropolarimetric measurements

During the all period of my Phd, I have performed high resolution linear spectropolarimetry observations of the selected stars with CAOS.

Data were reduced and Stokes Q/I, U/I and *null* spectra N obtained according to the procedures described in Chapter 3. The logbook of observations is given in Table 6.2. To reach very high Signal-to-Noise (S/N) I have often taken four more exposures, with a total of eight images per Stokes parameters.

In the reduced Stokes spectra, except for some few cases, we don't find any direct evidence of polarisation. In order to detect any possible polarimetric signature hidden in the Signal-to-Noise (S/N) level we have applied the LSD approach to the spectra.

Firstly, for each star we have constructed the line mask from a synthetic spectrum computed by SYNTHE (Kurucz 1993) with stellar parameters given in Table 6.1. We have choosen the spectral region between 4250 Å and 8000 Å. Lines weaker than the noise level were excluded, as well as specific elements like H_α, H_β, CaI, NaI and telluric lines. Finally, for each atomic line we adopted the strength of the specific line as a weight.

In the final columns of Tab. 6.2 we give some information on the LSD results: the achieved Signal-to-Noise (S/N), the number of selected lines and the total polarization $P = \int \sqrt{(\frac{Q}{I})^2 + (\frac{U}{I})^2} dv$, with errors determined from *null* spectra. The last column of Tab. 6.2, in particular, indicates if the star is detected as polarimetric (DD, definite detection) via the detection of a significant Stokes Q and U signature in its least square deconvolution profiles, or if the stars is not detected as polarimetric (ND, not detected). Fig. 6.4 and 6.5 shows the obtained Stokes LSD profiles.

6.2.1 Methodological and instrumental tests

To probe any possible dependence from the line mask construction procedure we have built the LSD profiles from three different submask. Each of them were constructed by selecting different spectral range (i.e. $4250 \div 8000$, $4500 \div 6100$, $5000 \div 6000$ Å) and with different lines selection rules. Results show that spectral widths and number of lines does not change significantly the Stokes Q and U profiles (see as example Fig. 6.2). This will allow us to compare LSD profiles calculated from a different number of lines and/or different wavelength ranges.

Since such measurements have never been made on our sample of stars, we can not compare, and therefore verify, our results with those taken from other instruments. An exception, in addition to the already discussed case of 89 Herculis, is the eclipsing binary of Algol type ϵ Aur. In ϵ Aur, Geise et al. (2012) detected, using ESPaDOnS, linear polarisation across spectral lines such H_α, H_β, CaI (442.6 nm), KI (769.9 nm) and LSD profile from metallic lines. They found that linear polarisation is complex

and variable; it consists at least of two contributors: 1) during the phase of the eclipse of the binary system there is an increasing of polarisation and it is due mostly to the Chandrasekhar effect[1], 2) in out-of-eclipse phase, linear polarisation seems to be not variable in time and its cause is still a matter of discussion. We therefore decided to take advantage of the temporal constancy of polarisation during the out-of-eclipse phase of ϵ Aur using this star as a *spectropolarimetric standard*.

In Fig. 6.3 we report a comparison between CAOS and ESPaDOnS Stokes LSD profiles, both acquired in out-of-eclipse phase: the good similarity between the two results confirms the goodness of the applied method and the stability of CAOS.

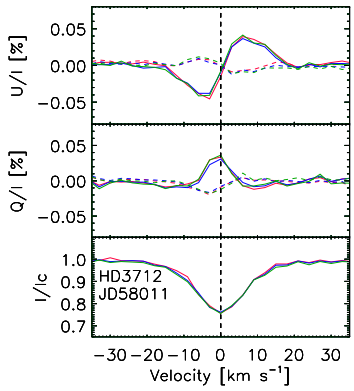

Fig. 6.2.: LSD profiles for HD3712 calculated from three different submask: Red, $4250 \div 8000$ Å and 3687 selected lines; Blue, $4500 \div 6100$ Å and 2309 selected lines; Green, $5000 \div 6000$ Å and 1208 selected lines. Dashed lines indicate *null* spectra.

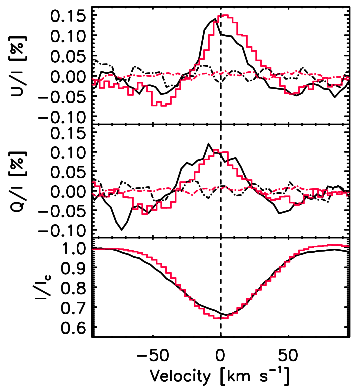

Fig. 6.3.: HD31964: Comparison between CAOS (black) and ESPaDOnS (red) LSD profiles. Dashed lines correspond to null polarisation. Both spectra were acquired in out-of-eclipse phase on HJD 57723.531 and HJD 56268.741 date respectively.

[1] As first shown by Chandrasekhar (1946), due to the center-to-limb variation, light coming from the interior of stars must emerge with a partial linear polarisation. While no net effect can occur in the overall light from a spherical star, the effect should be visible in eclipsing binaries, wherein the symmetry is disrupted.

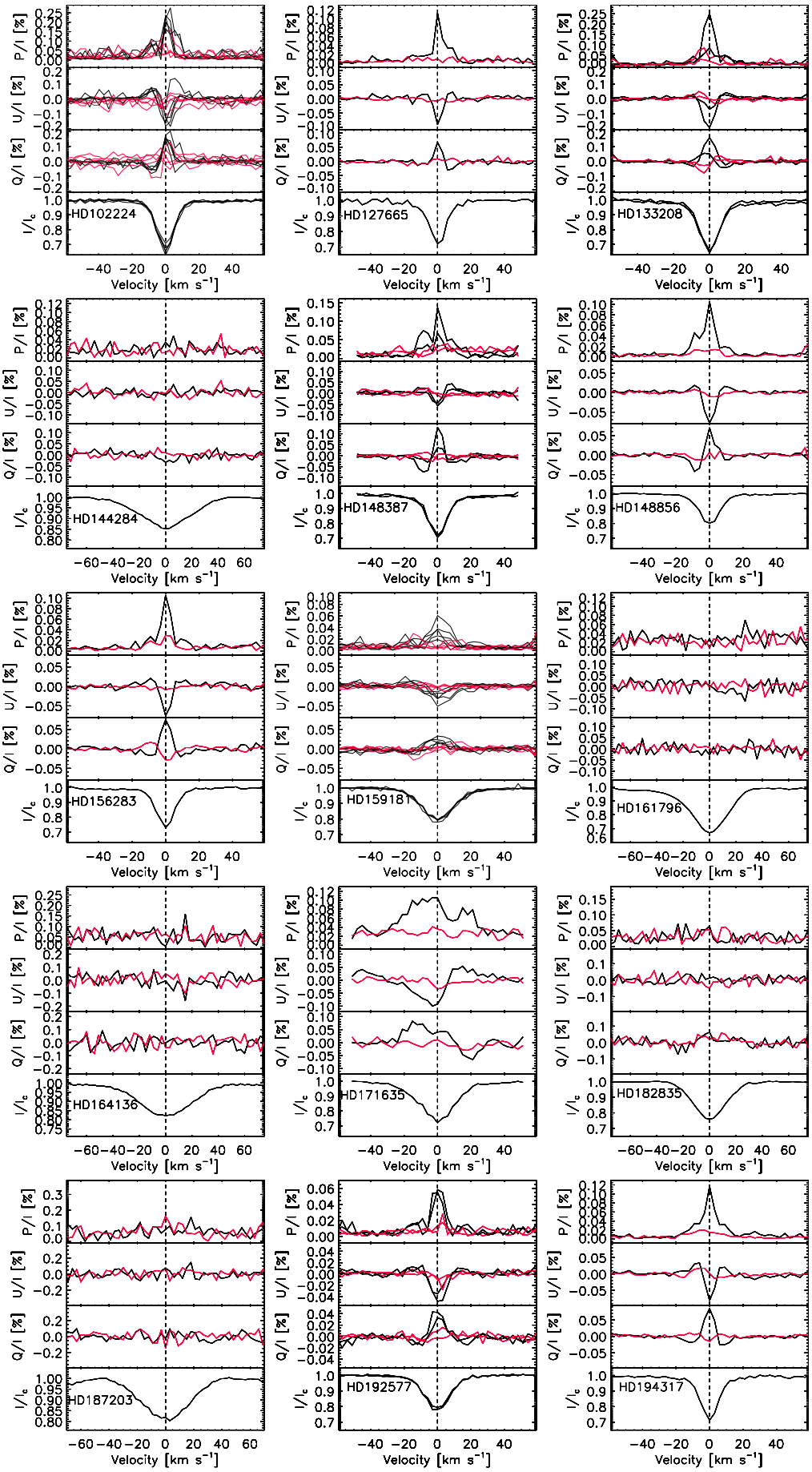

Fig. 6.4.: CAOS LSD profiles of the selected stars. Red lines indicate *null* spectra.

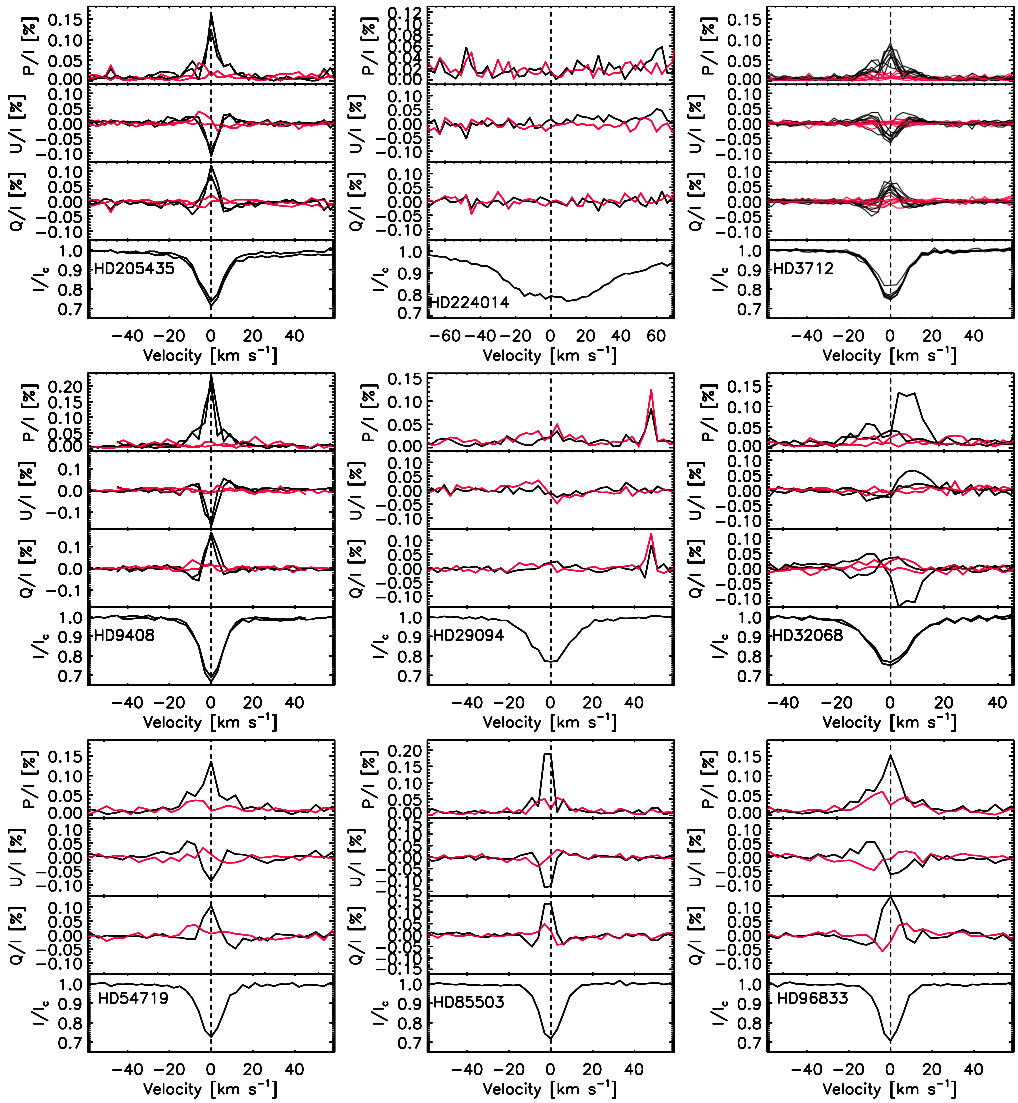

Fig. 6.5.: CAOS LSD profiles of the selected stars. Red lines indicate *null* spectra.

6.3 General properties of the linearly polarised spectra

Tab. 6.2 shows how about 71% of stars of our sample presents linear polarisation across the absorption LSD profiles. In the next subsections we will try to analyze the global properties of the data.

6.3.1 Temporal Variability

Referring to Fig. 6.4 and 6.5, we can not say anything about the time variability for eight stars of our sample (that is, for HD127665, HD148856, HD156283, HD171635, HD194317, HD54719, HD85503, HD96833), since only one measure was taken. Further data are needed for this type of investigation.

Regarding the other stars with detected linear polarisation, three of these (that is HD192577, HD205435 and HD9408) do not show variability. Measures were taken with a time separation of 6 days for HD192577, 41 days for HD205435 and 71 days for HD9408. That means that at present, it is not possible to exclude the possibility of a long-term variability.

Finally, the remaining six stars (that is HD102224, HD133208, HD148387, HD159181, HD3712, HD32068) show short times period variability in the intensities and/or morphologies of the Stokes Q and U parameters. Fig. 6.7 show the variable LSD Stokes profiles for this sub-sample of stars, that were vertically shifted for a better clarity. Unfortunately our data are not sufficient to find out any periodicity.

6.3.2 Wavelength dependence

We have studied the variation of linear polarisation with wavelength. This can be important to constrain the possible origin mechanisms. For example, Schwarz & Clarke (1984) found that the polarisation of the continuum in the visible range due to hot spots decreases with wavelength.

To do that, for each star we have calculated the LSD Stokes parameters from 7 sub-masks, restricting the wavelength-bandpasses of 4000-4500 Å, 4500-5000 Å, 5000-5500 Å, 5500-6000 Å, 6000-6500 Å, 6250-6750 Å and 6500-8000 Å. To eliminate any possible dependence with the line depth, we have firstly adopted an equal weight for each atomic line considered in the line mask. We have then normalized the calculated LSD Stokes Q and U profiles with a common Stokes I. The latter was obtained by mediating on all the selected Stokes I profiles.

Fig. 6.8 shows the obtained total LSD polarisation against wavelength. For six stars of our sample (top panel of the figure) it seems that polarisation increases from blue to red, reaching a maximum at about 6250-6500 Å, while for three stars (bottom panel of the figure) polarisation does not change with wavelength. For the remaining stars of our sample the errors on the measures are so high that we can not say anything about a possible variability with wavelength.

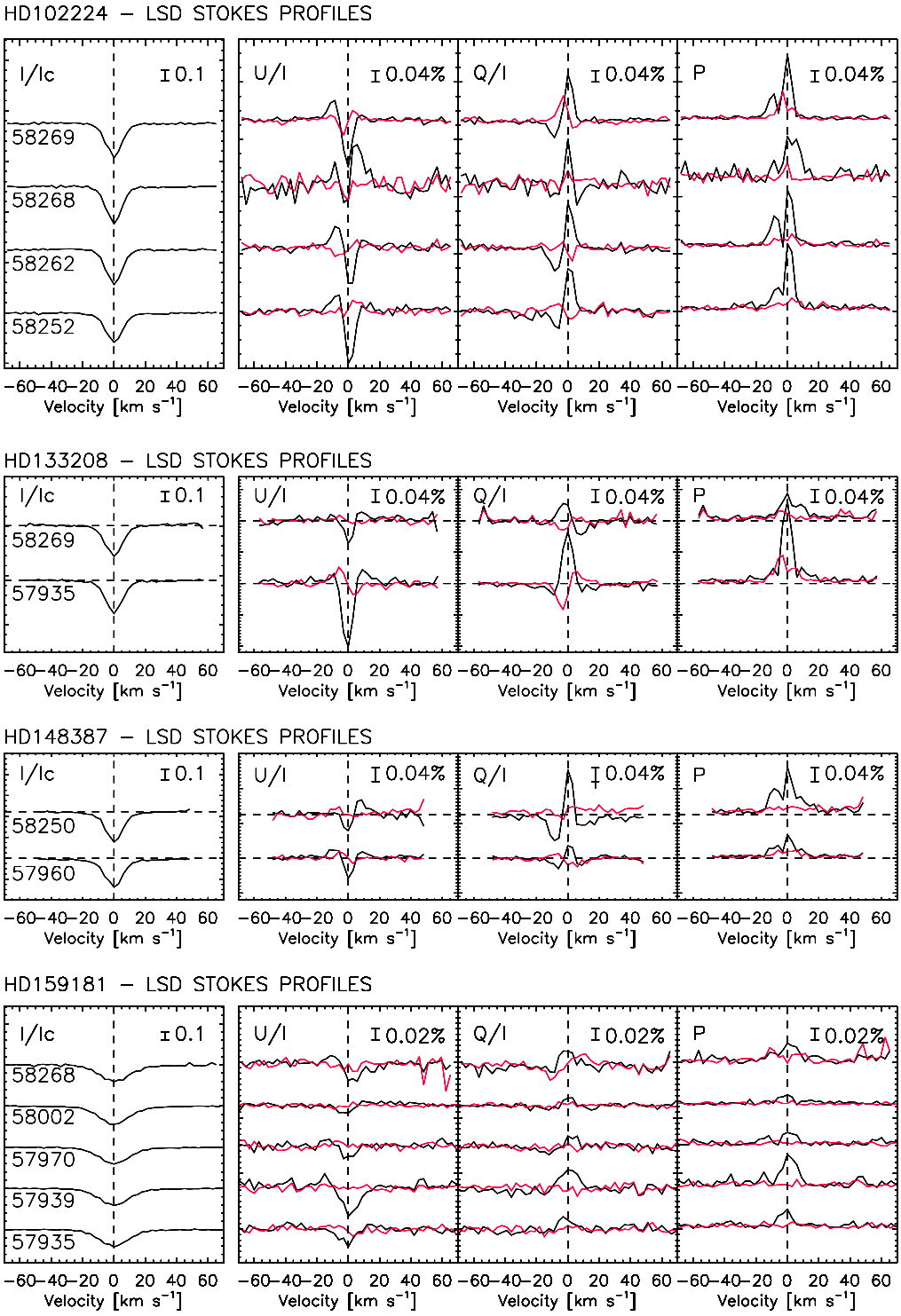

Fig. 6.6.: CAOS LSD profiles of the selected stars which show variable polarisation. Profiles were vertically shifted for clarity.

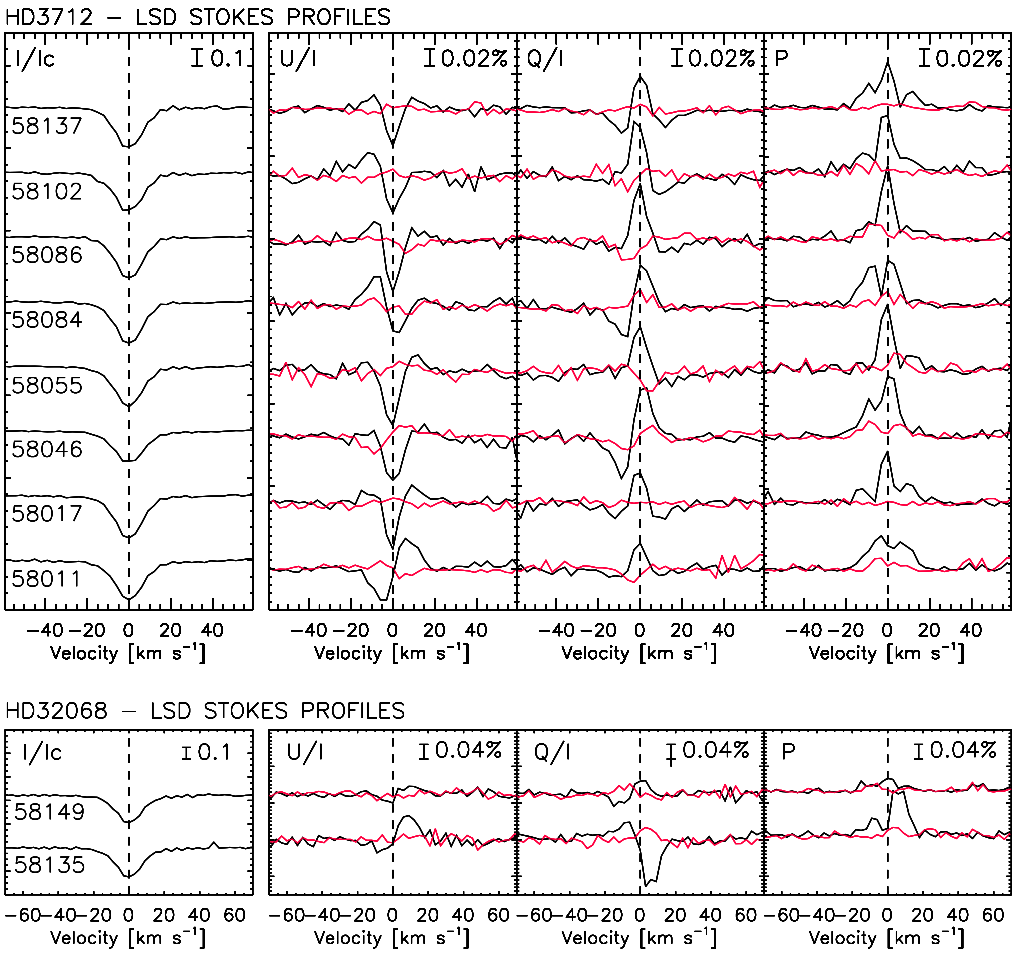

Fig. 6.7.: CAOS LSD profiles of the selected stars which show variable polarisation. Profiles were vertically shifted for clarity.

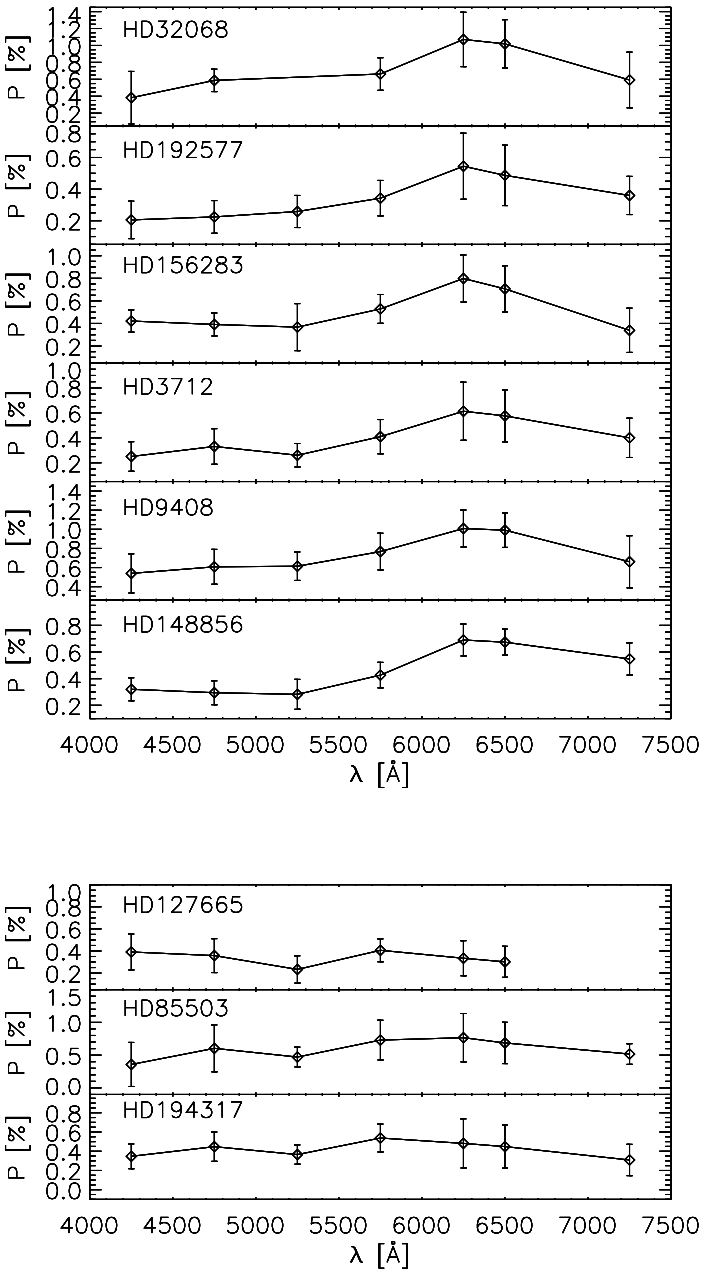

Fig. 6.8.: Wavelength dependence of the polarisation. Top panel: polarisation increases from blue to red, reaching a maximum at about 6250-6500 Å. Bottom panel: polarisation is constant, within errors, with wavelength.

6.4 Comment on single targets

6.4.1 HD102224, χ UMa

χ UMa is an evolved K0.5IIIb orange star. No polarimetric studies have ever been done on this star. Only one measure in circular polarisation was taken with Narval on July 3^{th} 2015, and it is present in the PolarBase database[2]. However the obtained Stokes LSD V profile is null.

In our four measurements, spanning 17 days, we have found Stokes Q and U not null and variable mostly in morphology (Fig. 6.7). In addition, we have clearly found polarisation across the H_α profile. Fig. 6.9 shows the Stokes Q and U parameters corresponding to the H_α absorption profile, measured on JD58252 and on JD58262. We notice that the polarisation signal is concentrated mainly in the core of the line and that Stokes profiles are quite different from those calculated with the LSD method (Fig. 6.7). Moreover, in a time scale of 10 days they change completely sign.

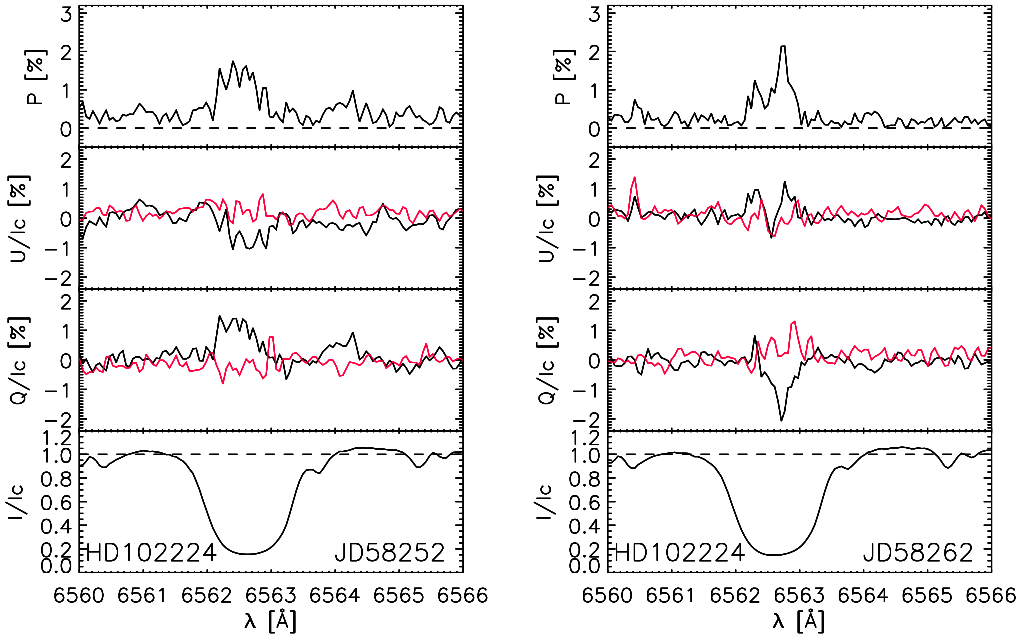

Fig. 6.9.: HD102224: linear polarisation across the H_α absorption profile. An important variability within a time interval of 10 days is present.

[2]**http://polarbase-dev.irap.omp.eu/Espadons_Narval/index.php**.

6.4.2 HD133208, β Bootis

β Bootis is a G8III type star. It is classified as a Flare star, since a X-ray flare was observed by ROSAT of 8 Ausut 1998 (Hünsch & Reimers 1995). This star was observed in circular polarisation with ESPaDOnS and Narval. However, from these observations Aurière et al. 2015 does not detected any polarisation signals, estimating an upper limit of 1 G for the effective magnetic field. This is confirmed by the fact that this star is known to be a low-activity giant.

We have found linear polarisation across the LSD absorption line in our two measures taken with a time interval of about one year (Fig. 6.7). In these measures we have obtained a very important variability in the intensity of Stokes parameters. From the conclusion of Aurière et al. (2015), we exclude the possibility that we are observing the linear polarisation of Zeeman components.

6.4.3 HD205435, ρ Cygni

ρ Cygni is a yellow G8III type evolved giant star. Aurière et al. (2015) detected magnetic field from Narval and ESPaDOnS observations with a maximum value of $7.3 \pm 0.5\ G$.

We have found linear polarisation across the LSD absorption line (Fig. 6.5). In our two measures, taken with a time interval of 41 days, we don't find any evidence of variability. Moreover, we find that the Stokes Q and U intensities are of the same order of magnitude of the Stokes V measured with Narval and ESPaDOnS. For this reason we exclude the possibility that the Zeeman effect is the major contributor to the observed linear polarisation.

6.4.4 HD3712, α Cassiopeia

α Cassiopeia is a K0IIIa red giant. No polarimetric studies have ever been done on this star. In our eight measurements, spanning 126 days, we have found Stokes Q and U not null and variable mostly in morphology (Fig. 6.7).

Dependence of the polarisation with the line depth

In this particular case, the obtained high S/N allowed us to investigate the dependence of the linear polarisation with the depth of the lines. To do that, we have made 3 sub-masks, restricting the individual spectral intensity line depths to 0.4-0.5,

0.6-0.7 and 0.8-0.9 of the continuum. We also checked the mean wavelength of the three sub-masks, finding that they were included in a 500 Å range; we can then exclude the possibility that the obtained differences can be ascribed to the wavelength dependence. Fig. 6.10 shows the LSD polarisation profiles calculated for the 3 selected mean depths. It is possible to note how the overall behavior is complex:

- In some days (e.g. in JD58011, JD58046, JD58102, JD58137) we find that, within errors, there is no dependence of polarisation with the line depth;

- In other days (e.g. JD58017, JD58055, JD58084, JD58086), on the contrary, in the core of the line polarisation clearly increases with the depth, while in the wings polarisation changes differently.

Referring to Fig. 6.10 and looking at the panel of JD58017, we see that in the wings of the line, polarisation decreases going from the weakest line (in red) to the middle line (in blue), then increases from the middle line to the strongest one (in green). Here we note also how the velocities corresponding to the maxima of polarisation in the wings of the strongest line deviate more to the core respect to the weakest line. On the contrary, looking at the panel of JD58086 we can easily see how the behavior of polarisation in the wings of the line is exactly the opposite of the previous case.

The interpretation of what is observed is not trivial. The only case in which a similar study was done concerns the linearly polarised spectrum of Betelgeuse. Aurière et al. (2016), in fact, investigating the dependence of the linear polarisation with the depth of the lines found that in the case of Betelgeuse polarisation strongly increases with line depth and the velocities corresponding to the maxima of polarisation deviate more and more from the photospheric velocity with increasing line depth (Fig. 6.11). The authors interpret this trend as due to the expansion of the atmosphere. In light of this, in our case we can surmise that the complex trend of polarisation with the depth of the line is strictly linked with the dynamics of the atmosphere itself. Consequently even the origin of the polarisation must be searched in this context.

Detection of polarisation across single lines

Crowding the spectra of HD3712, we have found some evidence of polarisation across single absorption lines. Fig. 6.12 shows the Stokes Q and U parameters measured across the BaII 6141.707 Å line on JD58011 and across the BaII 6141.707 Å, FeI 6498.939 Å, CaI 6499.65 Å lines on JD58017. Here we notice how even if the Stokes morphologies are compatible with the calculated LSD profiles (compare Fig.

6.7 with Fig. 6.12), there are differences between the lines. The polarisation across the FeI 6498.939 Å and CaI 6499.65 Å lines, for example, does not scale with the line depth and the Stokes Q morphology of BaII 6141.707 Å line measured on JD58017 is double-peaked.

These evidences converge towards the idea that the observed polarisation has an atomic contribution; a line-by-line analysis considering the various transitions involved is therefore important. Unfortunately, if on the one hand the LSD method produces a very high S/N average line profile, any information on the behaviour of single lines is generally lost.

6.4.5 HD32068, ζ Aurigae

$zeta$ Aurigae is an eclipsing binary of Algol type having the orbital plane oriented close to the line of sight and an inclination of $87°$ (Eaton et al. 2008); in this way an eclipse of one star by the other occurs during each orbit, causing a decrease in magnitude up to 3.99. The primary component (Zeta Aurigaes A) is classified as a K-type bright giant, while its companion (Zeta Aurigaes B) is a B-type main sequence star. The ephemeris of this binary system was determined by Eaton et al. (2008) from radial velocities:

$$JD(RV_{max}) = 2453039.9(\pm 0.1) + 972.162 \quad days. \tag{6.3}$$

Koch & Pfeiffer (1982) performed a polarimetric study of Zeta Aurigae during the 1979-1980 eclipse, finding intrinsic and variable polarisation in the optical wavelength-bandpasses. They suggested that the observed intrinsic polarisation cannot be due to the Chandrasekhar effect (i.e. it is not related to the eclipse) and not even to the binary condition, but can be explained in context of not well specified chromospheric inhomogeneities of the supergiant.

We have found linear polarisation across the LSD absorption line (Fig. 6.7). According to the ephemeris expressed in Eq. 6.3, our two measures correspond to the orbital phases $\phi = 0.24$ and $\phi = 0.26$, and present important variability, both in intensity and in the morphology of Stokes profiles. If the polarisation depended on the binary condition, we would not expect a variability in the observed Stokes profiles with a phase difference of only $\Delta\phi = 0.02$.

We then agree with the conclusion of Koch & Pfeiffer (1982); we are not yet able to say if the linear polarisation that we measure across the absorption profiles totally comes from the depolarisation of the continuum observed by Koch & Pfeiffer (1982) or if there is an intrinsic atomic contribution. We can simply say that our measures

are unlikely to be compatible with the binary condition of the system. Further measures will be necessary.

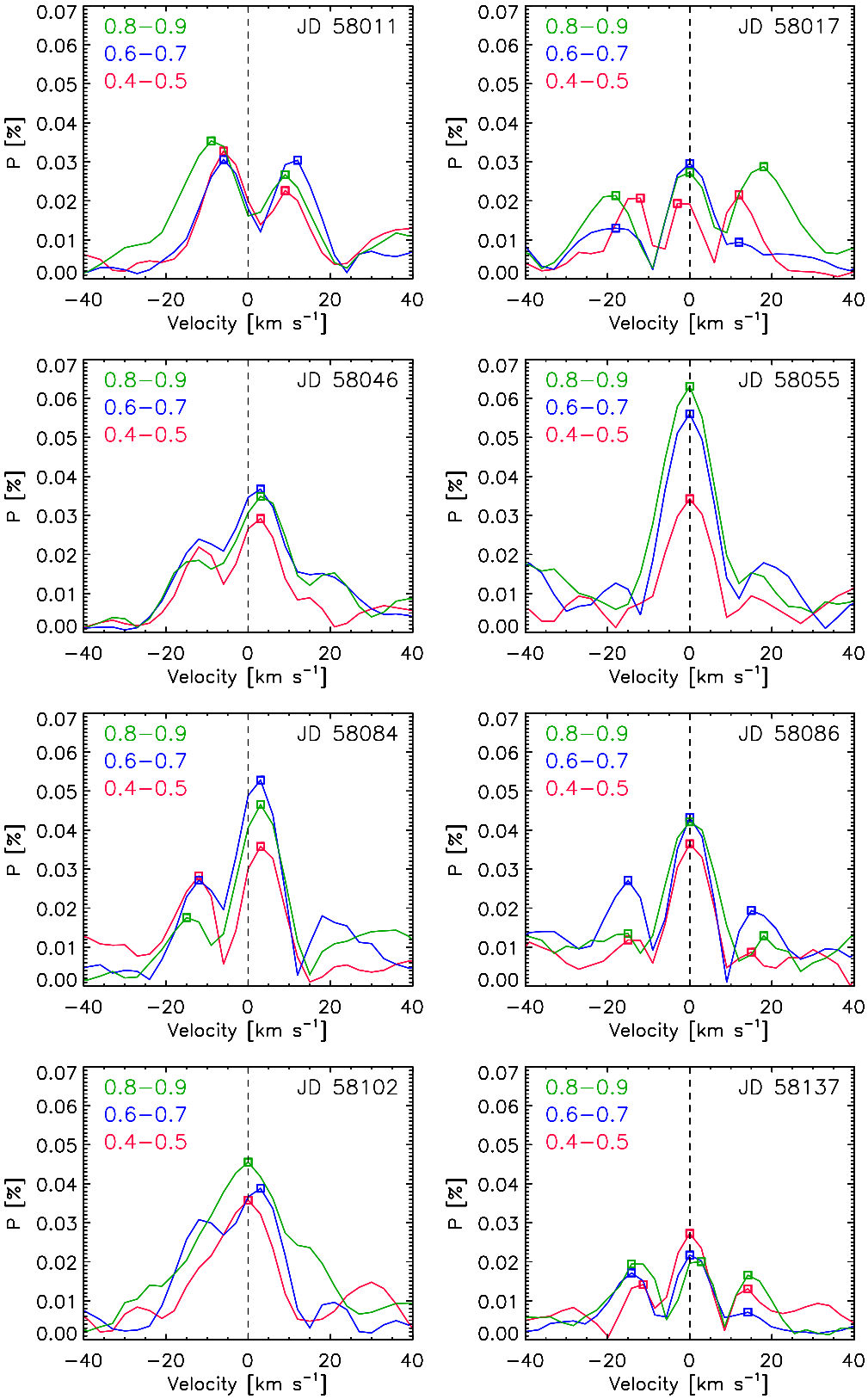

Fig. 6.10.: Variations of the linear polarisation of HD3712 from the LSD profiles with the depth of the lines. Three sub-masks are used with line depth domains as indicated on the graph.

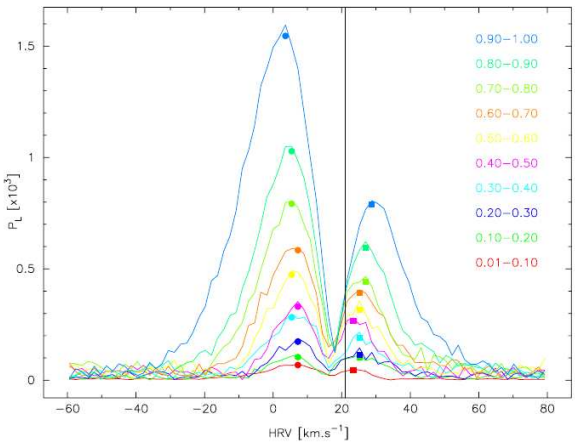

Fig. 6.11.: Variations of the linear polarisation of Betelgeuse with the depth of the lines. Image adapted from Aurière et al. (2016).

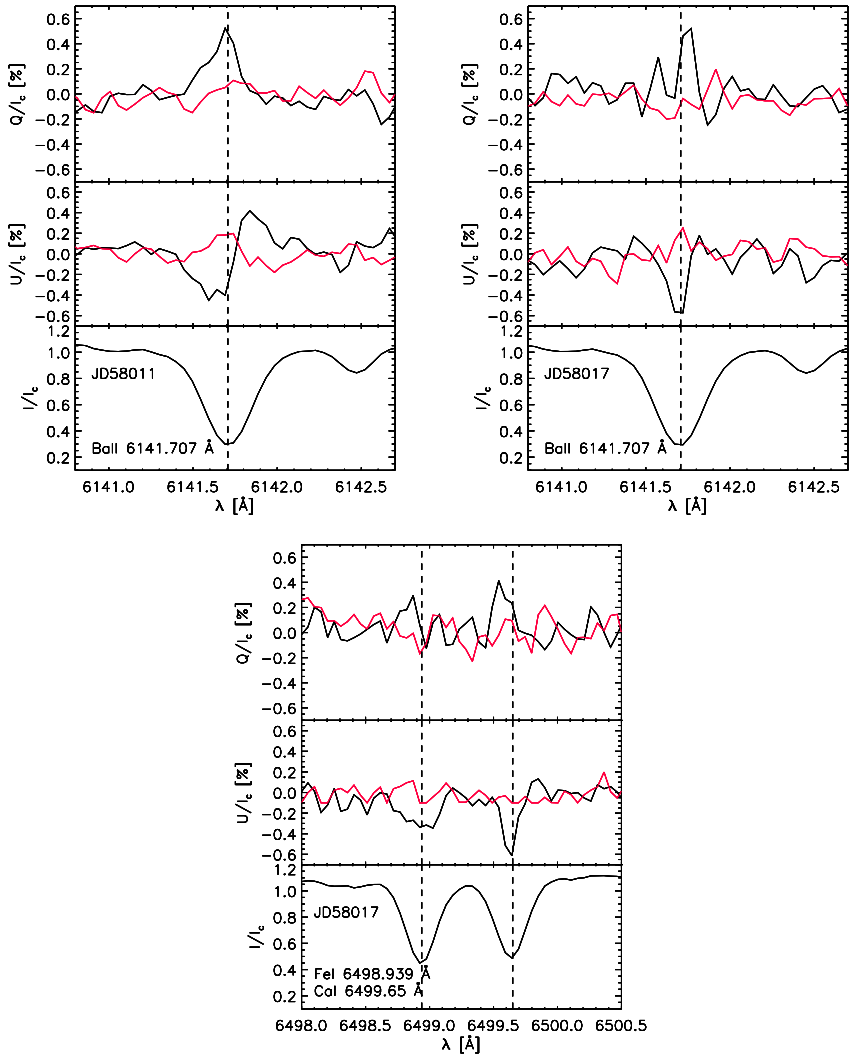

Fig. 6.12.: HD3712: linear polarisation across single lines in absorption.

Tab. 6.1.: Properties of the selected stars and associated references. Spectral classes come from SIMBAD database. An asterisk indicates data calculated from equations 6.1 and 6.2.

HD	Sp Type	T_{eff} [k]	Ref	$log\ g$	Ref	$[Fe/H]$	Ref	L [$L_\odot$]	Ref	R [$R_\odot$]	Ref	$v \sin i$ [$km\ s^{-1}$]	Ref	P_{rot} [days]	Ref
003712	K0-IIIa C	4594	**44**	2.14	**44**	−0.10	**44**	708*		42.1	**11**	21	**14**	≥ 101*	
009408	G9IIIb C	4746	**46**	2.21	**46**	−0.34	**46**	67.6	**46**	11.0	**38**	0.44	**18**	≥ 1263*	
029094	K0II-III+B9V C	4500	**37**	2.21	**44**	−0.20	**1**	1698	**1**	56	**44**	11.0	**44**	≥ 257*	
031964	A9Ia C	6108	**9**	1.50	**9**	−0.11	**9**	37875	**15**	143 − 358	**23**	54	**43**	≥ 335*	
032068	K5II+B7V C	3920	**35**	1.33	**35**	+0.26	**35**	3254	**35**	123.93*		68	**3**	≥ 93*	
054719	K2III C	4528	**16**	2.22	**38**	+0.14	**38**	224	**38**	27	**23**	5.8	**23**	≥ 235*	
085503	K2IIIbCN1Ca1 B	4436	**36**	2.50	**36**	+0.17	**36**	63	**36**	14	**36**	4.5	**36**	≥ 157*	
096833	K1III B	4520	**50**	2.36	**50**	−0.13	**50**	148	**7**	19.7	**7**	5.5	**50**	≥ 181*	
102224	K0.5IIIb C	4416	**50**	2.20	**50**	−0.44	**50**	158	**50**	20.8	**38**	2.3	**50**	≥ 457*	
127665	K3-III B	4298	**2**	2.22	**46**	−0.17	**5**	131.9	**2**	21.57	**2**	17	**14**	≥ 64*	
133208	G8IIIaFe-0.5 C	4966	**44**	2.93	**44**	+0.21	**44**	252*		21.5	**25**	4.10	**25**	200	**25**
144284	F9V C	6198	**34**	4.13	**34**	+0.20	**34**	8.75	**34**	2.57*		27	**14**	≥ 5*	
148387	G8-IIIab B	5055	**45**	2.82	**45**	−0.04	**45**	60.25	**45**	10.14*		8	**3**	≥ 64*	
148856	G7IIIaFe-0.5 B	4887	**36**	2.50	**36**	−0.27	**36**	151	**36**	17	**36**	3.0	**36**	≥ 286*	
156283	K3II C	4170	**13**	1.42	**6**	−0.07	**6**	1406*		72	**12**	6.12	**13**	≥ 594*	
159181	G2Ib-IIa B	5160	**28**	1.86	**28**	+0.14	**34**	1017	**34**	40	**20**	13	**14**	≥ 155*	
161796	F3Ib C	6750	**15**	0.50	**31**	−0.40	**31**	3000	**15**	41	**15**				
164136	F2II C	6410	**29**	2.29	**29**	−0.33	**32**	977	**1**	25*		27	**47**	≥ 47*	
171635	F7Ib C	6151	**26**	2.40	**26**	−0.04	**26**	5450	**37**	65*		10	**29**	≥ 328*	

Continued on next page

Tab. 6.1 – continued from previous page

HD	Sp Type	T_{eff} [k]	Ref	$log\ g$	Ref	$[Fe/H]$	Ref	L $[L_\odot]$	Ref	R .. Ref $[R_\odot]$	Ref	$v \sin i$ $[km\ s^{-1}]$	Ref	P_{rot} [days]	Ref
182835	F2Ib C	6700	**28**	1.43	**28**	-0.03	**30**	21000	**19**	104	**19**	13	**3**	$\geq 404^*$	
187203	F8Ib-II C	5750	**28**	2.15	**28**	-0.24	**28**					25	**28**		
192577	K3Ib+B2IV-V C	4186	**41**	1.23	**41**	$+0.03$	**41**	4300	**7**	197	**8**	25	**14**	$\geq 398^*$	
194317	K2.5IIIFe-0.5 B	4230	**4**	2.16	**4**	-0.17	**4**	159	**38**	25.35	**38**	19	**14**	$\geq 67^*$	
205435	G8IIIFe-0.5 B	5100	**42**	2.68	**44**	-0.16	**44**	37.1	**42**	7.81	**42**	19	**14**	$\geq 20^*$	
224014	G2 0 C	7200	**10**	0.10	**22**	$+0.30$	**17**	$5 \cdot 10^5$	**10**	$400 - 500$	**10**	25	**16**	$\geq 1010^*$	

Tab. 6.1.: **References:** **1** Anderson & Francis (2012); **2** Berio et al. 2011; **3** Bernacca & Perinotto 1970; **4** Cayrel de Strobel et al. 2001; **5** Cardini 2005; **6** Cenarro et al. 2007; **7** di Benedetto & Ferluga 1990; **8** Eaton 1993; **9** Giridhar et al. 2013; **10** Gorlova et al. 2006; **11** Hajian et al. 1998; **12** Hatzes & Cochran 1999; **13** Hekker & Meléndez 2007; **14** Hoffleit & Warren 1995; **15** Hoogzaad et al. 2002; **16** Hohle et al. 2010; **17** Israelian et al. 1998; **18** Jofré et al. 2015; **19** Jones et al. 2011; **20** Kaler 2011; **21** Kervella et al. 2004; **22** Klochkova et al. 2014; **23** Kloppenborg et al. 2015; **24** Koncewicz & Jordan 2007; **25** König et al. 2006; **26** Kovtyukh et al. 2012; **27** Levesque et al. 2005; **28** Lyubimkov et al. 2010; **29** Lyubimkov et al. 2012; **30** Lyubimkov et al. 2015; **31** Luck et al. 1990; **32** Luck 2014; **33** Luck 2015; **34** Mallik 1999; **35** McWilliam 1990; **36** Massarotti et al. 2008; **37** McDonald et al. 2012; **38** Nordgren et al. 1999; **39** Pasinetti Fracassini et al. 2001; **40** Piau et al. 2011; **41** Prugniel et al. 2011; **42** Reffert et al. 2015; **43** Royer et al. 2002; **44** Soubiran et al. 2008; **45** Takeda et al. 2007; **46** Takeda et al. 2008; **47** Uesugi & Fukuda 1970; **48** Valdes et al. 2004; **49** Wu et al. 2011; **50** Jennens & Helfer 1975.

Tab. 6.2.: Logbook of the observational data and spectropolarimetric results.

HD	JD (+2400000)	SN	Lines	P [%]	Det.
3712	58011.530	18816	2305	0.92 ± 0.28	**DD**
	58017.530	21541	3683	0.87 ± 0.14	
	58046.441	18325	1183	1.27 ± 0.50	
	58055.423	16471	1187	0.99 ± 0.41	
	58084.312	11578	2986	1.00 ± 0.31	
	58086.323	19141	3645	1.06 ± 0.43	
	58102.273	17404	1195	1.13 ± 0.31	
	58137.212	13030	3662	0.89 ± 0.17	
9408	58011.565	11937	1554	1.80 ± 0.41	**DD**
	58086.397	9594	2374	2.11 ± 0.66	
29094	58137.336	4907	3293	0.59 ± 0.90	ND
31964	57723.531	1757	453	10.36 ± 1.75	**DD**
	58055.608	2831	339	6.60 ± 2.46	
32068	58135.382	10008	2494	2.34 ± 0.53	**DD**
	58149.355	12613	2492	0.94 ± 0.47	
54719	58150.464	8981	1416	1.61 ± 0.72	**DD**
85503	58137.570	2008	3701	1.77 ± 0.96	**DD**
96833	58149.595	6961	3320	2.00 ± 1.10	**DD**
102224	58252.360	9168	2527	2.39 ± 0.80	**DD**
	58262.392	10406	2432	2.17 ± 0.88	
	58267.316	3560	829	3.42 ± 1.89	
	58268.337	5471	1807	2.67 ± 1.30	
	58269.307	8740	2558	2.24 ± 0.99	
127665	57940.348	20283	3629	0.91 ± 0.28	**DD**
133208	57935.373	7466	2070	2.55 ± 1.18	**DD**
	58269.406	8508	2084	1.35 ± 0.52	
144284	57939.365	6903	631	1.76 ± 1.58	ND
148387	57960.317	10589	1891	0.85 ± 0.41	**DD**
	58250.518	3148	3007	1.98 ± 0.58	**DD**
148856	57961.353	21503	3251	1.13 ± 0.30	**DD**
156283	57970.333	13852	2859	1.09 ± 0.43	**DD**
159181	57935.454	25611	999	0.48 ± 0.30	**DD**
	57939.438	26839	1014	0.88 ± 0.23	
	57970.376	18958	997	0.46 ± 0.24	
	58002.322	25257	1000	0.35 ± 0.17	

Continued on next page

Tab. 6.2 – continued from previous page

HD	JD (+2400000)	SN	Lines	P [%]	Det.
	58268.533	7303	3286	0.75 ± 0.55	
161796	56842.427	5703	239	2.60 ± 2.00	ND
164136	57940.444	2681	265	4.60 ± 4.98	ND
171635	57969.414	7017	1401	3.82 ± 1.08	**DD**
182835	56861.442	3633	180	3.46 ± 3.17	ND
	57584.497	5020	124	1.92 ± 1.89	
	57631.356	4293	159	2.49 ± 2.70	
187203	56860.485	2178	1083	5.56 ± 5.39	ND
	56893.397	1424	866	9.44 ± 8.77	
192577	58011.384	29603	1615	0.71 ± 0.28	**DD**
	58017.462	17719	3029	0.85 ± 0.34	
194317	57960.483	16415	1385	1.30 ± 0.45	**DD**
205435	57961.526	2547	1792	1.49 ± 0.34	**DD**
	58002.435	9122	1607	1.27 ± 0.60	
224014	58002.558	2473	1800	1.39 ± 1.48	ND

7 Conclusions

> *There are known knowns; there are things we know we know. We also know there are known unknowns; that is to say we know there are some things we do not know. But there are also unknown unknowns – the ones we don't know we don't know [...]. It is the latter category that tends to be the difficult ones.*
>
> **— Donald Henry Rumsfeld**

The main goal of the work carried out during my PhD was to demonstrate the diagnostic potential of high resolution linear spectropolarimetry in a stellar context. I used the *Catania Astrophysical Observatory Spectropolarimeter* (CAOS) on a large sample of stars improving the data acquisition and analysis. In addition, from a theoretical point of view, I used numerical codes to interpret the acquired data. The main obtained results are:

- we have found, for the first time, evidence of the *Second Solar Spectrum* in a star different than the Sun: 89 Herculis. The absorption metal lines with low excitation potentials present linear polarisation, varying in time with the orbital period;

- we have investigated the possible origins of the observed polarisation. Because of the variability with orbital period, we rule out pulsations as the origin of the variability. Moreover, we can also rule out hot spots as the possible origin of continuum depolarisation, because of the lack of dependence of polarisation on wavelength. According to Kuhn et al. (2011), the linear polarisation we detected in the CaII 8662-Å line rules out scattering polarisation from free electrons of the circumbinary environment and suggests that the origin of the Second Solar Spectrum we observed in 89 Herculis is the anisotropic radiation field due to the secondary star. In this framework, the periodic variability of polarised profiles, particularly the closed loop described by the polarisation angle, can be ascribed to the jets at the basis of the hourglass structure being differently illuminated by the secondary orbiting around the primary;

- we have found, for the first time, evidences of linear polarisation across the emission metal lines of 89 Herculis. We have then performed numerical simulations to show that polarised profiles are consistent with electron scattering in an undistrupted rotating disk. Such a disk appears to be rotated by $45°$ (clockwise) from the north-south direction, as observed by interferometric observations;

- we have conducted a spectropolarimetric survey on a sample of 25 F-G-K bright stars, discovering that about 71 % of them present linear polarisation across the absorption LSD profiles, often variable over time;

- we have studied the main polarisation properties of the stars arguing that for some of those it is probable that we are dealing with intrinsic polarisation of atomic origin, rather than depolarisation of the continuum.

Regarding the first three points, if it is possible to generalize the result of our observational campaign of 89 Herculis, we conclude that the inner regions of stellar envelopes can be probed via high-resolution spectropolarimetry and that this appears to be the only diagnostic for stars still too far away for interferometric studies.

Regarding the last two points, it appears that the presence of linear polarisation is widespread in the F-G-K type stars. Our study is certainly not conclusive, since more data are needed in longer time intervals with a robust theoretical support able to interpret the observations.

However, these results seem to open a new perspective in the study of stellar atmospheres: it is no longer possible the a priori assumption of unpolarised stellar flux and *spectropolarimetry* must become the natural evolution of *spectroscopy*. In this context we want to stress that a line-by-line study is necessary, taking into account the particular transitions involved. The LSD method gives us only a very high S/N *average* profile, loosing any information on the behaviour of single lines. Nowadays, only in very few cases we manage to obtain S/N levels such as to have evidence of polarisation across single lines. It is therefore necessary to sensitize the scientific community towards the use of this diagnostic technique and towards the development of new high resolution spectropolarimeters on large telescopes.

Appendix

A

A.1 An Atlas of the *Second Stellar Spectrum* of 89 Herculis

This atlas represent an high resolution full I, Q, U Stokes spectrum of 89 Herculis which shows polarisation patterns across single lines. This result, until now, had never been obtained for stars other than the Sun. For this reason, in analogy to the solar case, we call it the "*Second Stellar Spectrum*". In the following we show the highest S/N spectra, acquired with ESPaDOnS on JD53961.

For each panel, the Stokes I, Q, U profiles and the total polarisation P are shown in black, while in red we indicate the corresponding null spectrum.

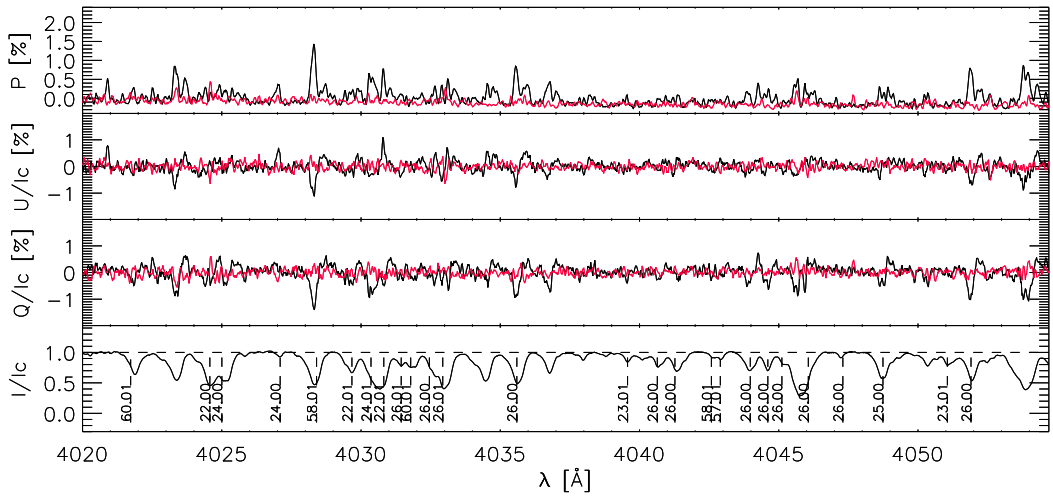

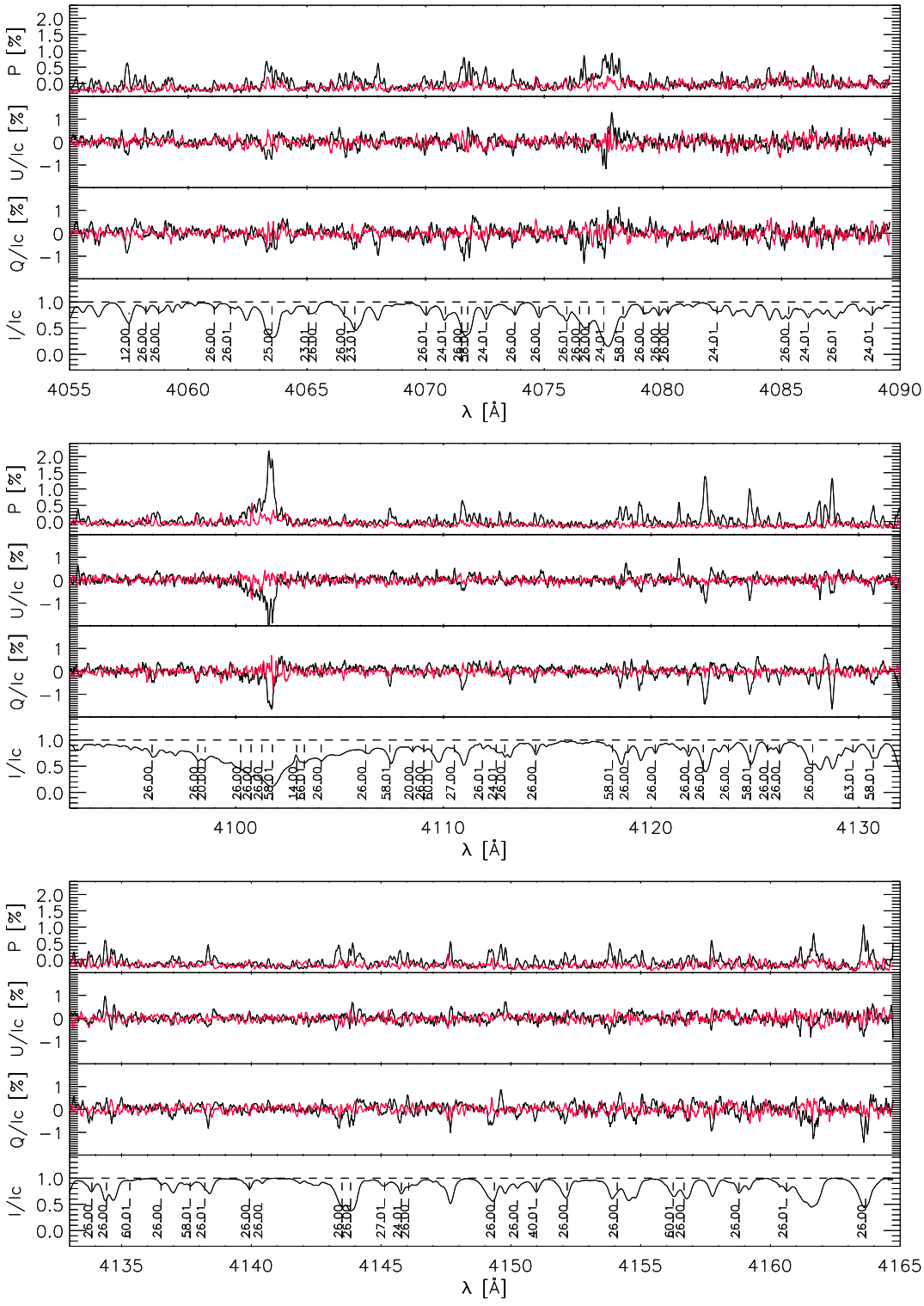
P [%]
U/Ic [%]
Q/Ic [%]
I/Ic
λ [Å]

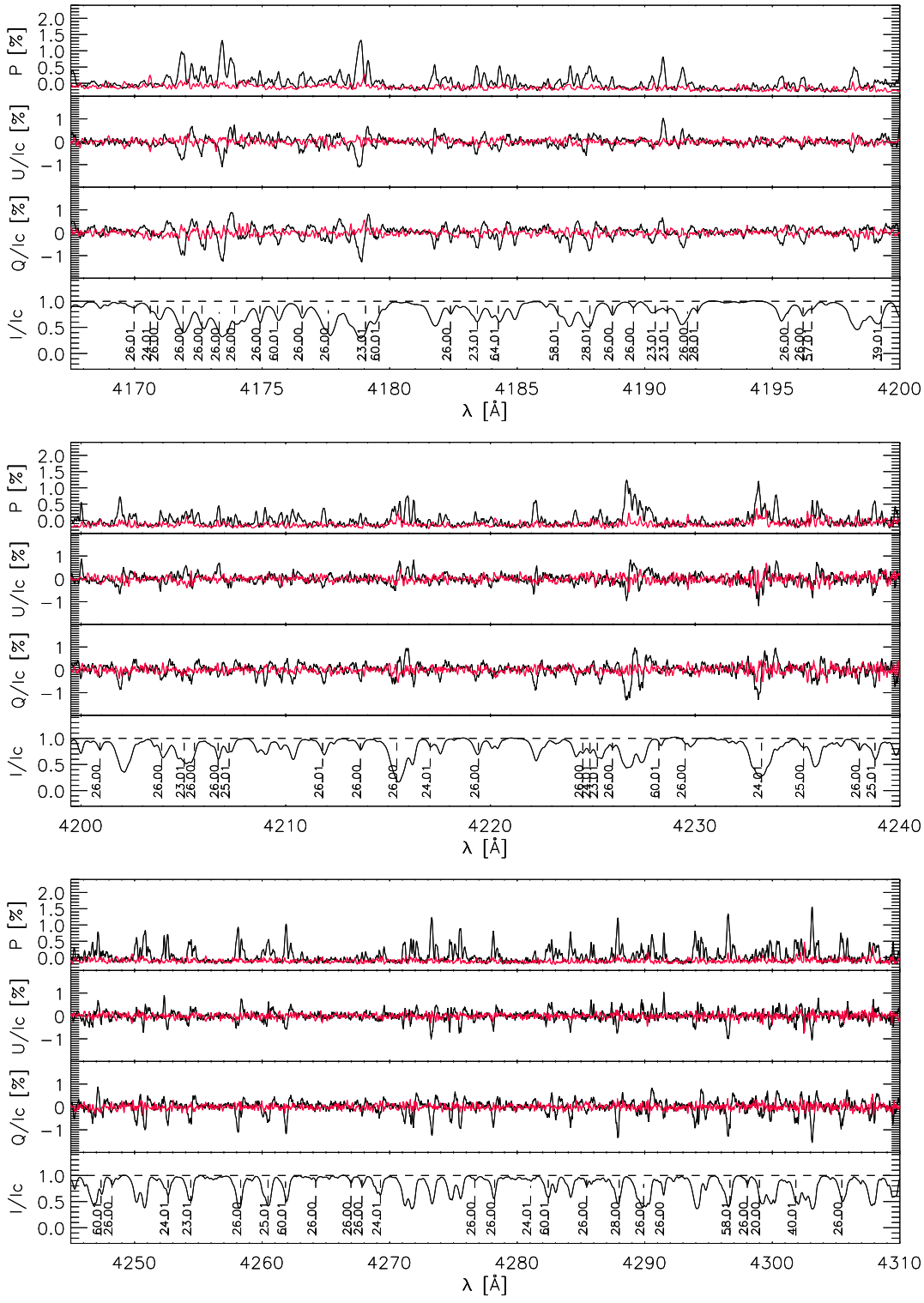
P [%]
U/Ic [%]
Q/Ic [%]
I/Ic
λ [Å]

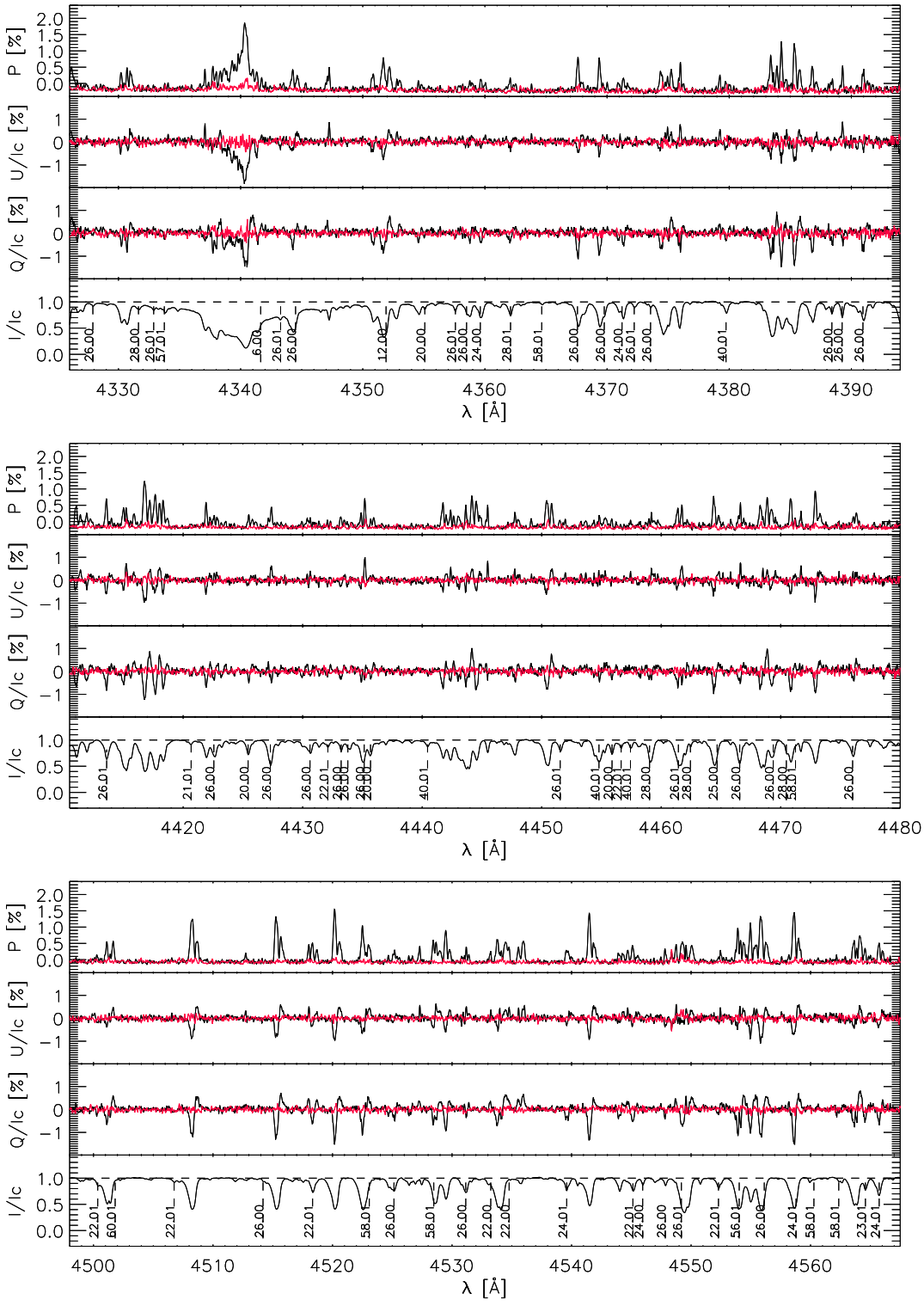
P [%]
U/Ic [%]
Q/Ic [%]
I/Ic
λ [Å]

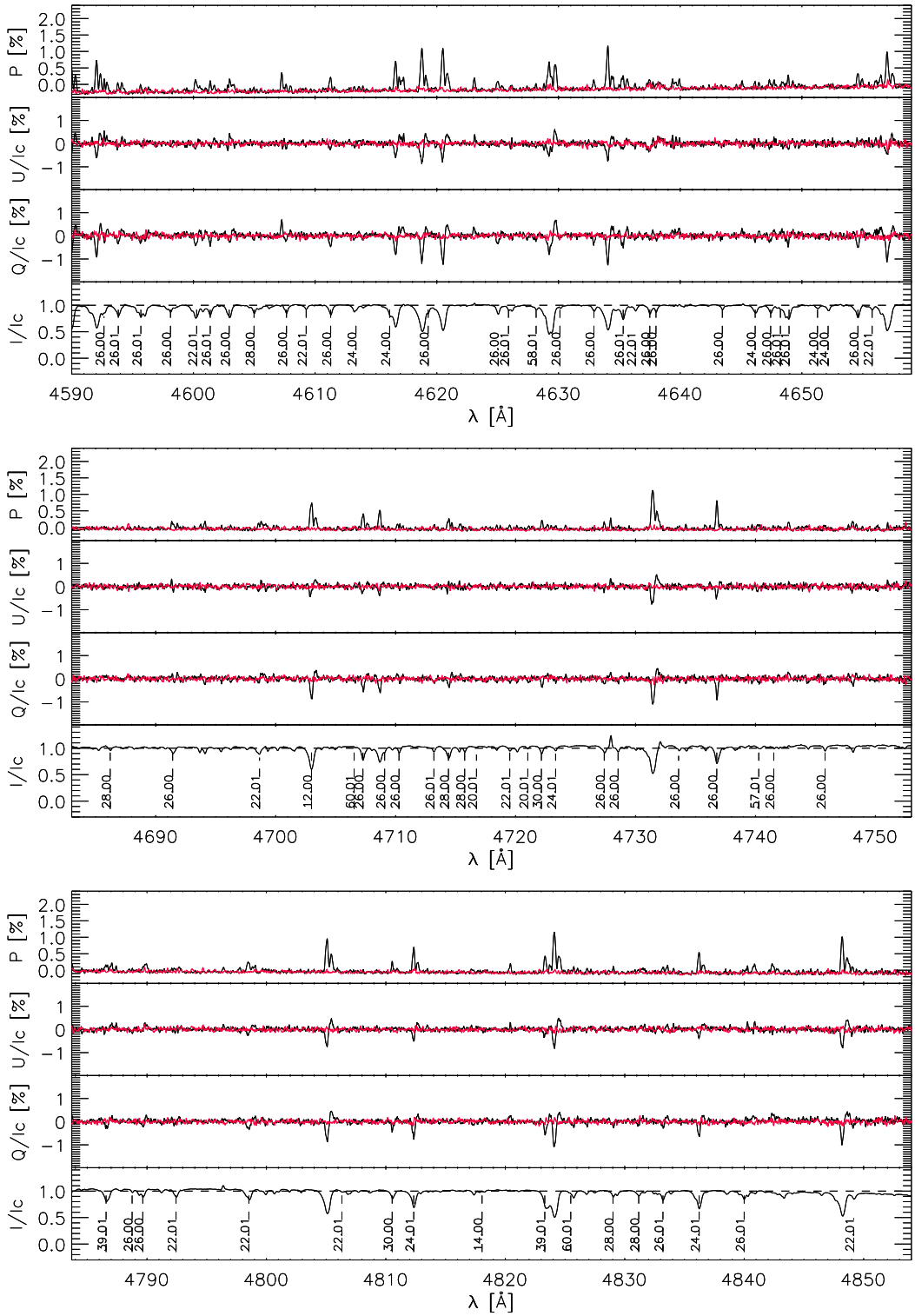
P [%]
U/Ic [%]
Q/Ic [%]
I/Ic
λ [Å]

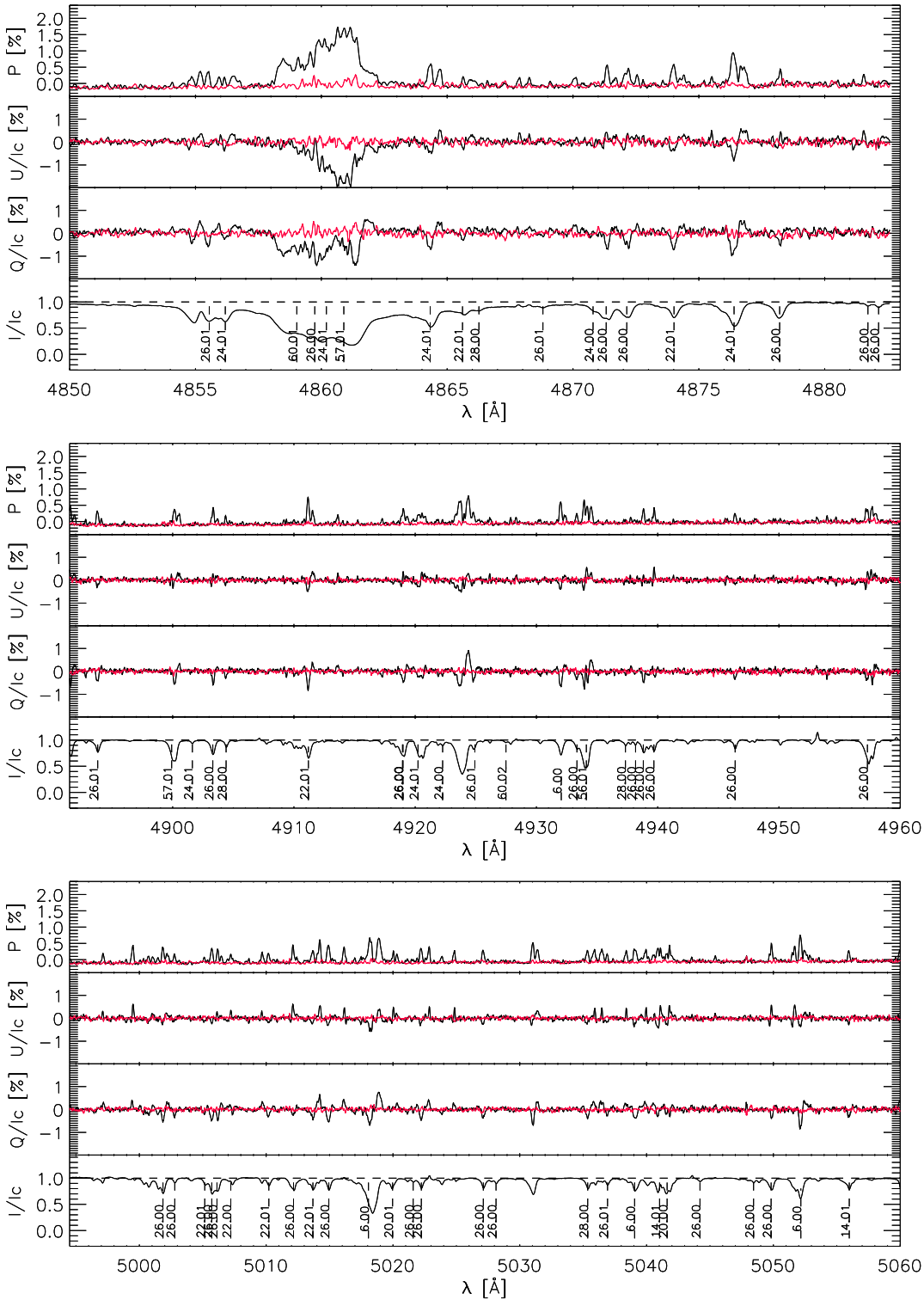
P [%]
U/Ic [%]
Q/Ic [%]
I/Ic
λ [Å]

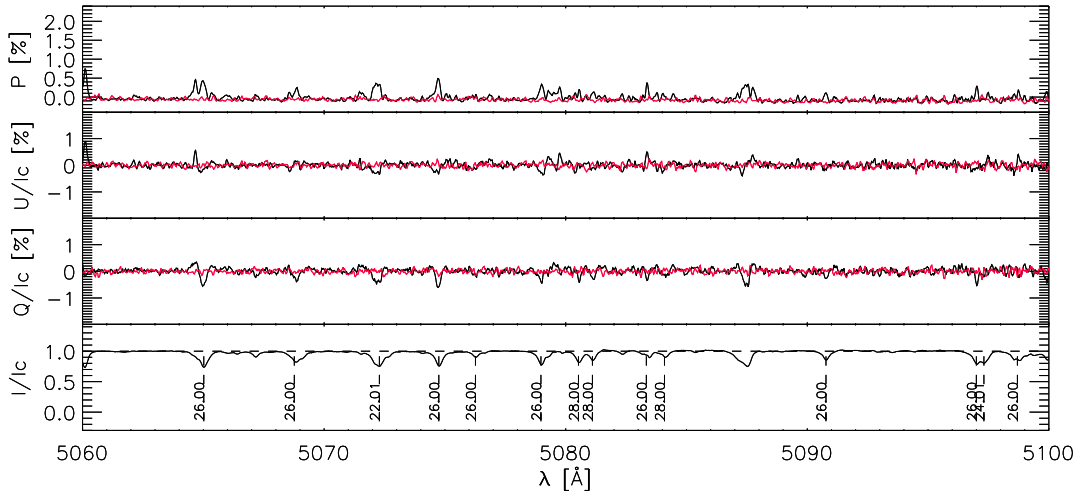
P [%]
U/Ic [%]
Q/Ic [%]
I/Ic
λ [Å]

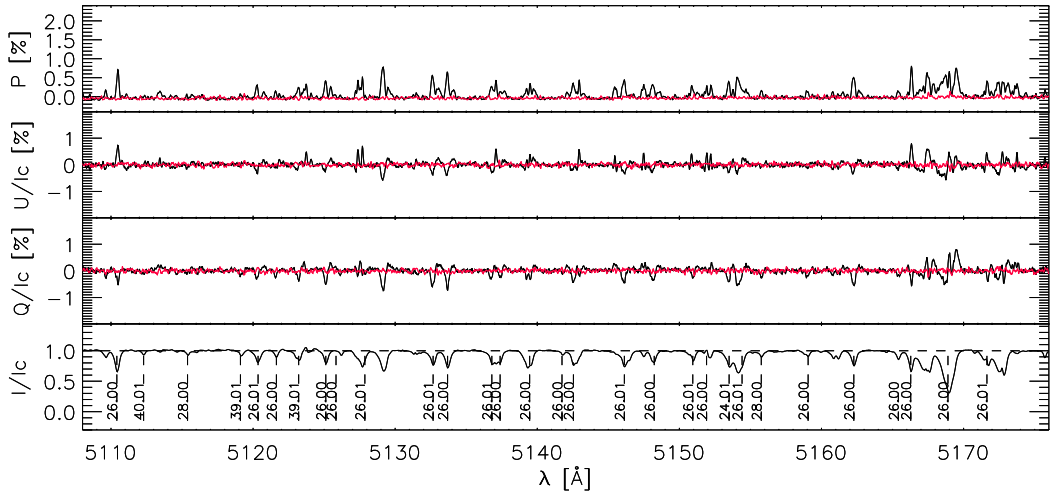
P [%]
U/Ic [%]
Q/Ic [%]
I/Ic
λ [Å]

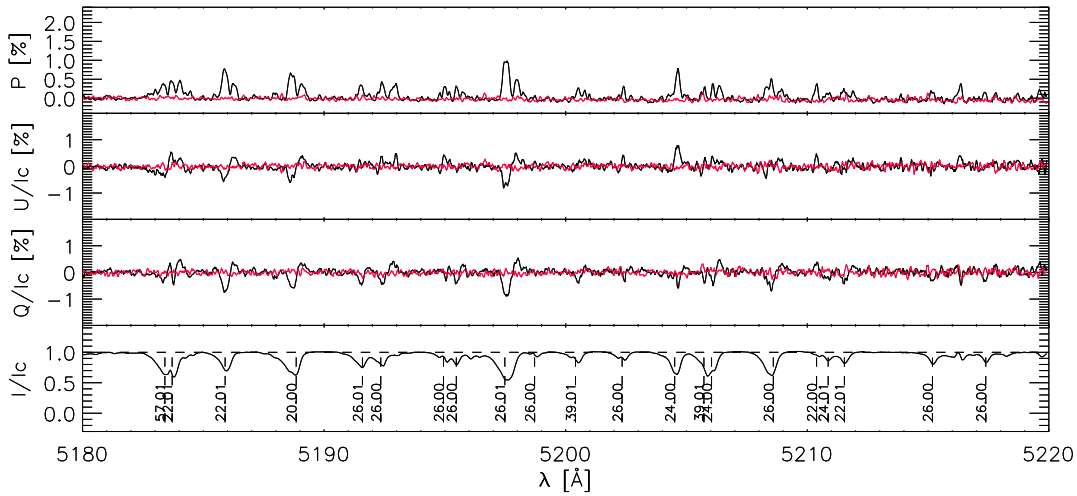
P [%]
U/Ic [%]
Q/Ic [%]
I/Ic
λ [Å]

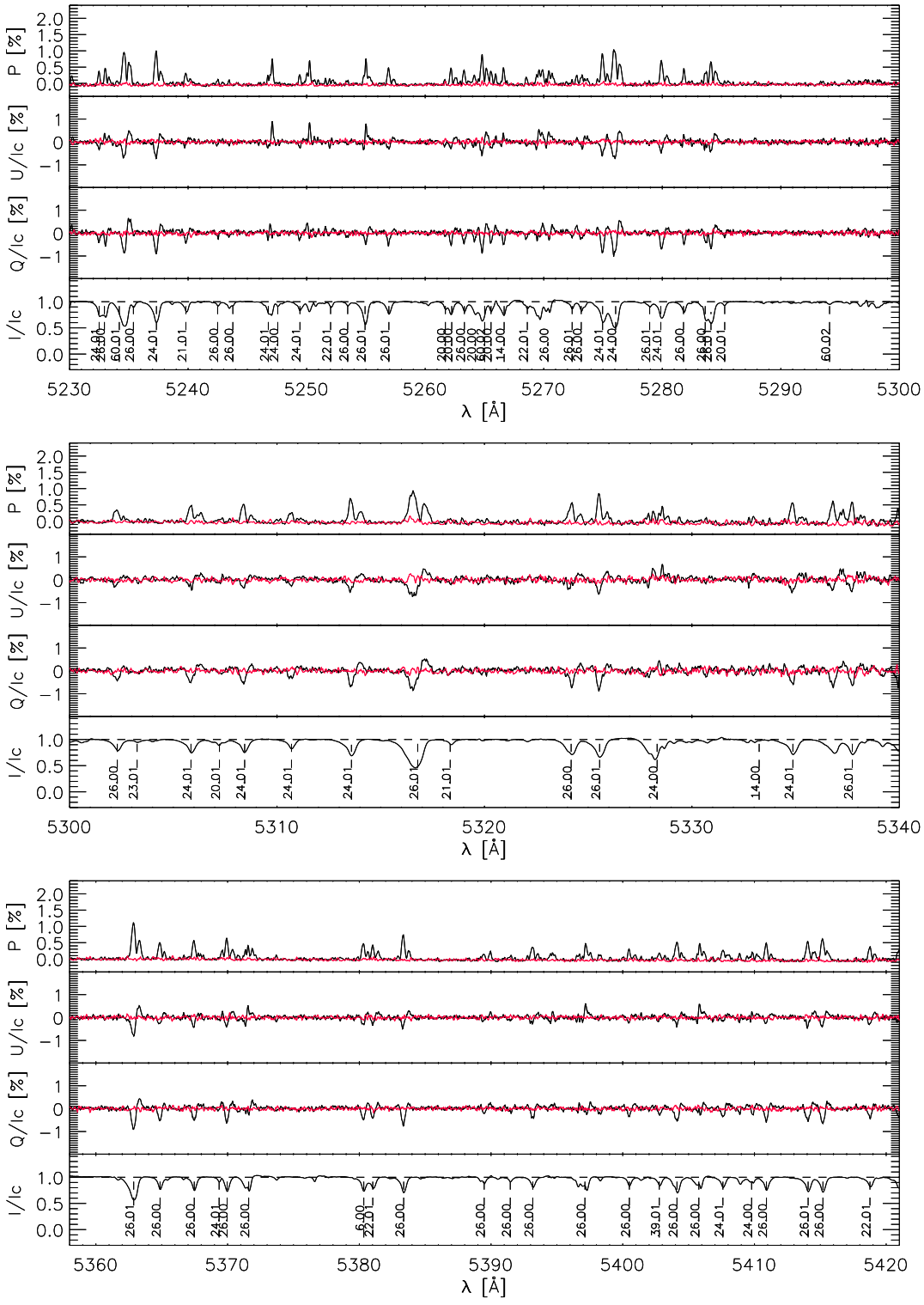
P [%]
U/Ic [%]
Q/Ic [%]
I/Ic
λ [Å]

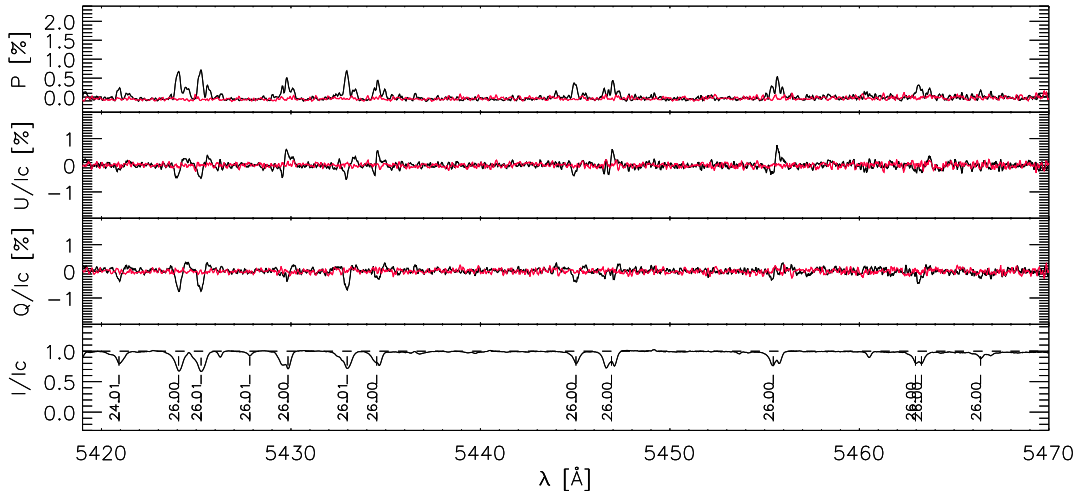
P [%]
U/Ic [%]
Q/Ic [%]
I/Ic
λ [Å]

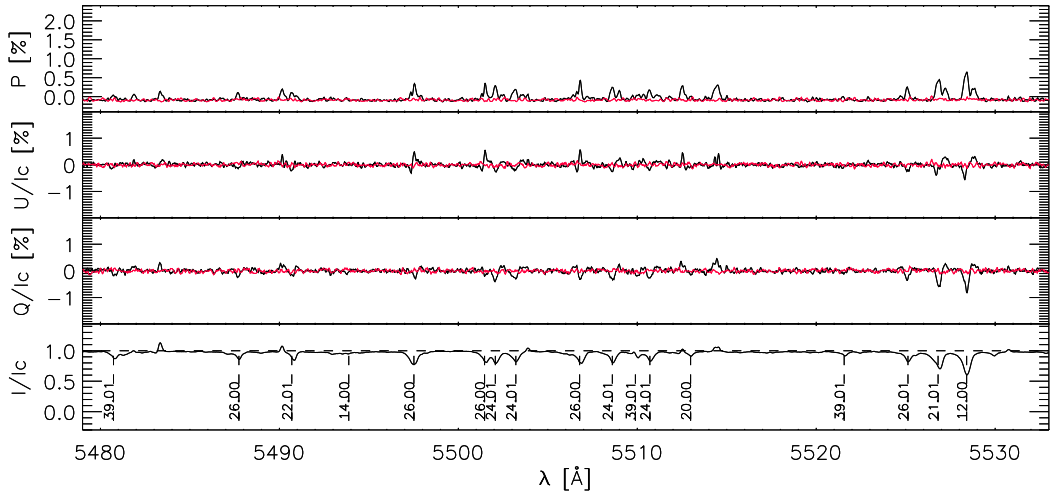
P [%]
U/Ic [%]
Q/Ic [%]
I/Ic
λ [Å]

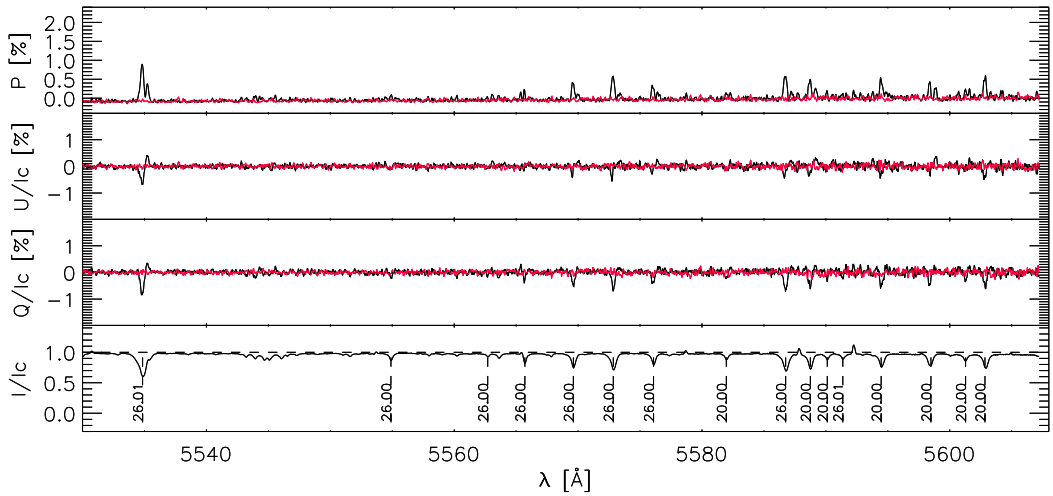
P [%]
U/Ic [%]
Q/Ic [%]
I/Ic
λ [Å]

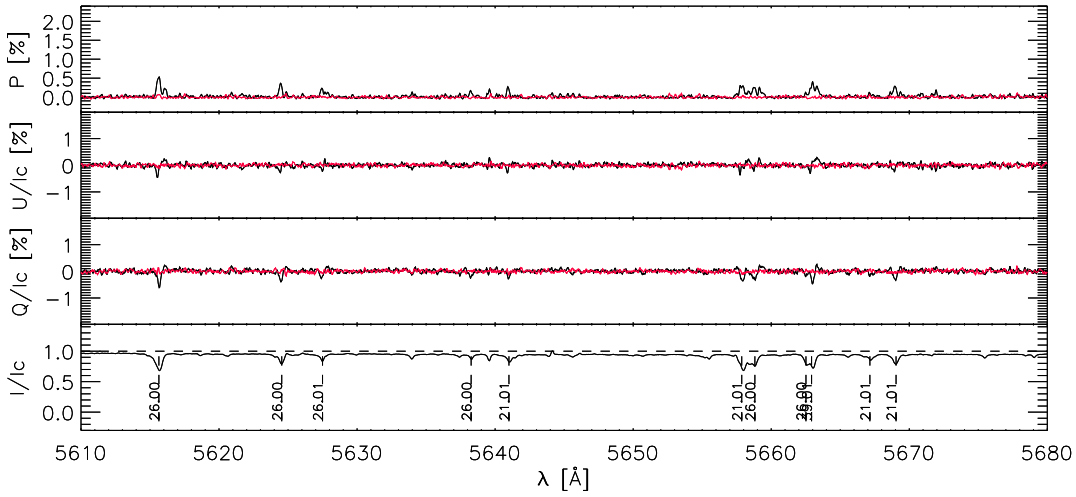
P [%]
U/Ic [%]
Q/Ic [%]
I/Ic
26.00
26.00
26.01
26.00
21.01
21.01
26.00
21.01
21.01
5610
5620
5630
5640
5650
5660
5670
5680
λ [Å]

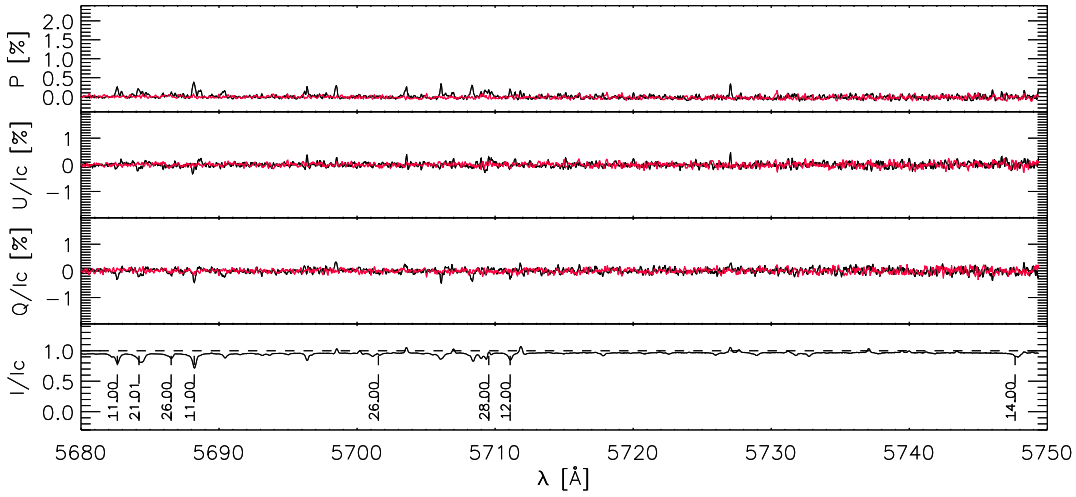
P [%]
U/Ic [%]
Q/Ic [%]
I/Ic
11.00
21.01
26.00
11.00
26.00
28.00
12.00
14.00
5680
5690
5700
5710
5720
5730
5740
5750
λ [Å]

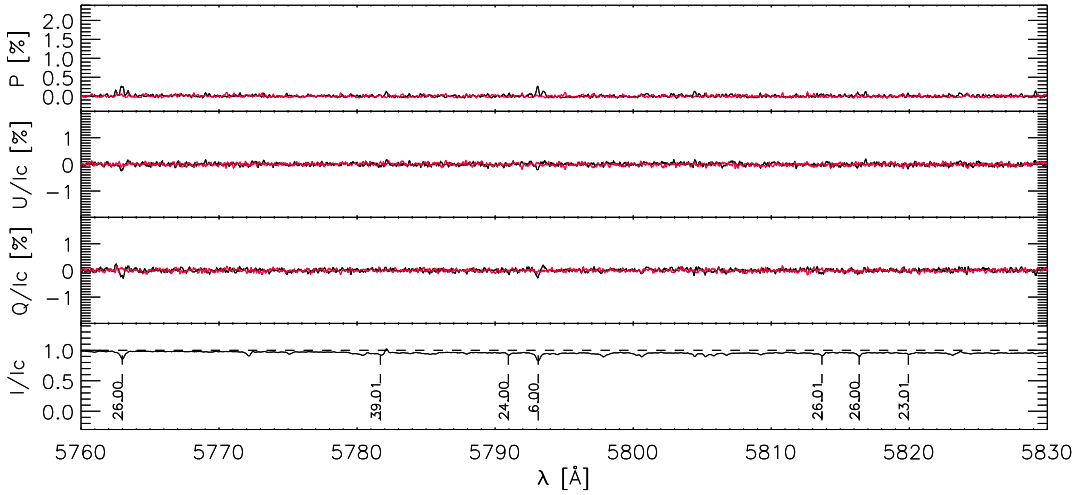
P [%]
U/Ic [%]
Q/Ic [%]
I/Ic
26.00
39.01
24.00
6.00
26.01
26.00
23.01
5760
5770
5780
5790
5800
5810
5820
5830
λ [Å]

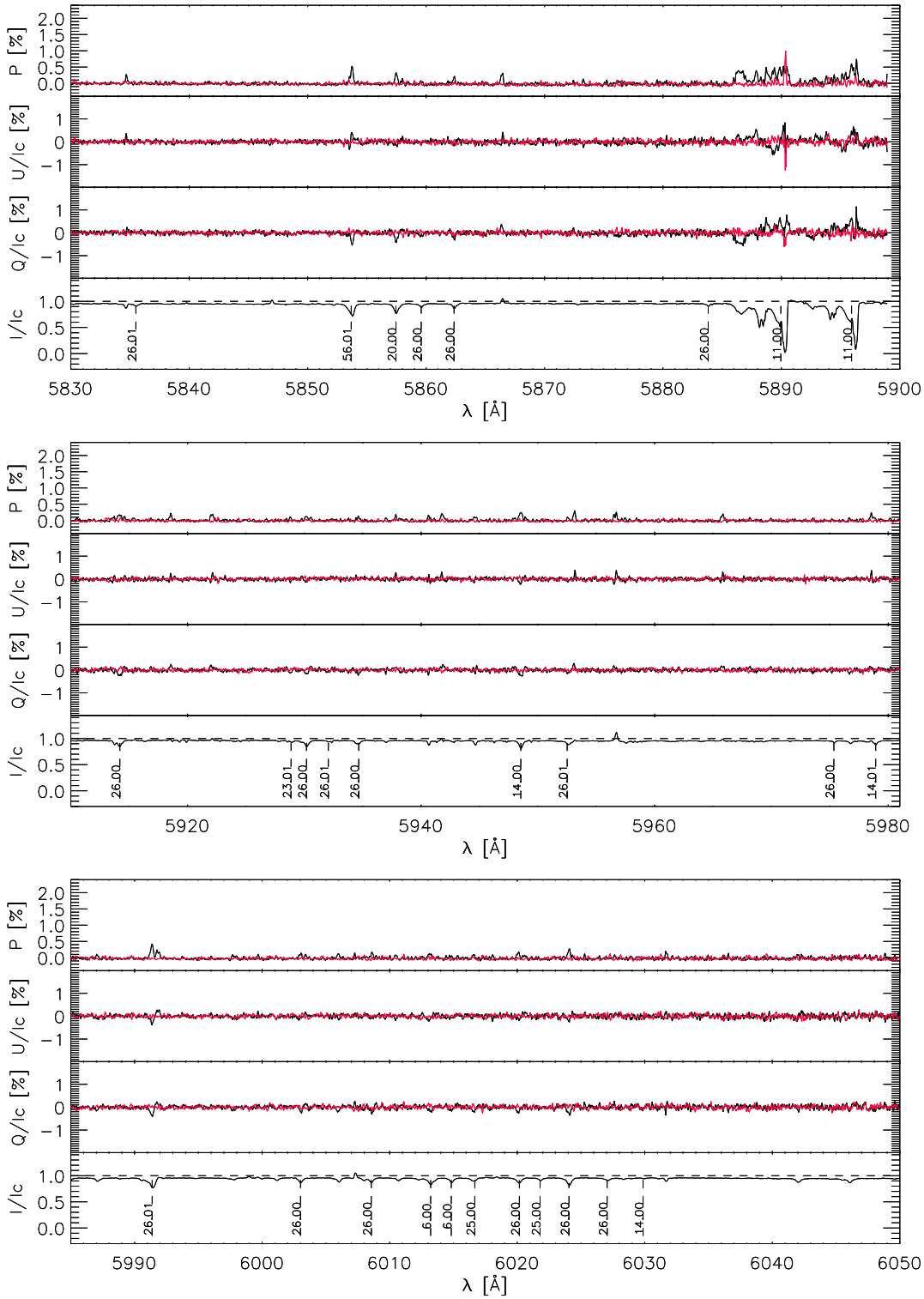
P [%]
U/Ic [%]
Q/Ic [%]
I/Ic
26.01
56.01
20.00
26.00
26.00
26.00
11.00
11.00
λ [Å]
26.00
23.01
26.00
26.01
26.00
14.00
26.01
26.00
14.01
λ [Å]
26.01
26.00
26.00
6.00
6.00
25.00
26.00
25.00
26.00
26.00
14.00
λ [Å]

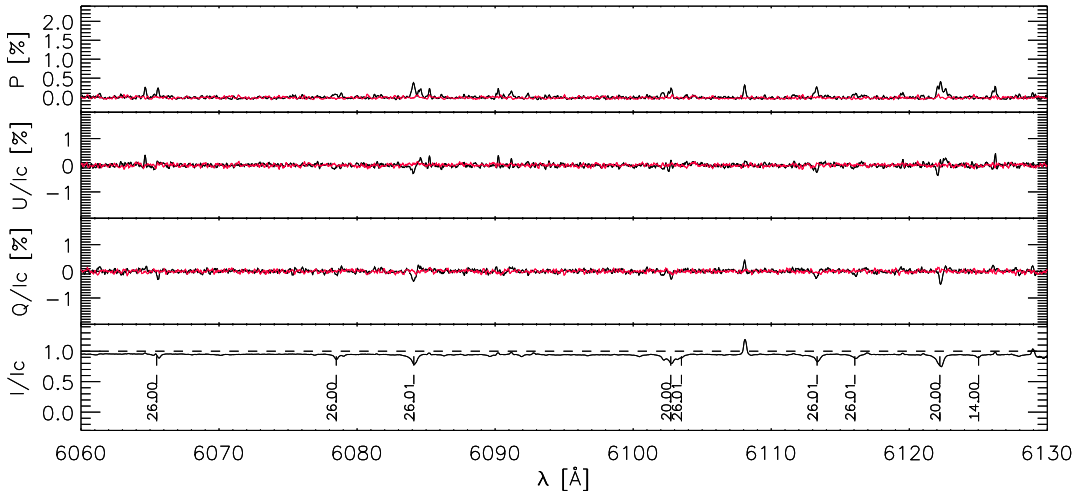
P [%]
U/Ic [%]
Q/Ic [%]
I/Ic
26.00
26.00
26.01
20.00
26.01
26.01
20.00
14.00
6060
6070
6080
6090
6100
6110
6120
6130
λ [Å]

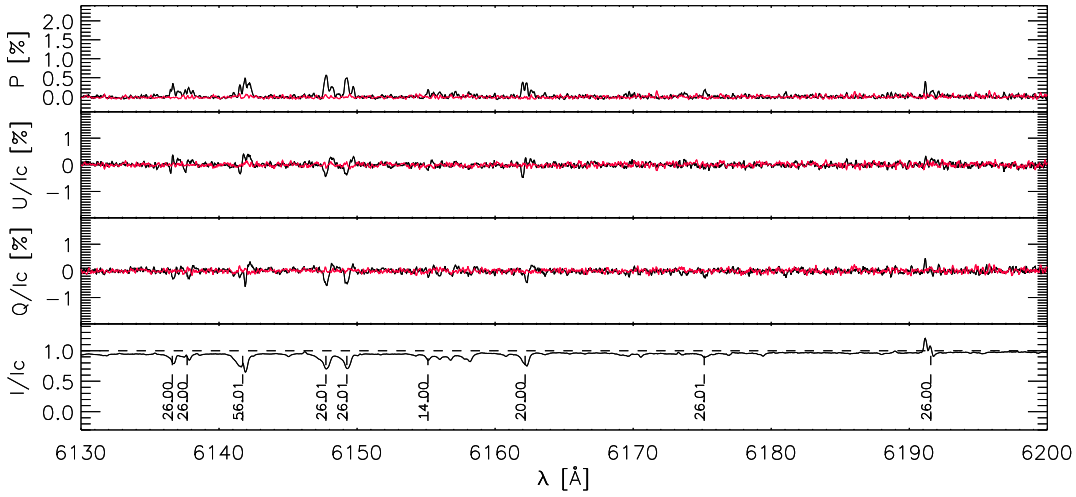
P [%]
U/Ic [%]
Q/Ic [%]
I/Ic
26.00
26.00
56.01
26.01
26.01
14.00
20.00
26.01
26.00
6130
6140
6150
6160
6170
6180
6190
6200
λ [Å]

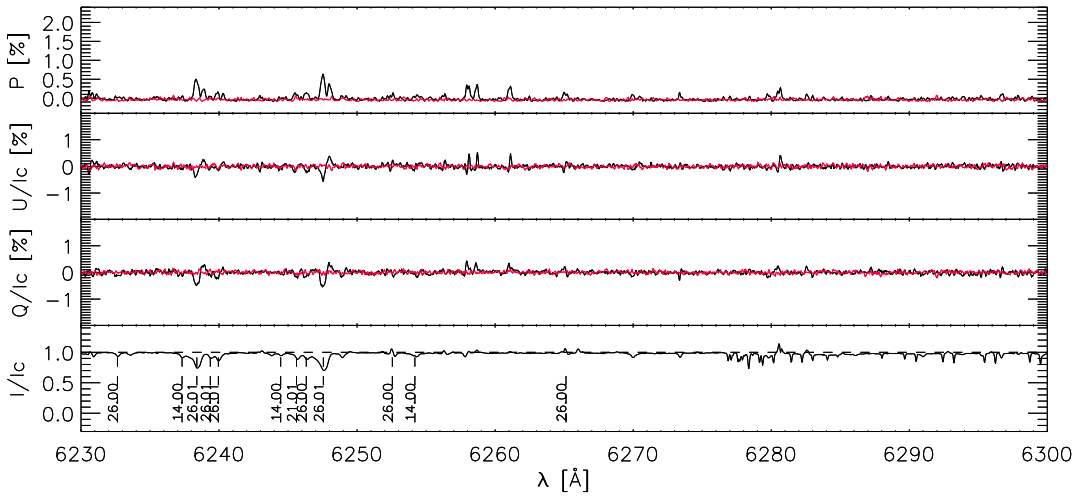
P [%]
U/Ic [%]
Q/Ic [%]
I/Ic
26.00
14.00
26.01
26.01
14.00
21.00
26.01
26.00
14.00
26.00
6230
6240
6250
6260
6270
6280
6290
6300
λ [Å]

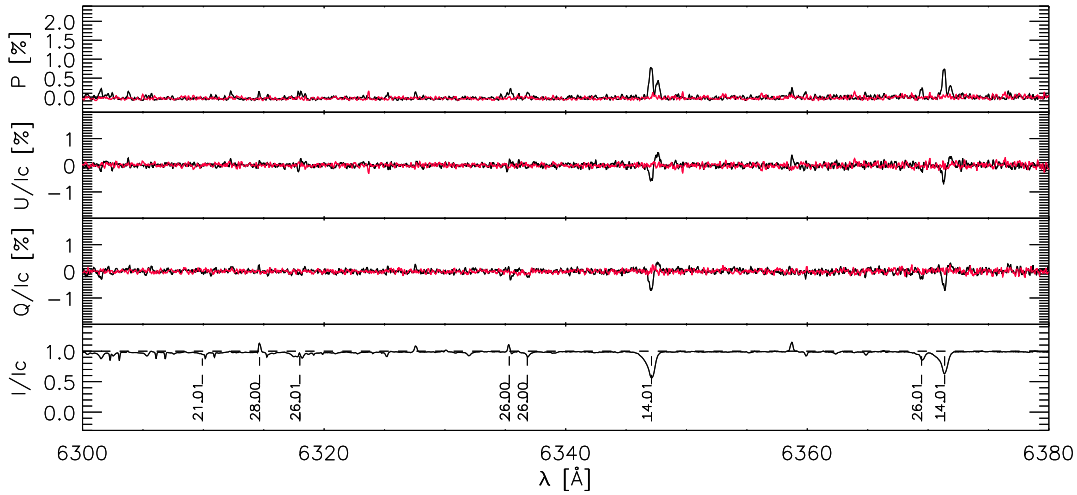
P [%]
U/Ic [%]
Q/Ic [%]
I/Ic
21.01
28.00
26.01
26.00
26.00
14.01
26.01
14.01
6300
6320
6340
6360
6380
λ [Å]

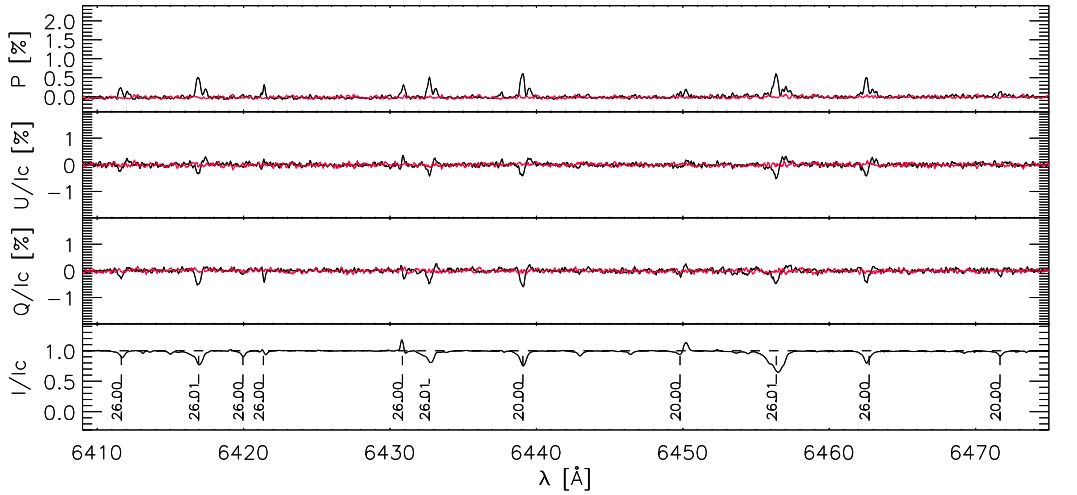
P [%]
U/Ic [%]
Q/Ic [%]
I/Ic
26.00
26.01
26.00
26.00
26.00
26.01
20.00
20.00
26.01
26.00
20.00
6410
6420
6430
6440
6450
6460
6470
λ [Å]

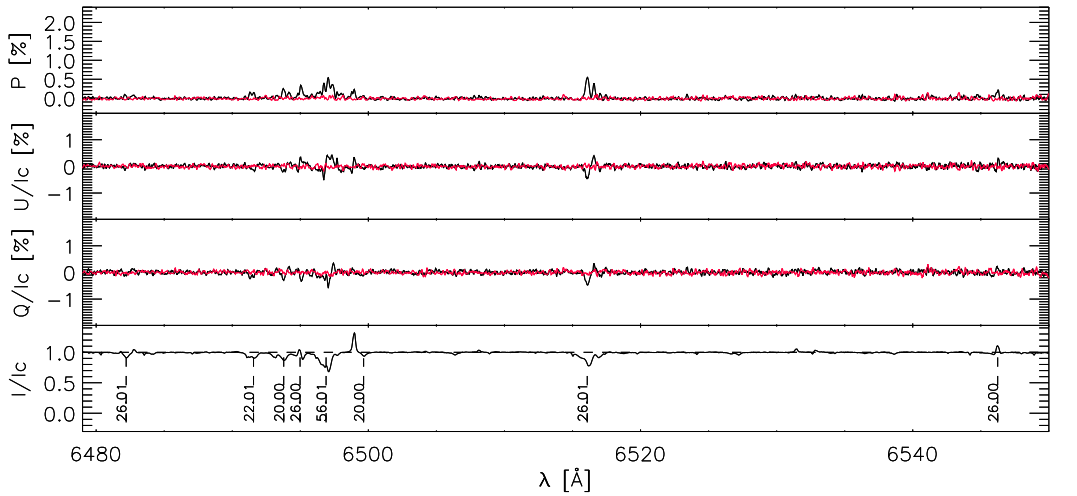
P [%]
U/Ic [%]
Q/Ic [%]
I/Ic
26.01
22.01
20.00
26.00
56.01
20.00
26.01
26.00
6480
6500
6520
6540
λ [Å]

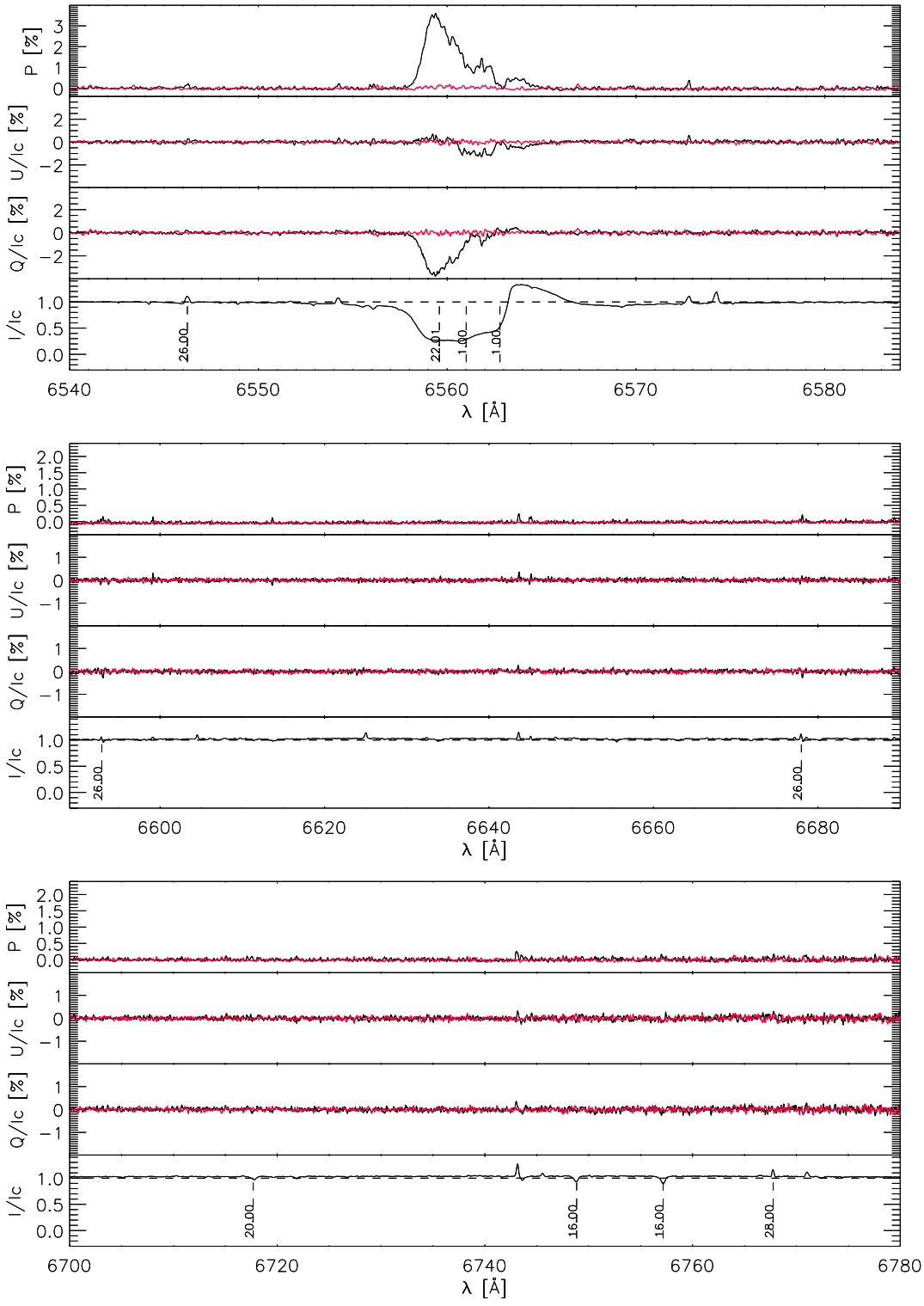
P [%]
U/Ic [%]
Q/Ic [%]
I/Ic
26.00
22.01
1.00
1.00
λ [Å]
26.00
26.00
λ [Å]
20.00
16.00
16.00
28.00
λ [Å]

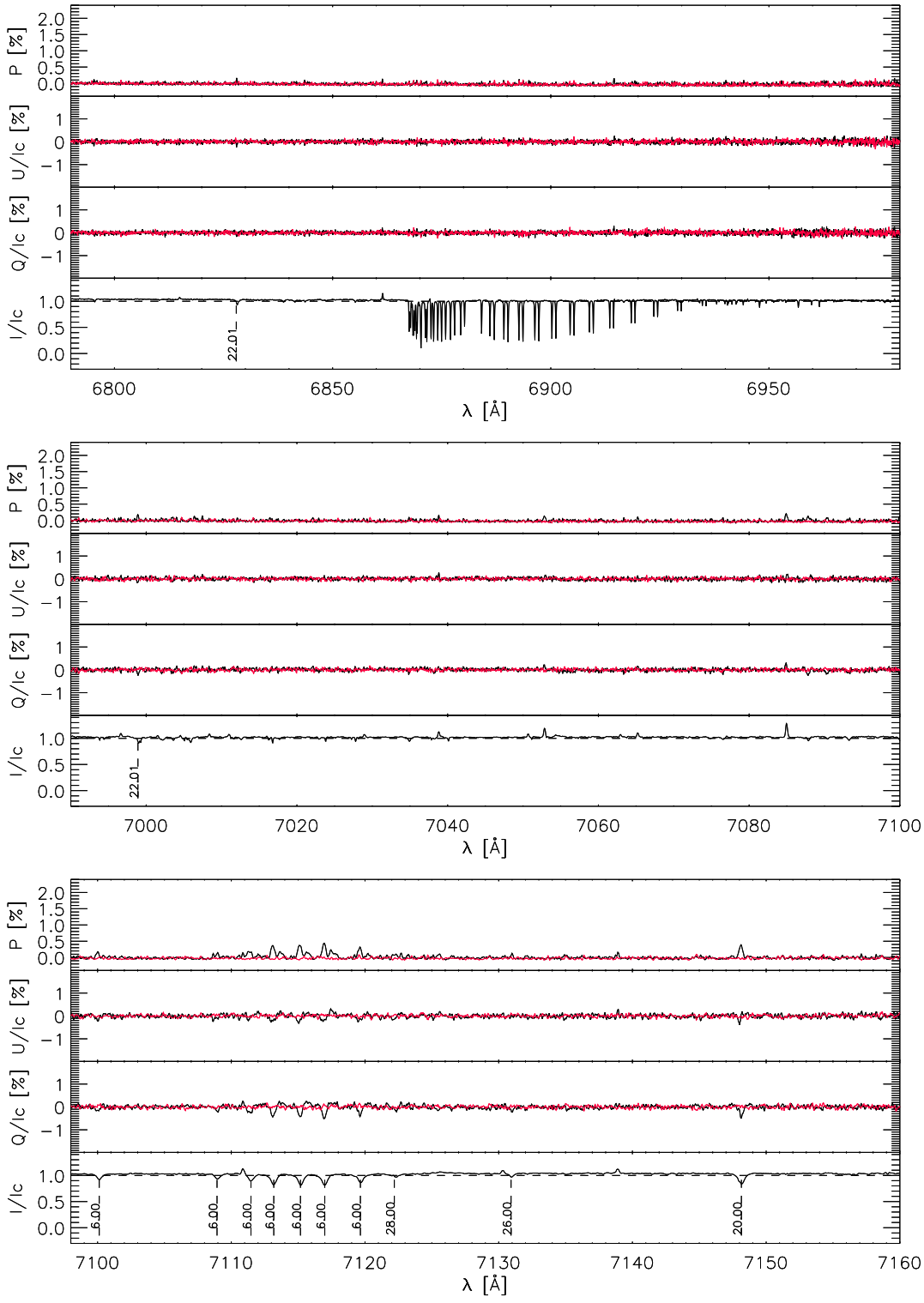
P [%]
U/Ic [%]
Q/Ic [%]
I/Ic
22.01
λ [Å]
6800
6850
6900
6950
7000
7020
7040
7060
7080
7100
7110
7120
7130
7140
7150
7160
6.00
28.00
26.00
20.00

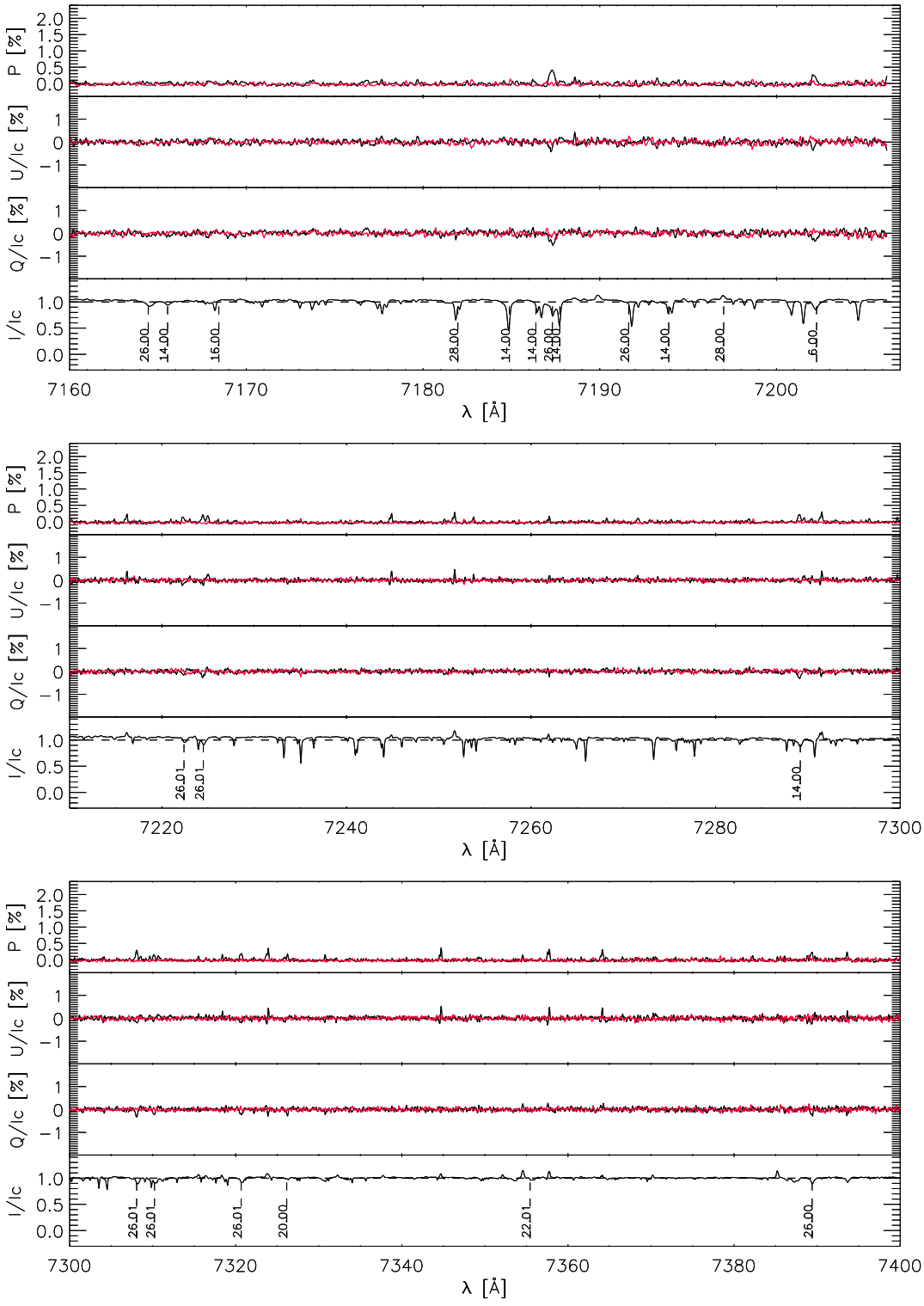
P [%]
U/Ic [%]
Q/Ic [%]
I/Ic
26.00
14.00
16.00
28.00
14.00
14.00
26.00
14.00
26.00
28.00
6.00
7160
7170
7180
7190
7200
λ [Å]
26.01
26.01
14.00
7220
7240
7260
7280
7300
26.01
26.01
26.01
20.00
22.01
26.00
7300
7320
7340
7360
7380
7400

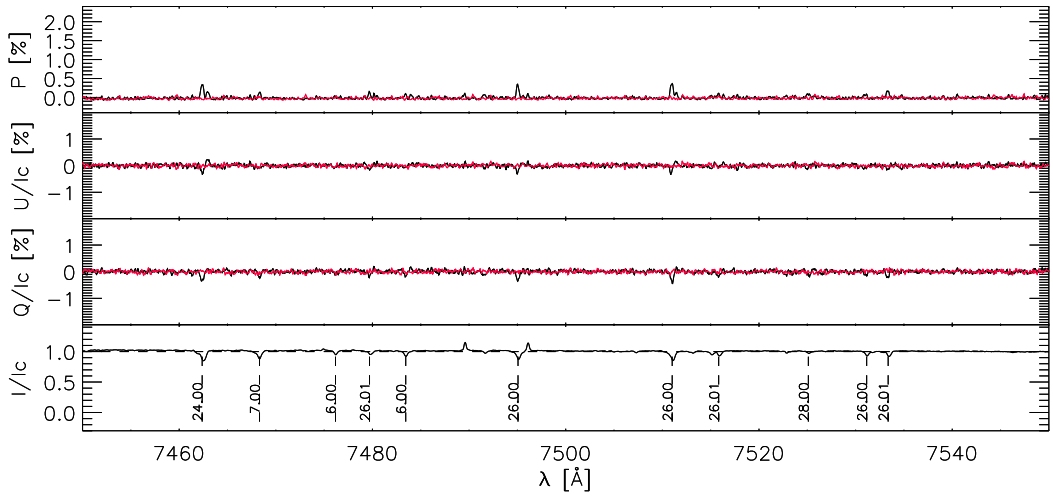
P [%]
2.0
1.5
1.0
0.5
0.0
U/Ic [%]
1
0
−1
Q/Ic [%]
1
0
−1
I/Ic
1.0
0.5
0.0
24.00
7.00
6.00
26.01
6.00
26.00
26.00
26.01
28.00
26.00
26.01
7460
7480
7500
7520
7540
λ [Å]

A.2 The Stokes Code

The STOKES computer program (Marin et al. 2012, Goosmann et al. 2014) is a Monte Carlo radiative transfer code for modeling multi-wavelenght polarisation, designed to model astrophysical objects of various geometries and considers polarisation induced by electrons and dust scattering. Here we present an overview of the program, the particular implementation and the tests we have conducted for our purpose.

A.2.1 General overview

The STOKES code follows single photons from their generation inside emission and/or absorption regions through various scattering processes until they become absorbed or manage to escape from the model region. In the latter case photons are registered by a web of virtual detectors arranged in a spherical geometry (Figure A.1). The emission and scattering regions can be realized in cylindrical, toroidal, double-cone, spherical and flared-disk geometries (Figure A.2). For the emission, the flux spectrum of the continuum radiation can be defined as a power law $F(\nu) \propto \nu^{-\alpha}$ with spectral index α, while line photons are sampled with a Lorentzian emission profile. The scattering regions can be filled with free electrons or with dust particles and accurate algorithms for Thomson and dust scattering are used for the radiative transfer calculation. Intrinsically, line and continuum photons are assumed to be unpolarised. During the photon's journey the flux and polarization information is obtained by adding up the Stokes parameters.

The STOKES code is written in C^{++} and it is composed by different *routines*. Each of these deals with a specific aspect of the problem. The photon is generated by the *source-routine*. If it is generated inside a scattering region, the *proceed-routine* shifts the photon by a path-length that is sampled using the Monte Carlo method. If the photon does not leave the cloud, which is checked by the *inside-cloud-routine*, a scattering event is simulated by the *dust-scattering-routine* or by the *electron-scattering-routine*. In case of dust scattering the routine might set up the absorpition flag, hence destroy it, and make the cycle start over by creating a new photon inside the source region. If the photon leaves the scattering region or if it was not generated within one, the *shift-routine* detects any other scattering region along its flight direction. If there is another scattering cloud, the photon moves to the cloud's border, and the *proceed-routine* takes over again. If there is no further scattering cloud on the way, the photon escapes from the model region and, finally, it is detected by the *register-routine*.

In Figure A.3 a flowchart presents a schematic execution of the program.

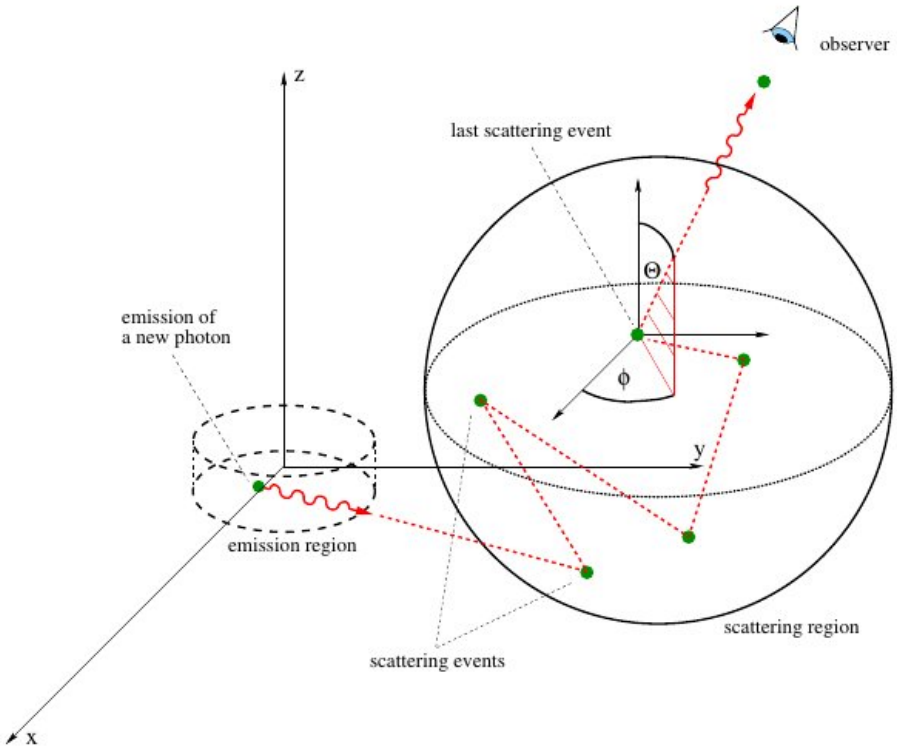

Fig. A.1.: A photon's journey from its emission point toward scattering processes and its final recording by a virtual detector.

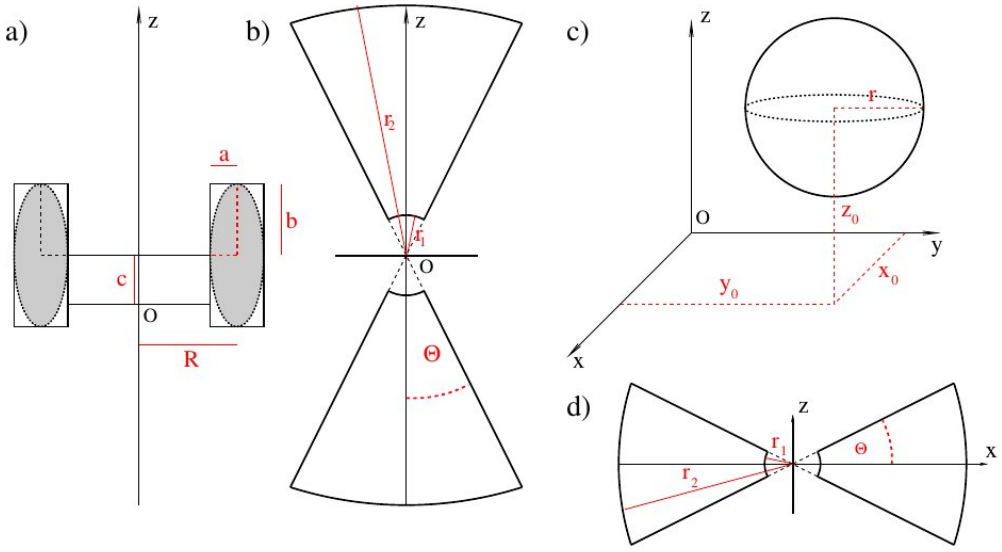

Fig. A.2.: Different geometries of emission and scattering regions implemented in *STOKES*.

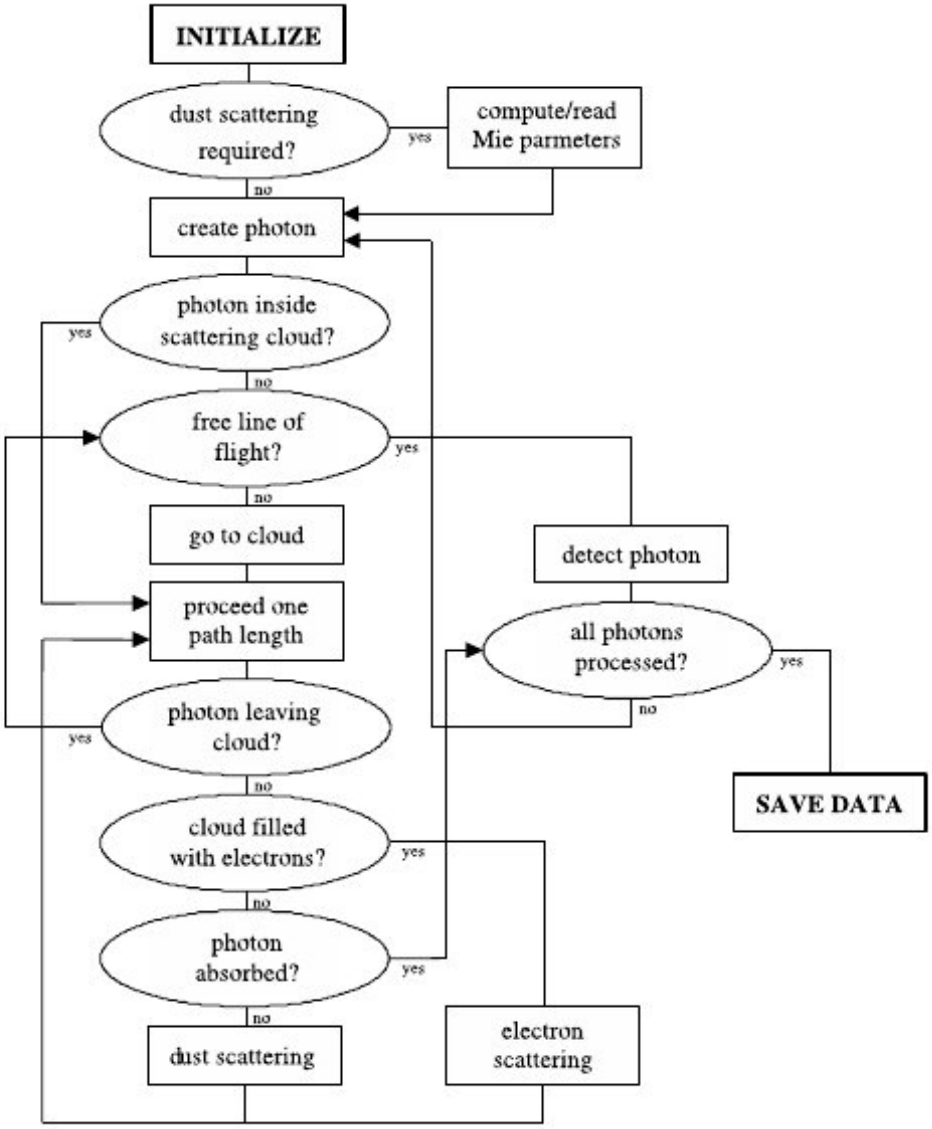

Fig. A.3.: Flowchart showing the execution of *STOKES*.

A.2.2 Implementation for line in absorption

To perform numerical tests with the STOKES code to investigate the role of scattering polarisation in spectral lines in absorption we need, as input, an absorption profile. For this reason we have modified the *source-routine* by introducing an algorithm capable of sampling an observed line in absorption (Fig. A.5). The problem is, therefore, how to contrive a Monte Carlo sampling of a discrete variable (as can be an absorption line). To do that, we follow the subsequent mathematical approach:

considering a random variable X, the *cumulative probability function* is defined as a function that associates the probability of the event to each X value

$$F(X) : \mathbb{R} \longrightarrow [0, 1] \tag{A.1}$$

with

$$F(X) \geq 0 \quad \forall X \tag{A.2}$$

$$\lim_{X \to +\infty} F(X) = 1, \quad \lim_{X \to -\infty} F(X) = 0. \tag{A.3}$$

If X is a *discrete* random variable, then F(X) is a *step function* (Fig. A.4). Referring to Fig. A.4, P_i represent the cumulative probability relative to X_i; graphically it is represented by the length of the vertical segments.

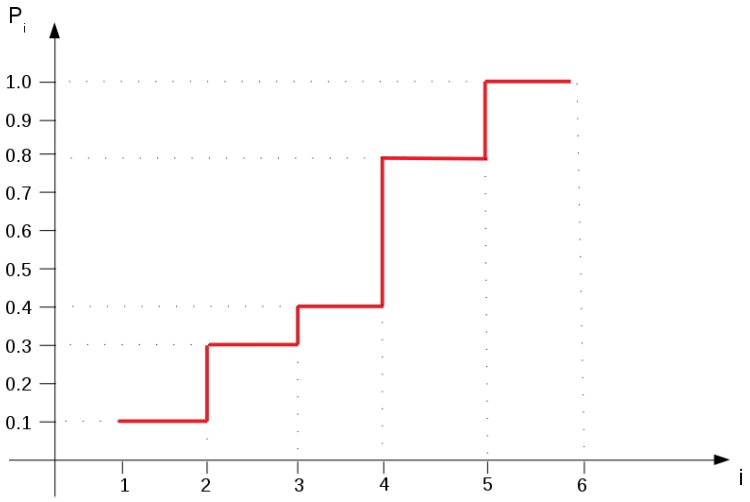

Fig. A.4.: Example of step function. P_i represent the cumulative probability relative to X_i.

Considering a random variable X that can assume the discrete values $\{x_i\}$, $i = 1, 2, ...$ n with probability $\{p_i\}$, if we extract a random number with uniform distribution in $[0, 1]$, it will fall into the i^{th} segment with probability equal to its length (i.e. p_i).

We define, now, the *cumulative probability* as

$$P_0 = 0 \quad P_i = \sum_{k=1}^{i} p_k \quad i = 1, 2, ...n \tag{A.4}$$

and from the uniform distribution in $[0, 1]$ we generate a random number η. Finally we determine the integer i such that

$$P_{i-1} \leq \eta \leq P_i \tag{A.5}$$

the corresponding x_i will be the sampled value for the random variable X.

In A.6 we show some numerical tests with the FeII 5018.4358 Å pure absorption line and with the H_α 6562.83 Å PCygni-like profile of 89 Herculis star.

```
// READING INPUT TO BE SAMPLED (i.e. observed line profile)
    #define MAXR 1000
double mat[MAXR] [2];

ifstream dati("input_sampling.txt");
int k=0;
while(!dati.eof())
  {
    dati >> mat[k][0] >> mat[k][1];
    k++;
  }
dati.close();

int dimensione = k;

//MAXIMUM INTENSITY DETERMINATION
double massimo = mat[0][1];

  for(i=0; i<dimensione; i++) {
    if (mat[i][1]>massimo) {
      massimo=mat[i][1];
    }
  }

//NORMALIZATION
  for(i=0; i<dimensione;i++){
    mat[i][1]=mat[i][1]/massimo;
  }

    //CALCULATION OF CUMULATIVE PROBABILITIES
  double pc[dimensione];
    for(k=0;k<dimensione;k++){
      pc[k]=0;
      for(i=0;i<k;i++){
       pc[k]=mat[i][1]+pc[k];
    }
  }

//NORMALIZATION OF CUMULATIVE PROBABILITIES
    for(i=0; i<dimensione;i++){
   pc[i]=pc[i]/pc[dimensione-1];
  }
```

Fig. A.5.: Part of the implemented code.

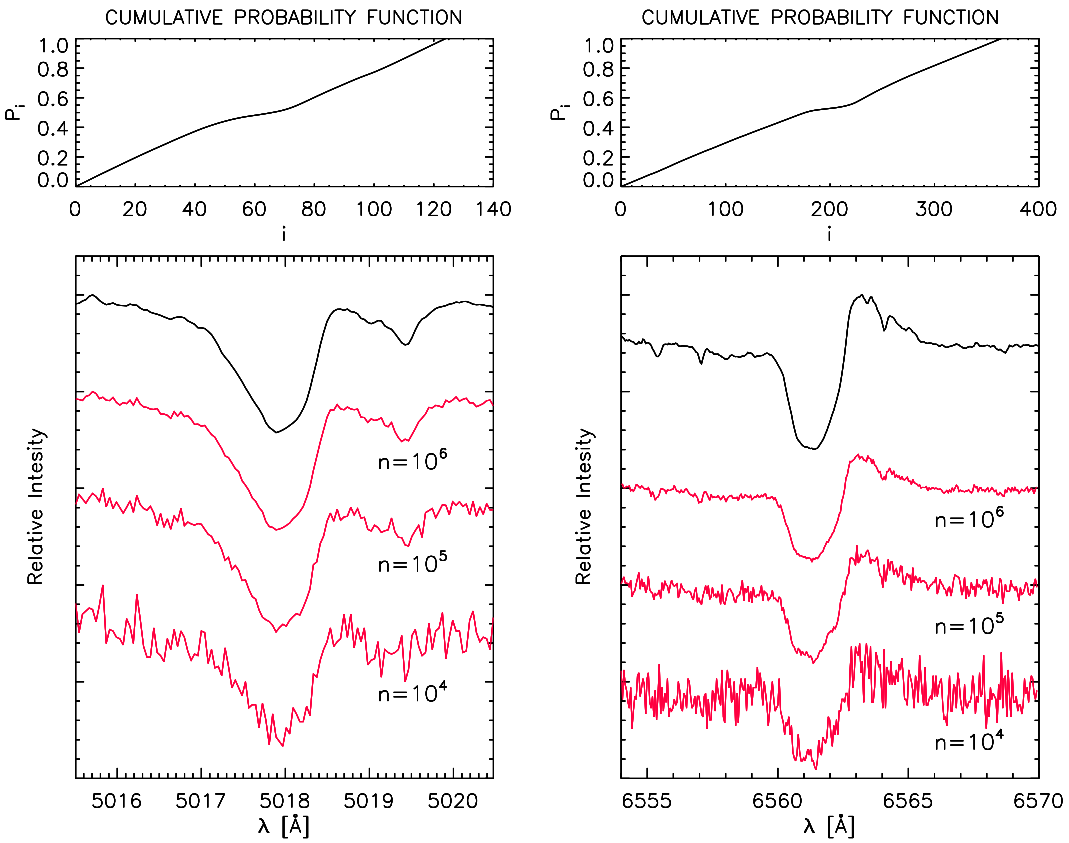

Fig. A.6.: Numerical tests of the STOKES implemented code using the FeII 5018.4358 Å pure absorption line (left) and the H_α 6562.83 Å PCygni-like profile (right). Top panel: cumulative probability function. Bottom panel: in black the observed profile, in red the corresponding Monte Carlo sampled profiles by using different number of random points n, uniformly distributed in $[0, 1]$. A good result is obtained with $n = 10^6$ points. Profiles were arbitrarily shifted along the y-axis for clarity.

A.2.3 Lines in emission

In the case of lines in emission, photons are sampled with a Lorentzian profile. We have modelled a flared illuminated disk, to investigate the role played by its geometrical and physical properties. As a general rule, we found that the morphologies of Stokes parameters are strongly influenced by the disk velocity field while the intensity depend on the density and on the disk opening angle. The viewing direction plays a crucial role in determining both the intensity and the morphology of Stokes parameters. Moreover there is a marked difference between scattering by a disk with and without an inner hole.

This demonstrate the diagnostic potential of spectropolarimetry in determining the disk dynamics.

Varying the velocity field

Fig. A.7 shows the triplots of the polarisation spectra for a 30° opened undisrupted disk with different velocity fields, seen at $\theta = 32^\circ$ and at $\theta = 81^\circ$.

The presence of a pure rotational velocity field (top panel of Fig. A.7) leads to a Stokes Q profile consisting of an emission central lobe and two absorption symmetric wings. The increase of velocity causes an increase of the intensity and a broadening of the Stokes Q and I profiles. We also note that when the viewing direction lies within the disk aperture (case $\theta = 81^\circ$) there is an increase of the broadening for the Stokes Q profile and a decrease of broadening for the Stokes I profile, compared to the case of an off-disk viewing direction ($\theta = 32^\circ$).

In the case of a pure expanding or inflating disk (middle and bottom panel of Fig. A.7) we obtain null Stokes profiles for off-disk viewing direction. On the contrary, when the viewing direction is within the disk aperture, we obtain a bi-lobed Stokes Q profile with amplitude increasing with the velocity.

Finally, in the case of an expanding rotational disk (Fig. A.8) the Stokes profiles correspond to a convolution between the morphologies obtained in the two previous cases.

Varying density and opening angle

The disk opening angle and the electron density only modify the degree of polarisation and the intensity of the Stokes I; these parameters do not alter the morphology of Stokes profile.

In Fig. A.9 we show the total polarisation calculated across the emission line for a rotating disk with different opening angles. As a general behaviour, we notice how the degree of polarisation decreases as the disk aperture angle increases. This is understandable, because as the angle increases there is a greater geometrical symmetry.

In Fig. A.10 we show the total polarisation calculated across the emission line for a rotating disk with different electron density. Here the degree of polarisation decreases as the electron density increases. This is understandable considering the fact that as the density increases, the intensity of the line decreases due to greater absorption. Also in this case we notice how the viewing direction can alter this trend.

Polarisation from undisrupted and inner hole disks

The presence of a gap between the line source and the disk leads to a decrease of linear polarisation. However such difference tends to reduce with increasing view angles.

Fig. A.11 shows the ratio ξ between polarisation from scattering by undisrupted disk and by disk with inner hole versus θ view angles for different disk opening angles α. There is a marked increase of ξ with decreasing α and, for fixed α, ξ decrease with θ. Moreover when the line of sight is within the disk aperture, ξ falls to unit, i.e. there is no more difference between undisrupted disk and disk with inner hole.

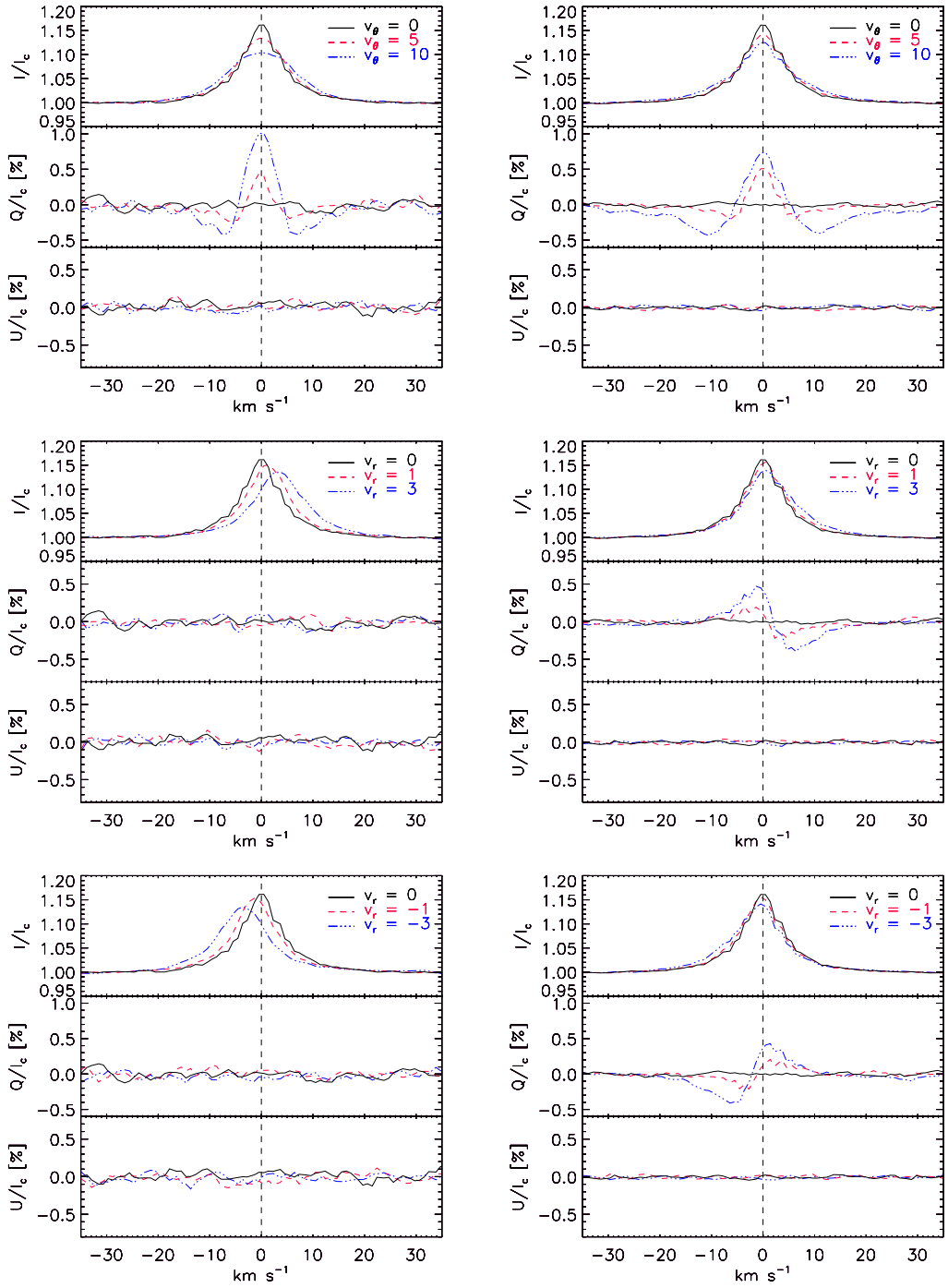

Fig. A.7.: Triplots of the polarisation spectra for a $30°$ opened undisrupted disk with different velocity field, seen at $\theta = 32°$ (left column) and $\theta = 81°$ (right column). Velocities are expressed in $km\ s^{-1}$. Top panel: pure rotational velocity field; middle and bottom panel: pure radial velocity field. Other parameters are: disk radius $R = 2AU$, electron density $n_e = 10^{10}\ cm^{-3}$.

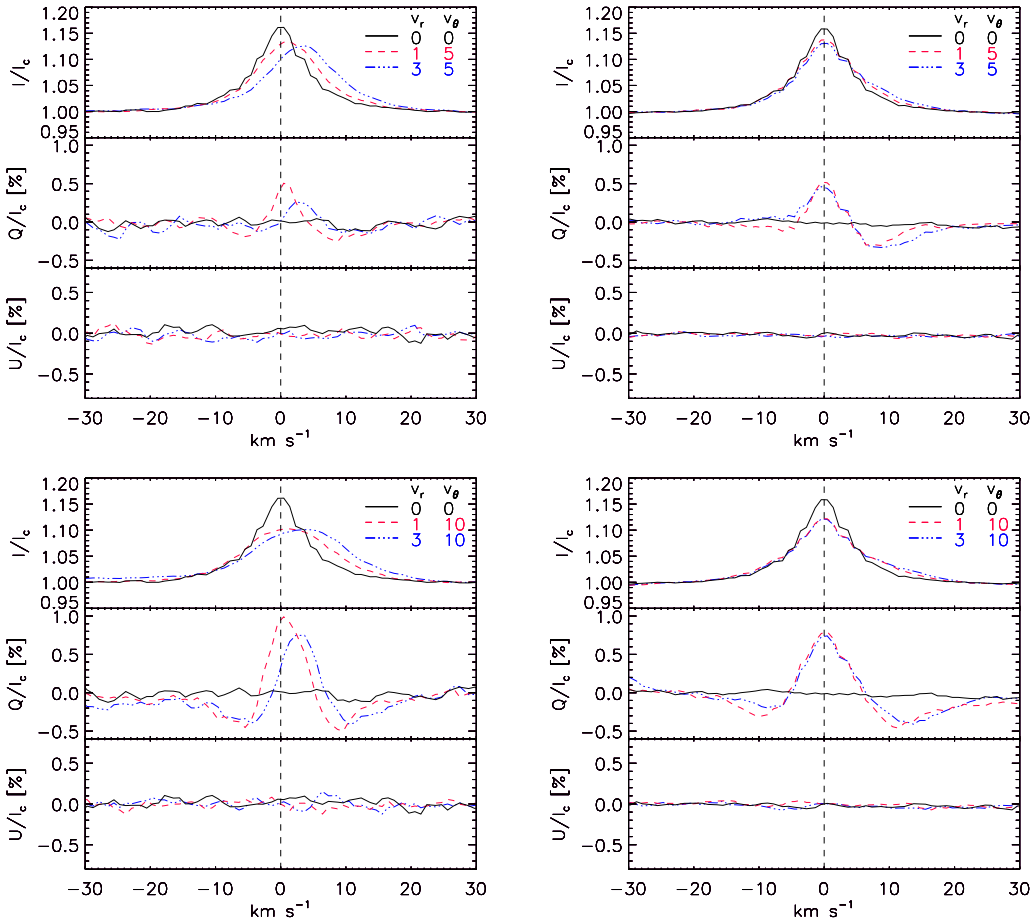

Fig. A.8.: Triplots of the polarisation spectra for a $30°$ opened expanding rotational undisrupted disk with different velocity field intensities, seen at $\theta = 32°$ (left column) and $\theta = 81°$ (right column). Velocities are expressed in $km\ s^{-1}$. Other parameters are: disk radius $R = 2AU$, electron density $n_e = 10^{10}\ cm^{-3}$.

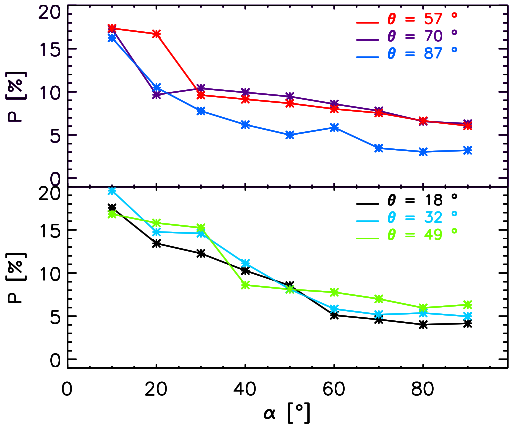

Fig. A.9.: Integrated polarisation for a rotating undisrupted disk versus disk opening angles for different θ view angles. Disk parameters are: disk radius $R = 2AU$, electron density $n_e = 10^{10}\ cm^{-3}$.

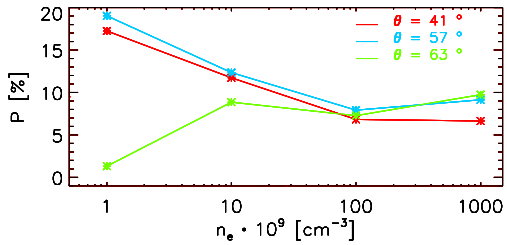

Fig. A.10.: Integrated polarisation for a rotating undisrupted disk versus disk electron densities for different θ view angles. Disk parameters are: disk radius $R = 2AU$, aperture angle $\alpha = 30°$.

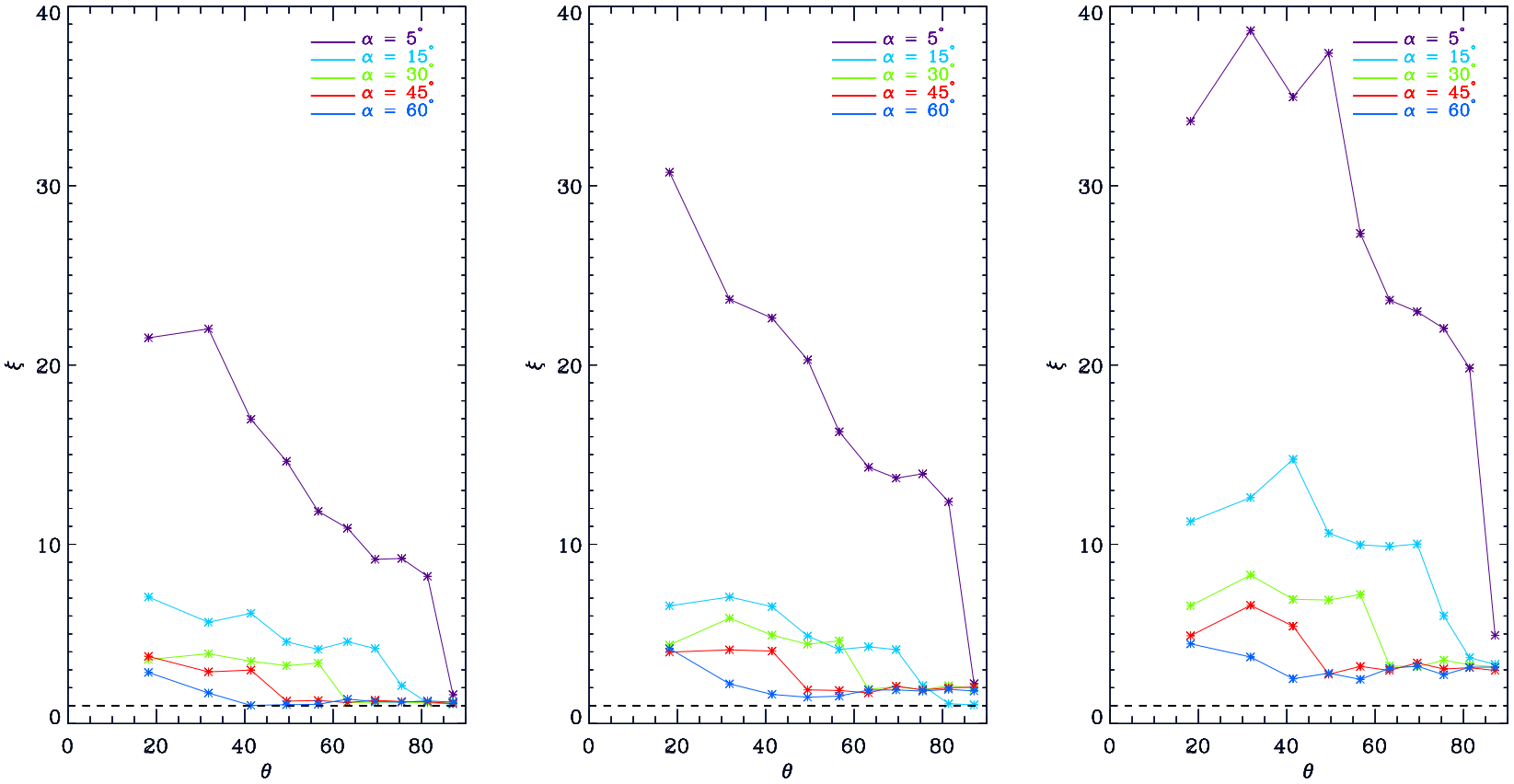

Fig. A.11.: ξ ratio between total polarisation from scattering by undisrupted disk and by disk with inner hole versus θ view angles fro different disk opening angles. Left: $R_{int}/R_{ext} = 0.1$. Center: $R_{int}/R_{ext} = 0.5$. Left: $R_{int}/R_{ext} = 0.75$.

A.3 The Hazel Code

The HAZEL (HAnle and ZEeman Light, Asensio Ramos et al. 2008) code is a computer program based on the quantum theory of spectral line polarisation. It is able to calculate Stokes profiles considering the all relevant polarisation mechanisms, such as optical pumping, atomic level polarisation, Zeeman, Paschen-Back and Hanle effect.

Here we present an overview of the program and the implementation used in our work.

A.3.1 General overview

HAZEL code consider a constant-property slab of atoms located at a height h above the stellar surface. It is possible to model a magnetic field, according to the geometry shown in Fig. A.12. All the atoms inside the slab, with a proper atomic model, are illuminated from below by the photospheric continuum anisotropic radiation. The atomic level polarisation and the presence of a magnetic field, produce polarisation in the emergent spectral line radiation.

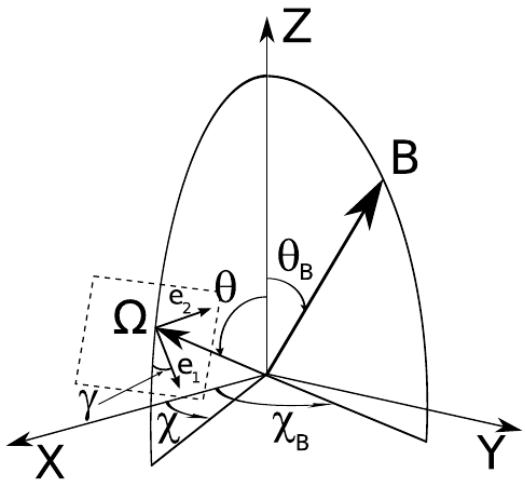

Fig. A.12.: The geometry for the scattering event. The Z-axis is placed along the vertical to the stellar atmosphere. The magnetic field vector, B, is expressed by its modulus, the inclination angle θ_B and the azimuth χ_B. The line-of-sight, indicated by the unit vector Ω, is defined by two angles, θ and χ. The reference direction for Stokes Q is defined by the vector e_1 on the plane perpendicular to the line-of-sight. This vector makes an angle γ with respect to the plane formed by the vertical and the line-of-sight.

After reading the configuration files, which define the anisotropy of the radiation field, the topology and intensity of the magnetic field and the atomic model, the code solves the statistical equilibrium equations to calculate the multipolar components of the atomic density matrix ${}^{\beta LS}\rho^K_Q(J,J')$. The latter are expressed using the spherical statistical tensor representation (Landi Degl'Innocenti & Landolfi 2004). The statistical equilibrium equations take into account: (1) the influence of the magnetic field on the atomic level polarisation, (2) the coherence transfer due to absorption from lower levels, (3) the spontaneous emission from upper levels, (4) the stimulated emission from upper levels, (4) the relaxation of coherences due to absorption to upper levels, (5) spontaneous emission to lower level and (6) the stimulated emission to lower levels.

The anisotropic properties of the radiation field, that plays a crucial role in the statistical equilibrium equations, are expressed through the spherical component of the radiation field tensor:

$$J^K_Q(\nu) = \oint \frac{d\Omega}{4\pi} \sum_{i=0}^{3} \mathrm{T}^K_Q(i,\Omega) S_i(\nu,\Omega), \tag{A.6}$$

where $\mathrm{T}^K_Q(i,\Omega)$ are spherical tensors that depend on the reference frame and on the ray direction Ω.

Once the multipolar components ${}^{\beta LS}\rho^K_Q(J,J')$ are known, the coefficients ϵ_I and ϵ_X (with $X = Q,U,V$) of the emission vector and the coefficients η_1, η_X, and ρ_X of the propagation matrix for a given transition between an upper term ($\beta L_u S$) and a lower term ($\beta L_l S$) can be calculated with the Eq. 7.6.b in Landi Degl'Innocenti & Landolfi (2004), here not reported for simplicity.

Finally, we have all the ingredients to solve the radiative transport equation:

$$\frac{d\bar{I}}{d\tau} = \bar{K}^* \bar{I} - \bar{S}, \tag{A.7}$$

with:

$$d\tau = -\eta_I ds \tag{A.8}$$

$$\bar{K^*} = \frac{\bar{K}}{\eta_I} \tag{A.9}$$

$$\bar{K} = \begin{Bmatrix} \eta_I & \eta_Q & \eta_U & \eta_V \\ \eta_Q & \eta_I & \rho_V & -\rho_U \\ \eta_U & -\rho_V & \eta_I & \rho_Q \\ \eta_V & \rho_U & -\rho_Q & \eta_I \end{Bmatrix} \tag{A.10}$$

$$\bar{I} = \begin{Bmatrix} I \\ Q \\ U \\ V \end{Bmatrix} \quad \bar{S} = \begin{Bmatrix} \frac{\epsilon_I}{\eta_I} \\ \frac{\epsilon_Q}{\eta_I} \\ \frac{\epsilon_U}{\eta_I} \\ \frac{\epsilon_V}{\eta_I} \end{Bmatrix}. \tag{A.11}$$

A.3.2 The implemented atomic model

It is assumed that the atom can be correctly described under the framework of the L-S coupling. Moreover the code neglect the influence of hyperfine structure and assume that the energy separation between the J-levels pertaining to each term is very small compared with the energy difference between different terms.

For our purpose, we have modeled the Fe II 4508.288 Å line. Atomic data are from NIST database and shown in Tab. A.1.

Fig. A.13 shows the implementation of the atomic model we have made in the code. Referring to this figure, the first two numbers define the general properties of the atom. In particular, the first is equal to $2S$ (with S the value of the spin of the terms), while the second represent the number of terms included in the model atom. In our case $S = 2/3$ and we decided to take into account simply 2 terms. The following lines define the term levels included in the model. The infromartion for each term consist of a line with an idex (in our case 1 and 2) that is used just to label each term and the value of $2L$ (with L the electronic orbital angular momentum). Then, for each term, there is a list containing the energy separation in cm^{-1} between each J-level and the level with the smallest absolute value of J. Finally, we provide the list of transitions; the first number simply indicates the number of radiative transitions included in the model. Then, the list contains the following numbers

for each transitons: index number, index of the lower level, index of upper level, Einstein coefficient for spontaneous emission A_{ul} of the transition, the modification factor $f(n)$, modification factore $f(w)$ and value of J^1_0/J^0_0. The modification factors $f(n)$ and $f(w)$ are used to modify the intensity and the anisotropy of the radiation field, respectively. As discussed in 5.3.4, we have fixed these values to reduce the number of free parameters. The value J^1_0/J^0_0 is different from zero if the radiation illuminating the atoms has non-zero net circular polarisation; we set this parameter to zero.

Tab. A.1.: Data transition for the Fe II 4508.288 Å line, taken from NIST database.

E_i $[cm^{-1}]$	Conf	Term	J_i	E_f $[cm^{-1}]$	Conf	Term	J_f
23031.2829	$3d^6(^3F2)4s$	b^4F	$3/2$	45206.4704	$3d^6(^5D)4p$	z^4D°	$1/2$

iron_4508.mod

```
3
2
1        6
                605.912
                779.062
                908.068
                0.00
2        4
               -759.562
               -421.684
               -162.277
                0.00
 1
1    1    2    7.00d5    4508.288    1.0000000    4.0000000    0.0000000
```

Fig. A.13.: The implemented atomic model.

A.4 Hazel code results

Here we report the complete collection of the variable Stokes Q/I and U/I LSD profiles of 89 Herculis (black lines), fitted with HAZEL code. As explained in 5.3.4, three slabs (dashed lines) are necessary to reproduce the observational data: a stationary feature in absorption (black), a blueshifted (blue) and a redshifted (red) emission lines. The solid (green) continuum represent the sum of the three components.

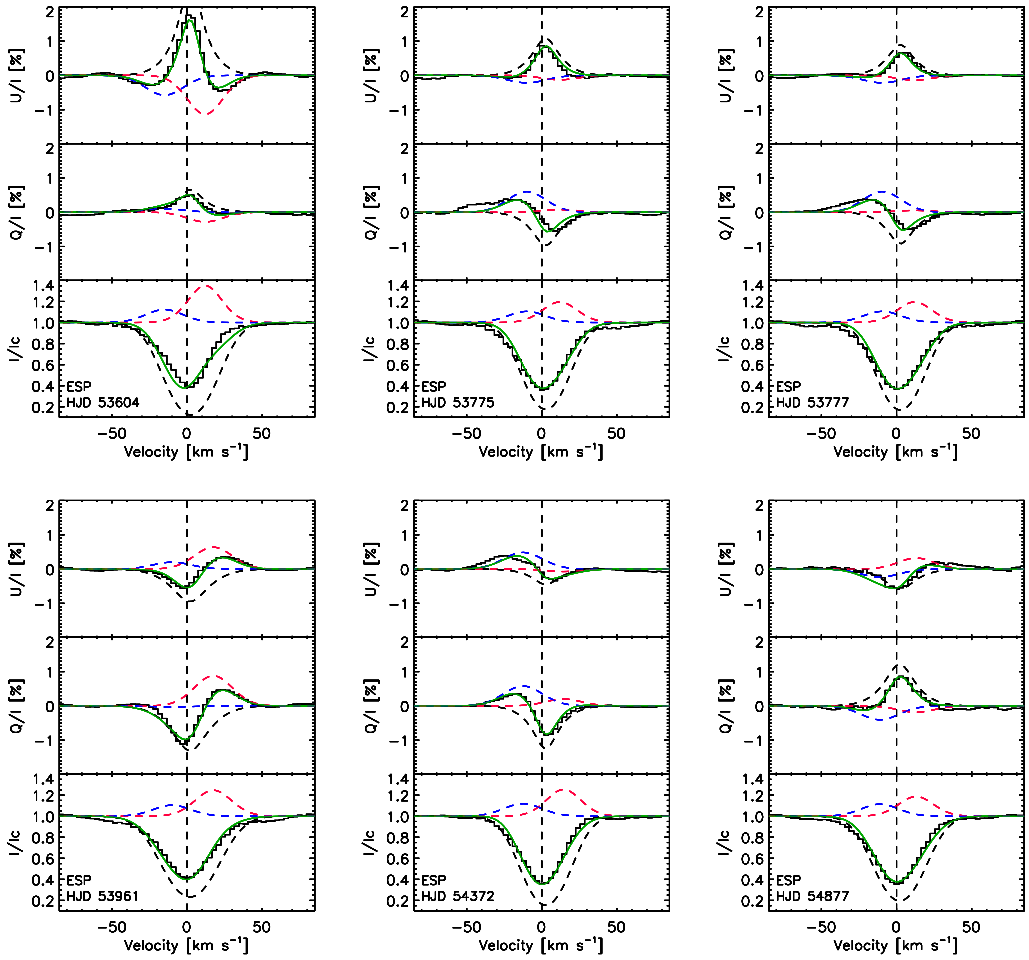

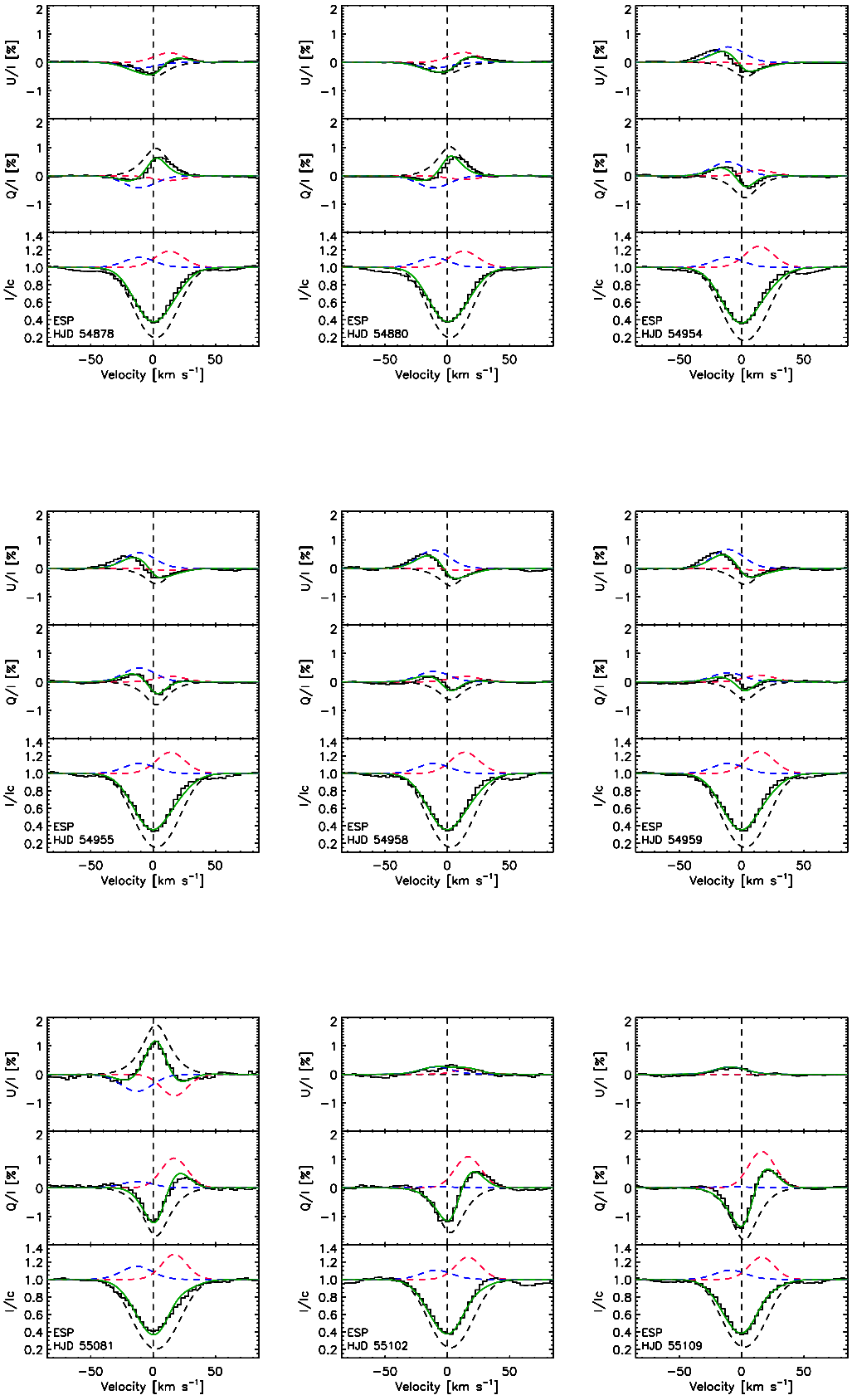
U/I [%]
Q/I [%]
I/Ic
ESP
HJD 54878
HJD 54880
HJD 54954
HJD 54955
HJD 54958
HJD 54959
HJD 55081
HJD 55102
HJD 55109
Velocity [km s^{-1}]

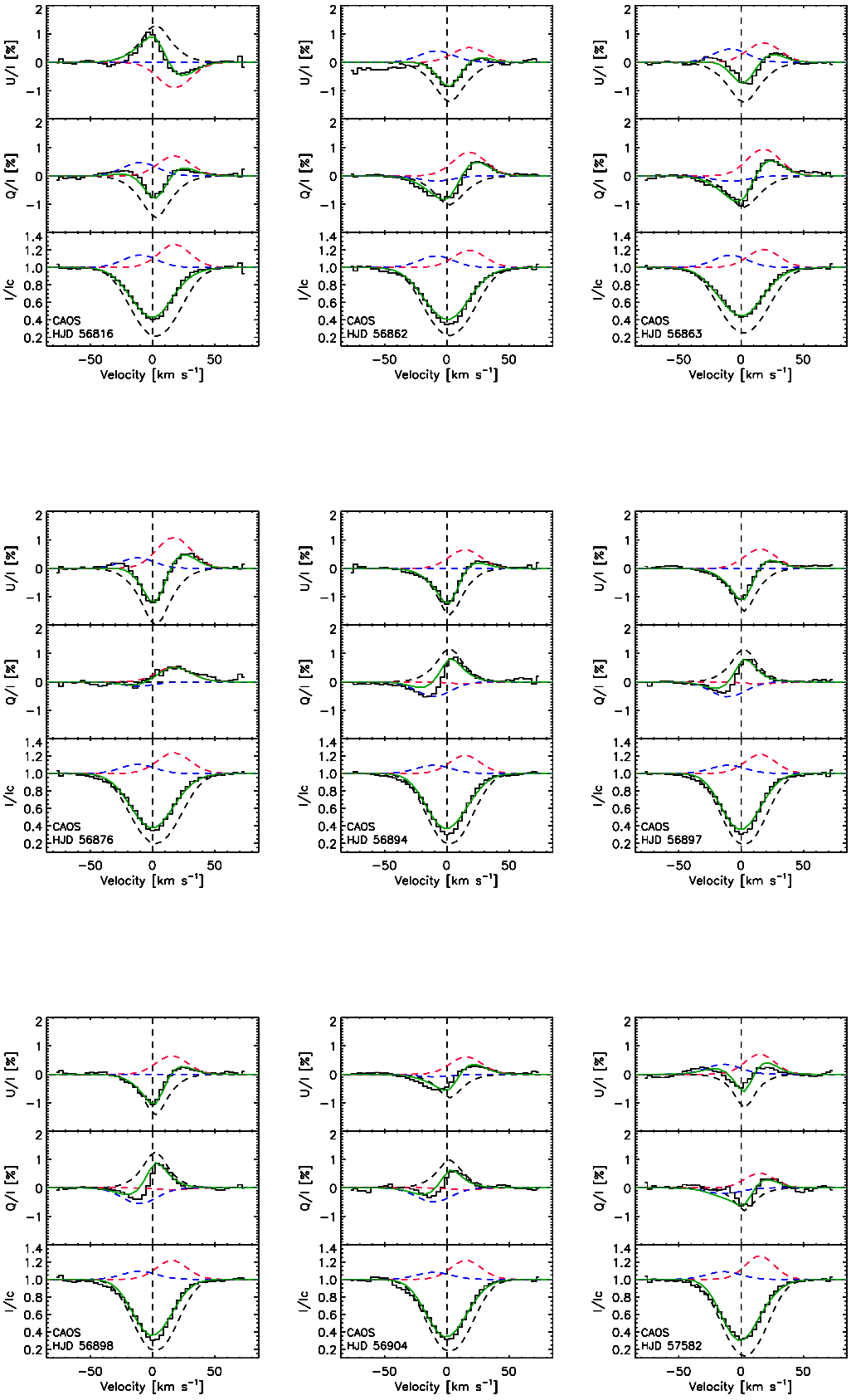
U/I [%]
Q/I [%]
I/Ic
CAOS
HJD 56816
HJD 56862
HJD 56863
HJD 56876
HJD 56894
HJD 56897
HJD 56898
HJD 56904
HJD 57582
Velocity [km s^{-1}]

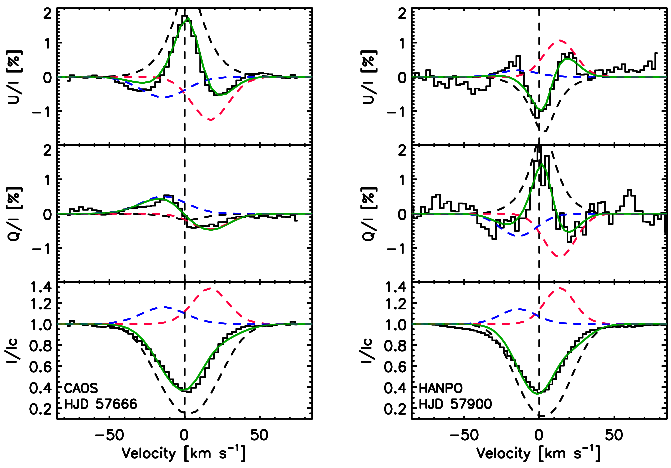
U/I [%]
Q/I [%]
I/Ic
CAOS
HJD 57666
HANPO
HJD 57900
Velocity [km s^{-1}]

Bibliography

Aerts C., Christensen-Dalsgaard J., Kurtz D. W., 2010, aste.book

Akras S., Ramírez Vélez J. C., Nanouris N., Ramos-Larios G., López J. M., Hiriart D., Panoglou D., 2017, MNRAS, 466, 2948

Alecian E., et al., 2008, A&A, 481, L99

Anderson E., Francis C., 2012, AstL, 38, 331

Appenzeller I., et al., 1998, Msngr, 94, 1

Arellano Ferro A., 1984, PASP, 96, 641

Asensio Ramos A., Trujillo Bueno J., Landi Degl'Innocenti E., 2008, ApJ, 683, 542

Asensio Ramos A., Martínez González M. J., Manso Sainz R., Corradi R. L. M., Leone F., 2014, ApJ, 787, 111

Aurière M., et al., 2009, A&A, 504, 231

Aurière M., et al., 2015, A&A, 574, A90

Aurière M., et al., 2016, A&A, 591, A119

Bagnulo S., Wade G. A., Donati J.-F., Landstreet J. D., Leone F., Monin D. N., Stift M. J., 2001, A&A, 369, 889

Bagnulo S., Szeifert T., Wade G. A., Landstreet J. D., Mathys G., 2002, A&A, 389, 191

Bagnulo S., Fossati L., Landstreet J. D., Izzo C., 2015, A&A, 583, A115

Babcock H. W., 1947, ApJ, 105, 105

Balick B., 1987, AJ, 94, 671

Balick B., Frank A., 2002, ARA&A, 40, 439

Berio P., et al., 2011, A&A, 535, A59

Bernacca P. L., Perinotto M., 1970, CoAsi, 239

Beuzit J.-L., et al., 2008, SPIE, 7014, 701418

Berdyugina S. V., Berdyugin A. V., Fluri D. M., Piirola V., 2008, ApJ, 673, L83

Berdyugina S. V., Berdyugin A. V., Fluri D. M., Piirola V., 2011, ApJ, 728, L6

Berdyugina S. V., Kuhn J. R., Harrington D. M., Šantl-Temkiv T., Messersmith E. J., 2016, IJAsB, 15, 45

Böhm-Vitense E., 1956, PASP, 68, 57

Boyle R. P., Aspin C., Coyne G. V., McLean I. S., 1986, A&A, 164, 310

Budker D., Romalis M., 2007, NatPh, 3, 227

Bujarrabal V., Castro-Carrizo A., Alcolea J., Sánchez Contreras C., 2001, A&A, 377, 868

Bujarrabal V., van Winckel H., Neri R., Alcolea J., Castro-Carrizo A., Deroo P., 2007, A&A, 468, L45

Burki G., Mayor M., Rufener F., 1980, A&AS, 42, 383

Bressan A., Marigo P., Girardi L., Salasnich B., Dal Cero C., Rubele S., Nanni A., 2012, MNRAS, 427, 127

Cayrel de Strobel G., Soubiran C., Ralite N., 2001, A&A, 373, 159

Cardini D., 2005, A&A, 430, 303

Cenarro A. J., et al., 2007, yCat, 837,

Chandrasekhar S., 1946, ApJ, 103, 351

Clarke D., 1965, MNRAS, 130, 75

Clarke D., Schwarz H. E., 1984, A&A, 132, 375

Clarke D., 2009, Stellar polarimetry, John Wiley & Sons

Cohen-Tannoudji, C., Dupont-Roc, J., Haroche, S. and Laloë, F., 1969, Physical Review Letters, 22(15), p.758.

Cosentino R., et al., 2012, SPIE, 8446, 84461V

Degl'Innocenti M., Landolfi M., 2006, Polarization in spectral lines, Springer Science & Business Media, Vol.307

Dekker H., D'Odorico S., Kaufer A., Delabre B., Kotzlowski H., 2000, SPIE, 4008, 534

Deroo P., 2007, apn4.conf, 72

Diaz-Cordoves J., Claret A., Gimenez A., 1995, A&AS, 110, 329

di Benedetto G. P., Ferluga S., 1990, A&A, 236, 449

Donahue R. A., Rao L. M., Baliunas S. L., Dupree A. K., 1993, ASPC, 45, 285

Donati J.-F., Semel M., Rees D. E., 1992, A&A, 265, 669

Donati J.-F., Semel M., Carter B. D., Rees D. E., Collier Cameron A., 1997, MNRAS, 291, 658

Donati J.-F., Catala C., Landstreet J. D., Petit P., 2006, ASPC, 358, 362

Donati J.-F., et al., 2008, MNRAS, 386, 1234

Eaton J. A., 1993, AJ, 106, 2081

Eaton J. A., Henry G. W., Odell A. P., 2008, ApJ, 679, 1490

Emde C., et al., 2010, Atmospheric Chemistry and Physics, 10(2):383-96

Fabas N., Lèbre A., Gillet D., 2011, A&A, 535, A12

Fernie J. D., 1981, ApJ, 243, 576

Fernie J. D., 1983, ApJS, 52, 7

Fernie J. D., 1986, ApJ, 306, 642

Fernie J. D., 1989, PASP, 101, 171

Fernie J. D., 1990, PASP, 102, 1143

Fernie J. D., 1991, PASP, 103, 1087

Fernie J. D., Seager S., 1993, PASP, 105, 751

Ferrario L., de Martino D., Gänsicke B. T., 2015, SSRv, 191, 111

Foster L. V., 1938, JOSA, 124, 126

Geise K., Stencel R. E., Manset N., Harrington D., Kuhn J., 2012, JAVSO, 40, 767

Giridhar S., Goswami A., Kunder A., Muneer S., Selvakumar G., 2013, yCat, 355,

Gisler D., et al., 2004, SPIE, 5492, 463

Goosmann R. W., Gaskell C. M., Marin F., 2014, AdSpR, 54, 1341

Gorlova N., Lobel A., Burgasser A. J., Rieke G. H., Ilyin I., Stauffer J. R., 2006, ApJ, 651, 1130

Gray, D.F., 2005, The observation and analysis of stellar photospheres. Cambridge University Press.

Hajian A. R., et al., 1998, ApJ, 496, 484

Happer W., 1972, RvMP, 44, 169

Harrington D. M., Kuhn J. R., 2009, ApJS, 180, 138

Harrington D. M., Meech K. J., Kolokolova L., Kuhn J. R., Whitman K., 2009, diwo.conf, 155

Hatzes A. P., Cochran W. D., 1999, MNRAS, 304, 109

Hekker S., Meléndez J., 2007, A&A, 475, 1003

Herschel W., 1801, RSPT, 91, 265

Herwig F., 2005, ARA&A, 43, 435

Hilditch, Ronald W., 2001, An introduction to close binary stars, Cambridge University Press

Hillen M., et al., 2013, A&A, 559, A111

Hillen M., et al., 2014, A&A, 568, A12

Hoffleit D., Warren W. H., Jr., 1995, yCat, 5050

Hohle M. M., Neuhauser R., Schutz B. F., 2010, yCat, 1133,

Hoogzaad S. N., Molster F. J., Dominik C., Waters L. B. F. M., Barlow M. J., de Koter A., 2002, A&A, 389, 547

Hough J. H., Lucas P. W., 2003, ESASP, 539, 11

Hough J. H., Lucas P. W., Bailey J. A., Tamura M., 2003, SPIE, 4843, 517

Huggins P. J., Mauron N., Wirth E. A., 2009, MNRAS, 396, 1805

Huensch M., Reimers D., 1995, A&A, 296, 509

Hussain G. A. J., Alecian E., 2014, IAUS, 302, 25

Israelian G., Lobel A., de Jager C., Musaev F., 1998, ASPC, 154, 1601

Jennens P. A., Helfer H. L., 1975, MNRAS, 172, 667

Jofré E., Petrucci R., Saffe C., Saker L., de la Villarmois E. A., Chavero C., Gómez M., Mauas P. J. D., 2015, A&A, 574, A50

Johns-Krull C. M., 2007, ApJ, 664, 975

Jones M. I., Jenkins J. S., Rojo P., Melo C. H. F., 2011, A&A, 536, A71

Jordan S., Bagnulo S., Werner K., O'Toole S. J., 2012, A&A, 542, A64

Kafka S., 2016, acps.conf, 4

Kaler J. B., 2011, stsp.book

Kastler, A., J. phys. radium 11, no. 6 (1950): 255-265.

Kastler, A., JOSA 47.6 (1957): 460-465.

Kaufer A., Stahl O., Tubbesing S., Nørregaard P., Avila G., Francois P., Pasquini L., Pizzella A., 1999, Msngr, 95, 8

Kemp J. C., Swedlund J. B., Landstreet J. D., Angel J. R. P., 1970, ApJ, 161, L77

Kervella P., Thévenin F., Morel P., Berthomieu G., Bordé P., Provost J., 2004, A&A, 413, 251

Khalilov A. M., Hasanova A. R., Shustarev P. N., 2010, AzAJ, 5, 23

Kipper T., 2011, BaltA, 20, 65

Kitchin C. R., 2003, Astrophysical techniques, CRC press

Klochkova V. G., 2009, AstL, 35, 457

Klochkova V. G., 2014, AstBu, 69, 279

Kloppenborg B. K., et al., 2015, ApJS, 220, 14

Koch R. H., Pfeiffer R. J., 1982, AJ, 87, 1409

Kochukhov O., Makaganiuk V., Piskunov N., 2010, A&A, 524, A5

Koncewicz R., Jordan C., 2007, MNRAS, 374, 220

König B., Guenther E. W., Esposito M., Hatzes A., 2006, MNRAS, 365, 1050

Koning N., Kwok S., Steffen W., 2011, ApJ, 740, 27

Konstantinova-Antova R., et al., 2008, AIPC, 1043, 405

Kovtyukh V. V., Gorlova N. I., Belik S. I., 2012, MNRAS, 423, 3268

Kuhn J. R., Berdyugina S. V., Fluri D. M., Harrington D. M., Stenflo J. O., 2007, ApJ, 668, L63

Kuhn J. R., Geiss B., Harrington D. M., 2011, ASPC, 437, 245

Kunasz P. B., Morrison N. D., 1982, ApJ, 263, 226

Kurucz R. L., 1993, sssp.book

Kurucz R. L., 2005, MSAIS, 8, 14

Landi Degl'Innocenti E., Landolfi M., 2004, ASSL, 307

Leal-Ferreira M. L., Vlemmings W. H. T., Diamond P. J., Kemball A., Amiri N., Desmurs J.-F., 2012, A&A, 540, A42

Lèbre A., Fabas N., Gillet D., 2011, ASPC, 448, 999

Lèbre A., Aurière M., Fabas N., Gillet D., Herpin F., Petit P., Konstantinova-Antova R., 2014, IAUS, 302, 385

Leone F., Bruno P., Cali A., Claudi R., Cosentino R., Gentile G., Gratton R., Scuderi S., 2003, SPIE, 4843, 465

Leone F., Catanzaro G., 2004, A&A, 425, 271

Leone F., Martínez González M. J., Corradi R. L. M., Privitera G., Manso Sainz R., 2011, ApJ, 731, L33

Leone F., Corradi R. L. M., Martínez González M. J., Asensio Ramos A., Manso Sainz R., 2014, A&A, 563, A43

Leone F., et al., 2016a, AJ, 151, 116

Leone F., et al., 2016b, SPIE, 9908, 99087K

Leone F., Scalia C., Gangi M., Giarrusso M., Munari M., Scuderi S., Trigilio C., Stift M. J., 2017, ApJ, 848, 107

Levesque E. M., Massey P., Olsen K. A. G., Plez B., Josselin E., Maeder A., Meynet G., 2005, ApJ, 628, 973

Lignières F., Petit P., Böhm T., Aurière M., 2009, A&A, 500, L41

Luck R. E., Bond H. E., Lambert D. L., 1990, ApJ, 357, 188

Luck R. E., 2014, AJ, 147, 137

Luck R. E., 2015, yCat, 515

Lyubimkov L. S., Lambert D. L., Rostopchin S. I., Rachkovskaya T. M., Poklad D. B., 2010, MNRAS, 402, 1369

Lyubimkov L. S., Lambert D. L., Kaminsky B. M., Pavlenko Y. V., Poklad D. B., Rachkovskaya T. M., 2012, MNRAS, 427, 11

Lyubimkov L. S., Lambert D. L., Korotin S. A., Rachkovskaya T. M., Poklad D. B., 2015, MNRAS, 446, 3447

Mallik S. V., 1999, A&A, 352, 495

Manchado A., Villaver E., Stanghellini L., Guerrero M. A., 2000, ASPC, 199, 17

Manso Sainz R., Trujillo Bueno J., 2003, PhRvL, 91, 111102

Marin F., Goosmann R. W., Gaskell C. M., Porquet D., Dovčiak M., 2012, A&A, 548, A121

Martínez González M. J., Asensio Ramos A., Manso Sainz R., Corradi R. L. M., Leone F., 2015, A&A, 574, A16

Massarotti A., Latham D. W., Stefanik R. P., Fogel J., 2008, AJ, 135, 209

Mathias P., et al., 2018, arXiv, arXiv:1804.01831

Mathys G., 1989, FCPh, 13, 143

Mathys G., 1994, A&AS, 108, 547

Mathys G., 2017, A&A, 601, A14

Mathur S., et al., 2011, ApJ, 741, 119

McDonald I., Zijlstra A. A., Boyer M. L., 2012, MNRAS, 427, 343

McLean I. S., Coyne G. V., 1978, ApJ, 226, L145

McWilliam A., 1990, ApJS, 74, 1075

Molinari E., Conconi P., Pucillo M., 1997, MmSAI, 68, 231

Monnier J. D., 2003, RPPh, 66, 789

Morin J., et al., 2008, MNRAS, 390, 567

Moulds V. E., Watson C. A., Bonfils X., Littlefair S. P., Simpson E. K., 2013, MNRAS, 430, 1709

Moultaka J., Ilovaisky S. A., Prugniel P., Soubiran C., 2004, PASP, 116, 693

Mu T., et al., 2014, Optics Express 22.5, 5043-5051

Nordgren T. E., et al., 1999, AJ, 118, 3032

Odell A. P., 1979, PASP, 91, 326

Odell A. P., 1981, ApJ, 246, L77

Osmer P., 1968, PASP, 80, 563

Paletou F., 2012, A&A, 544, A4

Panchuk V., Klochkova V., Najdenov I., Yushkin M., 2007, uasb.conf, 179

Pasinetti Fracassini L. E., Pastori L., Covino S., Pozzi A., 2001, A&A, 367, 521

Percy J. R., Bakos A., Henry G., 2000, JAVSO, 28, 164

Petit V., Wade G. A., Drissen L., Montmerle T., Alecian E., 2008, MNRAS, 387, L23

Piau L., Kervella P., Dib S., Hauschildt P., 2011, A&A, 526, A100

Piirola V., 1973, A&A, 27, 383

Piirola V., 1988, prco.book, 735

Piirola V., Berdyugin A., Mikkola S., Coyne G. V., 2005, ApJ, 632, 576

Prugniel P., Vauglin I., Koleva M., 2011, A&A, 531, A165

Roberts D. H., Lehar J., Dreher J. W., 1987, AJ, 93, 968

Reffert S., Bergmann C., Quirrenbach A., Trifonov T., Künstler A., 2015, A&A, 574, A116

Reiners A., 2012, LRSP, 9, 1

Royer F., Grenier S., Baylac M.-O., Gómez A. E., Zorec J., 2002, A&A, 393, 897

Saar S. H., Seager S., 2003, ASPC, 294, 529

Sabin L., Wade G. A., Lèbre A., 2015, MNRAS, 446, 1988

Samus N. N., Kazarovets E. V., Durlevich O. V., Kireeva N. N., Pastukhova E. N., 2009, yCat, 1,

Sargent W. L. W., Osmer P. S., 1969, ASSL, 13, 57

Scalia C., Leone F., Gangi M., Giarrusso M., Stift M. J., 2017, MNRAS, 472, 3554

Scargle J. D., 1982, ApJ, 263, 835

Schmid H. M., et al., 2005, ASPC, 343, 89

Schwarz H. E., Clarke D., 1984, A&A, 132, 370

Seager S., Whitney B. A., Sasselov D. D., 2000, ApJ, 540, 504

Semel M., 1989, A&A, 225, 456

Semel M., Li J., 1996, SoPh, 164, 417

Semel M., Ramírez Vélez J. C., Martínez González M. J., Asensio Ramos A., Stift M. J., López Ariste A., Leone F., 2009, A&A, 504, 1003

Sennhauser C., Berdyugina S. V., Fluri D. M., 2009, A&A, 507, 1711

Soubiran C., Bienaymé O., Mishenina T. V., Kovtyukh V. V., 2008, A&A, 480, 91

Spencer, G. H., and M. V. R. K. Murty. "General ray-tracing procedure." JOSA 52.6 (1962): 672-678.

Stam D. M., 2003, ESASP, 539, 615

Stam D. M., Hovenier J., Waters R., 2003, ASPC, 294, 535

Stam D. M., Hovenier J. W., Waters L. B. F. M., 2004, A&A, 428, 663

Stam D. M., Hovenier J. W., Waters L. B. M. F., 2005, ASPC, 343, 207

Stam D. M., 2008, A&A, 482, 989

Sterzik M. F., Bagnulo S., Palle E., 2012, Natur, 483, 64

Takeda Y., Taguchi H., Yoshioka K., Hashimoto O., Aikawa T., Kawanomoto S., 2007, PASJ, 59, 1127

Takeda G., Ford E. B., Sills A., Rasio F. A., Fischer D. A., Valenti J. A., 2008, yCat, 216,

Tessore B., Lèbre A., Morin J., 2015, sf2a.conf, 429

Thompson A. R., Moran J. M., Swenson G. W., Jr., 2017, Interferometry and synthesis in radio astronomy, Springer

Tinbergen J., Rutten R., 1992

Trujillo Bueno J., Landi Degl'Innocenti E., 1997, ApJ, 482, L183

Trujillo Bueno J., 2005, ESASP, 600, 7.1

Uesugi A., Fukuda I., 1970, MmKyo, 33, 205

Valenti J. A., Marcy G. W., Basri G., 1995, ApJ, 439, 939

Valdes F., Gupta R., Rose J. A., Singh H. P., Bell D. J., 2004, ApJS, 152, 251

van Leeuwen F., 2007, A&A, 474, 653

van Winckel H., 2003, ARA&A, 41, 391

Vink J. S., Drew J. E., Harries T. J., Oudmaijer R. D., 2005, ASPC, 343, 232

Wade G. A., Donati J.-F., Landstreet J. D., Shorlin S. L. S., 2000, MNRAS, 313, 823

Waters L. B. F. M., Waelkens C., Mayor M., Trams N. R., 1993, A&A, 269, 242

Wiktorowicz S. J., Matthews K., 2008, PASP, 120, 1282

Wiktorowicz S. J., 2009, ApJ, 696, 1116

Wolff S. C., 1983, NASSP, 463

Worley C. E., 1956, PASP, 68, 62

Wu Y., Singh H. P., Prugniel P., Gupta R., Koleva M., 2011, A&A, 525, A71

Yan H., Lazarian A., 2006, ApJ, 653, 1292

Yan H., Lazarian A., 2007, AAS, 39, 19.09

Yan H., Lazarian A., 2008, ApJ, 677, 1401

Yan H., Lazarian A., 2012, JQSRT, 113, 1409

List of Figures

List of Tables

Acknowledgement

I would like to thank my thesis advisor Prof. Francesco Leone, for having accompanied me in these years, for his endless patience and for the passion that he conveyed to me. I would also like to thank all the group of the instrument CAOS, from astronomers to technicians, to night assistants, for their help with the use and the maintenance of the telescope.

I thank my friend and colleague Cesare Scalia, for all the nights spent together at the telescope and for his support in doing science.

I thank Prof. Huirong Yan and Dr. Heshou Zhang, for the time spent at DESY Institute.

Finally, I thank my family and my friends, for their support.

Vorrei innanzitutto ringraziare il Professore Francesco Leone, per avermi accompagnato in questi anni, per la sua infinita pazienza e per tutto l'entusiasmo che è riuscito a trasmettermi. Vorrei ringraziare tutto il team di CAOS, dagli astronomi ai tecnici, agli assistenti notturni, per il loro aiuto nell'uso e nella manutenzione del telescopio.

Ringrazio il mio amico e collega Cesare Scalia, per tutte le notti spese insieme al telescopio e per il suo supporto nel fare scienza.

Ringrazio la Professoressa Huirong Yan e Heshou Zhang, per il tempo trascorso insieme presso il DESY.

Infine, ringrazio la mia famiglia e i miei amici, per il loro supporto.